Atomistic simulation of the structure and stability of hydrated mineral surfaces

de Leeuw, Nora H.

Award date:
1997

Awarding institution:
University of Bath

Atomistic Simulation of the Structure and Stability of Hydrated Mineral Surfaces

Submitted by N.H. de Leeuw

for the degree of PhD

of the University of Bath

1997

ProQuest LLC
789 East Eisenhower Parkway
P.O. Box 1346
Ann Arbor, MI 48106-1346

ABSTRACT

In this thesis we have used atomistic simulation techniques to investigate the effect of dissociative and molecular adsorption of water on the surface structure, stability and morphology of some important oxides.

Chapter 1 gives an overview of some previous studies of surfaces and adsorbates, including both atomistic simulations and electronic structure calculations. We also discuss some important experimental techniques used for surface characterisation.

Chapter 2 introduces the theoretical methods employed in atomistic simulations. It describes the mathematical methods used in the calculations and the way in which surfaces are generated and surface energies are obtained.

In chapter 3 we discuss the potential model and list the various potential parameters used for the simulations in chapters 4, 5 and 6. In addition we describe the derivation of the potential parameters for the transferable water molecule which we had to develop in order to model physisorption of water on oxide surfaces such that the parameters would be compatible with the potential parameters of the oxides.

Chapter 4 describes the static energy minimisation simulations of chemisorption and physisorption of water onto various MgO and CaO surfaces in a series of partial coverages. The surfaces are chosen to give a range of adsorption sites of varying coordination number to model defects on experimental surfaces. The surface structure and stability are evaluated and the calculated hydration energies are compared with experimental and other computational results. We then present Molecular Dynamics results of MgO crystals in a liquid water environment.

In chapter 5 α-alumina is investigated. The potential model is first verified against the structure of an alumina hydroxide and a hydrated β-alumina. Results are presented on hydroxylated and molecularly hydrated surfaces. The surface relaxations are studied and the various morphologies compared. Hydration energies of chemisorption and physisorption are compared with experiment.

In chapter 6 the potential model is first verified against the structure and formation energy of calcium carbonate hexahydrate, ikaite, after which simulation results of the three calcium carbonate polymorphs calcite, aragonite and vaterite are presented. The surface structures are compared with experimental findings. The effect of hydration on the equilibrium morphology is discussed and compared with the growth morphology.

Acknowledgements

First and foremost I would like to thank my supervisor Dr S.C. Parker for his help and advice during my PhD. Without his patience and good humour my time in Bath would not have been either as productive or as pleasant.

I would also like to especially thank Drs G.W. Watson and P.M. Oliver whose help with anything computational was indispensible. Many thanks also to the rest of the solid state computational group at Bath, Toby Kelsey, Paul Baram, John Purton, Duncan Harris, Manon Higgins and Susan Redfern for their help and not least companionship throughout my PhD.

I would like to acknowledge EPSRC for my studentship and Molecular Simulations Inc. for the provision of Insight II which was used for many of the pictures in this thesis.

Finally, I would like to thank my family and friends without whose continuous interest and support this thesis would probably never have been written.

Nora H. de Leeuw

September 1997

Contents

1 INTRODUCTION

Over the last few decades computational methods have played an increasingly important role in the elucidation of the bulk and surface structures of minerals and the effect of adsorbent species on those surfaces. These tools were initially used to reproduce and interpret experimental data but in recent years they have become predictive (Catlow *et al.* 1984, 1993). The computational methods can roughly be divided into two techniques: (i) Atomistic simulation; based on the description of interatomic forces by pair potential functions, the accuracy of which dictates the quality of the simulation results (Voter 1996). These methods are often used for materials for which at least some experimental properties, such as structure and elastic properties and possibly phonon spectra, are known. (ii) In contrast, electronic structure calculations, which involve solving the Schrodinger equation for the investigated system to some level of approximation, have the objective to determine all these properties from first principles (Vitek 1996). We will give a brief overview of both methods, including a short section on programs used to model surfaces using atomistic simulation techniques, followed by a brief discussion of experimental methods used to investigate minerals and their surfaces.

1.1 Atomistic Simulations

Atomistic simulation methods have been used over the years to study a variety of problems ranging from the modelling of transport properties such as diffusion and conductivity in ionic crystals, to defect studies and even dislocation structures

(Catlow 1980, Catlow and Cormack 1982). Of particular interest, for example, to catalysis is the study of surface structure and reactivity and the importance of certain surface defects in chemisorption reactions (Colbourn and Mackrodt 1982).

Pioneering work on surface studies by Stewart and Mackrodt (1977) modelled point defects at surfaces while Tasker (1979, 1979a) developed methods more appropriate to the investigation of extended surfaces and ordered overlayers. Tasker (1979a) defined the three different types of surfaces which occur in an ionic crystal and which are described in more detail in chapter 2. He demonstrated that the divergence in surface energy which occurs for certain charged surfaces is a real effect which should be taken into account when interpreting LEED data. In another study Tasker (1979) determined the surface structure and energies of the low index faces of a range of alkali halide crystals, all with the rocksalt structure. One of his findings was that anions and cations in the surface give different relaxations resulting in a rumpled surface. In addition, his calculated surface energies decreased with increasing ion size and were in agreement with extrapolated experimental data.

Early simulations of oxides also concentrated almost exclusively on those with the NaCl structure, such as MgO and NiO. Apart from the fact that their relatively simple structure made calculations more straightforward, experimental data for these materials were known against which to test the models (Colbourn 1992). Most of these simulations concentrated on the planar surfaces although Tasker and Duffy (1984), for instance, studied the structure and properties of high index faces of MgO

and NiO as models for real stepped surfaces which are important in providing active sites for catalysis.

After the success of these early simulations a host of different problems have been addressed from the segregation of impurity ions at oxide surfaces (Colbourn *et al.* 1983, Tasker *et al.* 1985, Davies *et al.* 1989) to the simulation of more complex oxides such as Al_2O_3 and La_2CuO_4 (Mackrodt *et al.* 1987, Mackrodt 1989) and diffusion processes in grain boundaries (Duffy and Tasker 1986). With the introduction of temperature *via* Lattice Dynamics (Harding *et al.* 1989) or Molecular Dynamics simulations, studies of reconstruction or facetting of surfaces have also become more common, *e.g.* the work of Oliver *et al.* (1994a, 1995) on micro-facetted TiO_2 and NiO surfaces and Mulheran (1993) and Baudin *et al.* (1997) on the relaxation of the MgO {100} surface and reconstruction of the MgO {111} surface respectively.

In addition to metal oxides, the development of models for oxy-anions such as SO_4^{2-} and CO_3^{2-} meant that the surfaces of more complicated structures such as $CaCO_3$ (Titiloye *et al.* 1991, Parker *et al.* 1993a) and $BaSO_4$ (Parker *et al.* 1993) can now be modelled routinely. With the capability of modelling surfaces and defects therein, morphologies of various mineral structures have been evaluated and found to reproduce and hence explain experimental morphologies accurately. Titiloye and coworkers (Titiloye *et al.* 1991, 1993), for instance, predicted the influence of the growth additives Mg^{2+}, Li^+ and HPO_4^{2-} on the morphology of calcite which was confirmed by experiment, while Oliver *et al.* (1993) demonstrated the importance of

Ni^{3+} ions for the stabilisation of the {111} surface of NiO to obtain the experimental morphology.

Following calculations of impurity ions and defects in the lattice itself, the next type of simulations are the behaviour of adsorbates on surfaces which is of particular interest to processes such as catalysis and corrosion. Picaud *et al.* (1992), for instance, studied the geometry of NH_3 and H_2O clusters on MgO and Si surfaces and found different patterns of adsorption for the two adsorbates as well as the two substrates.

This work on surfaces has been facilitated by the development of simulation codes which are widely used by the community. The simulation code from which many of the recent codes stem is HADES (Harwell Automatic Defect Evaluation System) which was introduced by Lidiard and Norgett in 1972 to model point defects in ionic crystals. HADES and its successor CASCADE (Leslie 1982) are designed to model bulk material rather than surfaces and Lidiard and Norgett (1972) calculated the energies of rare gas impurities Ar and Kr in alkali halide crystals. CHAOS (Computer simulation HAdes On Surfaces) (Duffy and Tasker 1984), which is more fully described in chapter 2, is a direct modification of HADES used to model point defects, either charged or neutral, on surfaces. In this method the point defect is on the surface at the centre of a relatively small hemisphere of lattice ions which have complete freedom of movement while a wider layer of ions around this hemisphere is kept fixed at their equilibrium positions.

In the same way that HADES had a preprocessor which modelled the perfect lattice properties, PLUTO (Catlow and Norgett 1976) succeeded by first METAPOCS (Catlow *et al.* 1984) and then by PARAPOCS (Parker and Price 1989), Tasker (1978) introduced the code MIDAS (Minimisation for Interfacial Defects And Surfaces) to model perfect surfaces. Like HADES and CHAOS it also uses a two-region approach (chapter 2) but with the crystal divided into planes parallel to the surface and periodically repeating in two directions. The method is more fully described in chapter 2. In addition to studying surfaces this code can also model grain boundaries, both twist and tilt boundaries, and even epitaxy between different materials. Due to the periodic nature of this approach an array of point defects may be positioned at the surface allowing for different defect coverages and as the surface lattice vectors may be changed supercells can be introduced.

More recently two codes based on MIDAS have been developed; MARVIN and METADISE. MARVIN was introduced in 1995 (Gay and Rohl 1995) to model surfaces and interfaces and was used to simulate the surfaces of α-alumina and zircon and obtain growth and equilibrium morphologies. METADISE (Minimum Energy Techniques Applied to Dislocations Interfaces and Surface Energies) (Watson *et al.* 1996) is designed not only to model surfaces and interfaces but also dislocations in both bulk crystal and at surfaces. The various applications were demonstrated for magnesium oxide, showing calculations of a selection of tilt grain boundaries, planar and facetted surfaces and bulk dislocations.

1.2 Electronic Structure Calculations

Over the last few years increased computer power and memory has made it possible to model surfaces using electronic structure calculations. These methods fall roughly into two categories, Hartree Fock methods and calculations based on the Density Functional Theory (DFT) within the Local Density Approximation (LDA), with methods such as embedded clusters and tight-binding techniques intermediate between these *ab initio* calculations and atomistic simulations, for instance tight-binding investigations by Barrett *et al.* (1991) of iridium surfaces and Purton *et al.* (1995) of the low-index surfaces of TiO_2 .

It is usually the DFT method, often only treating the valence electrons explicitly and using pseudopotentials for their interactions with the atomic cores, which has been used for surface calculations. Initially used for the investigation of metal surfaces it continues to be applied successfully, *e.g.* the copper (001) surface (Klepeis *et al.* 1996), and metal/metal interfaces such as the investigation of gold layers on various silver surfaces (Leuken *et al.* 1992). The DFT approach is now extensively used for other compounds including oxides, for example Manassidis and Gillan's (1994) investigation of α-alumina surfaces and the work of Schroer *et al.* (1994) whose findings on the surface electronic structures of the semi-conductors ZnO and CdS were in good agreement with experimental results. Other compounds studied include semiconductors such as InAs (Swanston *et al.* 1994) and $ErSi_{1.7}$ (Stauffer *et al.* 1995) and oxides like MgO (Kantorovich *et al.* 1995) and SnO_2 (Goniakowski *et al.* 1996) while work by Ramamoorthy *et al.* (1994, 1994a) on the stoichiometric and

defective surfaces of TiO_2 agreed well with experimental findings of the surface structures of rutile.

Another aspect of surfaces which has been modelled extensively during the last few years is adsorption of various small molecules on metals, such as CO and NH_3 on palladium (Mijoule and Bouteiller 1991) and CO and CH_4 on nickel (Gorling *et al.* 1993, Burghgraef *et al.* 1993), and on oxides. Adsorption on magnesium oxide surfaces has been investigated extensively, *e.g.* the adsorption of NH_3 on the (001) surface by Pugh and Gillan (1994) which yielded adsorption energies in good agreement with thermal desorption measurements. Carbon monoxide on MgO is another well researched subject as for instance the study by Nygren and Pettersson (1996) measuring binding energies for regular and defective sites on the (001) surface. TiO_2 is another oxide whose adsorption behaviour has been the subject of many studies, *e.g.* the adsorption of CO on acid sites of the rutile (110) surface (Pacchioni *et al.* 1996). The adsorption of water on TiO_2 has also generated much interest, as for instance the periodic Hartree-Fock study by Fahmi and Minot (1994) of the physisorption and consequent dissociation of water on rutile and anatase surfaces. Goniakowski and Gillan (1996a) investigated both molecular and dissociative adsorption of water on the (110) surfaces of both TiO_2 and SnO_2.

Apart from these static calculations, electronic structure molecular dynamics simulations have also been performed by various groups as for example the dissociative chemisorption of Cl_2 on silicon (Payne *et al.* 1993, Stich *et al.* 1994). However, these methods are at present restricted by the number of atoms that can be

treated, typically a few tens of atoms, and hence the most efficient approach for modelling a complex inorganic surface or interface is via atomistic simulation methods.

1.3 Experimental Methods

In this section some of the many and varied experimental methods used to probe the surface structure of minerals and adsorbates thereon are briefly discussed. They can be subdivided into non-destructive and destructive techniques. In the first instance the surface structure is retained, but with a destructive technique the surface investigated is irreversibly damaged.

1.3.1 Temperature Programmed Desorption (TPD)

Temperature Programmed Desorption is a destructive technique. Desorption is an endothermic process and when the sample is heated desorbing species are detected by, for instance, a mass spectrometer. The energy of desorption E_d is obtained by measuring the mean stay time τ of an adatom on the surface as a function of substrate temperature T. The slope of a plot of τ (on a logarithmic scale) versus 1/T gives the value of E_d (Cvetanovic and Amenomiya 1972, Prutton 1983). A plot showing more than one peak indicates that different species are present on the surface (Campbell 1988). These may be different adsorbed molecules, identical molecules adsorbed at energetically different sites or physisorbed and chemisorbed species.

However, the magnitude of E_d for each peak is often difficult to interpret. Dunski *et al.* (1994) in their TPD study of water on MgO found four energetically different peaks which they interpreted as four differently coordinated sites at the surface. They found that their TPD profiles strongly depended on the degree of surface hydration and the degree of accuracy was only $\pm$20% in some cases. Ito *et al.* (1991) investigated the thermal desorption of methane on MgO and also found several different peaks. On the basis of the values for E_d, supported by Molecular Orbital calculations, they interpreted these to include CH_3 and OH species. Care had to be taken to investigate the sample under vacuum as the presence of molecules such as CO_2 had a poisoning effect by pre-adsorbing at certain sites.

1.3.2 Microcalorimetry

Another destructive technique is microcalorimetry which, on dosing the sample with an amount of gaseous adsorbate, simultaneously measures the adsorbed amount, the heat released, and the equilibrium pressure. Graphs of the evolution of heat with time and change of pressure with time can be plotted giving information of adsorption behaviour. As in TPD, the sample needs to be investigated under vacuum to prevent other species from pre-adsorbing on the surface.

Fubini *et al.* (1989), on investigating the adsorption of water vapour on CaO, found a constant heat of adsorption indicating dissociative adsorption. This was further confirmed by the fact that the adsorption was irreversible.

Although these techniques are destructive they are useful for comparison with simulation because they yield adsorption energies which can be calculated directly.

1.3.3 Photoelectron Spectroscopy

In contrast to the techniques described above, ultra-violet photoelectron spectroscopy (UPS) and X-ray photoelectron spectroscopy (XPS) are non-destructive techniques. However, they still need to be executed under ultra high vacuum (UHV) conditions to prevent contamination of the surface (Hugenschmidt *et al.* 1994).

In both techniques, the surface of the sample is bombarded by photons, ultra-violet radiation for UPS and X-rays for XPS. As a result electrons (photoelectrons) are ejected from the valence (UPS) and/or core (XPS) orbitals of the constituent atoms (Campbell 1988). By considering only elastic collisions, the binding energy E_b of the emitted electron can be obtained by measuring its kinetic energy E_k according to:

$$E_k = h\nu \; - \; E_b \qquad (1.1)$$

where $h\nu$ is the incident radiation. The kinetic energy of the emitted electron can be measured by one of several energy analysers, for instance a magnetic double-focusing spectrometer (Prutton 1983).

In UPS the binding energies concerned are of the order of 10 eV, so that the kinetic energies of the emitted electrons are expected to be in a range of 10-30 eV and hence this technique is associated with valence electrons. In XPS, however, the binding and kinetic energies are expected to be of the order of hundreds of electron-volts (Campbell 1988) and hence probes the core electrons. A plot of the number of photoelectrons versus binding energy shows one or more peaks with energies corresponding to the energies of the various shells. However, detection of the different peaks depends on the instrumental resolution. If the energy difference between two peaks is less than the instrumental resolution, typical 1-2 eV, only one peak will be observed (Hugenschmidt 1994). The difference in binding energies of different peaks in photoelectron spectra of adsorbed species indicate physisorption or chemisorption, at one or more different sites.

Onishi *et al.* (1987) used UPS and XPS to study the adsorption of H_2O and other species on the {100} and {111} surfaces of MgO. Their UPS and XPS data, comprising of a 2.4 eV difference between the binding energies of lattice oxygen and adsorbed oxygen, were consistent with adsorbed hydroxide anions and they therefore concluded that water chemisorbed on both MgO surfaces. Hugenschmidt *et al.* (1994) used TPD and XPS to study the adsorption of water on the TiO_2 {110} surface and found a chemisorbed oxygen peak at 2.7 eV above the peak of bulk oxygen.

Although a powerful technique it is not straightforward to compare directly with atomistic simulation, although comparison with the predicted band structure from electronic structure calculations is an important advantage of the latter. The only

possible way of comparing atomistic simulations is to compare the change of Madelung potential at the surface with the change in binding energy of the electrons.

1.3.4 Low Energy Electron Diffraction (LEED)

LEED is also a non-destructive technique which provides valuable information on the structure of the surface unit cell. Again, it needs to be carried out under UHV conditions.

A LEED pattern is produced when electrons with energies lower than 1000 eV are fired at the material. Any electrons which penetrate into the sample to a depth of more than about five atomic layers will not emerge. However, the electrons which are elastically scattered carry information on the surface atoms, including adsorbed species (Campbell 1988).

The incident beam in LEED experiments consists of mono-energetic electrons with a corresponding de Broglie wavelength λ similar to interatomic distances in surface structures. The LEED pattern produced by the scattered electrons can be analysed: the angular directions of the diffracted beams indicate the nature of the adsorbed species, the spot intensities can be related to interatomic distances and the shape of the spots and the geometry of the pattern determine the symmetry and regularity of the surface (Prutton 1983). However, the fitting procedure is very difficult and it is necessary to have a model as a starting point. Firment (1982), for instance, when investigating thermal facetting of rutile used a computer generated

model of facetted TiO_2 surfaces to help interpret his LEED patterns, clearly a useful potential role for simulations which could provide plausible structures with which to compare.

Henrich (1976) used LEED to investigate the MgO {110} and {111} surfaces. He found that under ion bombardment and annealing the surfaces micro-facet into sets of {100} faces. The facets had to be greater than about 80 Å to be visible on the scale of LEED. Both Lo *et al.* (1978) and Muryn *et al.* (1989) investigated the adsorption of water onto TiO_2 using LEED and found that water initially physisorbs onto the surface but that chemisorption takes place after annealing (Muryn *et al.* 1989) or when adsorbed onto a Ti^{3+} enriched {100} surface (Lo *et al.* 1978).

1.3.5 X-ray and Neutron Diffraction

A technique which is used mainly to study bulk structures is X-ray diffraction.

When a sample is irradiated by X-rays, they penetrate into the bulk and are diffracted by the charge distribution in and around the atoms. The diffracted X-rays are detected and by studying the pattern and taking especial note of the directions where spots are systematically absent due to destructive interference of the scattered waves, the unit cell of the material may be determined (Prutton 1983).

Although X-ray diffraction is a very useful and relatively cheap technique, its main drawback is that only heavy atoms scatter the radiation enough to be visible. A

technique related to X-ray diffraction is neutron diffraction where the sample is radiated by neutrons which are elastically scattered. As neutrons are scattered even less than X-rays by the atoms in the sample, they penetrate even further and this method is therefore even more of a bulk technique than X-ray diffraction (Prutton 1983). Although neutron diffraction is much more expensive than X-ray diffraction, with this technique it is possible to observe light atoms as the scattering factor is variable. It is therefore much used to elucidate the structures of the various phases of ice, for instance the deuterated forms of ice VII and ice VIII (Kuhs *et al.* 1984) and ice IX (La Placa and Hamilton 1972).

A similar method, which is surface sensitive, is X-ray photoelectron diffraction (XPD) whereby X-rays are again used to probe the sample. However, in this instance, as in XPS, photoelectrons are produced and their scattering pattern is observed, giving information about the arrangement of atoms at the surface. Varma *et al.* (1994) used this technique to study the rumpling of the MgO {100} surface.

1.3.6 Infra-red Absorption Spectroscopy

Infra-red spectroscopy is a non-destructive technique used extensively, which does not require ultra-high vacuum conditions (Campbell 1988).

The sample is irradiated with infra-red radiation and the absorption spectrum obtained consists of peaks characteristic of the species making up the sample. Different bonds shift the peaks and therefore the position of the peaks indicates the

presence and bonding of the several components. It is even possible to differentiate between molecules adsorbed on steps or on terraces as they absorb radiation of different frequencies (Campbell 1988).

Infra-red radiation generally penetrates a sample for about 1000 nm compared to about 1 nm in the case of LEED. As such it is a good technique for bulk analysis and adsorbates on surfaces can be detected if the adsorbed species absorb IR radiation while the substrate, usually a thin wafer, is transparent. In other cases however, where the substrate also adsorbs in the infra-red region, this technique is not suitable for surface studies.

Jones *et al.* (1984) investigated the adsorption of water on certain sites of MgO smoke cubes using IR spectroscopy. After treating the sample and exposing it to water vapour they found OH absorption bands in the spectra, indicating chemisorption of water molecules. In contrast, Kittake *et al.* (1993) determined two modes for the adsorption of molecular water on a hydroxylated Cr_2O_3 surface. Water itself was investigated by Marechal (1993) who used IR spectroscopy to study different types of HDO molecules.

Dynamical simulations can be analysed to obtain vibrational frequencies which can then be compared directly with infra-red absorption data.

1.3.7 Scanning Tunnelling Microscopy (STM)

Two techniques which have become almost indispensible over the last few years for probing the atomistic structure of oxide surfaces are scanning tunnelling microscopy (STM) (Binnig *et al.* 1982) and atomic force microscopy (AFM) (Binnig *et al.* 1986).

In STM electrons tunnel from the conducting surface of a sample to the tip of a scanning microscope giving a micrograph of atomic resolution (Sander and Engel 1994). Although STM is possible under a variety of conditions (vacuum, air, liquids) the process is generally carried out in vacuum to prevent surface contamination and care should be taken to keep the microscope head at a constant height of approximately 10 Å from the sample surface (Neddermeyer 1993). In addition, external vibrations and thermal effects should be eliminated as much as possible and it is often necessary to make allowances for any tilt of the head relative to the sample surface as for instance in the STM study of the Ni {111} surface in air by Maurice *et al.* (1993).

The main problem with applying this technique to oxides is that the surface must be conducting whereas most oxides are insulators. This has been overcome by laying thin oxide films on a conducting substrate (Murray *et al.* 1992).

Although adsorbate molecules have been detected using STM such as benzene rings on the Rh (111) surface (Ohtani *et al.* 1988) smaller species such as CO and

chemisorbed oxygen are often not recognisable which may be due to molecular reorientation induced by the STM tip (Ramos *et al.* 1990).

1.3.8 Atomic Force Microscopy

In AFM (Binnig *et al.* 1986), a technique similar to STM, the surface of a sample is probed with a tip, often made of silicon nitride, mounted on a cantilever. The tip needs to be in physical contact with the surface and the force between the tip and sample is measured by the bending or deflection of the cantilever. The vertical movement of the tip travelling over the surface is then measured, for instance by a laser beam, to a degree of less than 1 Å and an image is produced of atomic resolution (Hochella *et al.* 1990).

This technique is both more recent and more versatile than STM because it can probe both conductors and insulators and it can be operated in a vacuum, in air as demonstrated for the albite {010} surface (Hochella *et al.* 1990) and even in a liquid as for instance in the study of the $\{10\bar{1}4\}$ surface of calcite in water (Ohnesorge and Binnig 1990). However, care should be taken to eliminate any vibration of the instrument and fragile surfaces may be damaged by the tip (Hochella *et al.* 1990).

Adsorbed species such as solvent molecules may be detected using this technique by measuring the distance from tip to surface as a function of time (Cleveland *et al.* 1995).

These last techniques give the spatial arrangement of atoms which can be evaluated by simulation.

1.4 Aims of this Thesis

The aims of this thesis are to study both the molecular and dissociative adsorption of water molecules on oxide surfaces. To this end it was necessary to develop a potential model for the water molecule itself and its interactions with the oxides studied. In addition to the rocksalt structured oxides MgO and CaO, which apart from their cubic structure have the advantage that many experimental data including hydration energies are known, we have also investigated α-alumina which has a hexagonal spacegroup with a more complicated structure. Furthermore, we were interested to see whether our potential model could be applied to crystals of a more covalent character and to this end we studied the effect of physisorption of water on the surfaces of three calcium carbonates, calcite, aragonite and vaterite. In all cases, the effect of hydration on the equilibrium morphology was evaluated and compared to experimental morphologies. Hydration energies and surface structures were also compared with experimental findings when these were available. However, before describing the results of the simulations, the theoretical methods will be discussed first followed by a more detailed account of the derivation of the potential models used in this study.

2 THEORETICAL METHODS

In this chapter the key components of the computer codes used in this project are briefly described together with the approach for calculating the energies of ions at the surfaces and the bulk. In this work we have used atomistic simulations based on the Born model of solids. The methods used were static lattice simulations and molecular dynamics simulations which can evaluate structure and stability and mobility of the various species.

2.1 Atomistic Simulations

A central requirement of atomistic simulations is that the total interaction energy can be evaluated. This energy is defined as the energy released when the different ions making up the crystal are brought together from infinite distance to their lattice sites and is called the lattice energy. Thus, the lattice energy is made up of the electrostatic interactions between the ions and the short range interactions, such as the Van der Waals attractions and short range repulsions. Equations describing the short range interactions are treated in chapter 3, but as the mathematical methods dealing with the long range Coulombic interactions, which account for approximately 80% of the lattice energy, are an integral part of the simulation codes, these electrostatic interactions are described below.

2.1.1 Coulombic Summation

The sum of the Coulombic interactions between point ions i and j in the lattice is given by:

$$\Psi = \sum_{lij}' \frac{q_i q_j}{4\pi\varepsilon_0(\mathbf{r}_{ij} + 1)} \qquad (2.1)$$

where q_i and q_j represent the charges on atoms i and j, with r_{ij} being the distance between the atoms i and j, ε_0 is the permittivity of free space and l is the set of lattice vectors reflecting the periodicity of the lattice. The prime on the summation indicates that the interaction where i=j is not included. In a three dimensional solid l is the set of three lattice vectors describing the periodicity of the solid. Although this analytic expression may seem deceptively simple it is slow to converge as a function of r. This problem has been overcome by the mathematical methods of Ewald (1921) for the three-dimensional lattice and Parry (1975, 1976) in the two-dimensional case when l represents the surface lattice vectors.

2.1.2 Ewald Summation

The Ewald (1921) approach for evaluating the Coulombic interaction assumes that the lattice is periodic in three dimensions. When describing the Coulombic interaction, the charge density ρ for a point ion is given by:

$$\rho_i = q_i\delta(r_i - r_{lattice}) \qquad (2.2)$$

The function can thus take the value of 0 or 1. The basis of the Ewald method is to replace the delta function by a Gaussian function:

$$\rho_i = q_i \exp\left(-\frac{(\mathbf{r}_i - \mathbf{r}_{lattice})^2}{\eta^2}\right) \tag{2.3}$$

where η is the half width of the Gaussian. The original charge density is now given by:

$$\rho_i(\mathbf{r}) = q_i\left[\delta(\mathbf{r}_i - \mathbf{r}_l) - \exp\left(-\frac{(\mathbf{r}_i - \mathbf{r}_l)^2}{\eta^2}\right)\right] + \exp\left(-\frac{(\mathbf{r}_i - \mathbf{r}_l)^2}{\eta^2}\right) \tag{2.4}$$

The equation is solved using Poisson's equation, which relates the density ρ to the second derivative of the potential Ψ (Kittel 1953). The potential for the first part becomes:

$$\Psi(r) = q_i \sum_j \left(q_j \frac{1}{r_{ij}} \mathrm{erfc}(\eta r_{ij})\right) \tag{2.5}$$

which sums all interactions of ion i with ions i and j over the whole lattice.

The second part is Fourier transformed to converge rapidly in reciprocal space. The Fourier transformation of the second part, a series of continuous Gaussians, gives:

$$\rho(\mathbf{r}) = q_i \sum_k (C_k e^{i\underline{K}.R}) \qquad (2.6)$$

where K are the reciprocal lattice vectors and R is $\underline{r}_i - \underline{r}_l$ for all ions in the unit cell. The series converges because C_k decreases as K increases. Using Poisson's equation as above the potential of the second part of equation (2.4) then becomes:

$$\Psi_i(r) = q_i \sum \left[q_i \frac{1}{\pi V_K} \sum_K \left(\frac{1}{K^2} e^{-\pi^2 K^2 \eta^2} . e^{ik.r} \right) \right] \qquad (2.7)$$

When K=0 the second term in the equation would tend towards infinity. However, by assuming that the cell is charge neutral, i.e. the sum of the charges is zero, the K=0 term can be ignored.

When summing a periodic array of Gaussians the self-interaction needs to be removed. Thus, combining the potentials of part one and part two of equation (2.4) and including a term to deduct the self-interaction gives the following equation for the total Coulombic energy of ion i:

(2.8)

$$\Psi_i = q_i \sum \left[q_i \frac{1}{\pi V_K} \sum_K \left(\frac{1}{K^2} e^{-\pi^2 K^2 \eta^2} . e^{ik.r} \right) \right] + q_i \sum_j \left(q_j \frac{1}{r_{ij}} \mathrm{erfc}(\eta r_{ij}) \right) - q_i^2 \frac{2\eta}{\pi^{\frac{1}{2}}}$$

where the final term is the self-interaction.

2.1.3 Parry Method

The Parry method (Parry 1975, 1976) is a special application of the Ewald method (1921) for a two dimensional crystal. The crystal is assumed to consist of a series of charged planes of infinite size rather than an infinite lattice. When summing the electrostatic interactions the vectors are now divided into in-plane vectors, p_{ij} and vectors perpendicular to the plane, u_{ij}. We can no longer assume the total charge of a plane of atoms is zero as in the three dimensional cell and hence the K=0 term has to be evaluated. The part of the summation in reciprocal space then becomes:

$$\Psi = \frac{\pi}{A}\{-2u_{ij}\mathrm{erf}(\eta u_{ij}) - \frac{2e^{(-\eta^2 u_{ij}^2)}}{\pi^{\frac{1}{2}}\eta} + \tag{2.9}$$

$$\sum_{k\neq 0} \frac{e^{ik.p_{ij}}}{k}\left[e^{ku_{ij}}\mathrm{erfc}\left(\frac{k}{2\eta} - \eta u_{ij}\right) + \exp(-ku_{ij})\mathrm{erfc}\left(\frac{k}{2\eta} - \eta u_{ij}\right)\right]\}$$

Hayes *et al.* (1977) supply a detailed derivation of equation (2.9). The first and second derivatives of the energy which are needed for the energy minimisation procedure are given by Harding (1988).

2.1.4 Static Lattice Energy Minimisation

The calculated lattice energy should be the minimum lattice energy of the crystal if the potential parameters decribed the crystal perfectly. However, this is not usually

the case and the lattice energy must be minimised with respect to the positions of the ions making up the crystal. This can be done in two ways; at constant volume and at constant pressure.

(i) In a constant volume minimisation the cell dimensions are kept fixed but the ions are allowed to move. This method does not take account of the bulk lattice strain.

(ii) In a constant pressure minimisation introduced by Parker (1982, 1983) both cell dimensions and ion positions are allowed to vary.

In both techniques the ions are at their minimised positions when the strain on them is zero, *i.e.*

$$\frac{\delta U}{\delta \underline{r}} = 0 \qquad (2.10)$$

where U is the energy and $\underline{r}$ is ion position.

The minimisation procedure used in this work is the Newton-Raphson variable matrix method and below is a brief description of the method for the constant volume instance (Oliver 1994, Watson *et al.* 1997).

A crystal with lattice energy U_L is expanded about a point r to second order (Born and Huang 1954):

$$U_{L(\underline{r}')} = U_{L(\underline{r})} + \underline{g}^T.\underline{\delta} + \frac{1}{2}(\underline{\delta}^T.\underline{\underline{W}}.\underline{\delta}) \qquad (2.11)$$

where the superscript ^{T} corresponds to the transpose of the vector and $\underline{\delta}$ is the displacement of a given ion

$$\underline{\delta} = \underline{r}' - \underline{r} \tag{2.12}$$

$\underline{g}$ is a force vector, the first derivative of the energy

$$\underline{g} = \frac{\delta U}{\delta \underline{r}} \tag{2.13}$$

and $\underline{\underline{W}}$ is the second derivative matrix.

$$\underline{\underline{W}} = \frac{\delta^2 U}{\delta \underline{r}^2} \tag{2.14}$$

Hence at equilibrium, combining equations (2.10) to (2.14) gives:

$$\frac{\delta U}{\delta \underline{r}} = 0 = \underline{g} + \underline{\underline{W}}\underline{\delta} \tag{2.15}$$

U($\underline{r}$) has thus a minimum when

$$\underline{g} = -\underline{\underline{W}}\underline{\delta} \tag{2.16}$$

and the ion displacement to achieve the minimum energy is:

$$\underline{\delta} = -\underline{\underline{W}}^{-1}\underline{g} \tag{2.17}$$

In a harmonic system an optimum value of δ would be obtained and hence the minimum energy structure would be evaluated in a single step. However, in general several iterations have to be performed before the equilibrium configuration is obtained. The limitation of this approach is that the Newton-Raphson method requires calculation of the second derivative matrix of energy with respect to ion position and then its inverse ($\underline{\underline{W}}^{-1}$ in equation 2.17), which for large systems can become computationally very expensive with regard to time and memory. Another drawback is that the method is not very efficient when the system is a long way from the minimum energy position where the potential energy surface is not very harmonic.

One way to increase the speed of calculation is to approximate the inverted second derivative matrix instead of calculating it exactly for each iteration (Davidon 1959, Fletcher and Powell 1963). If we replace the Hessian $\underline{\underline{H}}$ in the following equation by the initial value of the inverse of the second derivative matrix $\underline{\underline{W}}^{-1}$:

$$\underline{\delta} = -\lambda \underline{\underline{H}} \underline{g} \tag{2.18}$$

where λ is a linear parameter initially set to 1 and $\underline{\delta}$ are the ionic displacements, then at the k+1 iteration the ionic displacements are given by:

$$\underline{\delta}_k = -\lambda_k \underline{\underline{H}}_k \underline{g}_k \tag{2.19}$$

where

$$\underline{\delta}_k = r_{k+1} - r_k \tag{2.20}$$

For the next iteration the Hessian can then be approximated as follows:

$$\underline{\underline{H}}_{k+1} = \underline{\underline{H}}_k - \frac{\left(\underline{\delta}_k \cdot \underline{\delta}_k^T\right)}{\left(\underline{\delta}_k^T \cdot \underline{\delta}_k\right)} - \frac{\underline{\underline{H}}_k \cdot \underline{\delta}_k \cdot \underline{\delta}_k^T \cdot \underline{\underline{H}}_k}{\underline{\gamma}_k^T \cdot \underline{\underline{H}}_k \cdot \underline{\gamma}_k} \tag{2.21}$$

where

$$\underline{\gamma}_k = \underline{g}_{k+1} - \underline{g}_k \tag{2.22}$$

and the superscript ^{T} again corresponds to the transpose of the vector and enables the new positions for k+2 to be calculated. In this way it is only necessary to calculate the first derivatives $\underline{g}$ for each iteration which is computationally fast, and hence this approximation method saves computer time. One drawback is that any errors are compounded each step and hence is is necessary to recalculate the inverted second derivative matrix $\underline{\underline{W}}^{-1}$ every 10-30 iterations to readjust the Hessian $\underline{\underline{H}}$.

An alternative method to the very reliable Newton-Raphson method is the conjugate gradients minimisation method (Fletcher and Reeves 1964). The conjugate gradients minimisation method has the advantage of not requiring the second derivative whose storage and manipulation can be computer intensive for large cells. It uses a method based on steepest descent where the energy is minimised by calculating the forces acting on the ions and the directions of these forces are used to find the minimum energy position (Watson 1994). Although each iteration is much faster than in the Newton-Raphson method it is not as efficient at locating the minimum energy position. This method is therefore more appropriate for large cells for which the Newton-Raphson method is prohibitively expensive computationally or

as an initial minimisation method to quickly guide the system towards a minimum where the potential energy surface becomes more harmonic and the Newton-Raphson method can take over.

With both methods it is possible that only a local potential energy minimum has been found instead of the global minimum. Figure 2.1 shows a two-dimensional potential energy surface with the potential energy plotted versus the configuration of water molecules on a surface. The structure is minimised from starting position (a) to local minimum (b) but does not continue to global minimum (c). In order to find the global miminum it is necessary to consider many different starting configurations and compare the final energies of the system. The final structure with lowest energy position is selected as the one most likely to be the global minimum.

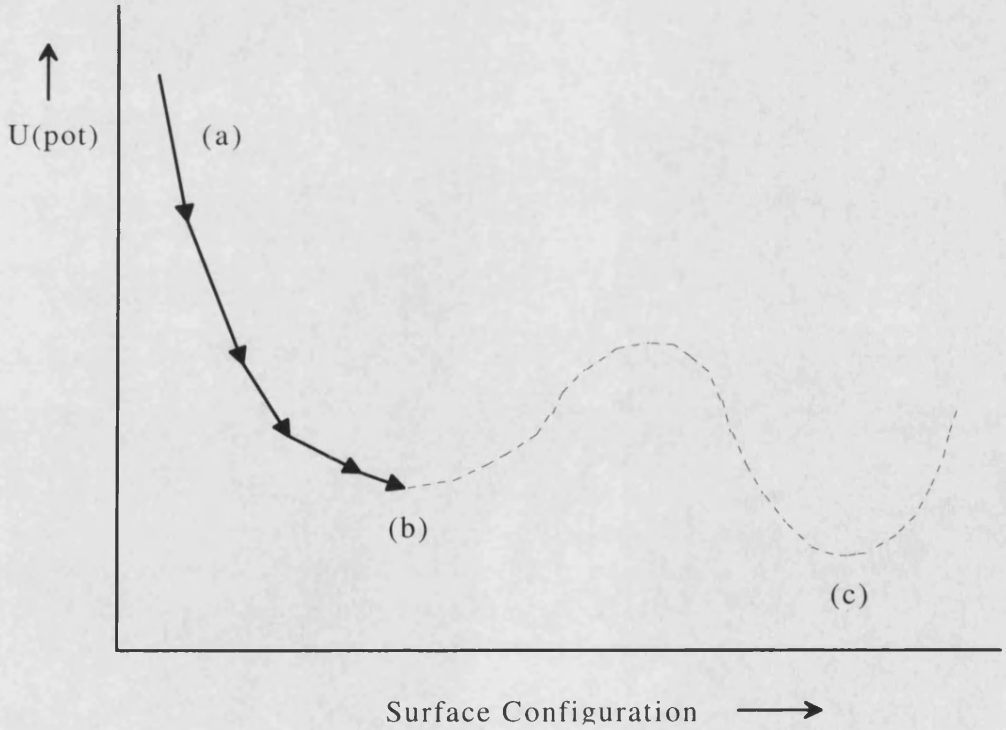

Figure 2. Energy minimisation with respect to some surface configuration. Starting from (a) the system finds local minimum (b) despite the presence of global minimum (c).

The code PARAPOCS (Parker and Price 1989) was used in this work to obtain the bulk properties of the crystals, such as lattice energies, elastic and dielectric constants and unit cell lattice vectors and angles. The simulations were performed at constant pressure using a Newton-Raphson method. The relaxed bulk unit cell was then used in static surface calculations to obtain surface and defect energies and in molecular dynamics simulations, to obtain properties such as diffusion coefficients.

2.1.5 Surface Simulation Codes

METADISE

The computer code METADISE (Minimum Energy Techniques Applied to Dislocation, Interface and Surface Energies) (Watson *et al.* 1996) used in this work to calculate the minimum energies and structures of the relevant surfaces was in part derived from the MIDAS code developed by Tasker (1978).

The crystal is considered to consist of a series of charged planes parallel to the surface and periodic in two dimensions. The crystal is then divided into two blocks, each of which is divided into two regions, region I and region II (fig. 2.2(a)). The ions in region I are allowed to relax explicitly while those in region II are held fixed at their bulk equilibrium positions, although the two region IIs are allowed to move relative to each other. It is necessary to include region II to ensure that the potential of an ion at the bottom of region I is modelled correctly (Tasker 1979). A surface is

created when block II is removed with the top of region I as the free surface (figure 2.2(b)). Interfaces such as stacking faults and grain boundaries can be studied by fitting two surface blocks together in different orientations.

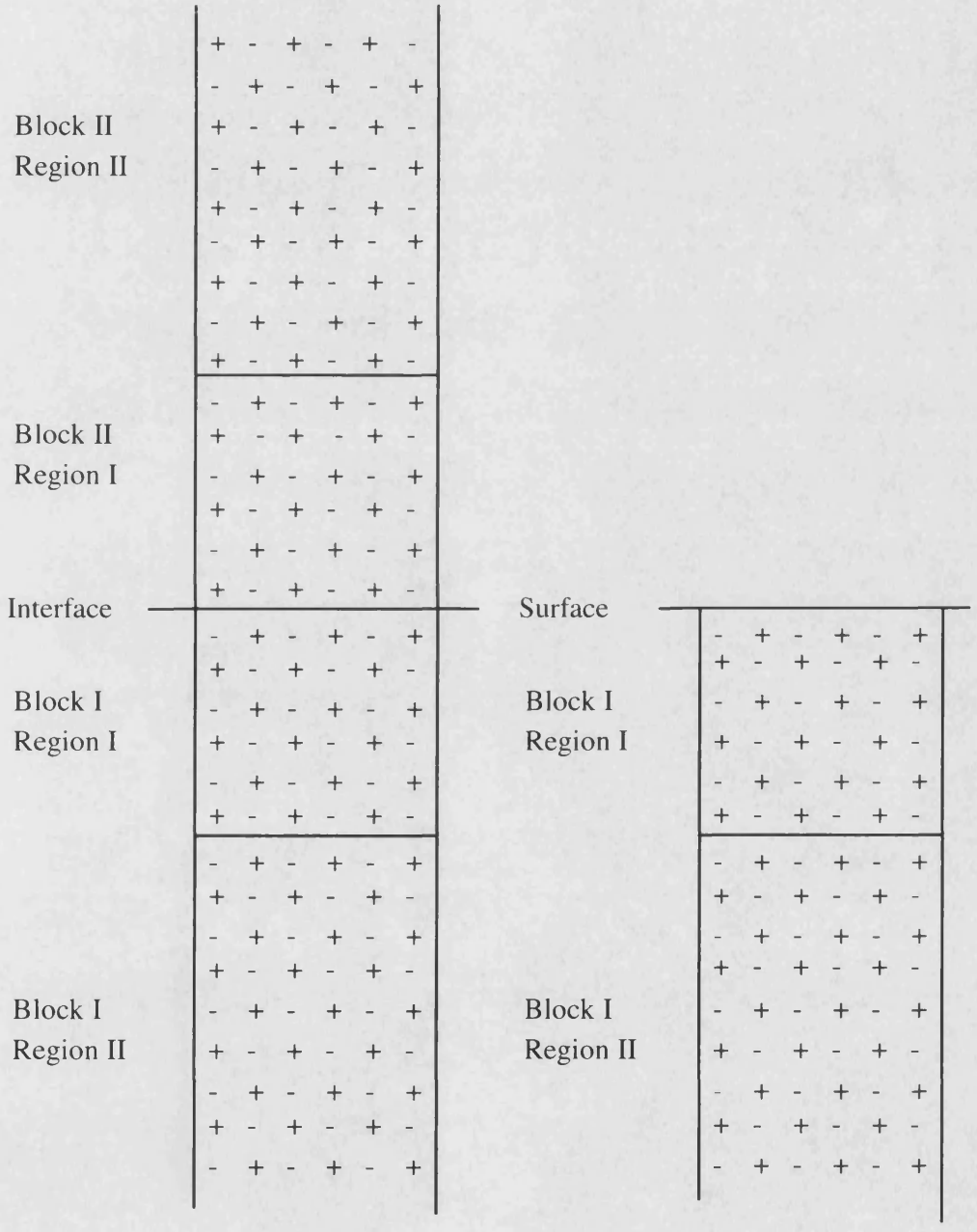

Figure 2.2. The two region approach used in METADISE, (a) the complete crystal and (b) half a crystal, exposing a surface

The energy of the crystal is made up of two parts:

$$U_{latt} = U_1 + U_2 \tag{2.23}$$

where U_1 and U_2 are the energies of the combined ions in region I and region II respectively. The energy of region I is given as follows:

$$U_1 = \sum_{\substack{i\in I \\ j\in I}}\sum_{1} \Psi_{ij}(|r_{ij} - r_1|) + \frac{1}{2}\sum_{\substack{i\in I \\ j\in II}}\sum_{1} \Psi_{ij}(|r_{ij} - r_1|) \tag{2.24}$$

where Ψ_{ij} is some suitable pair potential (chapter 3). The first term includes interactions between the ions in region I only and the second term describes the interactions between the ions in region I and those in region II, which is referred to as the boundary interaction energy. The energy of region II consists only of this boundary interaction energy because the ions are kept fixed and hence the interaction between the ions in region II itself is unchanged and can therefore be ignored. The energy contribution is thus as follows:

$$U_2 = \frac{1}{2}\sum_{\substack{i\in I \\ j\in II}} \Psi_{ij}(|r_{ij} - r_1|) \tag{2.25}$$

The Parry method as described above is used to calculate the Coulombic interactions between the ions.

CHAOS

In METADISE any defects in the bulk or on the surface are periodically repeated throughout the crystal and large supercells are used to model defects at low concentration. However, to simulate defects, for example water adsorption, at infinite dilution a different code was needed which allows modelling of point defects. The computer code CHAOS (Computer simulation HAdes On Surfaces) developed by Duffy and Tasker (1984) is derived from the code HADES (chapter 1). CHAOS calculates the structure and energy of point defects at the surface of the crystal. In this code the crystal is again divided into a region I and a region II. Region II is further subdivided into two regions, a and b. In this case the regions are hemispheres centred upon the point defect on the surface (figure 2.3).

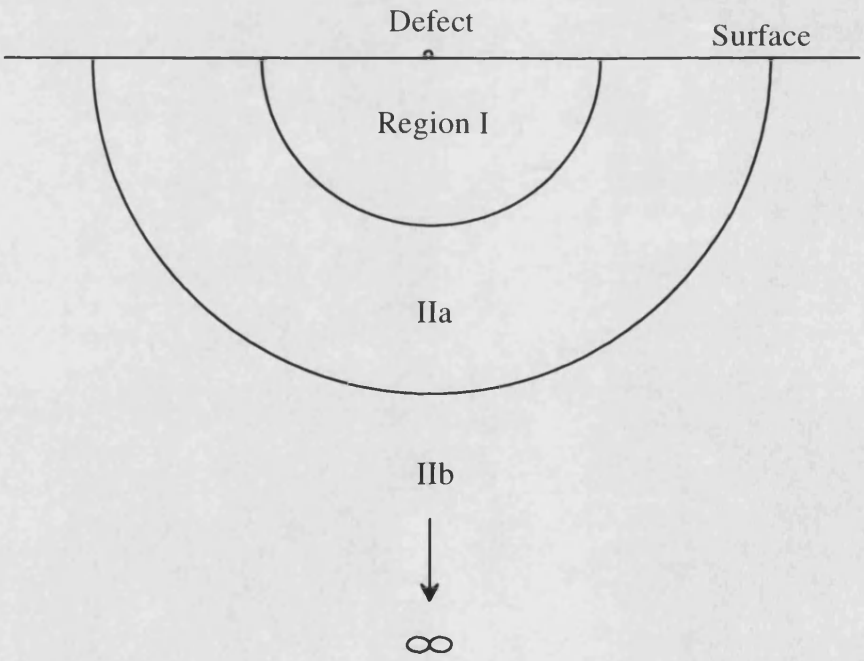

Figure 2.3 Two region strategy used in CHAOS

The interactions between ions in region I and region IIa are calculated explicitly just like the interactions between the ions in regions I and II in METADISE. The interactions between region I and the rest of the crystal are approximated (Mott and Littleton 1938) assuming the rest of the crystal is a dielectric continuum. In addition, the defect at the surface (dielectric discontinuity) creates a dipole which induces dipoles in region IIb and interactions between region I and IIb are modified to include these charge induced dipoles. These approximations assume that the effect of the defect on the local geometry of the crystal is only noticeable in the immediate surroundings of the defect but the energy of the rest of the crystal is modified by the charged defect. The total energy of the system therefore consists of three terms:

$$U(\underline{x}, \underline{y}) = U_1(\underline{x}) + U_2(\underline{x}, \underline{y}) + U_3(\underline{y}) \qquad (2.26)$$

where $U_1(\underline{x})$ is the energy of region I, $U_3(\underline{y})$ is the energy of region II and $U_2(\underline{x},\underline{y})$ is the energy of interaction between regions I and II. The vectors $\underline{x}$ and $\underline{y}$ represent the co-ordinates of the ions in region I, which are calculated explicitly, and the displacements in region II respectively. As $U_3(\underline{y})$ contains an infinite number of displacements, it cannot be solved exactly and we need to make assumptions. We assume that the distance between that defect and the innermost region of region II is large enough to consider the outer region to equal the perfect crystal. The charge induced dipoles due to the defect cause harmonic displacements of the ions only and hence $U_3(\underline{y})$ can be represented by a quadratic funcion of $\underline{y}$:

$$U_3(\underline{y}) = \frac{1}{2}\underline{y}\underline{\underline{A}}\underline{y} \qquad (2.27)$$

where $\underline{\underline{A}}$ is the force constant of the harmonic displacement. At equilibrium, when $\underline{y} = \bar{\underline{y}}$, the total force which is the derivative of the total energy is zero and hence when we substitute equation (2.27) into expression (2.26) we obtain:

$$\frac{\partial U(\underline{x}, \underline{y})}{\partial \underline{y}} = \frac{\partial U_2(\underline{x}, \underline{y})}{\partial \underline{y}} + \underline{\underline{A}}\,\bar{\underline{y}} = 0 \qquad (2.28)$$

If we multiply this equation by $\underline{y}/2$, this becomes:

$$-\left(\frac{\underline{y}}{2}\right)\frac{\partial U_2(\underline{x}, \underline{y})}{\partial \underline{y}} = \frac{1}{2}\underline{y}\underline{\underline{A}}\,\bar{\underline{y}} \qquad (2.29)$$

and thus, when $\underline{y} = \bar{\underline{y}}$ and the outer displacements are at equilibrium with a given set of displacements of the inner region we obtain an expression for the total energy as a function of $U_1(\underline{x})$ and $U_2(\underline{x},\underline{y})$ only:

$$U(\underline{x}, \underline{y}) = U_1(\underline{x}) + U_2(\underline{x}, \underline{y}) - \frac{1}{2}\frac{\underline{y}\partial U_2(\underline{x}, \underline{y})}{\partial \underline{y}} \qquad (2.30)$$

By iteratively minimising with respect to $\underline{x}$ until the forces on each ion in region I is zero, *i.e.*:

$$\frac{\partial U(\underline{x}, \underline{y})}{\partial \underline{x}} = 0 \qquad (2.31)$$

we obtain the total energy of the relaxed system including the defect. The energy is calculated in the same way as in METADISE (equations 2.23 to 2.25) using the Parry method (1975, 1976) and the defect energy is then obtained from the difference between the energy of the perfect surface and that with point defect, obtained by CHAOS. One consequence of using CHAOS to calculate defects at surfaces rather than in the bulk is that the calculation of the ionic displacements and the energy of the continuum needs to be modified with respect to a bulk calculation. In a bulk calculation using CASCADE the energy of the continuum is calculated by a r^{-4} summation (where r is the distance from the defect) which assumes that away from the defect in region II there is no structural deviation from the perfect crystal structure. This is an unrealistic assumption when surfaces are concerned and the energy is therefore calculated as a sum of planar integrals around the surface for the planes in region I and II defined by METADISE and a volume integral over the rest of the crystal. These planar integrals take explicit account of the dilation of the crystal at the surface and hence structural relaxation is allowed.

$$E_{IIb} = -\frac{Q^2}{2}(E_{planar} + E_{volume}) \qquad (2.32)$$

$$E_{planar} = \sum_{p \in I,IIa} \sum_{j} q_j M_j \int_{(R_{IIb}^2 - r_p^2)^{\frac{1}{2}}}^{\infty} \frac{1}{(r^2 - r_p^2)} 2\pi r dr \qquad (2.33)$$

$$E_{volume} = \sum_{j} q_j M_j \int_{R_{IIb}}^{\infty} \frac{1}{r^4} 2\pi r^2 dr \qquad (2.34)$$

where Q is the total charge of region I, q_j is the defect charge, M_j is the Mott-Littleton displacement factor, R_{IIb} is the cut-off radius, r_p is the perpendicular distance from the origin to plane p and r is the distance from the defect.

As noted above an additional consequence of charged defects at surfaces is that a surface causes a discontinuity in the dielectric constant. As a result the charged point defect induces an image charge situated half an interplanar distance above the plane containing the defect. The field due to the image charge needs to be taken into account when calculating the ion displacements in region IIa and the polarisation energy of region IIb. This image charge interaction is given by:

$$q_i = q_{defect}\left(\frac{\varepsilon_1 - \varepsilon_2}{\varepsilon_1 + \varepsilon_2}\right) \qquad (2.35)$$

where q_{defect} is the net charge of the defect, q_i is the charge of the image, ε_1 and ε_2 are the different dielectric constants of the adjoining materials and $\varepsilon_1 > \varepsilon_2$. In this work, only surfaces are considered and the value of ε_2 is therefore set to 1, the value of free space.

Types of Surfaces

As noted in the METADISE section, the crystal surfaces can be considered as a stack of planes. Tasker (1979a) then identified three different types of surfaces: In a type I surface each plane has overall zero charge as it consists of both anions and cations in stoichiometric ratio (figure 2.4a). A type II surface has a stacking sequence

of charged planes but the repeat unit consists of several planes in a symmetrical configuration and as a result there is no dipole moment perpendicular to the surface (figure 2.4b). As type I and type II surfaces have no dipole moment perpendicular to the surface the electrostatic energy converges.

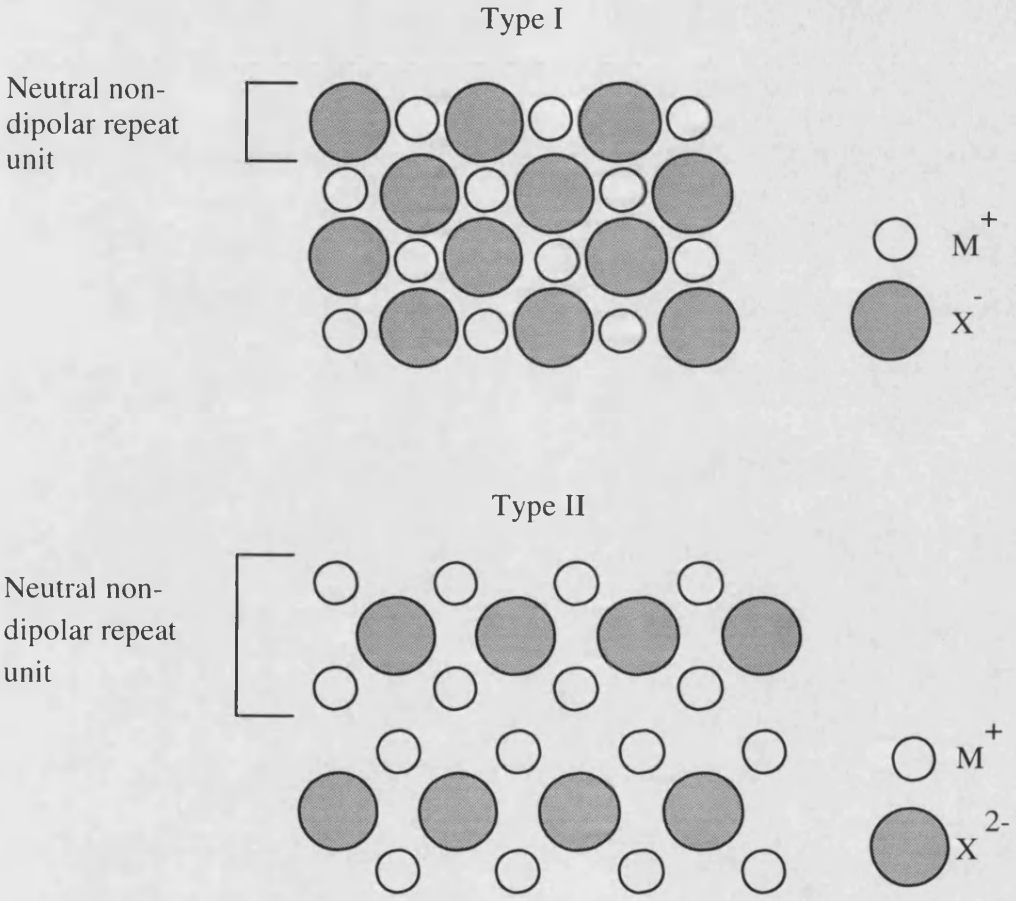

Figure 2.4 Stacking sequences showing type I surfaces consisting of charge neutral layers of positive and negative ions, and type II surfaces consisting of positively and negatively charged planes but with a charge neutral and non-dipolar repeat unit.

Type III surfaces, however, are made up of a stack of alternately charged planes (figure 2.5a) producing a dipole moment perpendicular to the surface. Bertaut (1958) showed that when a dipole moment perpendicular to the surface is present in the unit

cell, the surface energy diverges and is infinite. In order to study this type of surface we need to remove the dipole. One way of achieving this is to remove half the ions from the surface layer at the top of the repeat unit and transfer them to the bottom (Oliver *et al.* 1993) (figure 2.5b). As a result we obtain a surface which is partially vacant, either in cations or anions, and which may be particularly reactive towards for instance hydroxylation.

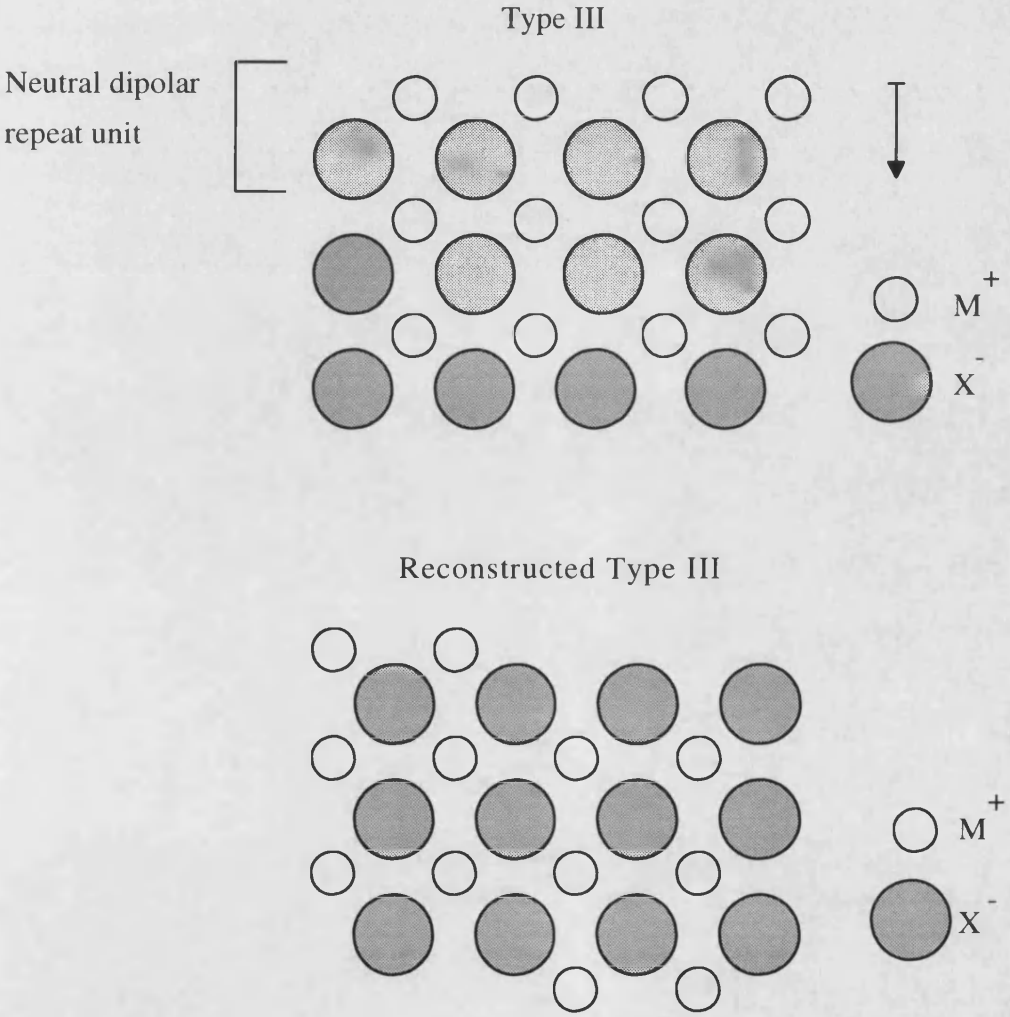

Figure 2.5 Stacking sequences showing a type III surface, consisting of alternating layers of positive and negative ions giving rise to a dipolar repeat unit, and a reconstructed Type III surface where half the surface ions have been shifted to the bottom of the unit cell, which has removed the dipole in the repeat unit.

Once a surface is generated, which has no dipole moment perpendicular to the surface, the surface energy can be calculated.

Calculation of Surface Energy

Static lattice energy minimisations have been used to obtain bulk and surface energies and energies of hydration. The vibrational properties of the crystal are not taken into account and in effect the simulation is of a crystal at zero Kelvin ignoring the zero point energy. Although this may seem like an unrealistic approximation, nevertheless these simulations give good agreement with experiment (Tasker 1979, Parker 1983). Furthermore, the vibrational and the zero point energy contributions to the surface free energies are small.

The excess energy for the surface has been defined by Stoneham (1976) as:

E_S = [cohesive energy of finite crystal] - (2.36)

[number of atoms] x [cohesion energy per atom in infinite crystal]

Throughout this work the surface energy is then defined per unit area as follows:

$$\gamma = \left(\frac{E_S}{\text{Area}}\right) x 16.021 \qquad (2.37)$$

where γ is in Jm^{-2}, E_S in eV is ($U_{surface}$ - $1/2U_{bulk}$) and the area is in $Å^2$. In liquids this expression is equivalent to the surface tension since a liquid surface cannot support a stress (Harding 1997). When stretching a liquid surface the number of atoms will increase to minimise the stress (Tasker 1979).

The energies for surface and bulk blocks are evaluated using the approach outlined in the METADISE section. The energy of block 1 comprising of region I and II is the energy of the finite crystal containing the surface and the energy of blocks 1 and 2 together yield the bulk energy or energy per atom in an infinite crystal. Regions I and II of both blocks need to be sufficiently large to ensure convergence of the surface energies. This work has shown that for both the oxides, *i.e.* the cubic oxides MgO and CaO and hexagonal α-Al_2O_3, and the calcium carbonate polymorphs calcite, aragonite and vaterite, it was sufficient to model four layers of repeat unit for regions I and forty for regions II.

2.1.6 Crystal Morphology

Gibbs (1928) proposed that the equilibrium morphology of a crystal should possess a minimum (free) energy for a given volume. According to Wulff's Theorem (Wulff 1901), which is a variation of Gibbs theorem, the equilibrium shape of a crystal is determined by the surface energies of its various surfaces, in such a way that the equilibrium morphology is the shape of the crystal with minimum total surface free energy. Or, if the crystal is limited in space by n flat faces, then:

$$\frac{\sigma_1}{h_1} = \frac{\sigma_2}{h_2} = \ldots\ldots\ldots = \frac{\sigma_i}{h_i} = \frac{\sigma_n}{h_n} \qquad (2.38)$$

where σ_i is the specific free energy of the ith face and h_i is the distance from the centre of the crystal to the plane of the ith face (Tauson *et al.* 1993) and is normal to the face. Thus the height of a face is directly proportional to its specific free energy. Thus if two faces, for instance with directions [100] and [110], have the same specific free energy they will have the same height. Figure 2.6 gives a schematic representation of the the two surfaces and the dark line indicates the resulting equilibrium morphology.

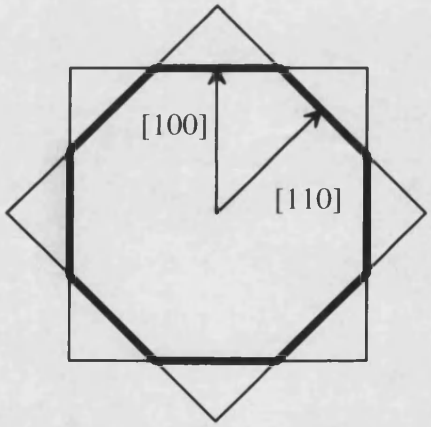

Figure 2.6 Schematic representation of two-dimensional equilibrium morphology due to two faces with equal specific free energy.

At zero Kelvin, the specific free energy is a close approximation of the surface energy as calculated by static lattice simulations. Masri *et al.* (1984) found that the entropy term included in the surface free energy is small compared to the enthalpy term because the difference between the energies of the bulk and the surface is small.

Thus the surface energies can be assumed to determine the equilibrium morphology of the crystal as follows:

$$E_S = \sum_i \gamma_i A_i = \text{minimum for constant volume} \qquad (2.39)$$

where E_S is as defined in equation 2.36 (Stoneham 1976) and γ_i and A_i are the surface energy and surface area of the ith crystallographic face. Again, if two surfaces have the same surface energy and the same area, the morphology will be as in figure 2.6 above. However, in the more likely case that the surface energies and areas are different, the surface with the highest surface energy will grow out fastest resulting in a small surface area (or a long distance from the crystal centre), while the face with the lower surface energy grows more slowly, resulting in a large surface area (or short distance from the crystal centre), and hence will be expressed in the equilibrium morphology. Figure 2.7 illustrates this process.

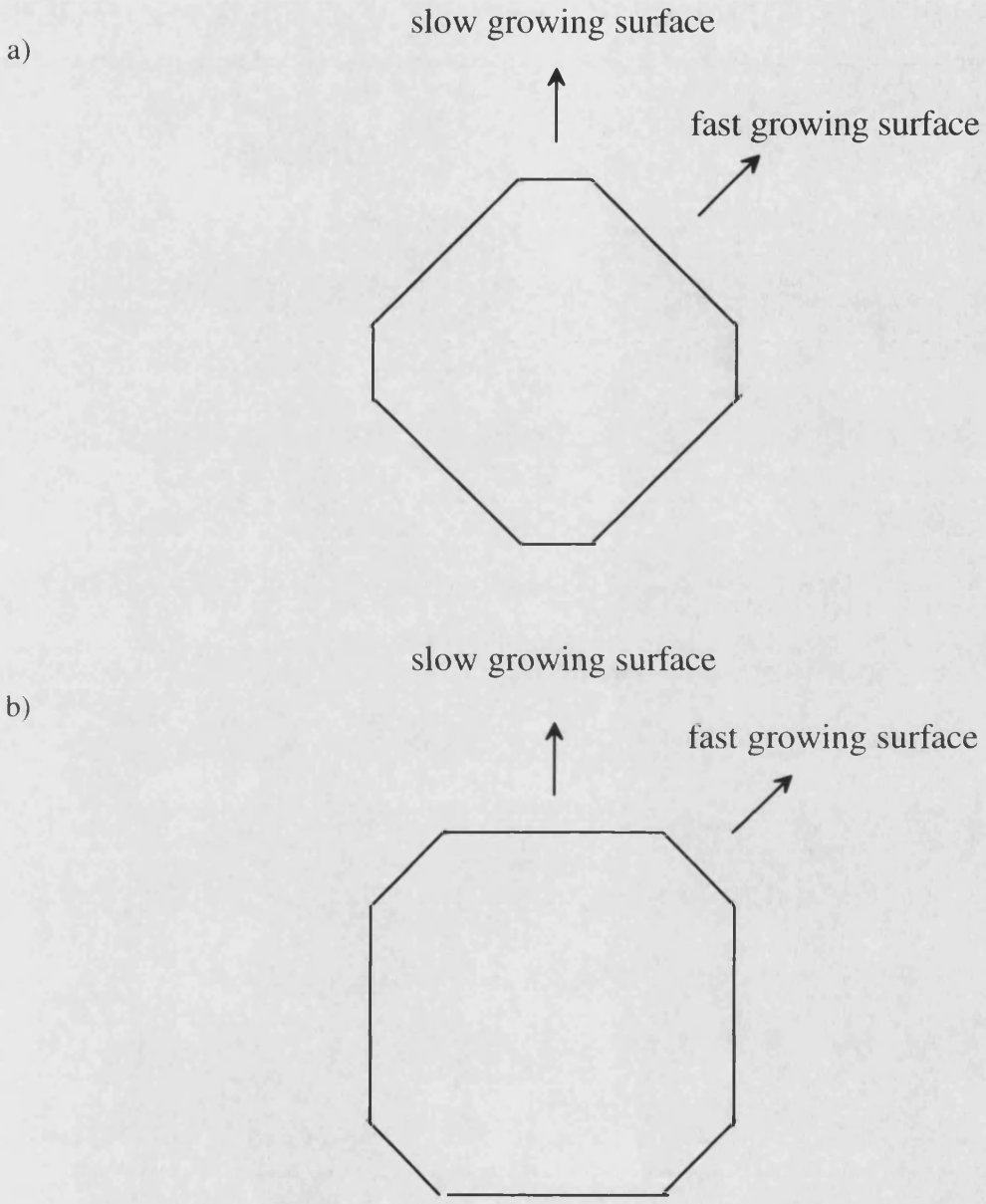

Figure 2.7 Schematic representation of the equilibrium morphology resulting from faces with different surface energies

This method of predicting crystal morphologies on the basis of thermodynamic factors has been very successful when the results were compared with experimentally found crystal shapes (Titiloye *et al.* 1991). However, rather than being determined

thermodynamically, experimental morphologies often depend on kinetic factors (Harding 1997). Hartman and Bennema (1980) have tried to overcome this problem by assuming attachment energies are proportional to the growth rate for each surface and hence determine the kinetic morphology. In this simple phenomenological model, a slice of material is added to an already existing face on the bulk and the energy released is the attachment energy, which is considered to be directly proportional to the growth rate (Woensdregt 1992). Unfortunately, attachment energies assume bulk termination of the surface and do not take into account surface relaxation and reconstruction which was shown to be of utmost importance by Mackrodt *et al.* (1987). Gay and Rohl (1995) have attempted to address this problem by including the relaxation energy but it is unclear what this corresponds to. As such, although attachment energies are a useful and often successful concept, they are not as yet entirely satisfactory (Harding 1997).

All of these methods fail to include the effect of temperature explicitly which can be overcome by using molecular dynamics simulations.

2.1.7 Molecular Dynamics Simulations

Molecular Dynamics (MD) simulations include temperature by treating the kinetic energy of atoms explicitly and then studying their behaviour. This has the advantage of being able to consider diffusion and anharmonic effects of the ions or molecules in the system over a period of time which cannot be studied by other atomistic simulation techniques such as lattice dynamics.

The technique is based on solving the classical equations of motion numerically for a box containing N particles (Allen and Tildesley 1993). The particles in the box are assigned coordinates, corresponding to a lattice in simulations of crystalline systems, and they are initially given random velocities in such a way that the components of linear momentum of the whole system are zero and the kinetic energy of the combined particles corresponds to the desired simulation temperature (Jacobs and Rycerz 1997), *i.e.*:

$$\sum_{i=1}^{N} m_i v_i(0) = 0 \qquad (2.40)$$

and

$$\sum_{i=1}^{N} m_i v_i^2(0) = 3Nk_B T \qquad (2.41)$$

where m_i and v_i are the mass and the velocity of ion i respectively, N is the number of particles, k_B is the Boltzmann constant and T is the simulation temperature.

Because the size of a molecular dynamics system is relatively small in the thermodynamic sense and because the initial configuration will inevitably not correspond to an equilibrium state, the temperature usually fluctuates wildly at the beginning of a run. Consequently the particle velocities are rescaled during an equilibration period which allows the ensemble to attain equipartition between potential energy and kinetic energy and a thermalised distribution of velocities, such that the temperature calculated from the kinetic energy of each species is restored to the desired simulation temperature (Jacobs and Rycerz 1997), although this

temperature may fluctuate by up to 40 or 50K. The number of timesteps required for equilibration varies with the complexity of the system studied and the nature of the interatomic forces, but it is usually between 5000 timesteps for a simple system, such as cristobalite modelled by a rigid ion potential containing only Coulombic interactions and two Buckingham potentials, to more than 10000 steps for a complex system containing an oxide surface with liquid water molecules, described by a whole range of potential parameters, including three- and four-body bonds and partial Coulombic subtractions (see chapter 3).

The production run begins after the equilibration period. The system is allowed to run for tens of thousands of timesteps without any scaling of velocities. The forces acting on the ions, as discussed in chapter 3, are used to update the velocity and position for each ion for an infinitely small timestep by solving Newton's Laws of Motion:

$$F_i(t) = m_i a_i(t) \tag{2.42}$$

$$v_i(t+\delta t) = v_i(t) + a_i(t)\delta t \tag{2.43}$$

$$r_i(t+\delta t) = r_i(t) + v_i(t)\delta t \tag{2.44}$$

Because a typical lattice vibration is of the order of 10^{-13} to 10^{-12} seconds, the timestep δt is usually set at about 10^{-15} to 10^{-14} seconds to make sure that the simulation samples all the lattice vibrations. Greater sampling will lead to smaller errors. However, it is computationally expensive to use timesteps of less than about a femtosecond as this means that the simulations have to run for a large number of

timesteps to allow the ions to move a significant distance and to accumulate useful statistics. As the calculation of the forces acting on each particle is the most time-consuming feature of an MD simulation it is necessary to limit the number of timesteps, and hence increase the size of the timestep, as much as possible. Unfortunately, in the simulation of our box of water as described in chapter 3 we initially needed a very small timestep of 0.05×10^{-15} second, which meant that even a run of 200,000 steps only resulted in 10 picoseconds of simulated time.

When updating the positions and velocities, errors occur both as a result of the timestep δt not being infinitesimally small, and because higher order terms in equations 2.42 to 2.44 have not been taken into account (Allen and Tildesley 1993). There are a number of algorithms available to correct these errors such as the Verlet leap-frog algorithm (Verlet 1967, Hockney 1970) which is perhaps the most widely used algorithm:

$$\underline{v}_i(t+\frac{\delta t}{2}) = \underline{v}_i(t-\frac{\delta t}{2}) + \underline{a}(t)\delta t$$

$$\underline{r}_i(t+\frac{\delta t}{2}) = \underline{r}_i(t) + \underline{v}_i(t+\frac{\delta t}{2})\delta t \qquad (2.45)$$

where the expression for the velocity calculated in one timestep is used to calculate the position in the next timestep. In this way both position and velocity are updated every other timestep in a leapfrog fashion. The velocity at time t is obtained from the average of the velocities half a timestep either side of time t:

$$\underline{v}_i(t) = \frac{1}{2}\left[\underline{v}_i(t-\frac{\delta t}{2}) + \underline{v}_i(t+\frac{\delta t}{2})\right] \qquad (2.46)$$

The instantaneous temperature T can then be obtained from the atomic velocities assuming the system has no net momentum:

$$T = \frac{\Sigma_{i=1}^{N} m_i v_i^2(t)}{k_B f} \qquad (2.47)$$

where k_B is the Boltzmann constant and f the number of degrees of freedom in the system which is 3N - 3 if the system is periodic and without constraints.
Advantages of this algorithm are that it is reversible in time and conserves total energy and linear momentum.

An alternative algorithm is the Beeman algorithm, used for example in the FUNGUS code (Mills and Hernandez 1993):

$$\underline{r}_i(t+\delta t) = \underline{r}_i(t) + \underline{v}_i(t)\delta t + \frac{1}{6}[4\underline{a}_i(t) - \underline{a}_i(t-\delta t)]\delta t^2$$

$$\underline{v}_i(t+\delta t) = \underline{v}_i(t) + \frac{1}{6}[2\underline{a}_i(t+\delta t) + 5\underline{a}_i(t) - \underline{a}_i(t-\delta t)]\delta t \qquad (2.48)$$

which is more accurate in calculating the velocities as these are not an average of two steps, but is more complex and hence computationally more expensive.

Finally there are more sophisticated algorithms such as the Gear predictor-corrector algorithm (Gear 1971) which uses a fifth order iterative process to calculate the terms. An initial prediction is made about the positions, velocities, accelerations and forces at time $t + \delta t$ by Taylor expansion to fifth order about time t, estimated from a continuous classical trajectory of the particles. However, because the equations of motion are not included in the Taylor expansion the trajectories will not be correct. Therefore the forces and hence the accelerations at $t + \delta$ are also calculated from the predicted positions. These can then be compared with the predicted forces and accelerations and this will allow the size of the error in the prediction step to be estimated. This error together with the results of the predictor step are fed into the corrector step which then gives a better approximation of the true positions, velocities, accelerations and forces. The corrector step may be iterated until the desired accuracy and even with a poor initial prediction the corrector iterations will converge rapidly onto the correct answer.

However, when this very sophisticated method is compared with the simple Verlet method the Gear method is more accurate at short δt and the Verlet algorithm is more attractive with a longer timestep and all three are essentially equivalent in that they have identical global errors and generate identical position trajectories (Allen and Tildesley 1993).

Shell model Molecular Dynamics

Historically simple rigid ion potentials (chapter 3) have been used for MD simulations. However, the increased computer speed and the availability of parallel supercomputers such as the Cray T3D in Edinburgh have made it possible to run MD simulations using more complex interatomic potentials, including the use of a shell model to include ionic polarisability (Dick and Overhauser 1958). The shell model as used in these calculations is fully described in chapter 3.

In the static energy minimisation calculations the shells have zero mass and relax instantaneously to their equilibrium position. Lindman and Gillan (1993) employed this type of shell in their MD simulations. They ran a standard MD simulation on the cores and at each timestep relaxed the shells to their minimum energy position by a minimisation method such as conjugate gradients. They found that the energy minimisation of the shells for every MD step needed about ten iterations resulting in an increase of simulation time by a factor of 10.

The alternative method, which we used, is to treat the shells as another species in the MD simulation with a small finite mass (Mitchell and Fincham 1993, Ferneyhough *et al.* 1994). It is important that no energy is exchanged between the shells and other species in the simulation shell, hence the requirement for a shell mass which is smaller than those of other species such as hydrogen atoms and as a result it is often necessary to use a significantly smaller timestep than for a rigid ion potential which thus increases the computer time required. If the timestep is more

than a factor of 10 smaller then this approach ceases to be so attractive in terms of computer CPU time.

In our simulations we initially relaxed the oxygen shells to their minimum energy position by conjugate gradients to ensure that the shells did not have an initial potential energy. We then used a shell mass of 0.2 a.u. in order to avoid energy exchange between the shell and the hydrogen atom (1.0 a.u.) and in order for the shells to remain at near zero Kelvin we needed a timestep of between 0.05 and 0.2 femtoseconds, which is a factor of between 5 and 20 smaller than for instance modelling cristobalite using a rigid ion potential with a timestep of 1 femtosecond.

Ensembles

Molecular dynamics simulations can be run under a number of conditions. These sets of conditions are called ensembles and by using statistical thermodynamics, they relate a finite collection of particles to an infinite system.

The simplest ensemble is the microcanonical ensemble (NVE) in which the number of particles (N), the volume (V) and the energy (E) are all kept constant, although the pressure and temperature are allowed to fluctuate. It represents a thermodynamically isolated system (Jacobs and Rycerz 1997).

Connection to a heat bath at constant temperature T creates the canonical ensemble (NVT), where temperature is kept constant (T) by allowing energy to be

transferred between the simulation box and the heat bath. Energy and pressure are allowed to fluctuate. It is easier to relate this ensemble to experimental conditions than the NVE ensemble and we used it to study oxide surfaces.

Connection to a constant pressure reservoir via a diathermic piston to a reservoir at constant temperature creates the isothermal-isobaric (NPT) ensemble where the number of particles, pressure and temperature are kept constant. This ensemble bears the closest resemblance to an experimental investigation while still being a realistic MD simulation and we have used this ensemble in this work to model a liquid water system and adsorption of liquid water at oxide surfaces.

There is one other ensemble which may be considered, which is the grand canonical ensemble (μVT) where the simulation is run at constant chemical potential, volume and temperature. However, within the constraints of the atomistic potential model and its inability to model the making or breaking of bonds, this ensemble is not widely used for inorganic solids.

DL_POLY

Relatively recently an MD programme was introduced which allows shell model potentials to be used. DL_POLY (Forester and Smith 1995) has been used in this work to run MD simulations on pure water at room temperature to obtain self-diffusion coefficients and on MgO surfaces with liquid water to study adsorption behaviour.

In the DL_POLY code the integration algorithms are based around the Verlet leap-frog scheme as described in section 2.1.7 above. In the NVE ensemble the simple Verlet leap-frog algorithm is implemented and the instantaneous temperature is calculated while the total energy of the system is conserved. For the NPT (or NST for constant strain) ensembles a heat reservoir was introduced with a Nose-Hoover thermostat to ensure constant temperature. Although there are a number of algorithms available we chose this one, which was first introduced by Nose (1984) but then refined by Hoover (1985), because only this algorithm generates trajectories in the NVT ensemble as well and thus we could keep our simulations, which were usually done at both NVT and NPT, consistent.

In the Nose-Hoover algorithm Newton's equations of motion are modified to read:

$$\frac{d\underline{r}_i(t)}{dt} = \underline{v}_i(t) \qquad (2.49)$$

$$\frac{d\underline{v}_i(t)}{dt} = \frac{\underline{f}_i(t)}{m_i} - \chi(t)\underline{v}_i(t) \qquad (2.50)$$

where χ is a friction coefficient which is controlled by the first order differential equation:

$$\frac{d\chi(t)}{dt} = \frac{1}{\tau_T^2}\left(\frac{T}{T_{ext}} - 1\right) \tag{2.51}$$

where τ_T is a specified time constant, χ has the dimension of (1/time) and is stored at half timesteps and T is again the instantaneous temperature. The integration then takes place as:

$$\chi(t+\frac{\delta t}{2}) = \chi(t-\frac{\delta t}{2}) + \frac{\delta t}{\tau_T^2}\left(\frac{T}{T_{ext}} - 1\right) \tag{2.52}$$

$$\chi(t) = \frac{1}{2}\left[\chi(t-\frac{\delta t}{2}) + \chi(t+\frac{\delta t}{2})\right] \tag{2.53}$$

$$\underline{v}_i(t+\frac{\delta t}{2}) = \underline{v}_i(t-\frac{\delta t}{2}) + \delta t\left[\frac{\underline{f}_i(t)}{m_i} - \chi(t)\underline{v}_i(t)\right] \tag{2.54}$$

$$\underline{v}_i(t) = \frac{1}{2}\left[\underline{v}_i(t-\frac{\delta t}{2}) + \underline{v}_i(t+\frac{\delta t}{2})\right] \tag{2.55}$$

$$\underline{r}_i(t+\delta t) = \underline{r}_i(t) + \delta t\underline{v}_i(t+\frac{\delta t}{2}) \tag{2.56}$$

As $\underline{v}(t)$ is required to calculate itself and T as well, the algorithm requires several iterations to become self consistent. The iteration procedure is started with the standard Verlet leap-frog prediction of $\underline{v}(t)$ and T.

Periodic Boundary conditions applied to Surfaces

Due to the expense of computer time it is not feasible to model more than a few thousand ions in any molecular dynamics system. However, periodic boundary conditions can be applied which enables a finite number of particles to generate realistic behaviour by mimicking an infinite system. The box of particles is surrounded by images of itself in such a way that when a particle leaves the simulation box an image rejoins the box on the opposite side with the same velocity and acceleration. In this way an infinite number of images is produced although the configuration and trajectories in the simulation box are exactly repeated in its images. Periodic boundary conditions are therefore very effective in modelling crystalline materials and it is also adequate for liquids or amorphous materials provided that any long-range properties are not considered.

One drawback of periodic boundary conditions is that it makes the system strictly three-dimensional and it is not possible to model surfaces in the same way as in static simulations as described in section 2.1.5. Our approach for modelling a surface in MD is first to simulate the bulk crystal, which has to be orientated such that two of the three lattice vectors lie in the surface plane. An MD simulation of the bulk crystal is run to obtain the lattice constant and crystal structure at the desired temperature and pressure. The surface is now created by expanding the lattice vector in the stacking direction (this is the third lattice vector which is the only one to have a component perpendicular to the surface) which creates a slab of material with two surfaces and a void between itself and its images in the stacking direction. It is most

important that the void is big enough so that no interactions occur between the one surface of the slab and its image across the void. Care must also be taken that the slab itself is thick enough to prevent ions at the surface experiencing interactions with the other face.

Once created, this system of slab and void is then again energy minimised by a conjugate gradient minimisation technique to make sure the surfaces are relaxed and, most importantly, that the shells have no potential energy, after which the MD simulation on this system can be run. If a pure surface is studied the void is maintained and MD simulations are limited to NVE or NVT ensembles. If the NPT ensemble were run the slabs would coalesce to reform the bulk material as this is always thermodynamically more favourable than separate slabs with two surfaces. However, when the void is filled with water molecules as we have done in this thesis, it is possible to run MD simulations at constant pressure as well (see chapter 4). Figure 2.8 illustrates the simulation cell with slab and void.

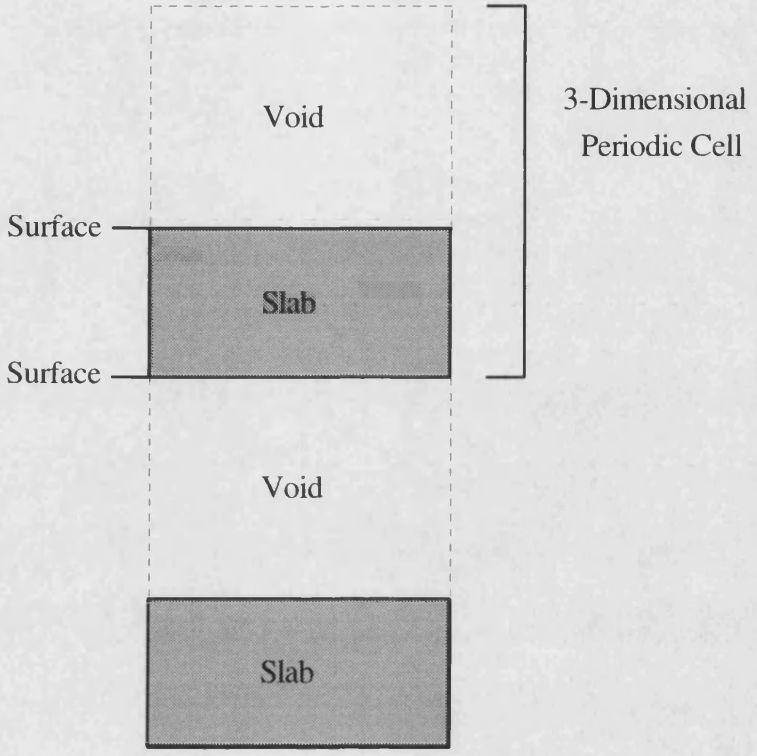

Figure 2.8 Schematic representation of the three-dimensional simulation cell for surface MD simulations

Properties from Molecular Dynamics

There is a whole range of properties which can be obtained from MD simulations, from thermal expansion to the phonon density of states and simulated neutron scattering data (Jacobs and Rycerz 1997). I will describe some of the properties most useful to this work in more detail.

MD simulations will provide us with the thermally averaged structure of the crystal or the surface. Similarly, rather than the surface energy of the lowest energy

surface, we can obtain a thermally averaged surface energy, and hence morphology (section 2.1.6), which may be more realistic when compared with experimental results. Rather than the energy of the whole surface slab and the whole bulk, the average surface energy is calculated from the average energy per ion of the surface slab and the bulk which are obtained from the MD simulations. The average surface energy then becomes:

$$<\gamma>=\left(\frac{N<E_{surf}>-N<E_{bulk}>}{Area}\right)x16.021 \qquad (2.57)$$

where N is the number of ions in the surface slab and bulk and $<E_{surf}>$ and $<E_{bulk}>$ are the average energy per ion in the surface slab and bulk respectively. The units are Jm^{-2}.

Another useful property which may be obtained from MD simulations is the Radial Distribution function (RDF) which gives a representation of the coordination and long-range order in a material. It is a plot of the average number of ions A from a central ion B at a given radius, usually normalised with respect to volume which means that at infinity the RDF converges to one. Figure 2.9 shows a schematic representation of the RDF of a crystalline solid at zero K. At higher temperatures the distinct peaks start to broaden and above melting point only the first peak assigned to the nearest neighbours will be distinctive. Hence the RDF together with the average structure will show whether a phase transition has taken place.

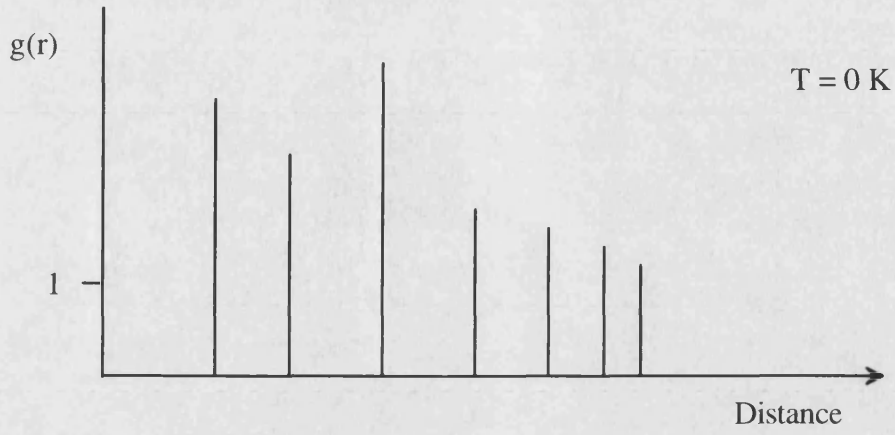

Figure 2.9 Schematic representation of the RDF of a crystalline solid at 0K

One of the most useful properties we obtain from MD simulations is the Mean Square Deviation (MSD) of the ions making up the simulated system. The MSD is the average displacement of an ion type from its initial coordinates:

$$< r_i^2(t) >= \frac{1}{N_i} \sum_{i=1}^{N_i} \left\{ [x_i(t) - x_i(0)]^2 + [y_i(t) - y_i(0)]^2 + [z_i(t) - z_i(0)]^2 \right\} \tag{2.58}$$

If the MSD for a given ion is constant and no increase is observed, the ion is not moving but is vibrating about its average lattice site. If, however, the MSD of an ion does increase with time, the ion is moving away from its mean lattice site indicating diffusion. When all different ion types making up the lattice are diffusing, the structure is considered to have melted, hence the MSD is a useful tool for determining melting points, when the lattice is simulated for a range of temperatures. The diffusion coefficient D_i is the gradient of the plot of MSD versus time:

$$< r_i^2(t) >= 6D_i t + B_i \qquad (2.59)$$

where B_i is the Debye-Waller factor of ion i which indicates the average distance it vibrates from the lattice site. The diffusion coefficient can be compared with experimental findings which is a useful aid when testing a new potential, such as when developing the water potential described in chapter 3, where the experimental self-diffusion coefficient can be compared with the one obtained from MD simulations.

Although the range of properties obtained from MD simulations is impressive, there are still some shortcomings, all of which relate to the amount of computer time the MD simulation can take. An obvious limitation is that the large number of timesteps necessary means that all but a very few simulations are limited to less than about 100 picoseconds of real time, and that any process that takes longer, such as the quenching of glass which can take several minutes, cannot be simulated. One way to overcome this problem is to use very simple models with only few potential parameters, such as a rigid ion model, and hence speed up the calculation of the forces at each timestep, but then the atomistic information distinguishing between different materials can be lost.

Another problem is that due to a lack of statistics no energy barriers larger than kT can be overcome as the ions are unable to jump the energy barrier.

3 POTENTIAL MODEL

The potential model describes the interatomic interaction energies in terms of a series of simple parameterised analytical functions. A good potential model is essential if reliable results are to be obtained. Quite often, the greatest uncertainties in the numerical results are due to the potential model rather than technical problems with the simulation itself (Harding 1990). Hence it would seem most appropriate to use electronic structure calculations to model the pure and hydrated surfaces. However, when using a good potential model, useful results may be obtained for a far larger system than is feasible with quantum mechanical methods and as we intended to study partial coverages of water on both planar, stepped and micro-facetted surfaces, all of which require large simulation cells, atomistic simulations employing potential models are the most appropriate for this work.

In this chapter we describe the potential model functions and the parameters used in these functions, which were used in this study. In addition, we fitted a new set of potential parameters for a water molecule to be used in conjunction with existing potential models in order to model the molecular adsorption of water at solid surfaces and details of how we obtained these parameters are also described.

3.1 The Born model of solids

Atomistic simulation techniques are based on the Born model of solids (1954) which assumes that the ions in the crystal interact via long-range electrostatic forces and short-range forces. The lattice energy of the crystal is the sum of the pairwise interactions between all ions i and j and is given by:

$$U_{r_{ij}} = \sum_{ij}' \frac{q_i q_j}{4\pi\varepsilon_0(r_{ij}+1)} + \sum_{ij}' \Phi_{ij}(r_{ij}) \qquad (3.1)$$

where the first term gives the Coulombic interaction described in chapter 2, equation (2.1). The second term is the short range contribution, which is described using simple parameterised analytical expresions. The prime on the summation indicates that the interaction where i = j is not included. The short-range interactions attempt to represent the repulsion due to overlap of neighbouring electron charge clouds and the van der Waals attractions which act over a few tens of Ångstroms. Other contributions may be included as well, such as bond-bending terms to convey the directionality of certain bonds in the crystal as for instance in the modelling of the covalent bonds in the carbonate groups of $CaCO_3$ (Pavese *et al.* 1996), and even four body interactions such as dihedral terms may be necessary to describe all interatomic interactions satisfactorily.

3.2 Electronic Polarisability

The simplest type of potential model is the *rigid ion* model which gives acceptable results over a wide range of systems (Harding 1990). The ions are treated as point charges and hence cannot be polarised, which implies that the high frequency dielectric constant becomes unity. Lattice vibrations are strongly coupled to polarisability (Catlow and Mackrodt 1982) and dynamical properties will therefore not be modelled very well using a *rigid ion potential*, such as the optic modes of the phonon spectrum. The accuracy of calculating segregation energies (Colbourn and Mackrodt 1985) and defect energies (Catlow and Mackrodt 1982) is also believed to be unfavourably affected. When a defect is introduced, polarisation *i.e.* the distortion of the electron cloud surrounding an ion in an electric field, would be expected to occur around the defect to stabilise it. It is possible to obtain the correct defect energies in a static simulation by modifying the short range interaction energies to accurately reproduce the static dielectric constants of the material (Gillan and Dixon 1980). The consequence is that the polarisation due to lattice relaxation is overestimated to compensate for the absence of electronic polarisability.

As described in chapter 2, the *rigid ion* model is often used in molecular dynamics simulations. As the inclusion of electronic polarisability increases the number of potential parameters required and the number of degrees of freedom of the molecular dynamics system, it is computationally less expensive to use a *rigid ion* potential than models which include electronic polarisability. However, because time is a factor of MD simulations the replacement of an almost instantaneous relaxation

due to electronic polarisability by a much slower lattice relaxation is not successful and it is really preferable to use a polarisable potential model both in static simulations of ionic solids, where each ion is situated in an electric field created by its neighbouring ions and hence electronic polarisation of the ions will occur, and MD simulations.

3.2.1 Point Polarisable Model

One simple way of including the electronic polarisability is to use the point polarisable model where each ion is allowed to develop a fixed point dipole of magnitude μ which is related to the polarisability α and the effective field E acting on the ions, as:

$$\mu = \alpha E \tag{3.2}$$

The energy of the interacting dipoles can then be calculated.

This model is computationally inexpensive and has been used in defect energy calculations (Norgett 1971). However, the defect energies were considerably lower than experimental values because this method does not account for the coupling between the short range repulsion and the polarisability. This coupling is strong since the displacement of the valence electrons as a result of the polarisation will affect the short range interaction between ions. The omission of this coupling causes the model to overestimate the polarisation leading to an underestimation of the defect energies.

Faux (1971) showed that there is a critical distance r_{crit} between the approaching ions beyond which the energy becomes divergent:

$$r_{crit}(ij) = (4\alpha_i\alpha_j)^{\frac{1}{6}} \tag{3.3}$$

Another way of modelling polarisability which largely overcomes this problem and introduces coupling between environment and polarisability is the shell model.

3.2.2 Shell Model

The shell model was first introduced by Dick and Overhauser in 1958. It describes the ion in a simple mechanical way by a shell of zero mass representing the electronic charge cloud connected to a core containing all the ion's mass (fig. 3.1). The total charge of the ion is the sum of the charge of the core, X and that introduced in the shell, Y. The position of the core represents the position of the ion in the crystal lattice but the position of the shell has no physical significance (Harding 1990). The shell and core are connected by a harmonic spring with force constant k:

$$\phi_i(r_i) = \frac{1}{2}k_i r_i^2 \tag{3.4}$$

where r_i is the distance between the centres of core and shell.

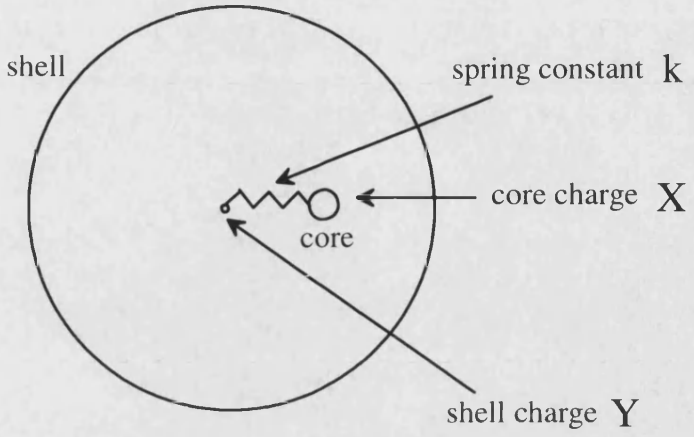

Figure 3.1 Schematic representation of the Shell model

The two new parameters, spring constant k and shell charge Y, give the polarisability α of the free ion as follows:

$$\alpha_i = \frac{Y^2}{4\pi\varepsilon_0 k_i} \tag{3.5}$$

Y and k are obtained by empirical fitting to the dielectric properties, elastic constants or dispersion curves of the material. The polarisation of an ion is described in terms of the displacement of its shell relative to the core. Unlike the point polarisable ion model the shell model does allow for coupling between polarisability and short-range interactions. The short-range forces are assumed to act between the shells while the Coulombic forces act between all shells and cores except between the core and shell of the same ion. Although the shell model is relatively simple, it has been very successful in modelling various properties and it is used in all static energy

minimisation calculations in this work to account for the polarisability of the oxygen ion.

As discussed in chapter 2.1.7 the shell model used in the molecular dynamics program DL_POLY is slightly different. The principle is the same as the shell model of Dick and Overhauser (1958) above but rather than zero mass, the shells of the ions have a mass, which is negligible compared to the mass of their cores in order that no exchange of energy between core and shell takes place during the simulation. Apart from assigning some of the mass to the shell (deducted from the core mass), the potentials used for the static simulations including shell charge and spring parameters are identical when used in DL_POLY.

A new alternative to the shell model for including polarisability in MD simulations is to parameterise polarisation effects by *ab initio* calculations (Wilson *et al.* 1996). The normal rigid-ion interatomic potential is supplemented with a representation of the induced dipoles and even quadrupoles on the ions. The dipole induced on an ion by both interionic electric fields and short-range interactions is calculated in a self-consistent way from the charges and dipoles on the other ions and included in the interatomic forces. The interatomic potential therefore includes the full many-body polarisation energy (Wilson and Madden 1994, 1994a). The use of these type of potentials in materials in which the stoichiometry is complicated and where polarisation effects have a strong influence on structure, has shown improved agreement with experimental properties such as phonon dispersion and liquid

structure (Wilson *et al.* 1994a, 1996) and no doubt will be used more widely in the future.

3.3 Short Range Potential Functions

The two body potential functions act between neighbouring charge clouds, the shells of polarisable ions and cores in the case of many cations, and come in a number of analytical forms, all describing the potential energy as a function of interionic separation. The potential functions act radially without taking into account directionality of bonds. Some of these functions will be described below.

Many-body potential functions act between three or four ions and are used when (partially) covalent bonds are present in the simulated system. The terms define angles and dihedrals between the ions and as such convey directionality to the bonds.

3.3.1 Bond Harmonic Function

The simplest potential used for a bonding pair of ions is the bond harmonic function:

$$\Phi(r_{ij}) = \frac{1}{2}k_{ij}(r_{ij} - r_0)^2 \qquad (3.6)$$

where k_{ij} is the bond force constant, r_{ij} the interionic separation and r_0 the separation at equilibrium. This harmonic potential is adequate for small deviations from the

equilibrium bond distance. However, the anharmonicity of bonds in real systems cannot be modelled using this function and thus we need more sophisticated potential functions to model a wider range of separations.

3.3.2 Morse Potential Function

The Morse potential is capable of modelling anharmonicity and as such interionic distances away from the equilibrium bond distance can be simulated using this potential function, for example the OH bond in an hydroxide group (Catlow *et al.* 1995):

$$\Phi_{ij}(r_{ij}) = D\left(1 - e^{[-\alpha(r_{ij}-r_0)]}\right)^2 - D \qquad (3.7)$$

where D is the dissociation energy of the bond, r_0 is the equilibrium separation as before and α is a variable which can be determined by spectroscopic data. The form of the Morse potential function ensures that at infinite separation of the two ions the potential energy is zero while the potential energy is at a minimum at the equilibrium bond distance (fig. 3.2), which is in keeping with the definition of lattice energy in chapter 2. The slope of the energy well is determined by the variable α.

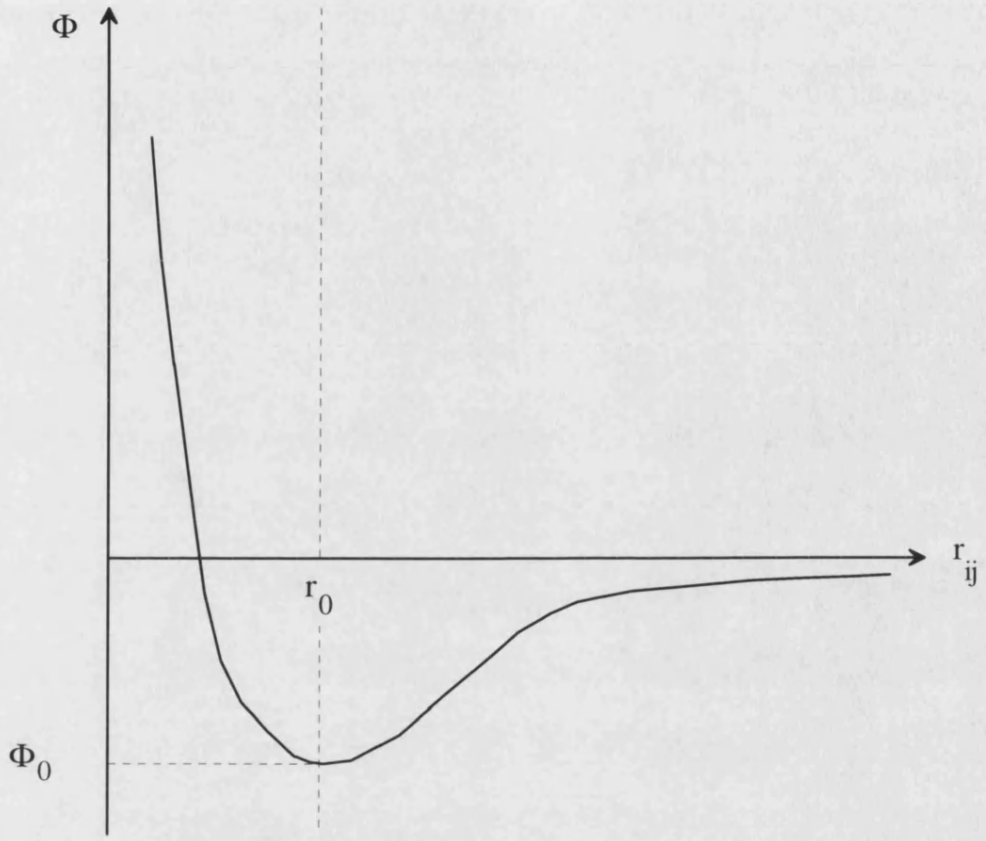

Figure 3.2 Diagram showing the Morse potential function

Sometimes, often in organic molecules, the Morse potential is used with subtraction of the Coulombic interaction and as such it is the only potential function describing a bond between two nearest neighbours. Interactions between second and further nearest neighbours can then be described by Coulombic interactions and another short-range potential function.

3.3.3 Lennard-Jones Potential Function

The most widely used potential function for non-bonded interactions is the Lennard-Jones potential, which has the following form:

$$\Phi(r_{ij}) = \frac{A}{r_{ij}^{12}} - \frac{B}{r_{ij}^{6}} \tag{3.8}$$

where A and B are variable parameters. The repulsive part is dependent on r^{-12} and thus acts at very close range while the attractive part, proportional to r^{-6} becomes dominant at longer range. The Lennard-Jones potential is often used for modelling oxygen-oxygen interactions in water potential models, such as the SCP and TIP4P models (Jorgensen *et al.* 1983, Rick *et al.* 1994).

3.3.4 Buckingham Potential Function

The Buckingham potential is the most widely used of the two-body potential functions and in this function the r^{-12} term of the Lennard-Jones function has been replaced by an exponential term:

$$\Phi_{ij}(r_{ij}) = A_{ij} e^{-\frac{r_{ij}}{\rho_{ij}}} - \frac{C_{ij}}{r_{ij}^{6}} \tag{3.9}$$

where classically the parameters A_{ij} and ρ_{ij} are the size and hardness of the ion respectively. The first term of equation (3.9) then represents the short-range repulsive interaction between the ions while the second term represents the attractive van der Waals forces. The Buckingham potentials used in this work, however, are effective pair potentials where the A_{ij} and ρ_{ij} terms have become more or less fused. Occasionally, the last term is omitted altogether (a Born-Mayer potential) and the A parameter is adjusted to take into account the longer-range attractive forces as well as the short-range repulsions.

3.3.5 Three-body Terms

The following bond-bending term is widely used to describe partial covalency in silicates (Sanders *et al.* 1984) and in carbonate groups (Titiloye *et al.* 1993):

$$\Phi_{ijk}(r_{ijk}) = \frac{1}{2}k_{ijk}(\Theta_{ijk} - \Theta_0)^2 \qquad (3.10)$$

which is a simple harmonic about the equilibrium bond angle, where k_{ijk} is the force constant and $(\Theta_{ijk} - \Theta_0)$ is the deviation of the bond from the equilibrium angle Θ_0. The function acts between a central ion i and two ions j and k bonded to i making the bond angle Θ (fig. 3.3).

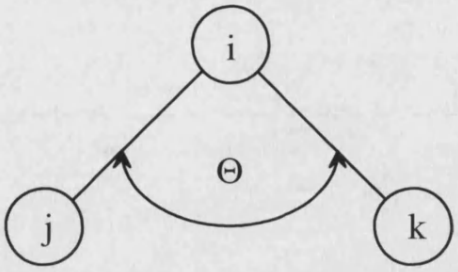

Figure 3.3 Diagram showing the three-body interaction

As in the Morse potential organic molecules neglect electrostatic interactions between ions i and j as well as between pairs i j and i k.

3.3.6 Four-body Terms

Four-body potential functions define a torsional angle between two planes each containing three ions. Figure 3.4 shows the arrangement of the ions and the planes making up the torsional angle.

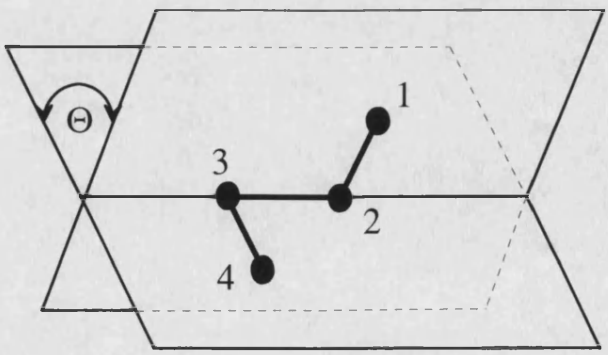

Figure 3.4 Diagram showing four atoms lying in two planes and the torsional angle Θ between the planes

A common four-body potential function used for example to model carbonate groups in calcite (Pavese *et al.* 1996) is:

$$\Phi_{ijkl} = K_{ijkl}[1 - s\cos(N\Theta)] \qquad (3.11)$$

where K is a force constant, s is $\pm$ 1 and N is an integer which gives the periodicity of the torsion, which is 2 in the case of the carbonate group. The above functional form means that the energy has a minimum value when Θ is 0 or π radians and all atoms lie in the same plane as is the case in the carbonate anion.

3.4 Derivation of Potential Parameters

The potential parameters for the short-range potential functions can be derived non-empirically by calculating the interactions or empirically by fitting to experimental crystal data such as structure, dielectric and elastic properties.

3.4.1 Non-empirical derivation

The non-empirical approach is to calculate the interaction energy between two ions as a function of distance and hence obtain a potential energy surface. The parameters can then be fitted directly to the potential energy surface. In this case the interactions are calculated using one of two methods:

In the electron-gas method as introduced by Jensen (1936) the electrons in an atom or ion are treated as a degenerate Fermi gas. The charge clouds around the separated ions are calculated by a Hartree-Fock procedure and simply summed to approximate the electron density for the interacting system (Allan and Mackrodt 1994). Having obtained the electron densities around the atoms, a density functional method, for instance that used by Gordon and Kim (1972), is used to obtain the electrostatic and kinetic energies and the exchange and correlation contributions of the total energy sought. Although originally only used for closed shell atoms and molecular systems, it has later been adapted to include ionic crystals and many-body effects (Muhlhausen and Gordon 1981).

Another way of determining the interaction energy as a function of interionic separation is to use *ab initio* Hartree-Fock methods. Although computationaly expensive this is an especially powerful technique if electron-gas methods are inadequate as for instance in the case of ZnO (Mackrodt *et al.* 1980).

Although potentials obtained by non-empirical methods have the advantage that they are valid over a wide range of interionic separations, they generally overestimate lattice parameters and experimental data are used to modify the parameters to compensate for deficiencies in the methods (Colbourn 1992). They are, however, particularly useful where there are few experimental data available.

3.4.2 Empirical derivation

In the empirical method the potential parameters are obtained by least squares fitting to a range of experimental data such as crystallographic data, unit-cell dimensions and atom coordinates (Freeman *et al.* 1993), elastic constants and phonon dispersion curves (Colbourn 1992).

The major limitation of empirical potentials is that there are often insufficient experimental data available. Another disadvantage is that strictly speaking the potential parameters are only valid if the ions are at the equilibrium separations when the potential is fitted. This is why it is so important to fit to properties, e.g. elastic and dielectric data, which probe the shape of the energy surface. This will then allow the potential to be used at different separations away from the equilibrium ion positions as will be the case at surfaces or when defects are present. In addition, rather than fitting to a single structure, concurrent fitting of multiple structures is found to enhance greatly the reliability of the derived potentials (Gale 1996).

Furthermore, in order to limit the number of variables and because experimental data are often not available, cation-cation interactions are assumed to be purely Coulombic while their short-range interactions are not taken into account. This is not believed to be a problem because the cations are usually small and do not overlap.

3.5 Transferability of Potentials for Surface Simulations

The surface environment of a crystal is different from the bulk and yet empirically derived potentials are fitted to properties obtained from the bulk material. However, Lawrence (1988) compared energies and surface relaxations of Cr_2O_3 using two different potentials reproducing bulk properties and did not find significant differences between the two potentials indicating that a potential reproducing bulk properties accurately can be expected do so for surface properties as well.

Finally, there remains the question whether a potential derived for a particular compound can be used for other compounds as well. Catlow *et al.* (1988) in their work on spinels, for instance, used the potentials of Lewis and Catlow (1985), obtained by fitting to rock-salt and corundum structural data. Although this transfer of potentials from one system to another is frequently successsful it may fail as the potentials can be dependent on local environment (Harding 1990). For instance, potential parameters for the alkali halides are transferable but those for oxides may not be since the oxide ion does not exist as a stable free ion (Lewis and Catlow 1985) and as such there will be a strong variation in electronic polarisability with crystalline environment as shown by Sangster and Stoneham (1980) in their work on the rocksalt structured oxides.

However, empirically fitted potentials have been successful for a range of structures and techniques including impurity segregation (Kenway *et al.* 1989), TiO_2 surfaces (Oliver *et al.* 1994a), morphology of carbonate minerals (Parker *et al.*

1993a), oxygen vacancies on ceria surfaces (Sayle *et al.* 1994) and molecular dynamics of fluoride-perovskites (Watson *et al.* 1992), and they will be used throughout this work.

3.6 Potentials used in this work

The CaO, MgO and Al_2O_3 potentials have been tested against experimental data on the bulk crystal properties and the simulation results were found to be reliable (Lewis and Catlow 1985). In addition, the MgO potential shows the same qualitative surface rumpling as observed experimentally.

The calcium carbonate potential parameters (Pavese *et al.* 1996) were fitted to the thermal properties of calcite, one of the calcium carbonate polymorphs, and reproduce the bulk properties, including elastic constants very well.

The potential for the hydroxide ion (Baram and Parker 1996) is compatible with the potential models for the ionic solids and was tested by modelling hydroxylated silica surfaces and the bulk structures of gibbsite $Al(OH)_3$ and brucite $Mg(OH)_2$.

3.6.1 CaO, MgO and Al_2O_3 Potentials

The potentials used for the pure CaO, MgO and one set of Al_2O_3 surfaces are those derived empirically by Lewis and Catlow (1985) to a number of experimental results including elastic constants, dielectric constants, cohesive energy and structure.

In their derivation they accepted the following assumptions (Catlow 1977, Sangster and Stoneham 1980):

1. The oxygen-oxygen interaction is taken to be the same for all crystals as this interaction is very small at the equilibrium separation.
2. Cation-cation interactions are assumed to be purely Coulombic. Since cations are generally smaller than oxygen ions, their interactions would be even smaller.
3. The attractive r^{-6} term of the short-range Buckingham potential is ignored in the cation-anion interactions and allowance for the van der Waals attraction will be made in the other parameters.

The oxygen atom is modelled as a core and shell to allow for its polarisability, but the cations are much less polarisable and consist of just a core, their charge being the full valence charge of +2 for Mg and Ca and +3 for Al. The overall charge of the oxygen ion is -2, the sum of the charges on the core and the shell.

The short range forces between the oxygen shells and cations are described by a Buckingham potential (equation 3.9) while the interaction between the oxygen ion's core and shell is given by equation (3.4). Table 3(I) gives the potential parameters used.

	Buckingham Potential		
Ion Pair	A (eV)	ρ (Å)	C (eVÅ^6)
Ca^{2+} - O^{2-}	1090.4	0.34370	0
Mg^{2+} - O^{2-}	1428.5	0.29453	0
Al^{3+} - O^{2-}	1474.4	0.30060	0
O^{2-} - O^{2-}	22764.0	0.14900	27.88
O^{2-}	core-shell interaction (eVÅ^{-2})	Mg	54.80
		Ca	47.96
		Al	60.78
	O core charge		+1.00
	O shell charge		-3.00

Table 3(I) Potential parameters by Lewis and Catlow (1985)

In our calculations of Al_2O_3 surfaces (chapter 5), we compared results we obtained using two slightly different potentials. One is the potential derived by Lewis and Catlow (1985) and given in table 3(I) above. The second is an earlier potential derived by Catlow *et al.* (1982) the potential parameters of which are given in table 3(II).

	Buckingham Potential		
Ion Pair	A (eV)	ρ (Å)	C (eVÅ^6)
Al^{3+} - O^{2-}	1460.3	0.29912	0.00
O^{2-} - O^{2-}	22764.3	0.14900	27.88
O^{2-}	core-shell interaction (eVÅ^{-2})	Al	103.07
	O core charge		+ 0.81061
	O shell charge		- 2.81061

Table 3(II) Potential parameters by Catlow *et al.* (1982)

3.6.2 Calcium Carbonate Potential

The potential parameters we used for the simulation of the calcium carbonate polymorphs calcite, aragonite and vaterite were derived by Pavese *et al.* (1996). They are empirically derived from the structure and thermal properties of calcite and reproduce the experimental properties such as elastic constants very well. The calcium ion has a full valence charge of +2, while the carbon and oxygen ions have fractional charges with the overall charge of the carbonate group -2. The oxygen-oxygen and cation-oxygen interactions are modelled by Buckingham potential functions, while the carbon-oxygen bond is described by a Morse potential. The covalency within the carbonate group is modelled by a three-body bond, see equation (3.10), and a torsional potential function (equation 3.11) to restrain the planar carbonate group from folding. As with the Lewis and Catlow (1985) potentials, the interactions between calcium and carbon atoms are only described by

the Coulombic interactions while any short-range forces are deemed negligible. The potential parameters used are given in table 3(III).

	Buckingham Potential		
Ion Pair	A (eV)	ρ (Å)	C (eV Å^6)
Ca^{2+} - $O^{1.045-}$	777.27	0.34370	0
$O^{1.045-}$ - $O^{1.045-}$	22764.00	0.14900	13.94
	Morse Potential		
	D (eV)	α (Å^{-1})	r_0 (Å)
$C^{1.135+}$- $O^{1.045-}$	4.61	3.80	1.18
	Many-Body Potentials		
		k (eV rad^{-2})	Θ_0
C-O-C		1.69	120^0
C-O-O-O		0.0917	180^0
$O^{1.045-}$	core-shell interaction (eV Å^{-2})		507.4
	O core charge		+0.587
	O shell charge		-1.632

Table 3(III) Potential Parameters by Pavese *et al.* (1996)

3.6.3 Hydroxide Potential

The potential employed for the interaction of the hydroxide ion with the rest of the crystal was developed by Saul *et al.* (1985) and successfully used by Wright *et al.* (1994) to study the hydrogarnet defect in grossular. The potential parameters for the hydroxide ion itself were modified by Baram and Parker (1996) to include a polarisable oxygen ion, and applied in their study of hydroxide formation at the surfaces of quartz and zeolites.

The forces between the atoms of the OH group are modelled by a Morse potential (equation 3.7) and are described by Catlow *et al.* (1995) in their work on protons in oxides. The charges for the hydrogen and hydroxyl oxygen are fractional so as to reproduce the experimental dipole moment of the OH radical (Catlow *et al.* 1995). They are +0.4 for the hydrogen core and -1.4 for the hydroxyl oxygen, the sum of core and shell charges. As a result of these fractional charges, the oxygen-cation Buckingham potential needs to be modified for the interaction between cations and hydroxyl oxygen ions to compensate for the reduction in electrostatic interaction (Schroder *et al.* 1992). To this end the ρ parameter of the Buckingham potential function is kept at the same value. The electrostatic interaction between cation and anion was kept fixed but the *A* parameter is adjusted in such a way that the electrostatic forces and the short-range forces described by the Buckingham potential are equal at the equilibrium bond distance. The potential parameters thus obtained were then tested against the metal hydroxides $Ca(OH)_2$, $Mg(OH)_2$ and $Al(OH)_3$ (Baram and Parker 1996) and were found to reproduce the bulk structures adequately. The potential parameters used are given in Table 3(IV).

	Buckingham Potential		
Ion Pair	A (eV)	ρ (Å)	C (eV Å^6)
Ca^{2+} - $O^{1.4-}$	777.27	0.34370	0
Mg^{2+} - $O^{1.4-}$	941.50	0.29453	0
Al^{3+} - $O^{1.4-}$ [1)]	1032.08	0.30060	0
Al^{3+} - $O^{1.4-}$ [2)]	1142.6775	0.29912	0
O^{2-} - $O^{1.4-}$	22764.00	0.14900	13.94
$O^{1.4-}$ - $O^{1.4-}$	22764.00	0.14900	6.97
$H^{0.4+}$ - $O^{1.4-}$	311.97	0.25000	0
	Morse Potential		
	D (eV)	α (Å^{-1})	r_0 (Å)
$H^{0.4+}$- $O^{1.4-}$	7.0525	3.1749	0.94285
$O^{1.4-}$	core-shell interaction (eV Å^{-2})		74.92038
	O core charge		+0.90000
	O shell charge		-2.30000

[1)] Obtained with Lewis Catlow (1985) potential, [2)] Baram and Parker (1996)

Table 3(IV) Potential parameters for hydroxide interactions

3.7 Water Potential

One of the aims of this work was to develop a reliable and consistent model for the interaction of water with oxide surfaces. Although there is a wealth of different water potentials available (Jorgensen 1981, 1982, Jorgensen *et al.* 1983, Trokhymchuk *et al.* 1993, Bernardo *et al.* 1994, Lau *et al.* 1994, Rick *et al.* 1994, Zhu and Wong 1994, Brodtholt *et al.* 1995, 1995a, Duan *et al.* 1995) from simple SPC models to point polarisable TIP models, none were compatible with the type of simulations done in this work, namely a potential model for modelling water molecules where the polarisability of the oxygen ion is included by the shell model of Dick and Overhauser (1958) described in section 3.2.2. As such it would be

compatible with the potentials described in section 3.6 used for simulating ionic and molecular crystals and we could then model molecular adsorption of water molecules onto crystal surfaces. The potential parameters were fitted to structure, infra-red data and diffusion coefficients and the resultant model was then tested against various ice structures.

3.7.1 Derivation of Potential Parameters

The potential model for H_2O which we developed is based on the hydroxide potential described in chapter 3.6.3 but, naturally, with two hydrogen atoms per oxygen atom. The fractional charges and potential parameters were then modified to reproduce the experimental dipole moment, OH bond length and HOH angle of the water molecule and the structure of the water dimer.

Two new short-range interactions needed to be introduced, the first being a bond-bending term (equation 3.10) to reproduce the directionality of the covalent bonds with a HOH angle of 104.5°. The second term introduced attempts to model the effect the oxygen atom's electron lone pairs have on the hydrogen positions and hence on the HOH angle. In an attempt to include the steric effect of the electron lone pairs we partially removed the electrostatic interactions between the two hydrogen atoms in the water molecule making them less repulsive. We found that if we removed 54% of the electrostatic force acting between the intramolecular hydrogen atoms we achieved a water molecule with the same geometry and dipole moment as that found experimentally (Rick *et al.* 1994).

$$\Phi_{ijk}(r_{ijk}) = -0.54\left(\frac{q_H^2}{r_{ijk}}\right) \qquad (3.12)$$

where q_H is the (fractional) charge of the hydrogen ion, which was kept at +0.4, in line with both the hydroxide potential (chapter 3.6.3) and a host of other potential models for water (Jorgensen *et al.* 1983, Lau *et al.* 1994, Rick *et al.* 1994). This charge and the resultant charge of -0.8 on the oxygen ion, a combination of core and shell charges, reproduced the dipole moment of the gaseous water molecule (exp. 1.85 D, Rick *et al.* 1994).

The intermolecular short-range interactions between the hydrogen cores and oxygen shells are given by a Buckingham potential (equation 3.9) while a Morse potential (equation 3.7) describes the intra-molecular forces between oxygen shell and hydrogen cores. The interactions between the oxygen shells are described by a Lennard-Jones potential (equation 3.8). The potential parameters are given in table 3(V).

	Buckingham Potential		
Ion Pair	A (eV)	ρ (Å)	C (eV Å^6)
$H^{0.4+}$ - $O^{0.8-}$	96.27	0.2300	0
	Lennard-Jones Potential		
	A (ev Å^{12})	B (eV Å^6)	
$O^{0.8-}$ - $O^{0.8-}$	29344.98	42.15	
	Morse Potential		
	D (eV)	α (Å^{-1})	r_0 (Å)
$H^{0.4+}$ - $O^{0.8-}$	7.0525	3.1749	0.94
	Three-Body Potential		
		k (eV rad^{-2})	Θ_0
H-O_{core}-H		6.0	104.5
$O^{0.8-}$	core-shell interaction (eV Å^{-2})		75.0
	O core charge		+0.750
	O shell charge		-1.550

Table 3(V) Potential parameters of the water molecule

The potential parameters describing the water molecule as given in table 3(V) adequately model the water monomer and dimer. Table 3(VI) compares the calculated properties of the monomer and dimer, obtained with the above potential, with the experimental values.

H_2O	Properties	calculated	experimental
Monomer	R_{OH} (Å)	1.01	0.96[a]
	θ_{HOH}	104.5°	104.5° [a]
	Dipole (D)	1.86	1.85[b]
	E (eV)	-6.90	-
Dimer	R_{OO} (Å)	2.90	2.98[cde]
	θ_{α}	31.2°	57 ± 10° [cd]
	θ_{d}	50.6°	51 ± 10° [cd]
	$E_{binding}$ (eV)	-0.184	-0.23[d]

[a] (Zhu and Wong 1994) [b] (Rick *et al.* 1995) [c] (Odutola and Dyke 1980) [d] (Curtiss *et al.* 1979) [e] (Dyke *et al.* 1977)

Table 3(VI) Calculated and experimental properties of water monomer and dimer

θ_d in table 3(VI) refers to the angle in the dimer between the O-O vector and the C_2 axis of the water molecule donating its one hydrogen for hydrogen bonding to the oxygen molecule of the acceptor molecule (figure 3.5). θ_a refers to the angle between the O-O vector and C_2 axis of the acceptor molecule (figure 3.5) (Dyke *et al.* 1977, Bernardo *et al.* 1994).

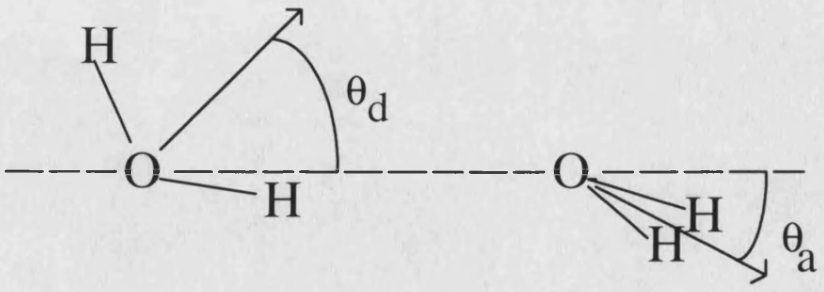

Figure 3.5 Configuration of the water dimer (Dyke *et al.* 1977 Bernardo *et al.* 1994)

Having derived the above potential parameters we decided to test them by simulating various structures of ice. We felt that if the potential was able to reproduce these structures accurately we could be confident that the water potential was a viable potential for static simulations.

3.7.2 Structures and Energies of Ice

It would be both interesting and of practical importance to learn about the crystallisation process and morphology of ice under various conditions. The icecream industry, for example, prefer not to have crystalline ice occurring during their manufacturing process as this diminishes the smoothness of their product. In another area, biologists, when studying frozen tissue, would like to avoid water crystallising into ice as this ruptures the cells.

Thirteen different ice structures are recognised, including a vitreous form and two relatively unknown phases. Table 3(VII) (Kamb 1969) shows the different phases and some of their properties. Some of the ices invert into other phases or form a solid-solid phase transition into another structure.

Phase	Density g cm^{-3}	Pressure kb	Limits of Temperature range		Transition at upper limit
			Lower ^{0}C	Upper ^{0}C	
I*h*	0.92	0	-273	0	melts
I*c*	0.92	0	-150	-90	inv. to I*h*
vitreous	0.94	0	-273	-120	inv. to I*c*
II	1.21	3	-273	-30	trans. to III
III	1.15	3	-90	-20	melts
IV	1.29	5	-40	-25	melts
V	1.28	5	-150	-10	melts
VI	1.38	14	-150	50	melts
VII	1.57	25	2	110	melts
VIII	1.63	25	-273	2	trans. to VII
IX	1.19	3	-273	-105	trans. to III
X *	~1.4	-	-273	-150	trans. to VI
XI *	~1.3	5	-273	-150	trans. to V

Table 3(VII) Ice Phases * Provisional designation

Apart from ice I, consisting of two forms, hexagonal I*h* and cubic I*c*, which is metastable and occurs on condensation of water vapour or can be obtained by the interconversion of ice II, III, and V (Franks 1976), all other ice structures are formed at high pressures and low temperatures. However, once formed the phases are metastable and hence can be retained at atmospheric pressure when kept at liquid nitrogen temperature. Most structural information has been obtained at this temperature (Kamb 1972) and as our simulations neglect temperature this is adequate for modelling the various ice phases.

One feature that all ice phases have in common is the nearest-neighbour geometry. Each oxygen is hydrogen-bonded to four neighbouring oxygen atoms in a

tetrahedral coordination. Of the four hydrogen atoms tetrahedrally surrounding each oxygen atom, two are bonded to the oxygen and lie close to it at about 1 Å distance while the other two are hydrogen-bonded to the oxygen atom at a distance of about 2 Å. Each hydrogen lies on the line connecting two adjacent oxygen atoms, as was confirmed by neutron diffraction (Dorsey 1940, Kamb 1972, Franks 1976). In an ideal tetrahedral coordination, as exists in ice I, there are six equivalent orientations of the distinct water molecules which have the same bond energy and hence occur with equal probability. Even in a less perfectly tetrahedral coordination, as occurs in the denser ice phases, at high temperatures the gain in configurational entropy accompanying disorder of the hydrogen atoms outweighs the energy expended by some orientations departing from the ideal angle. However, some orientations where the HOH angle differs substantially from the tetrahedral HOH angle (109.5^0) or the HOH angle in the free molecule (104.5^0) will be avoided, and thus some hydrogen order develops at lower temperatures (Kamb 1972). In ice I the HOH angle is at its ideal tetrahedral value but as the pressure increases this angle becomes progressively distorted in such a way as to reduce the distances between the non-bonded water molecules (Franks 1976).

The experimental techniques used for the elucidation of the ice structures are X-ray crystallography, neutron diffraction, infra-red and Raman spectroscopy (Kamb 1972). One of the problems with reproducing experimental ice structures is that not all the atom positions have been determined, particularly as far as hydrogen is concerned. In some cases this is because the experimental ice structure is an average of two or more different structures with the hydrogens moving between different

positions, e.g. for ice II. In other instances, i.e. for ice I, the hydrogen atoms may not be resolved by the experimental technique used such as X-ray methods (Franks 1976).

Structure of Ice II

In ice II, the hydrogen atoms in the structure are ordered, in that the water molecules making up the framework are in a distinct orientation with regard to each other (Kamb 1972). The experimental structure used for comparison in this work is that of MacFarlan (1936) which was determined by X-ray diffraction. Hydrogen atoms cannot be resolved by X-ray methods and they placed the protons midway between neighbouring oxygens. The experimental structure is shown in figure 3.6.

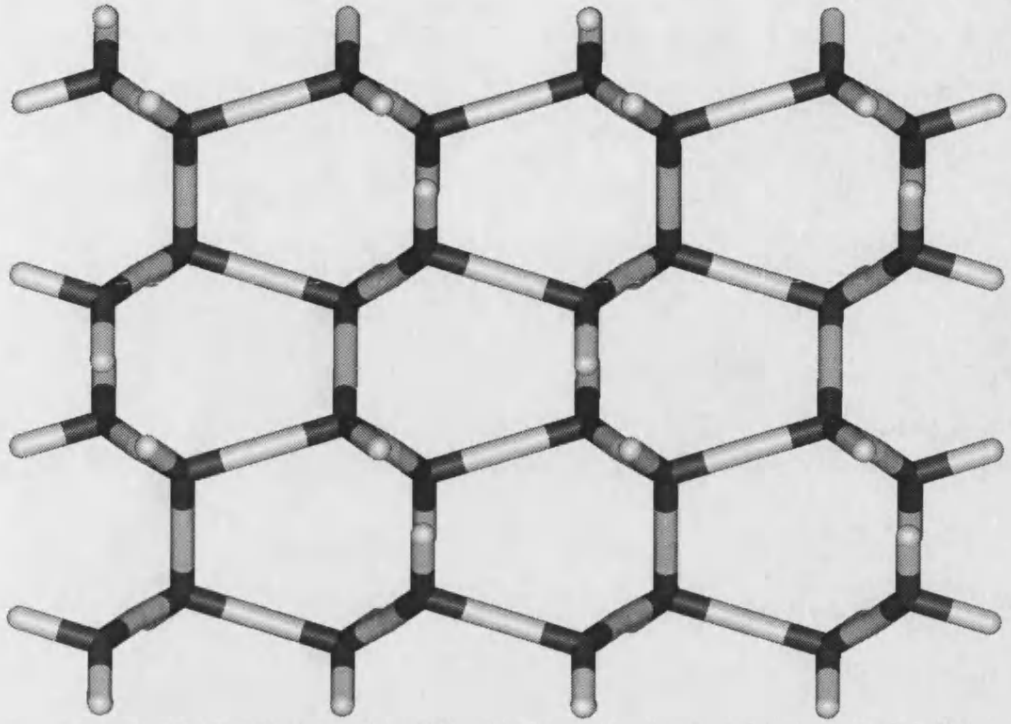

Figure 3.6 Experimental structure of ice II (Macfarlan 1936)

This structure is really an average of two structures each of which consists of distinct water molecules where the hydrogen atoms are not placed midway, *i.e.* at 1.35 Å, between the oxygens. We have simulated these complementary identical structures and the resulting average structure is shown in figure 3.7. Table 3(VIII) shows the bondlengths and interatomic distances of the experimental and calculated structures.

	experimental / Å	calculated / Å
r_{OO}	2.71	2.78
r_{OH}	-	1.01
r_{OH} (average)	1.35	1.38
r_{HH}	-	1.58
r_{HH} (average)	2.21	2.21
r_{OH} (hydrogen bond)	-	1.81
θ_{HOH}	109.9^{O}	102.9^{O}
ρ / gcm^{-3}	1.23	1.19

Table 3(VIII) Experimental and calculated data of ice II

The energies of the ice II structures as determined after energy minimisation by PARAPOCS (Parker and Price 1989) are -27.8 eV and -28.4 eV for a unit cell of 4 H_2O molecules giving an energy of -7.0 ± 0.1 eV per water molecule.

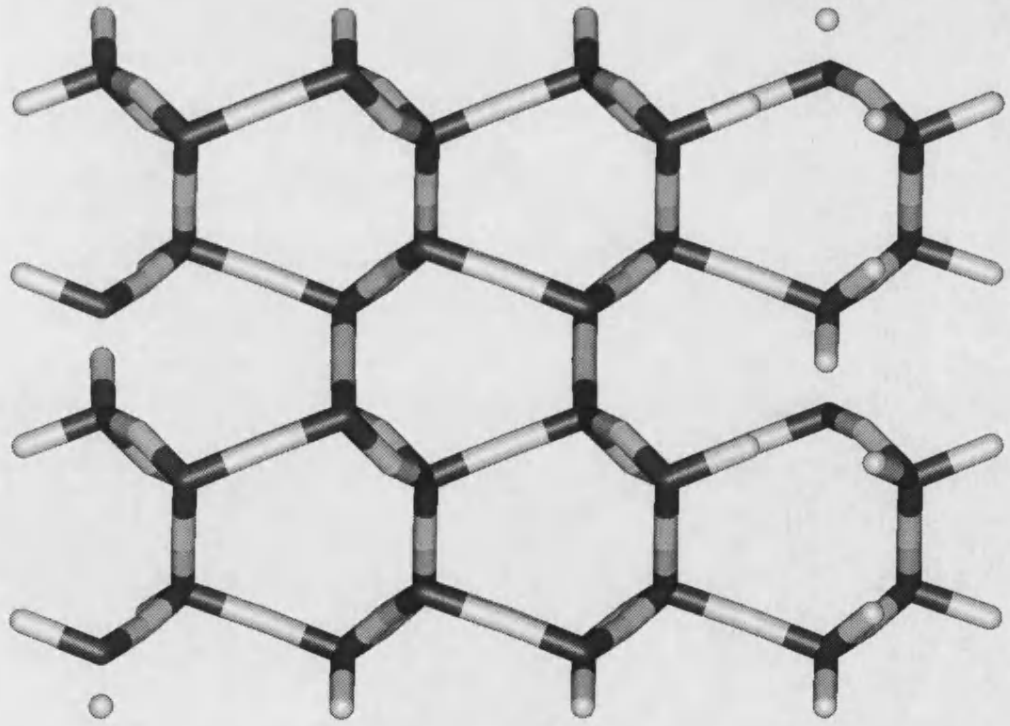

Figure 3.7 Calculated structure of ice II

Structure of Ice VII

Unlike ice II where the hydrogen atoms oscillate between two positions, in ice VII the hydrogen atoms are disordered. The coordination of the hydrogens around the oxygen atoms is perfectly tetrahedral favouring no particular configuration of water molecules over another. The structure of ice VII consists of two separate, interpenetrating networks of hydrogen bonds, each identical to the network in ice I*c* (Franks 1976).

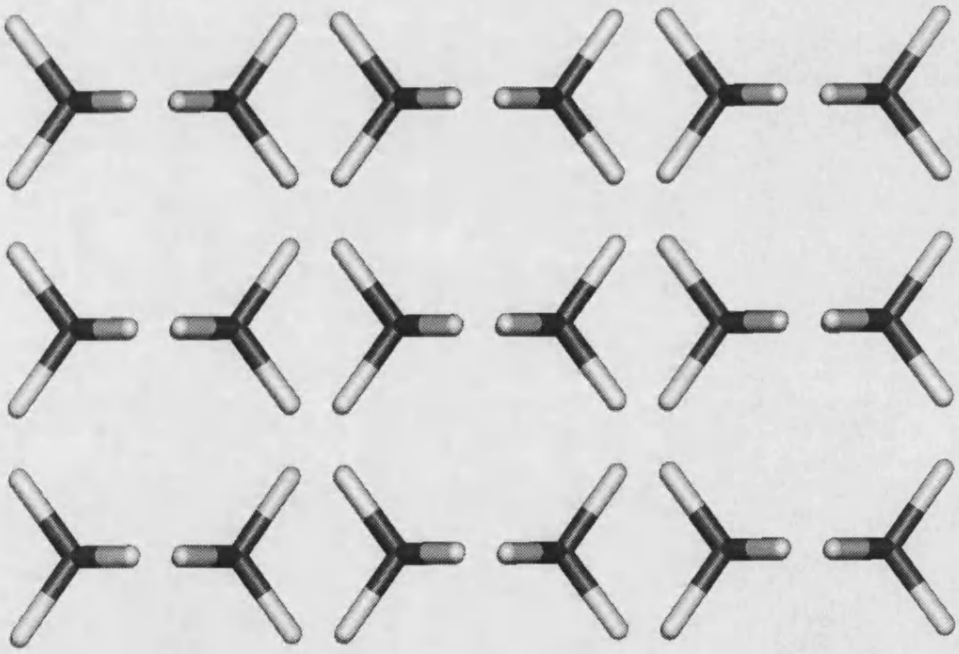

Figure 3.8 Experimental structure of ice VII with double hydrogen occupancy

The experimental structure of ice VII studied in this work was determined by Kamb and Davis (1964) using TEM and shown in figure 3.8. They found definite positions for the hydrogen atoms, but each position has an occupancy of a half. However, each position is energetically equivalent and mutually exclusive with one other position. We simulated two ice structures with identical energy of -13.6 eV per unit cell of two H_2O molecules giving an energy of -6.8 eV per water molecule. A combination of the two structures gives the structure shown in figure 3.9 which is similar to the structure determined by Kamb and Davis (1964). Table 3(IX) shows bondlengths and interatomic distances in the experimental and calculated structures.

	experimental / Å	**calculated / Å**
r_{OO}	2.86	3.03
r_{OH}	0.97	1.01
r_{HH}	1.59	1.57
r_{OH} (hydrogen bond)	1.89	2.02
θ_{HOH}	110.1^{o}	102.4^{o}
ρ / gcm^{-3}	1.66	1.49

Table 3(IX) Experimental and calculated data of ice VII

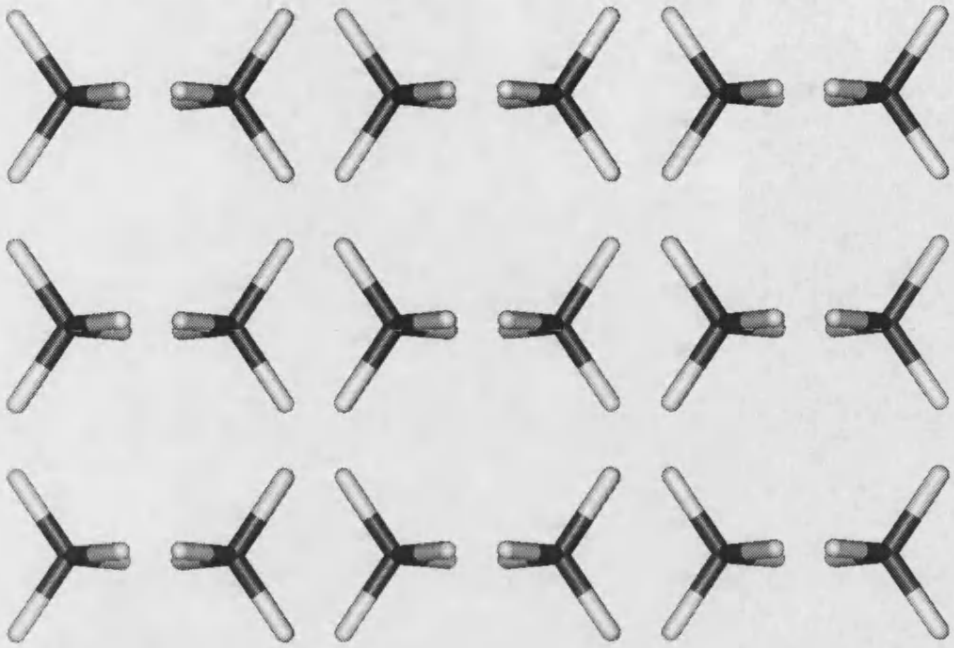

Figure 3.9 Calculated structure of ice VII with double hydrogen occupancy

We have also simulated some other ice structures which gave similar bond distances and comparable energies (table 3(X)) to ice phases II and VII.

Ice Phase	**Energy (eV) / H_2O**
I_h	-6.8605
II	-7.0292
III	-6.8745
VII	-6.8032
IX	-7.3250

Table 3(X) Calculated energies of ice phases

3.7.3 Oxide-Water Potential Parameters

The water potential developed so far adequately models the monomer and dimer of water as shown in section 3.4.3. It is also able to reproduce the structures of various ice phases relatively well. We were thus confident that the intermolecular interactions between the water molecules were modelled adequately for static simulations and our next step was to model interactions between water molecules and the surfaces of MgO and $CaCO_3$ using the above water potential. Again, as discussed in section 3.6.3, short-range potential parameters for the interactions between the solids' ions and the water molecule's oxygen atom were adjusted to allow for the fractional charges and these are shown in table 3(XI).

	Buckingham Potential		
Ion Pair	A (eV)	ρ (Å)	C (eV Å^6)
Mg^{2+} - $O^{0.8-}$	490.00	0.29453	0
O^{2-} - $O^{0.8-}$	22764.00	0.14900	28.92
$O^{1.4-}$ - $O^{0.8-}$	22764.00	0.14900	8.12
Ca^{2+} - $O^{0.8-}$	1186.60	0.29700	0
$O^{1.045-}$- $O^{0.8-}$	12533.60	0.21300	12.09
$O^{1.045-}$- $H^{0.4+}$	311.97	0.23000	0

Table 3(XI) Potential parameters for water-oxide interactions

Static simulations of molecular adsorption of water onto MgO and calcium carbonate surfaces were done and are described in chapters 4 and 6. The results agree well with previous calculations and experimental findings.

3.7.4 Adjustment of Water Potential Parameters

From static simulations it was logical to extend to model oxide surfaces under aqueous conditions at liquid water temperatures, namely performing molecular dynamics simulations. We first had to test the water potential model by modelling a system of just water molecules on their own from which we would obtain liquid water properties such as RDFs and a self-diffusion coefficient which could be compared with experiment. The water potential as described in chapter 3.7.1 and used in our static simulations (chapter 4 and 6) gave a self-diffusion coefficient of approximately 9 x 10^{-9} m^2/s compared to 2.3 x 10^{-9} m^2/s for the experimental value (Lau *et al.* 1994, Rick *et a*l. 1994). Although self-diffusion coefficients obtained from water potentials are often higher than the experimental self-diffusion coefficient (Lau *et al.* 1994) this value was rather large.

Another short-coming of the static water potential was the discrepancy between calculated and experimentally observed infra-red frequencies. We thus decided to adjust the intramolecular Morse potential describing the OH interaction to obtain a better fit to experimental infra-red frequencies using GULP (Gale 1997). After some refitting of the other intra- and intermolecular parameters to the monomer and dimer structures and experimental dipole moment, we obtained the potential given in table 3(XII).

	Buckingham Potential		
Ion Pair	A (eV)	ρ (Å)	C (eV Å^6)
$H^{0.4+}$ - $O^{0.8-}$	396.27	0.2500	10.0
	Lennard-Jones Potential		
	A (ev Å^{12})	B (eV Å^6)	
$O^{0.8-}$ - $O^{0.8-}$	39344.98	42.15	
	Morse Potential		
	D (eV)	α (Å^{-1})	r_0 (Å)
$H^{0.4+}$ - $O^{0.8-}$	6.203713	2.22003	0.92376
	Three-Body Potential		
		k (eV rad^{-2})	Θ_0
H-O_{shell}-H		4.19978	108.69
H-O	Coulombic Subtraction (%)		50
H-H			50
O	Core-shell interaction (eV Å^{-2})		209.449602
O	Core charge		+1.250
O	Shell charge		-2.050

Table 3(XII) New water potential parameters

The properties of the monomer and dimer obtained using this new potential are given in table 3(XIII). The calculated infra-red vibrations agree well with the experimental data and the structural properties are in slightly better agreement with experiment than in the previous model, as is the binding energy for the dimer.

H_2O	Properties	calculated	experimental
Monomer	R_{OH} (Å)	0.98	0.96[a]
	θ_{HOH}	104.5°	104.5° [a]
	Dipole (D)	1.86	1.85[b]
	E (eV)	-9.0986	-
	ν (cm^{-1})	1581.95	1594.59
	ν (cm^{-1})	3624.56	3657.05
	ν (cm^{-1})	3783.00	3755.79
Dimer	R_{OO} (Å)	2.97	2.98[cd]
	θ_{α}	30.1°	57 ± 10° [cd]
	θ_{d}	48.5°	51 ± 10° [cd]
	$E_{binding}$ (eV)	-0.209	-0.23[d]

[a] (Zhu and Wong 1994) [b] (Rick *et al.* 1995) [c] (Odutola and Dyke 1980) [d] (Curtiss *et al.* 1979) [e] (Dyke *et al.* 1977)

Table 3(XIII) Calculated and experimental water properties using new potential

These parameters were then used for Molecular Dynamics simulations of hydrated MgO surfaces and static energy minimisation calculations of physisorption of water onto α–alumina surfaces. The potential parameters used for the interactions between water molecules and aluminium atoms are given in table 3(XIV).

	Buckingham Potential		
Ion Pair	A (eV)	ρ (Å)	C (eV Å^6)
Al^{3+} - $O^{0.8-}$ 1)	590.0400	0.30060	0
Al^{3+} - $O^{0.8-}$ 2)	584.1107	0.29912	0
O^{2-} - $O^{0.8-}$	22764.00	0.14900	28.92

Derived from [1] Lewis and Catlow (1985), [2] Catlow *et al.* (1982)

Table 3(XIV) Potential parameters for water-alumina interactions

3.7.5 Molecular Dynamics

We used the DL_POLY program (Forester and Smith 1995) to simulate a box containing 256 water molecules at a temperature of 300K. The simulation conditions were set initially at the experimental density of $\rho = 1.0$ g/cm^3 and scaling and proper runs were done at NVE and NVT. When those were successful, scaling runs and finally proper data collection runs were done at NPT.

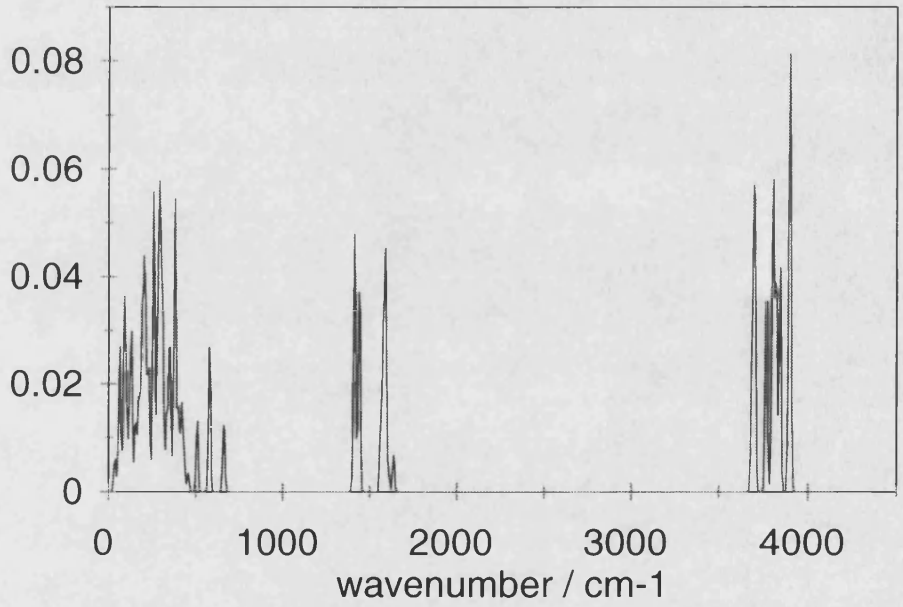

Figure 3.10 Phonon density of states for iceVII with the pseudo-shell model. The first group of peaks corresponds to acoustic and low-lying optic modes, the second group is due to H-O-H bending and the third group is the O-H stretching mode.

We had to assign mass to the oxygen shell as discussed in section 3.2.2. This mass was chosen to be 0.2 a.u., small compared to the mass of the hydrogen atom of

1.0 a.u. This ensured that there would be no exchange of energy between vibrations of oxygen core and shell and oxygen shell and hydrogen core. We checked this as shown in figure 3.10 for iceVII. The acoustic and some optic modes are the vibrations up to approximately 700 cm^{-1}, while the vibrations around 1500 cm^{-1} are the OH bending modes. The OH stretching mode frequencies are around 3700 cm^{-1}. Figure 3.11 shows the whole spectrum for iceVII including the core-shell vibrational frequencies between 17000 and 20000 cm^{-1}. It is clear from figure 3.11 that there is no overlap between the OH and core-shell frequencies and we may thus be confident that there will be no exchange of energy between the hydrogen ions and the shells in our MD simulations.

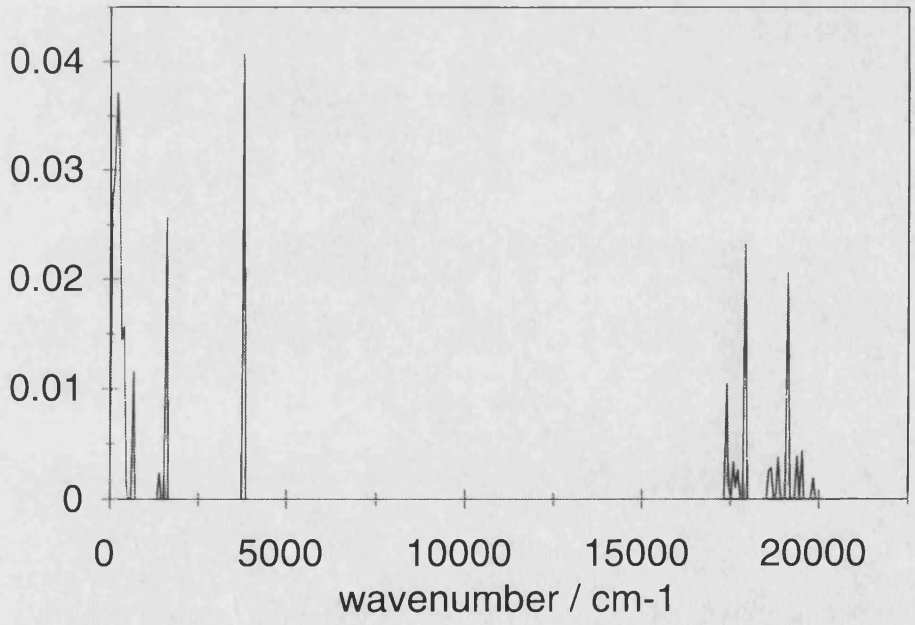

Figure 3.11 Diagram showing absence of overlap between OH and oxygen core-shell vibrational frequencies

However, it was only possible to run the simulation with this small shell mass by using a very small timestep of between 0.05 and 0.2 femtoseconds without the oxygen shell acquiring energy and heating up. These short timesteps restricted any runs to initially about 10 picoseconds. However, ten picosecond runs employing different timesteps gave different results for the self-diffusion coefficient (table 3(XV)).

Timestep (10^{-15} s)	**Self-diffusion coefficient (m^2s^{-1})**
0.05	2.30
0.10	1.35
0.20	1.54
0.50	2.62

Table 3(XV) Dependency of self-diffusion coefficient on timestep

As the self-diffusion coefficient should not be dependent on timestep used, this indicated that the MSD plot had not yet levelled out into a straight line and we needed a longer simulation run to obtain the correct self-diffusion coefficient. As the timestep of 0.20 femtoseconds gave a stable simulation without the shells heating up we decided to do a longer run of 100 picoseconds with this timestep and figure 3.12 shows that the MSD plot of this run has indeed levelled to a straight line only after about 50 ps.

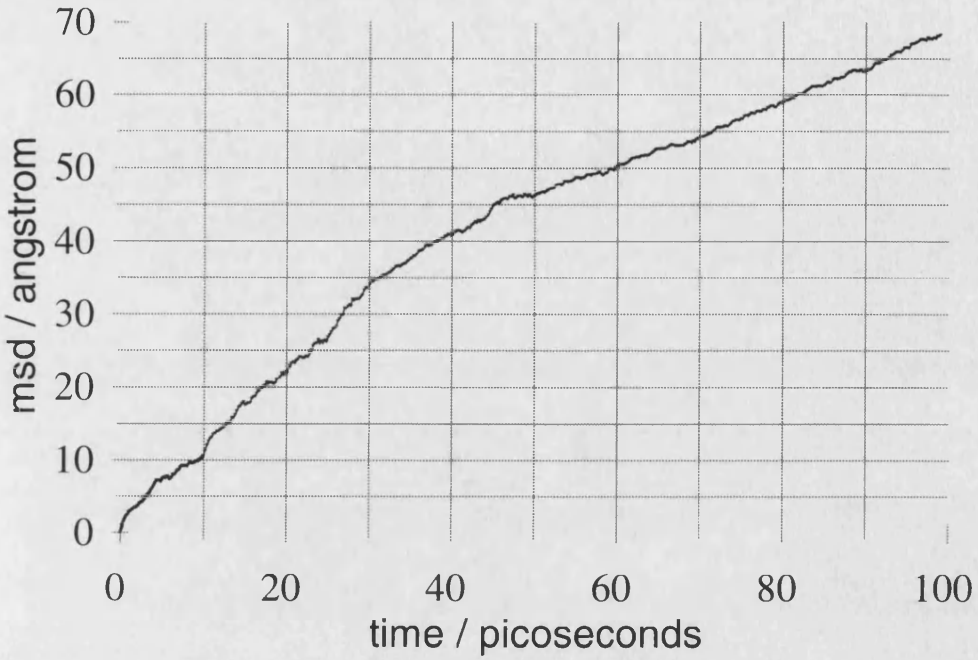

Figure 3.12 Graph of raw MSD with time of water at 300K and timestep of 0.2×10^{-15} s

The self-diffusion coefficient is obtained from the MSD as follows (Allen and Tildesley 1993):

$$D = \frac{1}{6t}\langle (r_i(t) - r_i(t_0)^2 \rangle \qquad (3.13)$$

where D is the diffusion coefficient, $r_i(t)$ is the molecule position i at time t, $r_i(t_0)$ is its initial position and $\langle (r_i(t) - r_i(t_0)^2 \rangle$ is the mean square deviation (MSD). The diffusion coefficient is in fact the slope of the MSD versus time. The self-diffusion coefficient obtained from the MSD of our MD simulation is 1.15×10^{-9} m^2s^{-1} (exp. 2.3×10^{-9} m^2s^{-1} at 298K). This value is low compared to the experimental value at

298K, but agrees with an experimental value of 1.17 x 10^{-9} m^2s^{-1} for a water temperature of 275K (Krynicki 1978). This indicates that although the calculated diffusion coefficient is too low for the simulation temperature of 300K, it still falls within the range for liquid water.

Another property of the MD simulation to verify against experimental data are the radial distribution functions (RDF) of the various ions in the system.

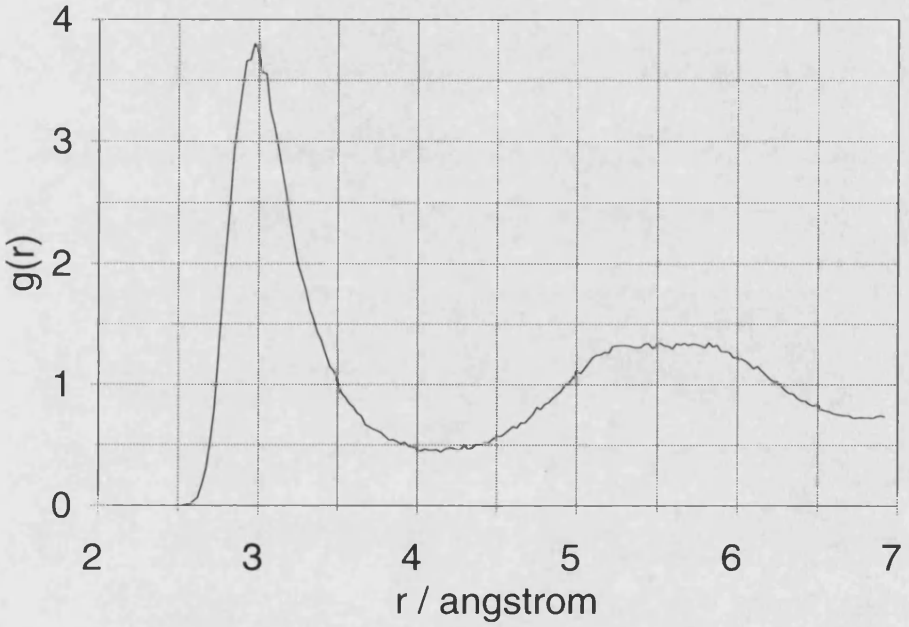

Figure 3.13 O-O radial distribution function

Figure 3.13 shows the RDF between oxygen and oxygen ions. There is a very clear peak at 2.97 Å and a broader area between 5 and 6 Å. The first peak is in good agreement with experimental findings (2.88 Å (Soper and Phillips 1986)) although the experimental value for the second peak at 4.6 Å (Narten and Levy 1971) is

somewhat smaller than the calculated value, although in line with other water potential models (cf. 5.4 Å for a flexible TIPS model (Dang and Pettitt 1987).

The heights of the peaks of 3.8 and 1.3 compare to experimental values of 3.1 and 1.1 experimentally (Soper and Phillips 1986). This indicates that our model shows ordering of the water molecules which agrees well with experimental findings.

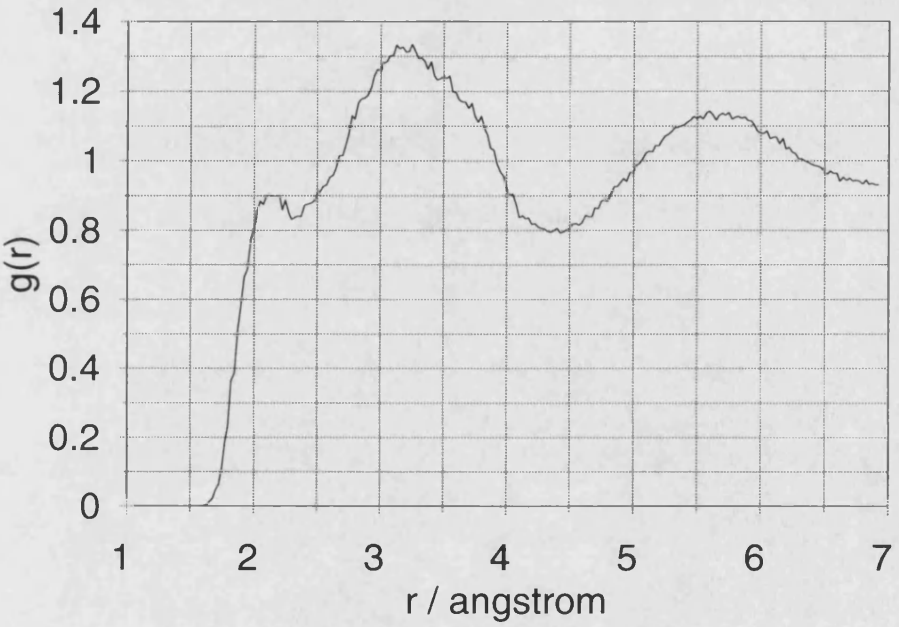

Figure 3.14 OH radial distribution function, ignoring intramolecular OH bond at 0.96 Å

In the OH RDF, the first peak is at 2.12 Å, again somewhat larger than the experimental value of 1.9 Å, although the second maximum at 3.13 Å agrees very well with experimentally observed RDFs (3.2 Å). The heights of the peaks of 0.9 and 1.3 compare favourably with experimental values of 1.0 and 1.3 (Soper and Phillips 1986), again showing similar ordering of experimental and simulated system.

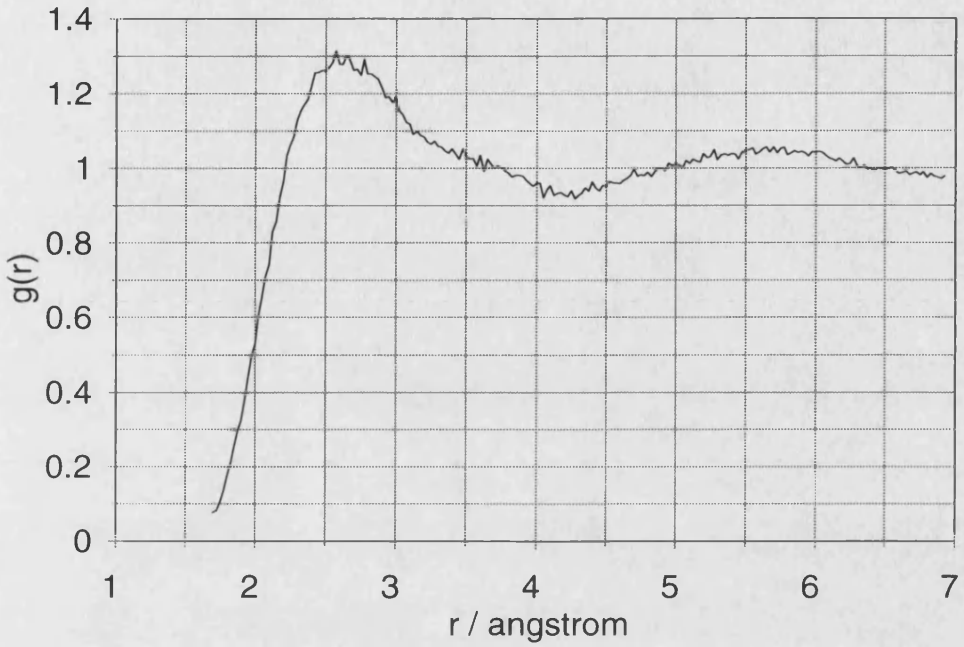

Figure 3.15 HH radial distribution function, ignoring intramolecular HH interaction

Finally, the HH RDF shows peaks at 2.6 Å of height 1.3 and 5.7 Å with a height of 1.1. In addition there is a shoulder at about 3.5 Å (height $\pm$ 1.0). This compares with experimental peaks at 2.3, 3.7 and 4.9 Å, heights 1.3, 1.2 and 1.0 respectively which again is in good agreement (Soper and Phillips 1986).

As we are interested in obtaining hydration energies for the adsorption of water molecules onto solid surfaces, a good test of our potential model would be to obtain a vaporisation energy from our MD simulations. We calculated this vaporisation energy from the interaction energies between the water molecules. The calculated energy of vaporisation is 43.0 $kJmol^{-1}$ which is in excellent agreement with the experimental value of 44.0 $kJmol^{-1}$ (Johnson 1982).

Table 3(XVI) compares some data from our water potential model with those of some other potential models and experiment (Lau *et al.* 1994). Apart from our shell model water potential only the ST2 potential model has been run at NPT conditions, although that was a Monte Carlo and not a Molecular Dynamics simulation. It is clear from table 3(XVI) that the ST2 model (Stillinger and Rahman 1974) is in better agreement with experimental data than our shell model. This is a very sophisticated potential model involving five sites, two charged hydrogens and two charged lone pair positions oriented tetrahedrally around the oxygen and as such it gives directionality to the intermolecular hydrogen bonds. However, this model is not compatible with the shell model potentials which was one of the aims for the development of our shell model water potential. From table 3(XVI) it is clear that the shell model does not reproduce the experimental density or self-diffusion coefficient accurately. However, apart from the ST2 potential model, the other potential models have been simulated using NVT ensembles which keeps the density fixed at the pre-set value and all of these models show a self-diffusion coefficient which is far too large. Our self-diffusion coefficient is too small which is probably due to the higher density. This high density may be due to the fact that the geometry of our calculated dimer does not agree entirely with the experimentally found structure. The angle θ_a (fig. 3.5) at 30.1^0 is smaller by at least 16^0 than its experimental counterpart (57 ± 10^0) which makes the calculated water dimer too flat. This would induce the formation of a layered structure and these layers would be able to approach more closely increasing the density at fixed pressure. Alternatively the hydrogen bonding

between the water molecules may be too strong as the potential takes no account of the directionality of the H-bonding but is identical in all orientations.

Properties of Different Water Models								
Model	Calculation	G_{OO} Å	Height	$\langle E_i \rangle$ $kJmol^{-1}$	ρ gcm^{-3}	C $Jmol^{-1}K^{-1}$	κ $Mbar^{-1}$	$D / 10^{-5}$ m^2s^{-1}
Shell	MD NPT	2.97	3.80	-42.7	1.3	98.2	37.1	1.15
CVFF	MD NVT	2.75	2.51	-41.2	0.968	86.4	37.7	5.32
ST2	MC NPT	2.81	3.18	-43.6	0.925	93.6	63.0	1.90
SPC rigid	MD NVE	2.75	2.80	-39.6	-	77.4	-	4.69
TIP rigid	MD NVE	2.79	2.46	-34.1	-	68.4	-	6.69
SPC flexible	MD NVT	2.78	2.76	-42.5	-	73.8	-	-
TIPS flexible	MD NVT	2.83	2.29	-38.2	-	61.2	-	-
experi-ment		2.88	3.02	-41.7	0.997	75.6	45.7	2.30

(Jorgensen *et al.* 1983, Lau *et al.* 1994)

Table 3(XVI) Calculated and experimental properties of water

Despite the above shortcomings of the shell model water potential, we feel that its compatibility with other interatomic potentials for polarisable ions and its agreement with experimental parameters such as geometry of monomer and dimer, dipole moment, dimer binding energy, average intermolecular energy $\langle E_i \rangle$ and radial distribution functions make it a valid model to study interactions between oxide surfaces and water.

4 DISSOCIATIVE AND MOLECULAR ADSORPTION OF WATER ON CaO AND MgO SURFACES

4.1 Introduction

The ceramic oxide MgO is widely used as a support material for metal catalysts and high-temperature superconductors (Langel and Parrinello 1994). It is also a catalyst in its own right, catalyzing for example the H_2 and D_2 exchange reaction, the dehydrogenation of formic acid and methanol (Wu *et al.* 1992) and it is important industrially as a sorbent in the reduction of SO_2 (Pacchioni *et al.* 1994) and as a catalyst in methane oxidative coupling (Li *et al.* 1994). Catalytic behaviour of many oxides may be influenced by the hydroxylation of their surfaces (Dunski *et al.* 1994) and water itself is an effective catalyst for the sintering of MgO aggregates (Beruto *et al.* 1993). Furthermore, many oxide surfaces in addition to MgO are hydroxylated which influences many properties such as their mechanical response (Langel and Parrinello 1994) and catalytic behaviour (Dunski *et al.* 1994). As a consequence of these factors and its structural simplicity, the structure and hydration of MgO surfaces has been frequently investigated, both experimentally (Wu *et al.* 1992, Dunski *et al.* 1994, Coluccia *et al.* 1979, Coluccia *et al.* 1981, Jones *et al.* 1984, Onishi *et al.* 1987, Duriez *et al.* 1990, Coustet and Jupille 1997) and theoretically (Picaud *et al.* 1992, Scamehorn *et al.* 1993, Noguera *et al.* 1993, Langel and Parrinello 1994, Harms *et al.* 1994, Scamehorn *et al.* 1994, Langel and Parrinello 1995, Goniakowski and Noguera 1995, Kantorovich *et al.* 1995, Refson *et al.* 1995, Gerson and Smart 1997). It is generally agreed that hydroxylation of the five-coordinated surface atoms on the perfect {100} surface does not take place, *e.g.* Noguera *et al.* (1993) who used a

numerical CNDO-like self-consistent method to investigate the hydroxylated MgO (001) surface and Refson *et al.* (1995) who investigated the (001) surface of MgO using density functional theory within the local density approximation.

However, a truly perfect surface cannot be obtained experimentally and every real surface contains defects: kinks, corners and edges (Coluccia *et al.* 1979, Duriez *et al.* 1990, Abriou *et al.* 1996). It has been suggested (Colbourn and Mackrodt 1982, Jones *et al.* 1984, Kobayashi *et al.* 1990, Ito *et al.* 1991, Nygren and Pettersson 1996) that these sites, consisting of three- or four-coordinated atoms, rather than the five-coordinated atoms of the pure {100} surface, are the sites where chemical reactions take place. Scamehorn *et al.* (1994), who investigated three-, four- and five-coordinated surface sites on the (001) surface of MgO using periodic Hartree-Fock calculations, and Goniakowski and Noguera (1995), using Hartree Fock with periodic boundary conditions to study hydroxylated oxide surfaces, agree that these sites will be hydroxylated. This higher reactivity of lower coordinated sites has also been inferred from experimental results (Kobayashi *et al.* 1990, Ito *et al.* 1991) although no conclusive quantitative experimental evidence has been shown. Jones *et al.* (1984) studied the erosion of MgO smoke particles by water observing considerable surface roughening and infrared spectroscopic measurements showed that this increase in low-coordinated sites coincided with an increase in surface hydroxylation (Coustet and Jupille 1997). Onishi *et al.* (1987) used UPS and XPS to probe the adsorption of water on the MgO {100} and {111} surfaces and found that chemisorption took place leading to hydroxylation of surface atoms. They suggested that this adsorption takes place at surface defects on the {100} and low-coordinated

edge sites of the {111} surfaces. Ito *et al.* (1991) used temperature programmed desorption (TPD) to investigate methane adsorption on magnesium oxide and they found the active sites to have low coordination. Finally, Dunski *et al.* (1994), upon dehydroxylating the MgO surface by TPD found four different peaks, ascribing these to a physisorbed species and three chemisorbed species, adsorbed onto three-, four- or five-coordinated sites.

In this chapter we describe our investigation of the effect of chemisorption of water molecules onto the {100}, {110}, micro-facetted {110}, {111} and {310} surfaces of MgO and CaO as a function of coverage. By considering partial coverages, we can compare the results directly with microcalorimetry and TPD and by calculating the energies for adsorption both at the normal five-coordinated {100} surface atoms and at four-coordinated atoms supplied by the {110} and {310} surfaces, we can identify the energetically favoured configurations to investigate the assumption that low-coordinated sites should be more amenable to hydroxylation. CaO, which has the same rock-salt structure as MgO has been studied as well because it is easily hydrated and microcalorimetric studies by Fubini *et al.* (1989) have identified the hydration energies of CaO after dosing with controlled amounts of water vapour.

In addition, after developing our shell model water potential, we have investigated the effect of physisorption of water molecules onto three-, four- and five-coordinated sites of MgO surfaces. Here the three-coordinated sites are supplied by a facetted {111} surface which has been observed experimentally (Henrich 1976, Onishi *et al.* 1987).

4.2 Method

4.2.1 Dissociatively adsorbed water

Every surface was hydroxylated in a series of partial coverages from infinite dilution to a full monolayer coverage, consisting of a dissociated water molecule adsorbed on every surface cation-oxygen pair. In effect every surface oxygen was replaced by two hydroxyl groups, *i.e.* in Kroger-Vink notation:

$$H_2O + O_O^x \rightarrow (OH)_O^\bullet + (OH)_i^{'} \qquad (4.1)$$

where O_O^x is the lattice oxygen atom, $(OH)_O^\bullet$ is the hydroxylated lattice oxygen and $(OH)_i^{'}$ is the interstitial hydroxyl group adsorbed onto the surface cation. In each case the adsorption process was modelled by dissociating the water molecule such that the OH was bonded to a surface cation and the H atom to a surface oxygen atom.

The calculation of the hydration energies required a value for the energy of dissociation of a water molecule:

$$H_2O_{(g)} + O_{(g)}^{2-} \rightarrow 2OH_{(g)}^{-} \qquad (4.2)$$

However, this requires the second electron affinity of oxygen, which is material dependent (Harding and Pyper 1995). This can be overcome by using experimental heats of formation for the reaction:

$$MO_{(s)} + H_2O_{(g)} \rightarrow M(OH)_{2(s)} \qquad (4.3)$$

where M is either Ca or Mg. The dissociation energies for the reaction in equation (4.2) may be obtained from an energy cycle (4.4) where equation (4.2) is the sum of (1), (2) and (3).

(4.4)

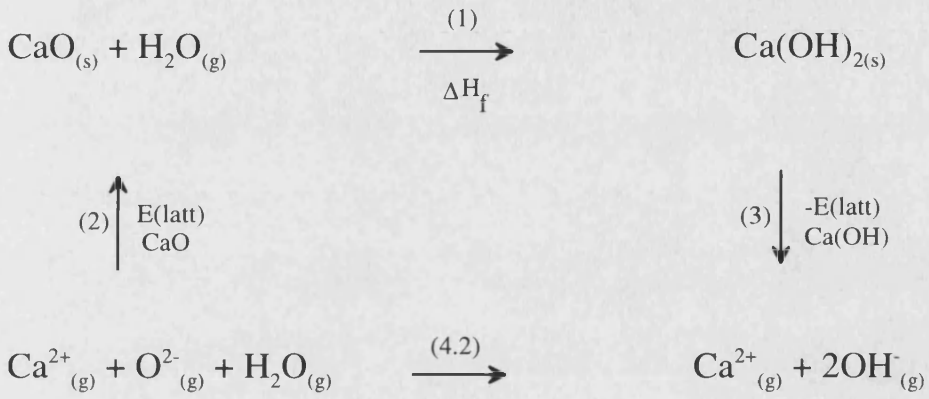

Lattice energies and experimental enthalpies (table 4(I)) were thus used to give the dissociation energies for reaction (4.2) for CaO and MgO of -663.9 $kJmol^{-1}$ and -690.0 $kJmol^{-1}$ respectively. As noted above, the discrepancy between the two values will be due to the difference in the second electron affinity but may also include deficiencies in the potential model.

	Lattice energy / $kJmol^{-1}$	**Enthalpy of formation[1] / $kJmol^{-1}$**
$CaO_{(s)}$	-3468.46	-635.10
$Ca(OH)_{2(s)}$	-2916.25	-986.10
$MgO_{(s)}$	-3984.80	-601.70
$Mg(OH)_{2(s)}$	-3378.26	-924.50
$H_2O_{(g)}$		-241.82

Table 4(I) Lattice energies and enthalpies of formation [1] Johnson (1982)

4.2.2 Physisorption of water

The hydration energy of adsorption of molecular water onto oxide surfaces was calculated by comparing the sum of the energy of the pure surface and of the isolated water molecule with the energy of the hydrated surface. The calculation of the hydration energies of physisorption required a self energy for the water molecule, which we calculated to be -621.4 $kJmol^{-1}$ for an isolated water molecule.

Surface cations and oxygen ions were elected as initial sites for adsorption of the water molecules after which the hydrated surface was allowed to relax. The water molecule can be adsorbed onto the surface in several different ways, *e.g.* coordinated by one hydrogen to a surface oxygen as is found experimentally at negatively charged clay surfaces (Delville and Letellier 1995), bonded by its oxygen to a surface cation as is sometimes found on uncharged clay surfaces (Bridgeman and Skipper 1997) or intermediate between these positions. In the case of binding to the cation sites, the oxygen atom of the water molecule was initially positioned at the experimental cation-oxygen distance for a hydrated salt, 2.0-2.1 Å for Mg-O and 2.4 Å for Ca-O (Forbes *et al.* 1992, Skipper *et al.* 1994) after which the surface was allowed to relax and find the minimum energy configuration. Adsorption on the surface oxygen sites was modelled by positioning one of the water molecule's hydrogen atoms at a hydrogen-bond distance of 1.8 Å [exp. 1.76-1.95 Å in ice (Kamb 1972)].

4.2.3 Hydration and Surface Energies

After energy minimisation, the resulting structure of the hydrated surface was studied and its stability evaluated in terms of surface energy and hydration energy. The hydration energy is defined as the difference in energy between the dehydrated surface with *n* individual water molecules and the hydrated surface, where *n* is the number of water molecules per simulation cell. For both the hydroxylated and the physisorbed surfaces, we defined the surface energy of the hydrated surfaces with respect to a liquid water environment. Thus we compared the energy of the hydrated surface block, containing *n* adsorbed water molecules, with the energy of an equivalent number of bulk ions and *n* liquid water molecules. We therefore needed the energy of condensation of gaseous water which is -44.0 $kJmol^{-1}$ (Johnson 1982). For physisorption this is added to the self energy of water of -621.4 $kJmol^{-1}$, mentioned above, and we obtain a value of -665.4 $kJmol^{-1}$ for each liquid water molecule. For chemisorption the value is obtained from an energy cycle as before and is -643.6 $kJmol^{-1}$ for MgO and -617.5 $kJmol^{-1}$ for CaO. The surface energy is then defined as the energy of cleaving the surface and reacting with water, and is given by:

$$\gamma_{defect} = \frac{U_d - (U_b + U_{H_2O})}{A} \qquad (4.4)$$

where U_d is the energy of the surface with adsorbed feature, U_b is the energy of the bulk crystal as usual and U_{H_2O} is the energy of *n* adsorbing molecules, in this case water molecules. A is the surface area as usual.

Both hydroxylation and molecular hydration of the surfaces were studied in a series of partial coverages. Thus, in addition to having to investigate a range of different positions for the water molecule to physisorb, many possible configurations of the relative positions of the water molecules adsorbed onto the partially hydroxylated and hydrated surfaces were investigated to make sure that the most stable configuration was located. For example, energy variations for different configurations of the 75% hydroxylated MgO {100} surface range from -3.9 $kJmol^{-1}$ to +21.5 kJmol and it is obviously important to find the surface configuration of lowest energy. The energies quoted in later sections refer to the energetically most favourable configuration obtained.

4.3 Pure Surfaces

Both MgO and CaO have a face-centered cubic structure where each cation and each oxygen atom is six-coordinate. The crystals were cut to obtain four different surfaces, the {100}, {110}, {111} and {310} surfaces, and their relaxed surface structures and energies were calculated.

The pure {100} surfaces are the most stable surfaces considered. As expected from previous calculations both atomistic (Tasker and Duffy 1984, Tasker *et al.* 1985, Mackrodt 1989) and *ab initio* (Causa *et al.* 1986) they have the lowest surface energies and are the dominant surfaces in the crystal morphologies. Table 4(II) shows the calculated surface energies for the planar MgO and CaO surfaces considered.

	Surface energy / Jm^{-2}			
Surface	**{100}**	**{110}**	**{111}**	**{310}**
MgO	1.25	3.02	3.86	1.84
CaO	0.77	1.95	2.47	1.15

Table 4(II) Surface energies of planar surfaces of MgO and CaO

The {110} and {111} surfaces both have much higher surface energies than the {100} surfaces. Previous simulations have assumed that the surface formed by cleaving the crystal is flat (fig. 4.1a, 4.2a) (*eg.* Tasker 1979). However, the planar surfaces may not be the most stable and we therefore considered micro-facetting of both the {110} and {111} surfaces.

By removal of alternate rows of ions the {110} surface micro-facets into steps of {100} planes, thereby reducing the surface energy drastically from 3.02 to 2.09 Jm^{-2} for the smaller MgO $(a\sqrt{2})/2$ facet ($(a\sqrt{2})/2$ is the depth from the uppermost ions to the first fully coordinated plane of ions) (fig. 4.1b), while further removal of rows of MgO leads to the even more stable $a\sqrt{2}$ micro-facetted surface (γ = 1.87 Jm^{-2}) (fig 4.1c) whose surface energy is closer to the surface energy of the {100} surface (table 4(III)). The facetted {110} surface, especially the $a\sqrt{2}$ facet can also be viewed as a collection of stepped {100} planes. The atoms at the surface of the {110} plane and those on the edges of the facetted {110} surfaces are all four-coordinated and as such these sites should be more amenable to chemical reactions than the five-coordinated surface atoms of the {100} surface (Coluccia *et al.* 1981, Jones *et al.* 1984, Duriez *et al.* 1990).

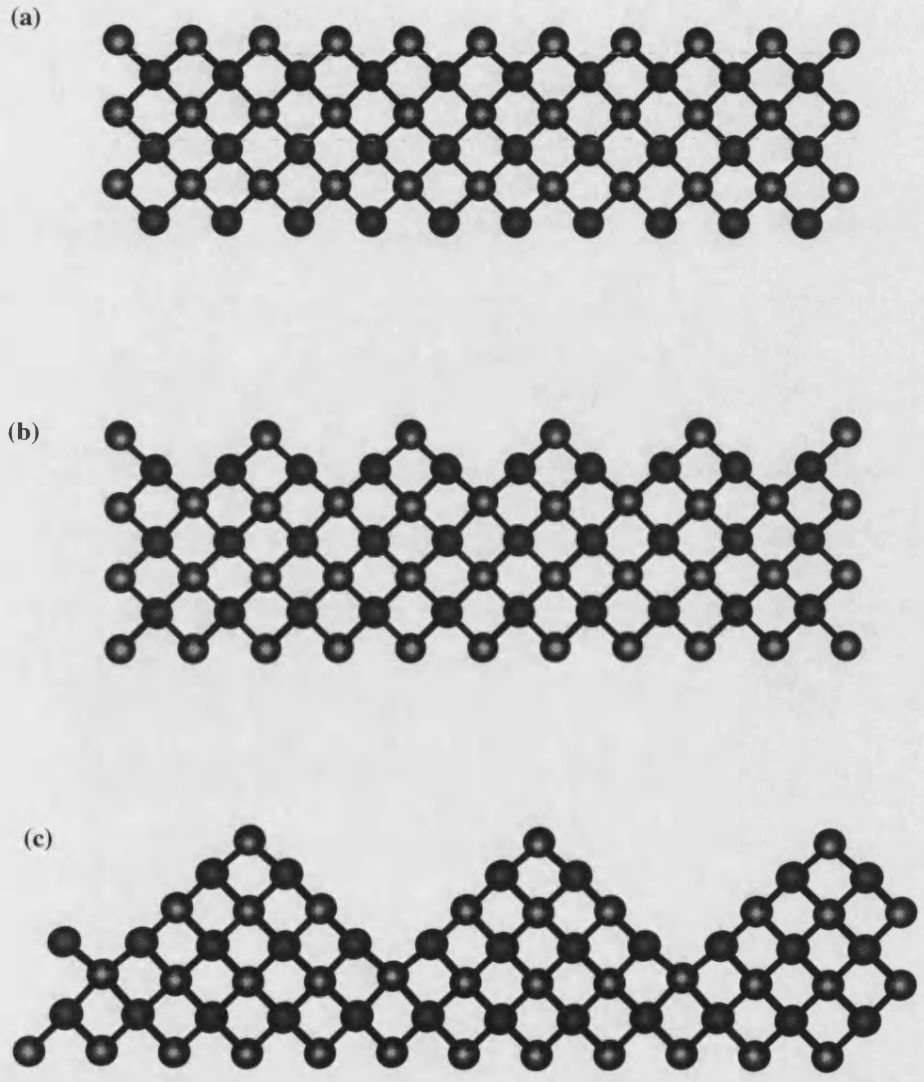

Figure 4.1 Relaxed structures of the {110} surfaces of MgO, (a) unfacetted $\gamma = 3.02$ Jm^{-2}, (b) $(a\sqrt{2})/2$ facetted $\gamma = 2.09$ Jm^{-2} and (c) $a\sqrt{2}$ facetted $\gamma = 1.87$ Jm^{-2} ($a\sqrt{2}$ refers to the distance between the top and bottom of the facet).

We also considered the hydroxylation of the {111} surface, which we terminated with a surface plane of oxygen atoms. The planar {111} surface is dipolar and as such the energy is divergent with crystal size (Bertaut 1958). The most obvious way of removing the dipole is to remove one half of the surface oxygen atoms to the bottom of the unit cell as described in chapter 2. However, the resulting surface is very unstable compared to the {100} surface and similarly to the {110} surface micro-facetting reduces the surface energy considerably. The {111} micro-facetted surface does not form parallel rows as on the {110} surface, but rather three-sided pyramids where the sides of the pyramids consist of {100} planes. These {100} planes are inclined at an angle of 54.7^0 to the original {111} surface and the pyramids are in fact the corners of MgO cubes with the edges consisting of four-coordinated atoms and a three-coordinated atom at the apex of the pyramid. Two micro-facetted {111} surfaces were created, the $(a\sqrt{3})/3$ and the $a\sqrt{3}$, (fig 4.2b+c) giving rise to exposed {100} planes and as with the {110} surface, the surface energy of the {111} plane is lowered by increased facetting (table 4(III)) from 3.86 to 2.83 and 2.39 Jm^{-2}.

(a)

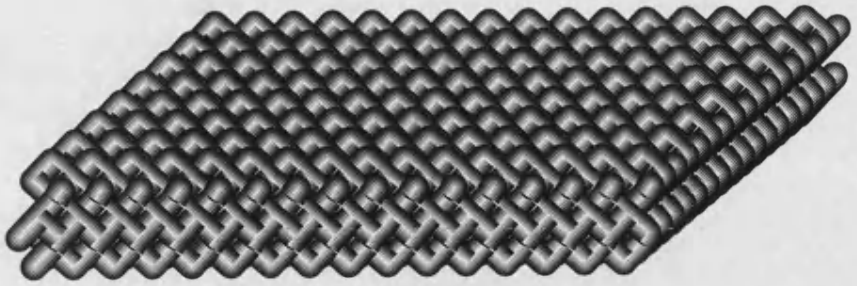

(b)

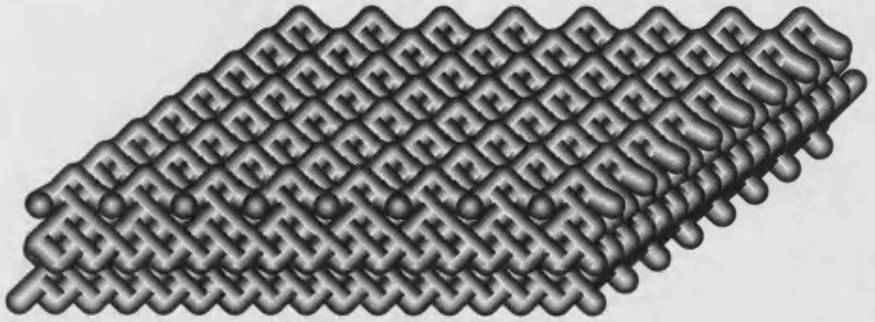

(c)

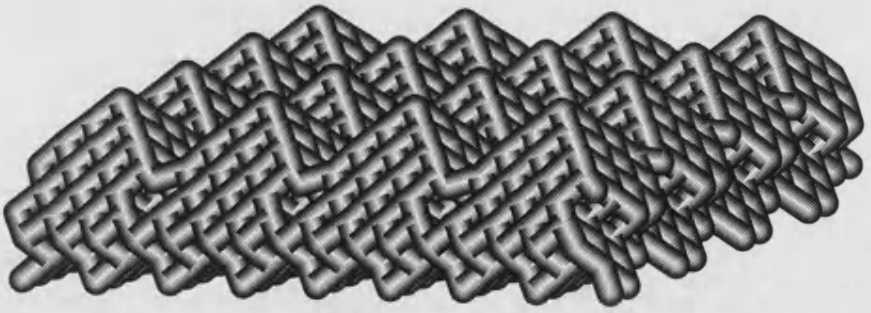

Figure 4.2 Relaxed structure of the {111} surfaces of MgO, (a) unfacetted $\gamma = 3.86$ Jm^{-2}, (b) $(a\sqrt{3})/3$ facetted $\gamma = 2.83$ Jm^{-2} and (c) $a\sqrt{3}$ facetted $\gamma = 2.39$ Jm^{-2}.

The observation that facetting of the {110} and {111} surfaces produces the very stable {100} planes is probably the reason for the lowering of the surface energy. This result also illustrates the potential difficulty with static simulations, namely that unless every significant surface configuration is considered (including facets) it is not possible to be confident that the global minimum has been found. The occurrence of facetting is confirmed by experiment for both the {110} and {111} surface of MgO. Henrich (1976), using low-energy electron diffraction (LEED) and scanning electron microscopy, observed facetting on both surfaces under ion bombardment at room temperature and after annealing at 900-1400K by means of electron bombardment. Facetting of the {111} surface was also observed by Onishi *et al.* (1987) using LEED. They found that the facetted surface structure, consisting of trigonal pyramids inclined at an angle of 54.7^0, is stable against repeated sputtering-annealing cycles which agrees with our findings that the surface energies are lowered and hence stabilised by facetting.

Surface energy / Jm^{-2}						
Surface	{110}	$(a\sqrt{2})/2$	$a\sqrt{2}$	{111}	$(a\sqrt{3})/3$	$a\sqrt{3}$
MgO	3.02	2.09	1.87	3.86	2.83	2.39
CaO	1.95	1.31	1.14	2.47	-	-

Table 4(III) Surface energies for the unfacetted and facetted {110} and {111} surfaces

The {310} surface with its higher surface energy is less stable than the dominant {100} surface, and not unlike the facetted {110} surface, it can be described as steps of {100} planes. No experimental {100} surface is free from defects such as kinks,

corners and edges and the {310} surface provides a model for edges consisting of low-coordinated atoms on a {100} surface in the same way as the three-coordinated corner sites are modelled by the facetted {111} surfaces.

4.4 Hydroxylated Surfaces

The surfaces were hydroxylated in a series of partial coverages and the surface and hydration energies evaluated. Table 4(IV) shows the surface energies as a function of coverage of the hydroxylated planar surfaces.

Surface energy / Jm^{-2}							
Surface		**0%**	**12.5%**	**25%**	**50%**	**75%**	**100%**
MgO	{100}	1.25	1.33	1.30	1.79	1.20	3.81
	{110}	3.02	2.56	2.12	1.26	1.24	2.32
	{111}	3.86	3.42	3.02	1.82	0.91	0.04
edge	{310}	1.84	1.74	1.63	1.42	1.23	1.03
valley	{310}	1.84	1.79	1.75	1.67	1.58	1.48
CaO	{100}	0.77	0.75	0.72	0.78	0.38	2.76
	{110}	1.95	1.62	1.30	0.70	0.35	1.58
	{111}	2.47	2.14	1.83	1.05	0.39	-0.28
edge	{310}	1.15	1.05	0.96	0.76	0.61	0.45
valley	{310}	1.15	1.10	1.04	0.98	0.89	0.80

Table 4(IV) Surface energies of hydroxylated planar surfaces as a function of coverage

4.4.1 {100} Surface

The hydration energies of the partial coverages of the {100} surface (shown in table 4(V) and figure 4.3a) show Langmuir behaviour until full monolayer coverage.

This we define as showing hydration energies which are reasonably constant with coverage, *i.e.* varying by less than a few tenths of an eV. 100% coverage was particularly unfavourable for both CaO and MgO while other coverages show MgO to be only slightly exothermic with the 50% coverage again energetically unfavourable. This agrees with results obtained by Refson (1997) whose DFT calculations of the 50% hydroxylated {100} surface showed hydroxyl groups recombining to form undissociated water molecules.

At low surface coverages in both MgO and CaO the lowest energy configuration for the water molecules is to be adsorbed in pairs giving rise to a surface cluster containing four OH groups coordinated by hydrogen bonds. At 75% partial coverage, extensive surface rearrangement takes place (figure 4.4) with cations from the surface layer relaxing upwards by 1.34 Å in the case of MgO and 1.29 Å in CaO. The hydroxyl groups adsorbed on the cations tilt by 15° and 20.3° for MgO and CaO respectively, relative to the surface normal, forming a second bond to the cations which have moved upwards. As a result, this surface is the most stable configuration as is shown from the surface energies in table 4(IV), even more stable than the pure unhydroxylated surface; *cf.* surface energy of pure CaO surface of 0.77 Jm^{-2} with 0.38 Jm^{-2} for the 75% covered surface. When considering MgO, the surface energies of the pure and 75% partially covered surfaces are comparable. This result of maximum stability at 75% coverage is not dissimilar to that of Oliver *et al.* (1993) who found in their study of the effect of Ni^{3+} holes on the morphology of NiO, which also has the rocksalt structure, that a minimum surface energy occurred at a Ni^{3+} hole coverage of 75%.

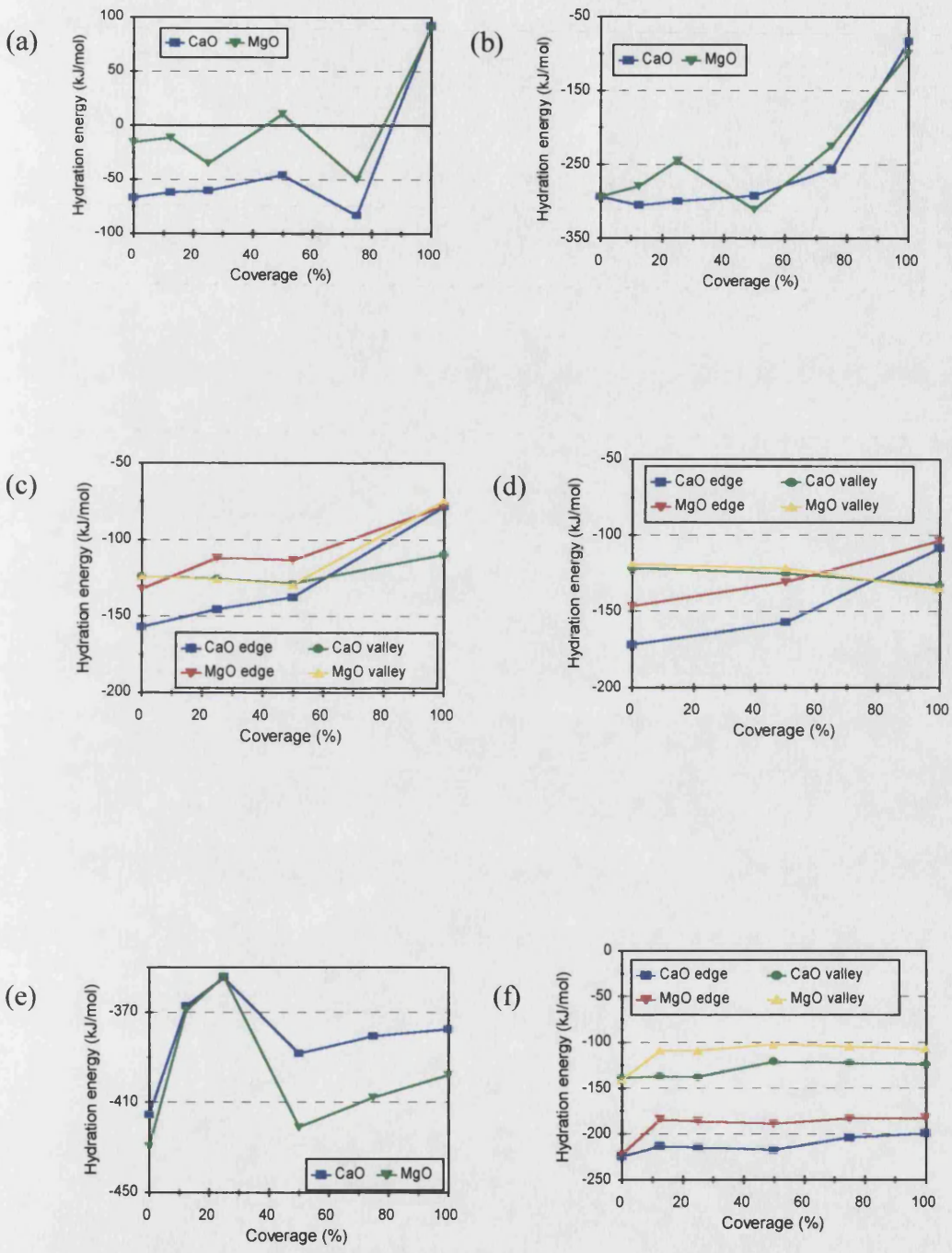

Figure 4.3 Energies of hydration of the hydroxylated surfaces with respect to gaseous water as a function of coverage for (a) {100} surface, (b) planar {110} surface, (c) {110} $(a\sqrt{2})/2$ facet, (d) {110} $a\sqrt{2}$ facet, (e) {111} surface and (f) {310} surface.

Hydration energy / kJmol^{-1}							
Surface		**0%**	**12.5%**	**25%**	**50%**	**75%**	**100%**
MgO	{100}	- 15.9	- 11.5	- 34.8	+ 10.9	- 49.7	+ 89.9
	{110}	-293.1	-278.9	-244.6	-310.5	-224.5	- 98.7
$(a\sqrt{2})/2$	{110}edge	-132.1	-	-112.0	-113.2	-	- 77.7
	{110}valley	-123.8	-	-125.7	-129.4	-	- 74.3
$a\sqrt{2}$	{110}edge	-146.6	-	-	-130.7	-	-103.2
	{110}valley	-118.7	-	-	-121.3	-	-135.0
	{111}	-429.4	-368.9	-354.1	-421.1	-407.9	-397.9
	{310}edge	-221.9	-184.0	-185.7	-188.7	-183.1	-181.9
	{310}valley	-141.1	-108.9	-109.2	-102.2	-104.5	-107.0
CaO	{100}	- 66.8	- 61.8	- 60.2	- 45.7	- 82.8	+ 92.1
	{110}	-293.3	-304.7	-299.2	-292.0	-256.5	- 82.4
$(a\sqrt{2})/2$	{110}edge	-157.1	-	-145.7	-137.6	-	- 78.0
	{110}valley	-123.9	-	-125.3	-128.3	-	-109.6
$a\sqrt{2}$	{110}edge	-171.7	-	-	-156.9	-	-108.1
	{110}valley	-121.3	-	-	-124.7	-	-132.5
	{111}	-415.5	-367.2	-354.5	-388.3	-380.4	-377.4
	{310}edge	-224.5	-213.0	-214.5	-217.1	-203.9	-199.1
	{310}valley	-138.4	-136.8	-137.6	-120.7	-122.3	-123.8

Table 4(V) Energies of hydration of hydroxylated surfaces relative to unhydrated surfaces as a function of coverage (see also figure 4.3)

Similar to the surface energies, in both CaO and MgO the hydration energies are at their most negative value for the 75% coverage. The remarkable stability of the 75% covered surface and large hydration energy together with the surface rearrangement where the cation seems to leave the surface may be an indication that this is the first step to dissolution whereby an MgO or CaO surface unit is replaced by a dissociated water molecule.

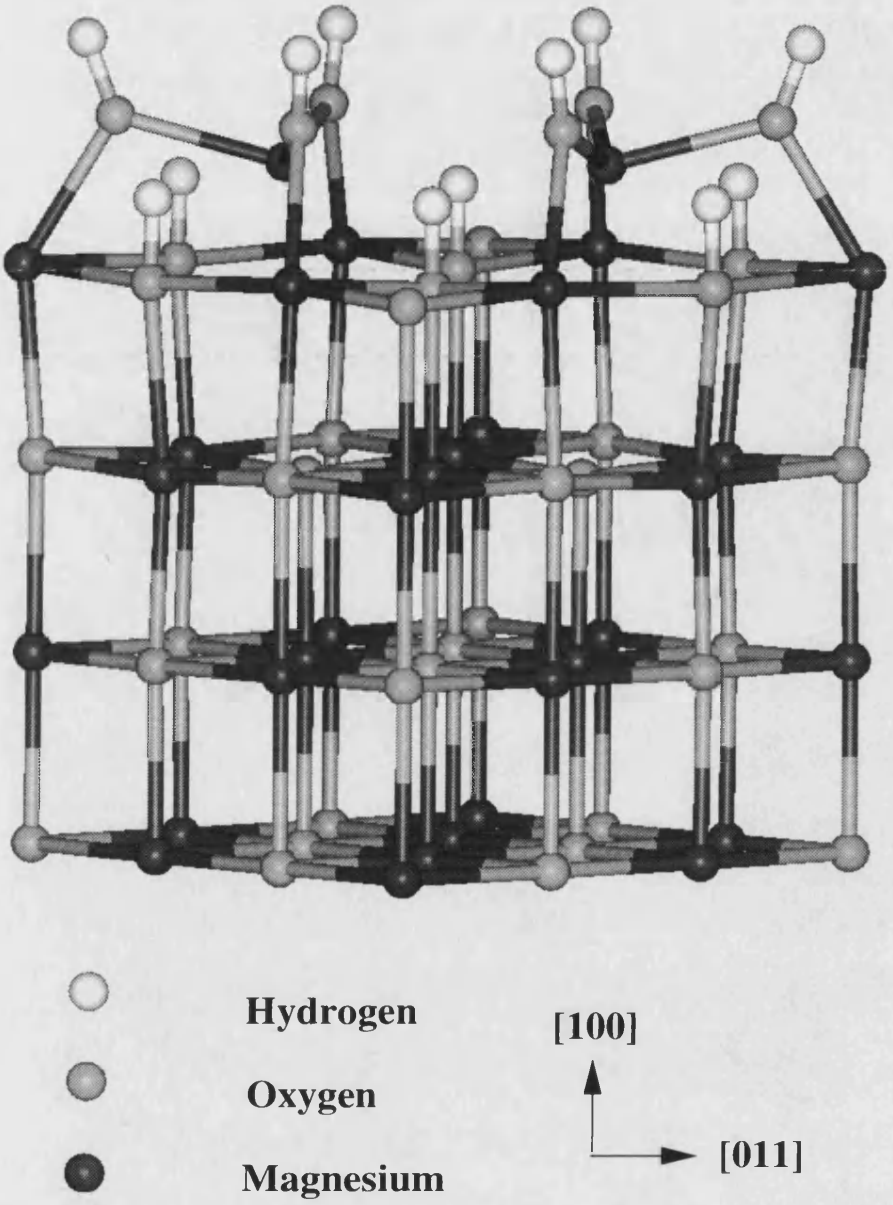

Figure 4.4 Relaxed surface configuration for the 75% hydroxylated MgO {100} surface, showing tilted hydroxides and raised surface magnesium ions

4.4.2 {110} and facetted {110} Surfaces

At all partial coverages considered of the planar {110} surface the lowest energies are achieved when water molecules adsorb onto the surface in pairs. This

may be due to attraction between the adsorbed hydrogen atoms and hydroxyl oxygen atoms as in the {100} surface above. When in addition the adsorbed hydroxyl groups and the adsorbed hydrogen atoms are able to tilt towards each other the surface energy is lowered even further. This is shown in the case of MgO by the partial coverage of 50% where the hydroxyl group tilts towards the hydrogen atom by 22.7° and the hydrogen towards the hydroxyls by 28.3°. The resultant surface energy is about two thirds of the surface energy of the nearest most stable configuration.

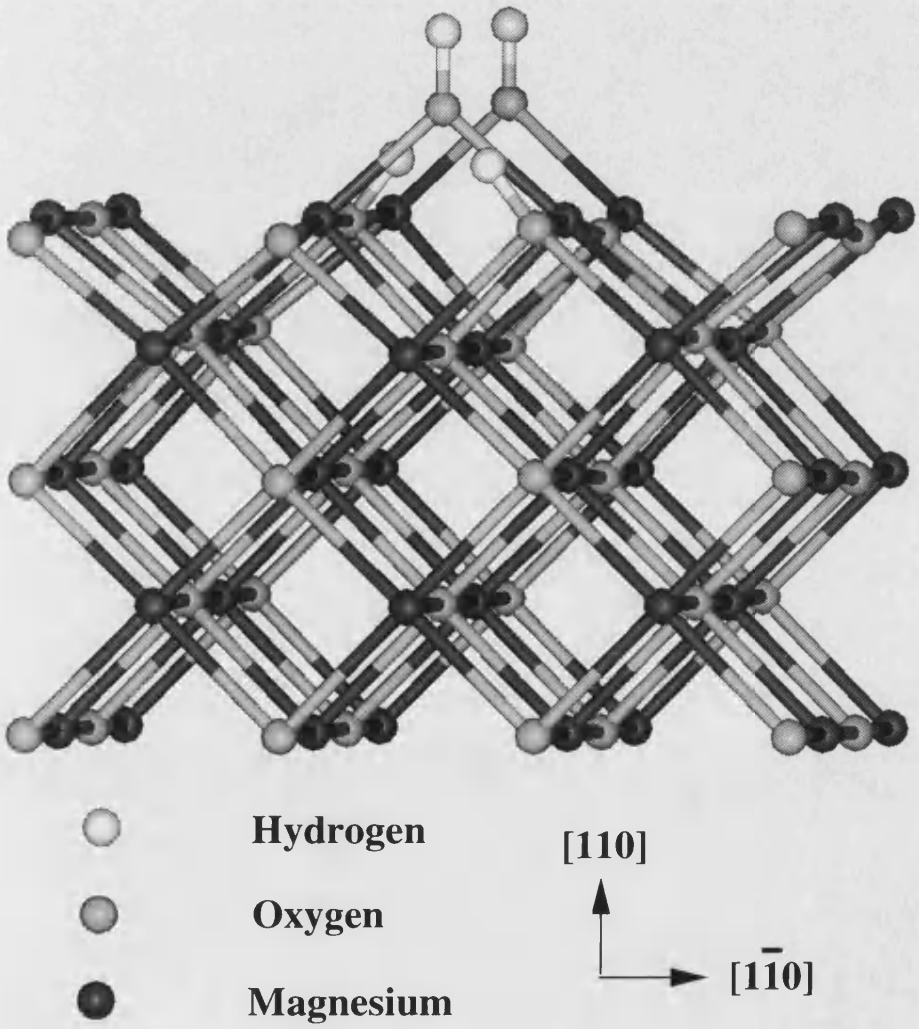

Figure 4.5 Minimum energy configuration for the 75% hydroxylated MgO planar {110} surface, illustrating bridging hydroxide groups and alternating hydrogens

There is a distinctly different behaviour for CaO at all coverages and MgO at coverages from about 75%. The oxygen of the hydroxyl group relaxes towards the site where a surface oxygen would be were the crystal one layer thicker, thus enabling the hydroxyl oxygen to form bonds with two cations in the surface layer. The adsorbed hydrogen tilts towards an empty cation site in the next layer. Figure 4.5 illustrates the configuration which shows that the adsorbed water molecules form a micro-facet on the planar {110} surface. As discussed above, micro-facetting of the {110} plane stabilises the surface and here micro-facetting of the hydroxylated surfaces also lowers the surface energy compared to the flat surface.

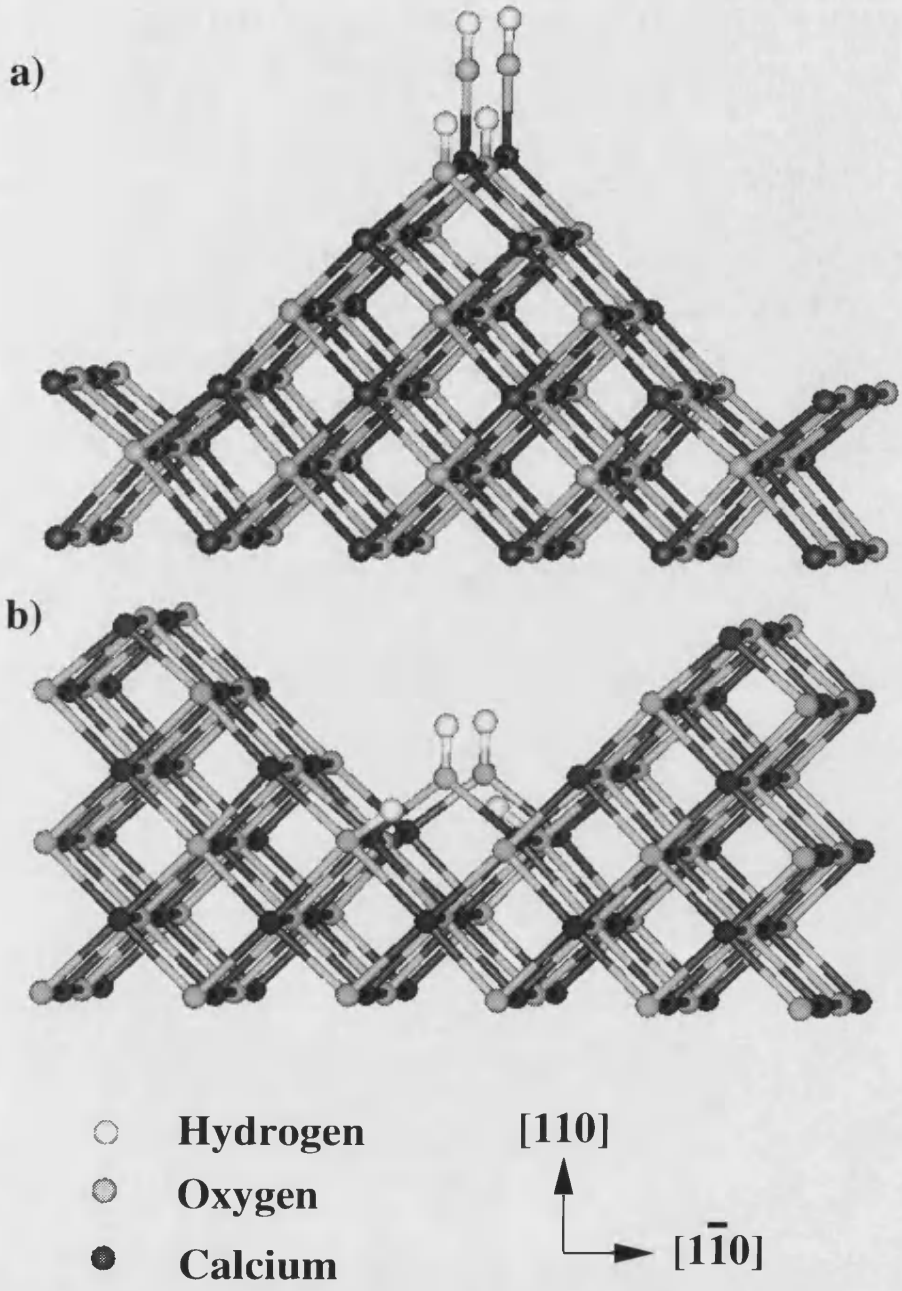

Figure 4.6 Minimum energy configuration for the hydroxylated CaO ($a\sqrt{2}$)/2 {110} facet: (a) adsorption on all edge sites giving rise to linear hydroxide groups, and (b) adsorption on all valley sites giving rise to bridging hydroxide groups and alternating hydrogens

In the case of the partial coverages of the facetted {110} surfaces, only adsorption on the edges or in the valleys was considered. The partial coverages are relative to

these sites only. Adsorption on the edges corresponds to adsorption at a low-coordinated site on a {100} plane, for instance on the edge of a step defect, whereas adsorption in the valleys corresponds to adsorption inside a step defect on a {100} plane. Figure 4.6 shows the two different positions. We added water molecules separately on either the edges or in the valleys and we did not consider the adsorption sites on the {100} planes exposed by the facetting process. We also considered the example where all sites on both the edges and in the valleys were covered by hydroxyl groups. This configuration was found to have a particularly low surface energy (table 4(VI)).

Surface energy / Jm^{-2}					
Surface		**0%**	**25%**	**50%**	**100%**
MgO	{110}	3.02	2.12	1.26	2.32
$(a\sqrt{2})/2$	edge	2.09	1.97	1.87	1.88
	valley	2.09	1.96	1.81	1.59
	edge+valley	2.09	-	-	1.11
$a\sqrt{2}$	edge	1.87	-	1.73	1.68
	valley	1.87	-	1.74	1.57
	edge+valley	1.87	-	-	1.39
CaO	{110}	1.95	1.30	0.70	1.58
$(a\sqrt{2})/2$	edge	1.31	1.18	1.08	1.16
	valley	1.31	1.21	1.10	0.99
	edge+valley	1.31	-	-	0.39
$a\sqrt{2}$	edge	1.14	-	1.00	0.99
	valley	1.14	-	1.05	0.93
	edge+valley	1.14	-	-	0.78

Table 4(VI) Surface energies of the hydroxylated planar and facetted {110} surfaces

When adsorbing on the edges of the facetted surface, the hydroxyl group and proton do not tilt towards each other when the edges are fully covered, unlike at lower coverages, for example in CaO the tilt angle of the OH bond to the CaO lattice is 26.4° and 29.4° for the adsorbed hydrogen atom towards the hydroxyl oxygen. In the valleys the hydroxyl groups can never tilt, because the oxygen atom from the dissociated water molecule energetically prefers to reside in the site of the oxygen of an unfacetted surface and is therefore coordinated to two cations instead of one, as in adsorption on the edge. The proton from the dissociated water molecule is bonded to a surface oxygen atom on the exposed {100} plane inside the valley. Langel *et al.* (1994), in their Car-Parinello simulation of water adsorption on a micro-facetted {110} surface of MgO, calculated that an initially undissociated water molecule placed inside the step, with the oxygen in the regular lattice position of an unfacetted surface, would dissociate and the proton would indeed form a bond with a surface oxygen on the {100} plane.

Simulations of hydroxylation of both the $(a\sqrt{2})/2$ and $a\sqrt{2}$ facets of CaO reveal that at low coverages of zero to 50% of the adsorption sites, the configurations with water molecules adsorbed on the edges are energetically more advantageous than adsorption in the valleys of the facet. However, at the higher surface coverage of 100% of the edge or valley sites, water adsorbs preferentially in the valleys. Similarly, the simulations on the $(a\sqrt{2})/2$ facet of MgO show that the configurations with water molecules adsorbed in the valleys are more stable and the hydration energies are lower for all partial coverages than the configurations with water adsorbed on the edges. However, at infinite dilution, the hydration energy of the edge

configuration is somewhat lower than the valley configuration (table 4(V) and fig. 4.3c). This would indicate that at low partial water pressure, water molecules initially adsorb on the low-coordinated edge atoms, even though this position is less stable than in the valley. Hydration in the valley then becomes more attractive with increased coverage. It is not clear why the edge position should be preferred at very low water concentrations other than that the edge atoms are lower coordinated and hence probably more reactive for initial adsorption when no stabilisitation due to a network of hydrogen bonds or extensive bonding to lattice cations as in the valley position can as yet occur.

The $a\sqrt{2}$ facet of MgO resembles the facets of CaO: hydration on the edges is more favourable at low partial coverage while at higher coverages the adsorption in the valleys is preferred.

Thus the simulation results suggest that on the facetted {110} surfaces water adsorbs at low-coordinated sites only at low partial coverages whereas at higher coverages the position in the valley is preferred. Although the surface adsorption sites in the valley are five-coordinated, the hydroxyl oxygen can become coordinated to two surface cations in an lattice oxygen site.

4.4.3 {310} Surface

As noted earlier, the {310} surface represents a simple step structure and as such we might expect it to be similar to the facetted {110} surfaces because the {310}

surface is a stepped surface where the height of the step is one atomic layer while the $(a\sqrt{2})/2$ and $a\sqrt{2}$ facetted {110} surfaces have step heights of two and four atomic layers respectively, hence these three surfaces are models for different step heights.

The {310} surface again allows us to model adsorption both on the edge and inside the step of the {100} plane. The steps are 15.2 Å and 13.3 Å apart in CaO and MgO respectively, sufficiently well separated that we do not anticipate significant interactions between steps. We found that the adsorbed oxygen atom of the OH-group on relaxation always takes up the same position essentially adding to the step and coordinating to two cations, one cation next to the step on the {100} plane and the other at a low coordination site on the edge of the step. There are, however, two configurations for the proton from the water molecule which are similar in energy, certainly at low coverage. These are (i) on the top of the step *i.e.* the 'edge' site and (ii) inside the step *i.e.* the 'valley' site. When the hydrogen atom is adsorbed at a surface oxygen on the {100} plane inside the step, *i.e.* at the valley site, it relaxes towards the position where a cation would have been had the step been extended. Thus the water molecules adsorb in such a way as to extend the crystal, occupying where possible the lattice sites. However, when adsorbed on the edge site *i.e.* at the top of the step the hydrogen atom relaxes towards the oxygen atom of the adsorbed hydroxyl group. Figure 4.7 shows the different configurations. At all coverages the surface energy of the edge configuration is lower than that of the valley configuration although they are quite similar at low coverages and only from 50% coverage onwards does the edge configuration start to be noticeably more stable (table 4(IV)).

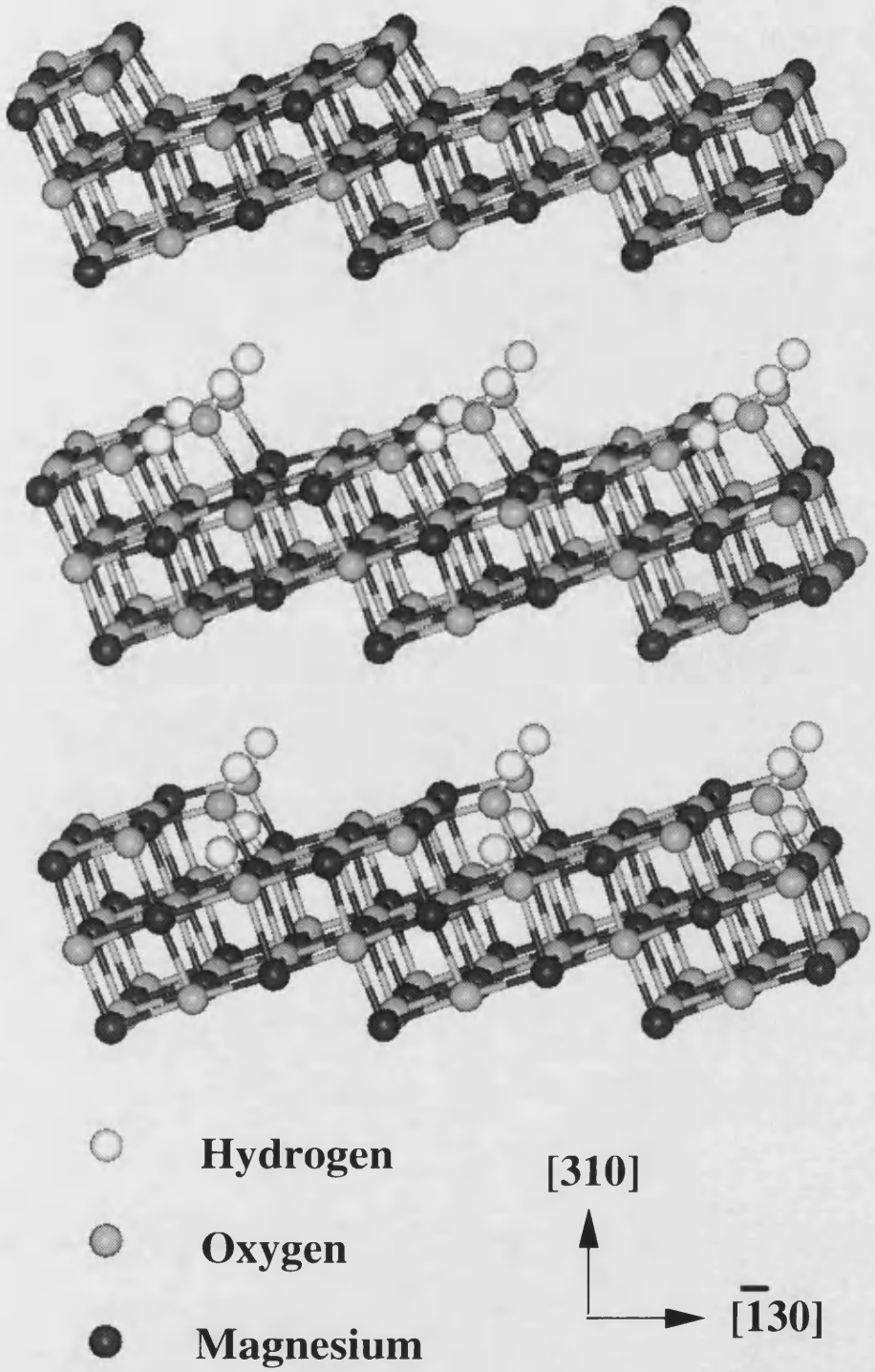

Figure 4.7 Minimum energy configuration of the MgO {310} surface: (a) unhydroxylated surface, (b) adsorption on the edge giving rise to bridging hydroxide groups with the edge hydrogens directed between the hydroxide groups, and (c) adsorption in the valley, again giving rise to bridging hydroxide groups with the valley hydrogens directed between the hydroxide groups

In the valley configuration at low coverages, up to 25%, the water molecules tend to adsorb separately at isolated positions. At higher coverages, however, the water molecules show a definite tendency to adsorb in full rows rather than spaced equally over the surface, resulting in alternating fully hydroxylated and empty edges. In this way, the adsorbed molecules form a smooth edge rather than kinks and corners. The same trend is shown in both CaO and MgO.

Unlike adsorption in the valley sites, at the edge of the step water molecules prefer to adsorb in a straight line from step to step rather than equally spaced over the surface. The hydration energy of adsorption on the edge is more favourable than in the valley for both CaO and MgO (table 4(V) and fig. 4.4f) and thus water should preferentially adsorb on the four-coordinated atoms on the edges as inferred by experiment (Jones *et al.* 1984, Onishi *et al.* 1987, Dunski *et al.* 1994) rather than on the five-coordinated {100} atoms inside the step.

4.4.4 Planar and facetted {111} Surfaces

On the planar {111} surface the oxygen atoms of the OH groups of the added water molecules were adsorbed in the oxygen vacancies left when half the oxygen atoms of the surface are moved to remove the dipole as described earlier. The hydrogen atoms of the water molecules were bonded to the remaining surface oxygen atoms. A full monolayer coverage would then result in a smooth surface plane of hydrogen atoms with a full oxygen layer below. Not surprisingly, this is a very stable

surface for both CaO and MgO and is structurally similar to the basal plane of $Ca(OH)_2$ and $Mg(OH)_2$.

In CaO the water molecules energetically prefer to adsorb in pairs again as on the {100} and planar {110} surface. At full monolayer coverage, the surface energy becomes negative (table 4(IV)) indicating that the crystal is not stable and would energetically prefer to form the hydroxide at the {111} surfaces.

In MgO, instead of adsorbing in pairs the water molecules prefer to adsorb in rows. This is possibly due to the smaller cation-oxygen distance in MgO which reduces the requirement of the hydroxyl groups to tilt to the hydrogen atom and all the adsorbed hydrogen and oxygen atoms stabilise each other.

The hydration energies for the various partial coverages of the planar {111} surface in both CaO and MgO are highly exothermic compared to those of the other surfaces (table 4(V) and fig. 4.3) and the {111} surface clearly prefers to be hydroxylated.

One of our aims was to investigate three-coordinated adsorption sites, thus we extended our study to include hydroxylating both the magnesium terminated and oxygen terminated $a\sqrt{3}$ facet of MgO as a model for corner sites on the experimental {100} surface. Partial coverages of the facetted {111} surface were not investigated as this would necessitate a prohibitively large unit cell of more than 8000 ions and only full monolayer coverage of the three-coordinated sites of MgO was modelled.

However, the hydration energies for the {310} surface show Langmuir behaviour, *i.e.* a constant value for both different partial coverages and different configurations of the same coverage. As the three-coordinated sites on the {111} facetted surface are far more separated than on the {310} surface, we may be reasonably confident that partial coverages of the three-coordinated sites have no great influence on the hydration energy of the facetted {111} surface.

The structure and stability of hydroxylating the three-coordinated ions was investigated, each time involving dissociative adsorption of a water molecule across a Mg-O pair at the top of the pyramid involving the three-coordinated ion, resulting in the formation of two hydroxyl groups (figure 4.8b+c). Hydroxylation of both surfaces proved to be energetically favourable: hydroxylating all three-coordinated ions on the magnesium terminated plane gave a hydration energy for dissociative adsorption of -168.3 $kJmol^{-1}$ and similarly on the oxygen terminated plane -165.6 $kJmol^{-1}$. The hydroxylated facets were also slightly more stable than their unhydroxylated counterparts, the surface energy of the magnesium terminated surface went down from 2.49 Jm^{-2} to 2.33 Jm^{-2} and similarly that of the oxygen terminated surface from 2.39 to 2.23 Jm^{-2}.

(a)

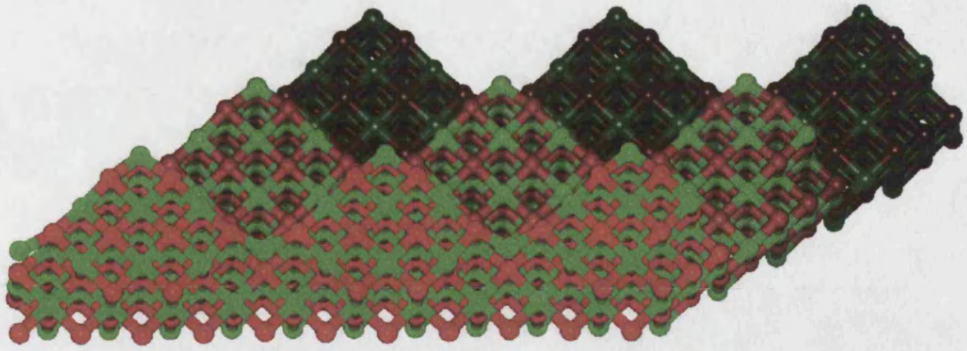

(b)

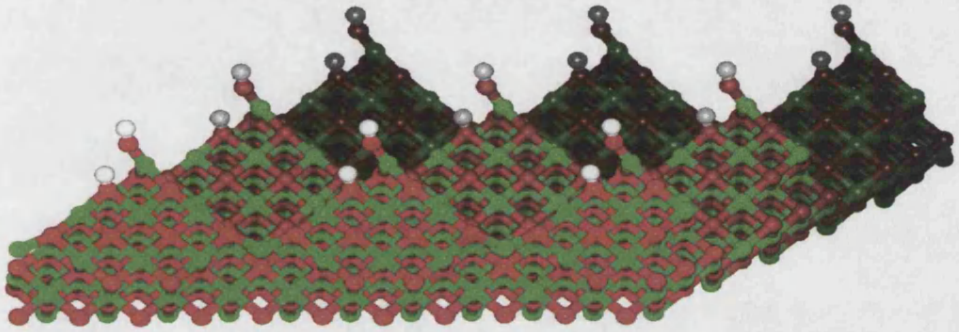

(c)

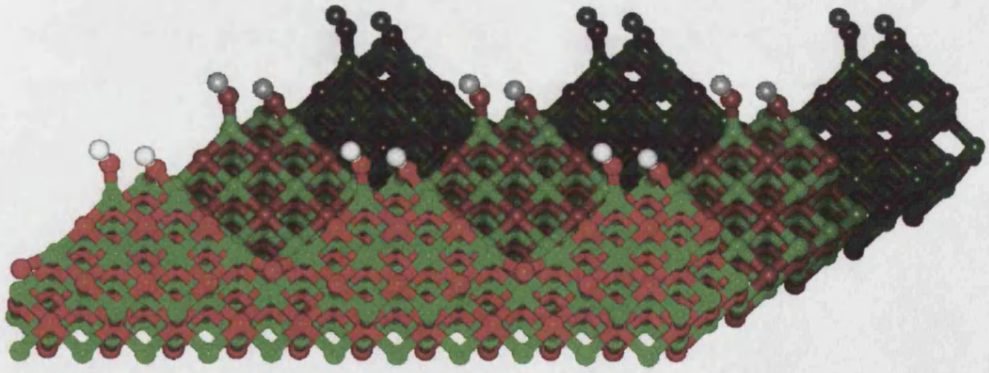

Figure 4.8 Minimum energy configuration of the $a\sqrt{3}$ facetted {111} surface of MgO: (a) unhydroxylated magnesium-terminated surface, (b) hydroxylated magnesium-terminated surface and (c) hydroxylated oxygen-terminated surface. (Mg = green, O = red, H = white)

4.5 Physisorption on MgO Surfaces

In addition to chemisorption we also studied physisorption of water molecules in a series of partial coverages on various MgO surfaces. As with the hydroxylated surfaces we are interested in the difference in hydration energies between the five-, four- and three-coordinated adsorption sites. Hence we have studied the perfect MgO {100} surface for the five-coordinated sites, while the {310} surface supplies four-coordinated edge sites. The three-coordinated sites are modelled by the $a\sqrt{3}$ {111} facet.

4.5.1 {100} Surface

The adsorption of water molecules on the {100} surface up to monolayer coverage was considered and we found that the energetically most favourable configuration for adsorption onto the planar five-coordinated {100} surface was for the water oxygen atom to be coordinated to a surface magnesium atom at a distance of 1.96 Å (fig. 4.9). Although at lower partial coverages the {100} surface is amenable to molecular adsorption (table (VIII) on page 153), at full monolayer coverage the hydration energy is only -3.9 $kJmol^{-1}$ and physisorption is only just energetically favourable. From the surface energies in table 4(VII) it is clear that the fully hydrated surface is also the least stable one with a relatively high surface energy of 2.00 Jm^{-2} while the surfaces with lower partial coverages, especially 50% and 75% are much more stable which is similar to hydroxylation of the {100} surface where the 75% coverage was unusually stable.

Surface energy / Jm^{-2}						
Surface	**Coordination no.**	**12.5%**	**25%**	**50%**	**75%**	**100%**
{111}Mg	3	-	-	-	-	2.41
{111}Ox	3	-	-	-	-	2.32
{310}	4	1.78	1.72	1.59	1.47	1.35
{100}	5	1.26	1.06	0.75	0.70	2.00

Table 4(VII) Surface energies of molecularly hydrated MgO surfaces

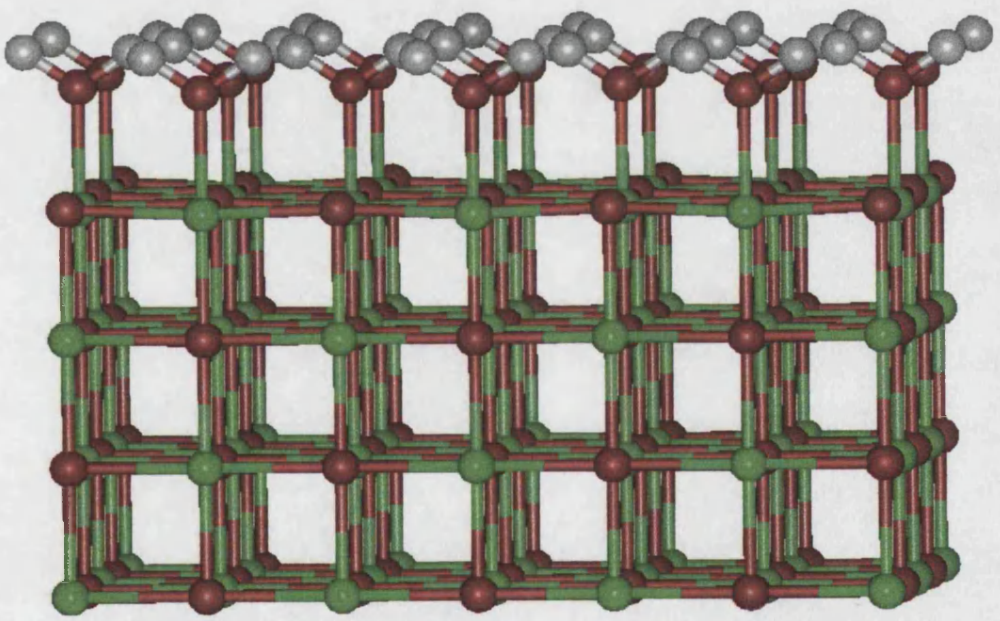

Figure 4.9 Relaxed surface structure of the {100} surface with a full monolayer of physisorbed water molecules. (Mg = green, O = red, H = white)

4.5.2 {310} Surface

On the four-coordinated sites, modelled by the edges of the {310} surface, there are two energetically comparable modes of adsorption: (i) coordination of the water molecule to the four-coordinated edge magnesium ion at a distance of 2.03 Å, where one of its two hydrogen ions was directed towards the four-coordinated oxygen ion on the edge at a distance of 1.58 Å, and the other to the five-coordinated oxygen ion on the plane below the step at a distance of 1.66 Å (fig. 4.10a), and (ii) coordination of the water oxygen atom to two magnesium ions, a four-coordinated one on the edge and a five-coordinated ion on the plane below the step (fig. 4.10b) and where one of the hydrogen ions was directed towards a four-coordinated oxygen ion on the edge. In both instances, the water molecule appears to position itself ready for dissociation and surface hydroxylation (fig. 4.7b).

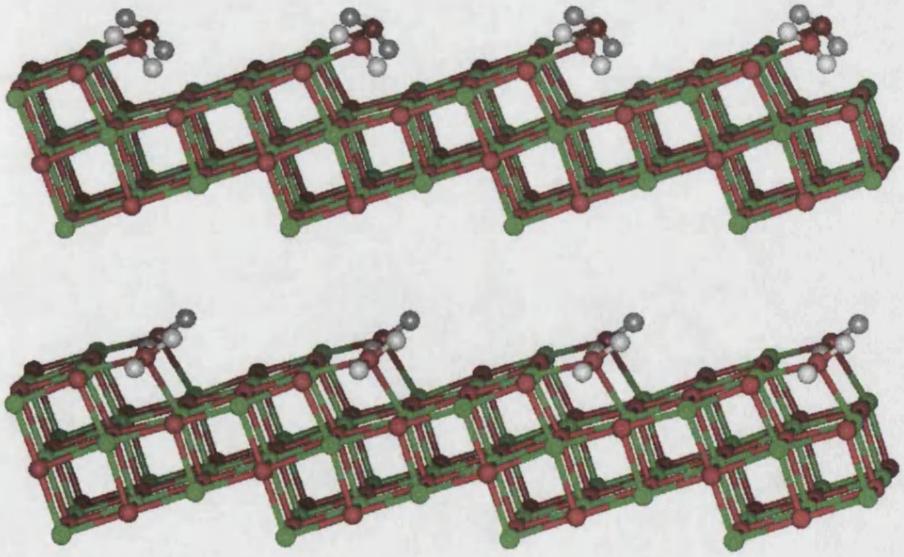

Figure 4.10 Minimum energy configuration of the MgO {310} surface: (a) oxygen atoms of the water molecules physisorbed onto the four-coordinated edge ions coordinate only to the four-coordinated magnesium ions, and (b) oxygen atoms of the physisorbed water molecules coordinate to two lattice magnesium ions (Mg = green, O = red, H = white)

Hydration of the edges has no great effect on the stability of the surface as the surface energies in table 4(VII) show. There is some progressive stabilisation with increasing coverage but the hydration energies (table 4(VIII) on page 153) show Langmuir behaviour, similar to hydroxylation of this surface.

4.5.3 Facetted {111} Surface

Physisorption onto three-coordinated ions was modelled by using a facetted {111} surface as discussed above. Adsorption on the magnesium terminated plane resulted in the water oxygen ion becoming bonded to the three-coordinated magnesium ion at a distance of 1.93 Å. This magnesium-oxygen bond was tilted by 37.4° to the surface normal, towards one of the lattice oxygen ions on the edge of the pyramid, while one of the hydrogen ions became coordinated to this lattice oxygen at a distance of 1.63 Å (figure 4.11a). On the oxygen terminated plane one hydrogen atom of the water molecule was placed above the three-coordinated oxygen atom. However, on minimisation the water molecule migrated towards the four-coordinated edge magnesium atom to which the water oxygen ion became bonded. This 1.97 Å long bond was tilted by 19.2° to the edge normal, pointing towards the three-coordinated oxygen atom to which one of the hydrogen ions became hydrogen-bonded at a distance of 1.56 Å (figure 4.11b). The hydration energies for the two configurations were similar at -106.1 $kJmol^{-1}$ and -99.4 $kJmol^{-1}$ for the magnesium and oxygen terminated surfaces respectively.

(a)

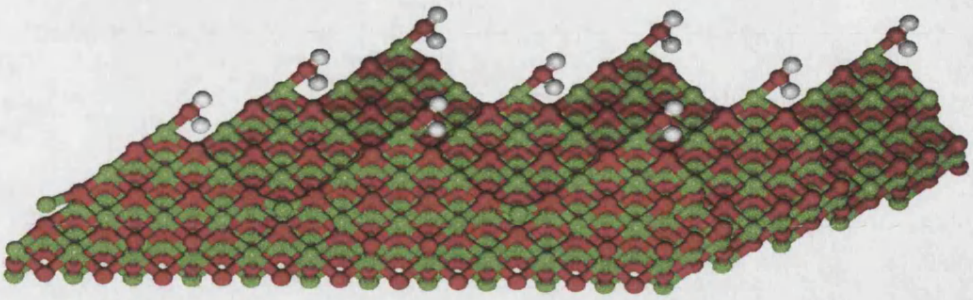

(b)

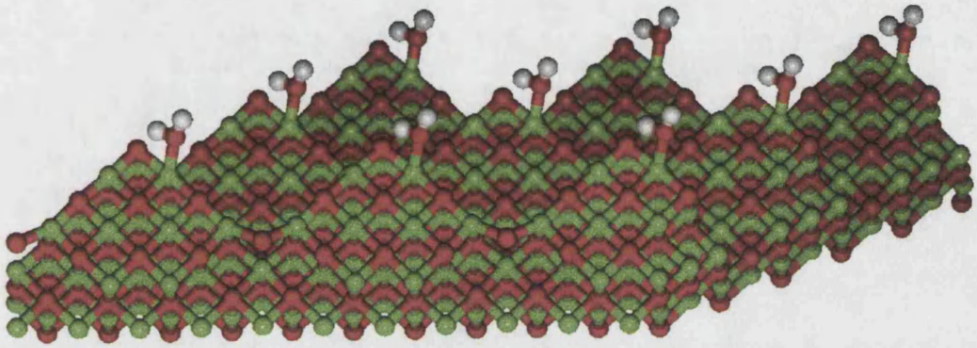

Figure 4.11 Minimum-energy configuration of the $a\sqrt{3}$ facetted {111} surface: (a) physisorption onto the magnesium-terminated surface and (b) physisorption onto the oxygen-terminated surface shows coordination of the water molecule's oxygen atom to the four-coordinated magnesium ion on the edge (Mg = green, O = red, H = white)

4.6 Physisorption on Hydroxylated MgO Surfaces

In addition to molecular hydration of pure MgO surfaces we also investigated physisorption of water molecules onto hydroxylated surfaces. The {100} surface is not amenable to hydroxylation and thus only physisorption on the hydroxylated {310} and {111} $a\sqrt{3}$ facetted surfaces were studied.

4.6.1 {310} Surface

Physisorption on the hydroxylated {310} surface took place in two different ways. The first was on the lattice edge atoms. The water molecule's oxygen ion became coordinated to the edge magnesium atom at a distance of 2.05 Å, while one of the hydrogen atoms tilted towards the hydroxide oxygen ion, at 1.92 Å virtually a hydrogen-bond distance (figure 4.12a).

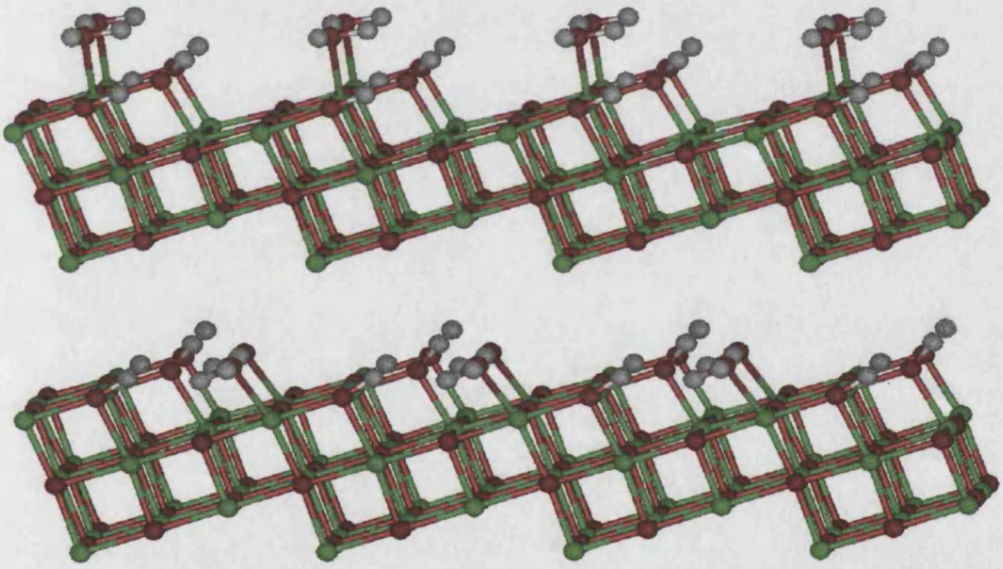

Figure 4.12 Minimum-energy configuration of physisorption onto the hydroxylated {310}surface: (a) physisorption onto the edge atoms and (b) physisorption onto the five-coordinated atoms on the plane, showing the hydrogarnet analogue (Mg = green, O = red, H = white)

The second configuration was one in which the water molecule was either positioned with its oxygen ion pointing towards a hydroxyl hydrogen ion or with one of its hydrogen atoms coordinated to a hydroxyl oxygen ion. The result was that the water molecule migrated away from the low-coordinated ions towards the five-coordinated sites on the plane below the step (figure 4.12b). The water molecule's oxygen ion became coordinated to a five-coordinated magnesium ion with a bondlength of 1.98 Å while it also coordinated to the hydrogen ion of one of the hydroxyl groups at a distance of 1.80 Å. One of the water molecule's hydrogen ions pointed towards the oxygen of a hydroxyl group at 1.94 Å. The other hydrogen ion together with the hydrogen of the other hydroxyl group both pointed toward an interstitial magnesium site. This is a structural analogue to the hydrogarnet defect in grossular (Wright *et al.* 1994) where four hydrogen atoms point towards an empty silicon site. We found that this was energetically the most favourable position for the water molecule to adsorb onto the hydroxylated {310} surface, with a hydration energy of -162.1 $kJmol^{-1}$ at full monolayer coverage compared to -53.1 $kJmol^{-1}$ for adsorption on the edge site. The hydration energies for the various coverages are given in table 4(VIII) page 153.

4.6.2 Facetted {111} Surface

On the hydroxylated magnesium-terminated surface the water molecules physisorbed to one of the hydroxyl groups. The water molecule's oxygen ion was coordinated to the hydrogen of the hydroxyl group on the magnesium ion at 1.47 Å, while it also became coordinated to the hydrogen of the hydroxylated four-coordinated lattice oxygen ion on the edge at a distance of 1.54 Å (fig. 4.13a).

Physisorption on the hydroxylated oxygen-terminated surface took place in two different ways: (i) The water molecule became physisorbed to the hydroxyl groups such that the water molecule's oxygen ion became coordinated to the hydroxyl hydrogen ion of the hydroxylated magnesium ion on the edge, while one of its hydrogen ions became coordinated to the hydroxyl oxygen ion of this same magnesium ion (fig. 4.13b). (ii) The oxygen ion of the water molecule became bonded to an unhydroxylated four-coordinated edge magnesium ion at a distance of 1.94 Å (fig. 4.13c). The latter was the energetically more favourable position for physisorption on this surface (table 4(VIII) page 153).

(a)

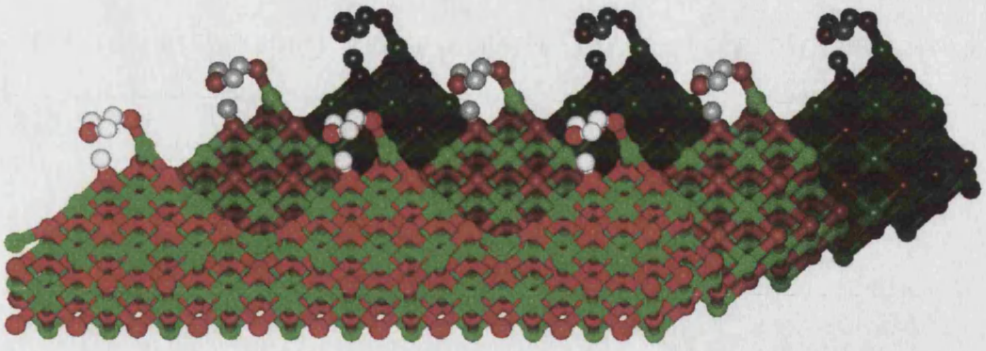

(b)

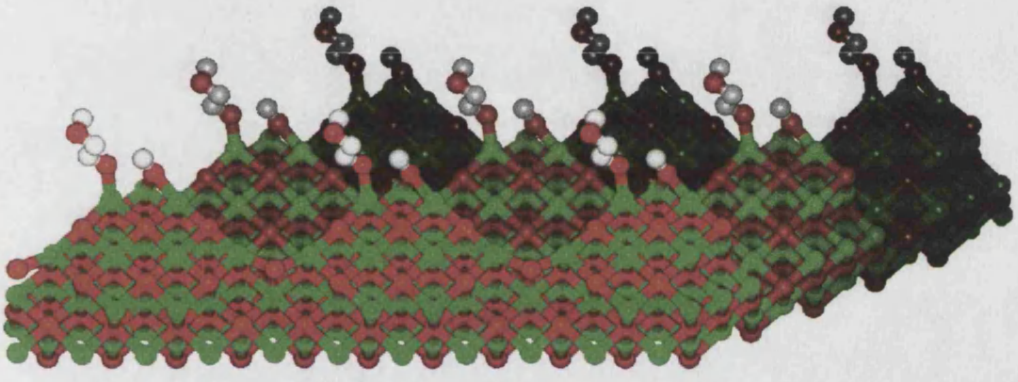

(c)

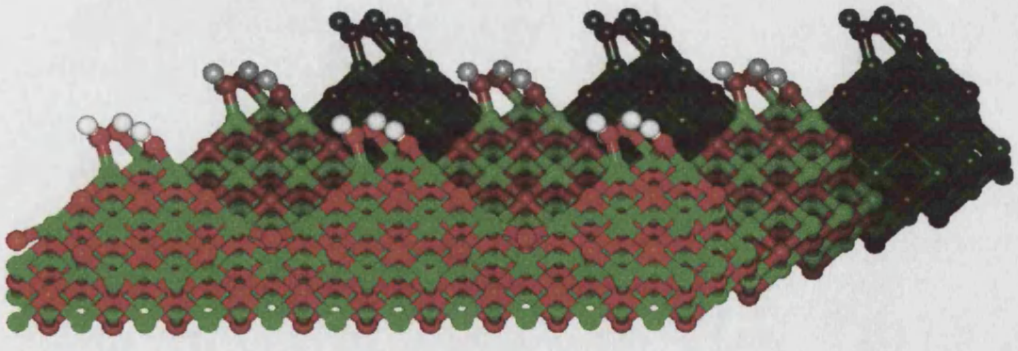

Figure 4.13 Minimum-energy configuration of the hydroxylated $a\sqrt{3}$ facetted {111} surface: (a) physisorption onto the magnesium-terminated hydroxylated surface, (b) physisorption onto the oxygen-terminated surface by hydrogen-bonding only and (c) physisorption onto the oxygen-terminated surface showing coordination of the water molecule's oxygen atom to the four-coordinated magnesium ion on the edge (Mg = green, O = red, H = white)

4.7 Discussion of Static Calculations

In addition to confirming the sites of chemisorption, we found in our simulations that surfaces which have high surface energies when flat are often stabilised by micro-facetting into steps of the dominant {100} plane. LEED patterns show that micro-facetting of the {110} and {111} surfaces indeed occurs (Henrich 1976, Onishi *et al.* 1987). Moreover, when hydrated, the initially planar {110} surface shows facets created by the adsorbed hydroxyl groups (fig. 4.5). Since publication of our results on facetted surfaces (de Leeuw *et al.* 1995, 1996) Baudin *et al.* (1997) have investigated the MgO {111} surface using Molecular Dynamics simulations and found considerable rearrangement of the surface which they compare to our facetted {111} surface. They found a surface energy of the unreconstructed oxygen {111} surface of 3.8 Jm^{-2} and 3.7 Jm^{-2} for the Mg terminated surface which decreased to 3.3 Jm^{-2} after facet-like reconstruction.

4.7.1 Chemisorption

The lowest hydration energies of the most stable of the CaO surfaces studied range from -82.8 $kJmol^{-1}$ on the {100} surface to -224.5 $kJmol^{-1}$ on the edges of the {310} surface. Fubini *et al.* (1989) in their experimental study of the reactivity of CaO with water vapour found an initial heat of adsorption of approximately -170 $kJmol^{-1}$ at very low coverage decreasing to about -145 $kJmol^{-1}$ at higher coverages. In

their study, no particular surface was prepared or studied and we can expect the hydration energy to reflect the properties of the most stable {100} surface with defect features such as steps and corners.

The edges of the {310} surface are the most accurate model for four-coordinated sites of chemisorption on a 'real' {100} plane. Our calculated hydration energies for the four-coordinated steps on this surface of CaO agree very well with those obtained experimentally by Fubini *et al.* (1989). At infinite dilution the hydration energy is -224.5 $kJmol^{-1}$ decreasing to -199.1 $kJmol^{-1}$ at 100 % coverage. This indicates that as expected the real experimental {100} surface containing defects is modelled more accurately by the {310} surface containing both steps and {100} planes than by the perfect {100} surface on its own.

The hydration energies for MgO of the more stable surfaces range from -49.7 $kJmol^{-1}$ on the {100} surface to -221.9 $kJmol^{-1}$ for initial adsorption on the edges of the {310} surface. The hydration follows a very similar pattern to CaO although hydration to full monolayer coverage of the dominant {100} surface in MgO is not energetically favourable in agreement with theoretical work by Scamehorn *et al.* (1993). When investigating water chemisorption on MgO at elevated temperatures under a vapour pressure of 613 Pa, Beruto *et al.* (1993) found an enthalpy of adsorption of water of between -189 $kJmol^{-1}$ at a partial coverage of 25% and -113 $kJmol^{-1}$ at a partial coverage of about 70% assuming that only the {100} surfaces were present and that chemisorption took place on fixed sites. If we assume that those fixed sites are the low-coordinated surface atoms, including four-coordinated atoms,

which are comparable to the atoms on the {110} surface and {310} edges, and three-coordinated atoms such as on the facetted {111} surface, rather than the five-coordinated atoms of the perfect {100} plane, then these values again agree well with the hydration energies calculated for the {310} surface which is -222 $kJmol^{-1}$ at very low coverage and decreases to -182 $kJmol^{-1}$ for the 100% coverage, and the facetted {111} surface with an average hydration energy for the three-coordinated oxygen and magnesium sites of -167 $kJmol^{-1}$. As in CaO, the highly stepped {310} surface and the corner sites of the facetted {111} surface of MgO provide a better model for the {100} surface of a real defective rocksalt oxide than the five-coordinated sites of the pure {100} surface.

4.7.2 Physisorption

The hydration energies for the different MgO surfaces used to study physisorption of water are given in table 4(VIII) and for the sake of clarity and direct comparison we have also added the hydration energies of chemisorption from table 4(V) for the relevant surfaces.

Surface	Coordination no.	Energy of Hydration / $kJmol^{-1}$				
		12.5 %	25 %	50 %	75 %	100 %
		Chemisorption on Pure Surfaces				
{111} Mg	3	-	-	-	-	-168.3
{111} Ox	3	-	-	-	-	-165.6
{310}edge	4	-184.0	-185.7	-188.7	-183.1	-181.9
{310}plane	5	-108.9	-109.2	-102.2	-104.5	-107.0
{100}	5	- 11.5	- 34.8	+ 10.9	- 49.7	+ 89.9
		Physisorption on Pure Surfaces				
{111}Mg	3	-	-	-	-	-106.1
{111}Ox	3	-	-	-	-	- 99.4
{310}	4	-127.4	-127.4	-127.4	-127.4	-127.4
{100}	5	- 37.6	- 83.0	- 96.5	- 83.0	- 3.9
		Physisorption on Hydroxylated Surfaces				
{111}Mg	3	-	-	-	-	-196.8
{111}Ox	3	-	-	-	-	-111.9
{111}Ox	4	-	-	-	-	-166.9
{310}edge	5	- 50.2	- 53.1	- 53.1	- 53.1	- 53.1
{310}plane	5	-163.1	-163.1	-163.1	-162.1	-162.1

Table 4(VIII) Energies of hydration of chemisorption onto pure surfaces and physisorption onto pure and hydroxylated surfaces of MgO

One way of examining the interaction energy between the adsorbed water molecules is to compare an attachment energy, which we define as the interaction of a complete layer of water molecules with the surface, with the hydration energy as described above. The energy difference per water molecule then represents the binding energy between the water molecules that are adsorbed on the surface. Table 4(IX) shows the binding energies thus obtained whereby a negative binding energy points to stabilisation, *i.e.* the energy of the relaxed water layer is lower than that of a collection of separate water molecules.

Surface	Coordination no.	Binding Energy / $kJmol^{-1}$				
		12.5 %	25 %	50 %	75 %	100%
		Physisorption on Pure Surfaces				
{111}Mg	3	-	-	-	-	+ 8.7
{111}Ox	3	-	-	-	-	+ 8.6
{310}	4	+17.4	+ 8.3	+17.7	+ 8.2	+ 8.2
{100}	5	+ 4.5	+ 1.1	-21.5	-26.3	+27.9
		Physisorption on Hydroxylated Surfaces				
{111}Mg	3	-	-	-	-	+ 1.2
{111}Ox	3	-	-	-	-	0
{111}Ox	4	-	-	-	-	+13.6
{310}edge	5	+ 3.8	- 1.2	- 1.6	- 1.9	- 2.3
{310}plane	5	+ 4.8	+ 4.6	+ 3.9	+ 2.4	+ 1.2

Table 4(IX) Binding energies of physisorption onto pure and hydroxylated MgO surfaces

It is clear from table 4(VIII) that physisorption is always energetically favourable, at the low-coordinated step and corner sites and even at the perfect five-coordinated surface sites. However, on the unhydroxylated planes, the four-coordinated edge ions are the energetically preferred sites for physisorption by water. The enhanced stabilisation is due to the oxygen of the water molecule binding at the site an oxygen ion would occupy should the crystal be extended. This oxygen ion usually coordinates to two magnesium ions, allowing at least one hydrogen ion to form a hydrogen-bond to a four-coordinated lattice oxygen ion. This surface configuration is very similar to the hydroxylated surface in the absence of physisorbed water and in part explains why the electronic structure calculations of Langel and Parrinello (1994) were able to show the water molecule breaking up. The hydration energy is

independent of the coverage of the step showing Langmuir behaviour. Table 4(IX) shows the binding energy to be positive by a small amount, highest at coverages of 12.5% and 50%. At these coverages the lowest energy configurations occurred when the water molecules adsorbed separately, across rows rather than next to each other in a row. As such they are not close enough to interact with each other to lower their energy by forming a network of hydrogen bonds. The lowest energy configurations at 25%, 75% and 100% provide some interaction between neighbouring water molecules in a row and here the destabilisation is less, although still positive indicating that adsorption on the MgO crystal surface outweighs the formation of an energetically unfavourable interaction of widely spread-out water molecules.

Although the three-coordinated magnesium, and to a lesser extent the oxygen ions, are also amenable to adsorption their topology does not provide the stabilising position of an extended surface lattice site for the water's oxygen atom to occupy. However, physisorption is still very favourable (table 4(VIII)) because of the strong interaction with the low-coordinated magnesium ion and the formation of hydrogen-bonds to the lattice oxygen ions.

The five-coordinated ions of the flat {100} plane differ from the lower coordinated ions by exhibiting non-Langmuir behaviour of the hydration energies as they vary with coverage. The configuration of the water molecules is also important, for example the lowest energy configuration at 75% coverage has a hydration energy which is larger by 24.5 $kJmol^{-1}$ than the next most favourable configuration at this coverage. Although physisorption is possible at all coverages, it is only just

energetically favourable at full monolayer coverage. Adsorption on the five-coordinated ions reveals that the stabilisation energy also plays a greater role, especially at the coverages of 50% and 75% where the interactions between the physisorbed water molecules stabilise the water layer and make physisorption more favourable. At 100% coverage, however, the physisorbed water layer is destabilised by the water molecules' interactions probably leading to the low energy of hydration at this coverage. From the above it is clear that as with hydroxylation, the lower-coordinated ions are more reactive towards physisorption than the five-coordinated ions of the perfect {100} surface.

In summary, chemisorption on the {100} surface is not energetically favourable. The hydration energy at full monolayer coverage was +89.9 $kJmol^{-1}$ (table 4(VIII) in agreement with the range of energies obtained by *ab initio* methods, notably Refson *et al.* (1995) who found an energy of +41.6 $kJmol^{-1}$ and Scamehorn *et al.* (1994) who obtained an energy of +102.9 $kJmol^{-1}$ for chemisorption of five-coordinated ions. Noguera *et al.* (1993) obtained an energy of +182.4 $kJmol^{-1}$ for chemisorption of the (001) surface and all agree that it is energetically unfavourable. Physisorption of the five-coordinated surface ions does take place with a hydration energy at full monolayer coverage of -3.9 $kJmol^{-1}$ (table 4(VIII)) compared with the energy found by Refson *et al.* (1995) of between -17.2 and -23.5 $kJmol^{-1}$. Table 4(X) lists the hydration energies of chemi- and physisorption for the most stable surfaces in this work compared with experimental values and other calculated hydration energies.

Surface	Coordination no.	Experiment	Calculated	This work
Hydration Energy of Chemisorption / kJmol^{-1}				
CaO	4,5	-145 to -170[1)]		-123.8 to -224.5
MgO	3,4,5	-113 to -189[2)]		
	3		-282.7 [3)]	- 167.0
	4		-30.7 [3)]	-107.0 to -221.9
	5		+102.9 [3)] +182.4 [4)] +41.6 [5)]	+89.9 to -49.7
Hydration Energy of Physisorption / kJmol^{-1}				
MgO	3		-86.9 [3)]	-99.4 to -106.1
	4		-27.3 to -44.1 [3)]	-127.4
	5		-17.2 to -23.5 [5)]	-3.9 to -96.5
Energy of Physisorption onto Hydroxylated Surface / kJmol^{-1}				
MgO	3,4,5	-84 to -252 [6)]		-50.2 to -196.8

[1)] Fubini *et al.* (1989), [2)] Beruto *et al.* (1993), [3)] Scamehorn *et al.* (1994), [4)] Noguera *et al.* (1993), [5)] Refson *et al.* (1995) [6)] Anderson *et al.* (1965)

Table 4(X) Comparison of previous calculated and experimental hydration energies of chemi- and physisorption with hydration energies of the most stable surfaces in this work

Both physisorption and chemisorption are favourable on the {310} and facetted {111} surface. The energies of chemisorption and physisorption on the four-coordinated ions of the {310} surface are -181.9 kJmol^{-1} and -127.4 kJmol^{-1} respectively at full monolayer coverage, and the position of the physisorbed species resembles the chemisorbed surface (figure 4.7). Scamehorn *et al.* (1994) in their periodic Hartree-Fock study of low- coordinated ions at a step on the (001) surface found a hydration energy for chemisorption of -30.7 kJmol^{-1} and -27.3 to -44.1 kJmol^{-1} for physisorption. However, due to computational expense they did not fully optimise the structure of the hydrated edges, only allowing the Mg-O and O-H bond

lengths to relax. We found that large structural relaxations take place. The oxygen atom of the adsorbed water molecule tilted with respect to the surface and coordinated to both the four-coordinated ions on the edge and the five-coordinated ions on the {100} plane below the edge. By applying the constraints on the atom positions within the atomistic simulation we found that the contribution to the hydration energy of 60.4 to 140.7 $kJmol^{-1}$ is attributable directly to surface relaxation and hence, where possible, relaxation should be included.

The three-coordinated oxygen and magnesium terminated facetted {111} surfaces behave differently. Both surfaces show that chemisorption is clearly preferred over physisorption, -168.3 $kJmol^{-1}$ versus -106.1 $kJmol^{-1}$ for the Mg terminated surface and -165.6 $kJmol^{-1}$ versus -99.4 $kJmol^{-1}$ for the oxygen plane. Scamehorn *et al.* (1994) investigated adsorption at three-coordinated oxygen ions and found hydration energies of -282.7 $kJmol^{-1}$ and -86.9 $kJmol^{-1}$ for chemisorption and physisorption respectively. However, our results do not compare with their calculation because they considered the water molecule bound to two three-coordinated oxygen ions of a four ion-defect cluster on the (001) surface. In our simulations the three-coordinated surface ions were isolated corner ions and formed part of a facetted {111} surface which was calculated to be the most stable form of that surface and has been observed experimentally (Henrich 1976, Onishi *et al.* 1987). This explains why Scamehorn *et al.* (1994)'s physisorption energy with only one atom of the water molecule adsorbed to a three-coordinated surface ion is similar to ours. Their energy of chemisorption is larger than our energy because in our simulation one hydroxyl

group is adsorbed to a four-coordinated ion while both their hydroxyls are adsorbed to three- coordinated ions.

The simulations of physisorption on the hydroxylated surfaces suggest that the largest energies of hydration occur for physisorption onto the hydroxylated {111} surface sites, -196.8 $kJmol^{-1}$ and -166.9 $kJmol^{-1}$ for the three-coordinated magnesium ions and four-coordinated oxygen ions respectively. This is probably due to the formation of a strong magnesium-oxygen bond aided by hydrogen-bonds between the hydroxyl groups and the water molecule. Physisorption of the five-coordinated surface ions is stabilised by the hydroxylation of the edge ions of the {310} surface and by the formation of the hydrogarnet analogue defect described above and has a hydration energy of -162.1 $kJmol^{-1}$, comparable to the physisorption of the hydroxylated four-coordinated oxygen ion. Adsorption onto the originally four-coordinated edge ions is still energetically favourable, but to a much lesser extent, -53.1 $kJmol^{-1}$, possibly because the water molecule's oxygen ion, although still coordinated to a magnesium ion (five-coordinated now that it has been hydroxylated), is not hydrogen-bonded to another hydrogen atom. It is noteworthy that on the unhydroxylated edge the interactions between the physisorbed water molecules had a destabilising effect (binding energies +8.2 to +17.7 $kJmol^{-1}$) while on the hydroxylated edge the intermolecular interactions stabilised physisorption (binding energies -1.2 to -2.3 $kJmol^{-1}$ for neighbouring water molecules). In fact, the hydration energies of physisorption on the hydroxylated edge ions (-50.2 to -53.1 $kJmol^{-1}$) resemble those of the lower coverages of the unhydroxylated {100} surface, -37.6 to -83.0 $kJmol^{-1}$. This is not surprising as in both cases physisorption takes place to a

five-coordinated surface ion without benefit of extensive hydrogen bonding to other oxygen or hydrogen ions.

Comparing our calculations with TPD measurements, for instance by Dunski *et al.* (1994) who found four different adsorption peaks, we would suggest that the highest energy peaks correspond to water chemisorbed to four-coordinated step sites and molecular water physisorbed onto a hydroxylated layer. Anderson *et al.* (1965) in their study of the interaction of water with the magnesium oxide {100} surface by sorption techniques, found values between -84 and -252 $kJmol^{-1}$ for the heat of desorption of molecular water physisorbed onto chemisorbed OH groups. These energies are compatible with our calculated energies of physisorption onto hydroxylated surfaces.

4.8 Molecular Dynamics Simulations

After adjusting the water potential parameters to bring the thermodynamic properties more in line with experimental values (chapter 3) we ran several Molecular Dynamics simulations of the MgO {100} and {310} surfaces, both *in vacuo* and in a box of liquid water molecules. Thus we can investigate whether the stability may be influenced by the mobility of the water molecules. All MD simulations were performed at a temperature of 300K.

4.8.1 {100} Surface

The simulation of the {100} surface in a box of water was run for 100 picoseconds, using the DL_POLY program as discussed in chapter 2, at NPT using a Hoover thermostat with parameters of 0.5 for both the thermostat and barostat relaxation times (ps). The timestep was set at 0.2 femtoseconds. Equilibration runs were carried out at NVE and NVT Hoover ensembles for 10000 timesteps each. A third scaling run at NPT was carried out before the production run was started. The simulation cell consisted of a MgO (4x4x4) supercell containing 256 MgO units consisting of cores and shells on the oxygen atoms. The gap between the surfaces of the repeated cell was 30 Å containing 275 water molecules, the whole system consisting of 1868 species including shells. The results were evaluated and are shown in figures 4.14 to 4.17 and table 4(XI).

The average surface energy of the unhydrated {100} surface we found to be γ = 1.31 Jm^{-2} which is comparable to that of the static simulations (1.25 Jm^{-2}).

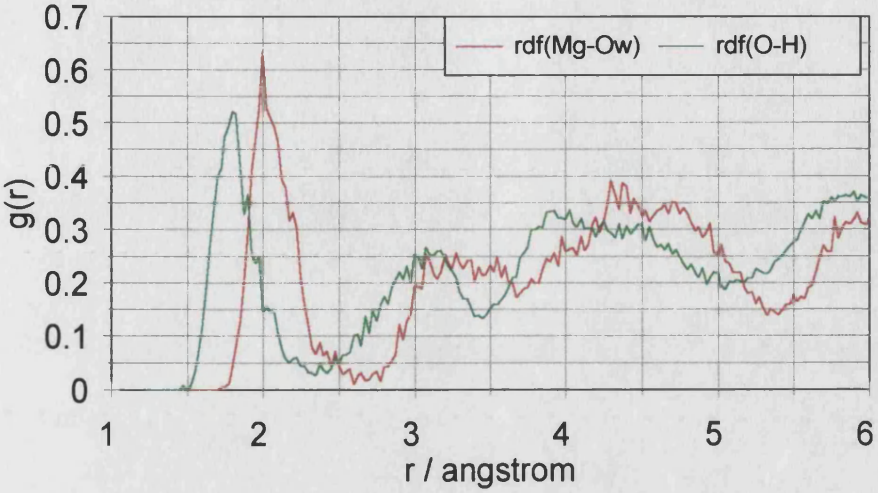

Figure 4.14 Mg-O_{water} and $O_{lattice}$-H radial distribution functions of NPT simulation

Figure 4.14 shows the radial distribution functions between magnesium and the water molecules' oxygen atoms and between the surface lattice oxygens and hydrogen atoms. The first peaks at 2.0 and 1.8 Å respectively are in accord with the static lattice simulations and experiment (Forbes *et al.* 1992, Skipper *et al.* 1994).

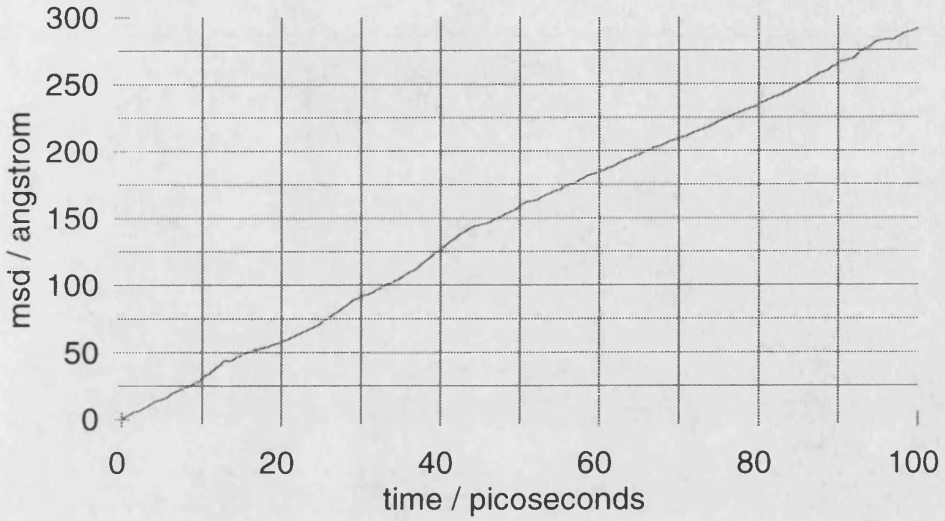

Figure 4.15 MSD of MD simulation at NPT of MgO {100} surface slab in water at 300K

Figure 4.15 shows the MSD of the water molecules between the slabs of MgO {100} surfaces. The diffusion coefficient of the water molecules has increased from the value of 1.15 x 10^{-9} m^2s^{-1} for the simulation box of pure water to 4.7 x 10^{-9} m^2s^{-1} between the two MgO slabs. This could be due to the fact that the density of the water between the MgO slabs at constant atmospheric pressure has decreased from the value of 1.3 gcm^{-3} in the box of pure water to 1.00 gcm^{-3}. As such the water molecules have more scope to move. The decrease in density implies that the water is repelled by the MgO surfaces or at least that the MgO surface disrupts the H-bonding in the water. However, when we look at a histogram of the number of water molecules as a function of distance from the MgO slab (fig. 4.16) it is clear that the water density is greatest near the MgO surface, decreases in the next few layers towards a fairly level density midway between the two slabs. Together with the lower

density this implies that the adsorption pattern on the surface forces the water molecules in subsequent layers to form an intermolecular configuration which is more open than in the pure water box.

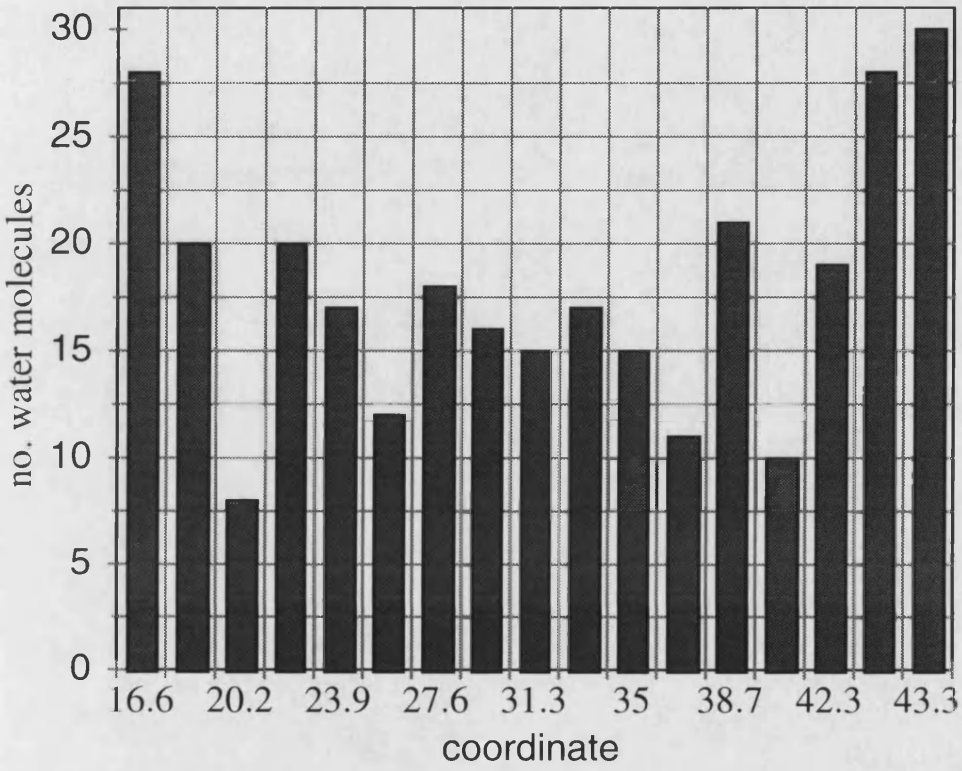

Figure 4.16 Histogram of the water molecules in the gap showing the average number of water molecules as a function of the position coordinate normal to the MgO slab surface.

Table 4(XI) shows the properties obtained from the MD simulation. Both the average surface energy of the hydrated surface and the average hydration energy are rather large and the hydration energy is positive which at first glance would indicate that hydration of the {100} surface is energetically unfavourable. However, from figure 4.16 it appears from the relative high density at the MgO surface (87-94% coverage) that water molecules prefer to adsorb to the surface which implies that the

high positive value for the average hydration energy is probably due to the intermolecular interactions between the adsorbed water molecules themselves which at high coverage was found to be unfavourable (table 4(IX)) and subsequent layers which are not in their preferred configuration.

Type of Simulation	**<ρ> / gcm^{-3}**	**water self-diffusion coefficient / 10^{-9} m^{2}s^{-1}**	**<E_{hydr}> /kJmol^{-1}**	**γ / Jm^{-2}**	**RDF / Å (Mg-O_{water})**	**RDF / Å ($O_{lattice}$-H)**
NPT	1.00	4.7	+ 28.5	2.89	2.0	1.8
NVT	0.53	20.5	+ 17.1	2.04	2.0	1.8
NVT	0.39	26.6	+ 9.5	1.60	2.0	1.8
NVT	0.23	36.7 18.1 [1)] 16.7 [2)]	+ 14.3 + 5.3 [1)] + 6.8 [2)]	1.57 1.40 [1)] 1.43 [2)]	2.0	1.8

after [1)] 100 ps, [2)] 150 ps

Table 4(XI) Data obtained from MD simulations of MgO {100} surface in water at 300K, NVT simulations run for 20 ps each (apart from ρ=0.23 gcm^{-3})

In order to investigate whether the diffusion coefficient, surface and hydration energies are dependent on the density of the water surrounding the slab, we performed three simulations at different densities of ρ1=0.52, ρ2=0.39 and ρ3=0.23 gcm^{-3}, which had to be run at NVT. The simulation at the lowest density of 0.23 gcm^{-3} is comparable to one monolayer of water molecules per surface of MgO. Figure 4.17 shows the MSDs of these three simulations and it can be seen from table 4(XI) that the self-diffusion coefficients are dependent on the density of the water surrounding the slab.

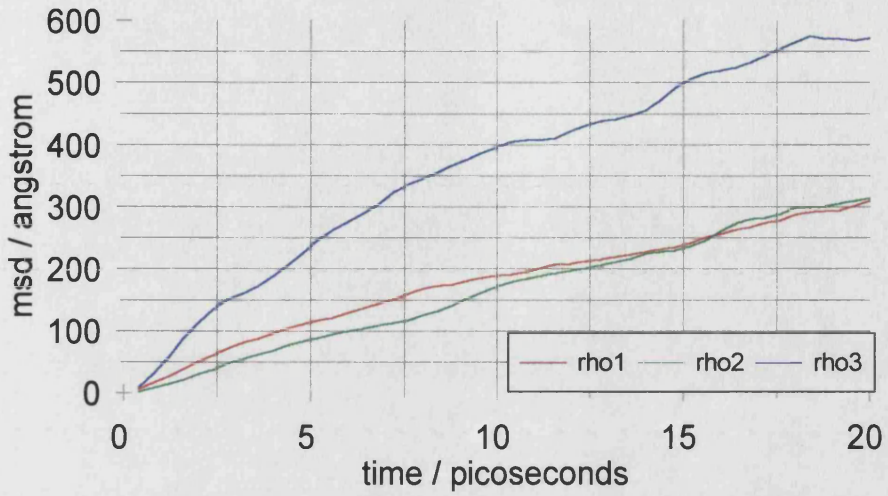

Figure 4.17 MSDs of NVT simulations of MgO {100} slab in water at 300K and different densities

The surface and hydration energies are also density dependent (table 4(XI)). The surface energies of the lower water density structures are now more in line with the surface energies of the (partially) covered {100} surface obtained by static simulations (table 4(VII) γ = 0.70 to 2.00 Jm^{-2}). The hydration energies are reduced considerably and as they are not decreasing progressively with decreasing density this may indicate that 20 picoseconds is not enough for the water molecules to distribute themselves over or away from the surface and through the gap between the slabs. We therefore ran the simulation at $\rho 3$ for 150 ps and as can be seen from table 4(XI) this had the effect of lowering both the diffusion coefficient and the surface and hydration energies. After approximately 100 ps the diffusion coefficient did not decrease much further and the hydration and surface energies had stabilised. The main differences between 100 ps and 150 ps occurred in the second layer of water molecules above the

molecules above the surface, which moved further into the space between the surface slabs, but the adsorbed layer of water on the MgO {100} surface did not change. This confirms that it is the interaction between adsorbed water molecules and subsequent layers which is energetically unfavourable, rather than the adsorbed species themselves.

Figure 4.18 shows snapshots at 100 ps and 150 ps of the MgO {100} slab in the NVT simulation of density $\rho 3 = 0.23$ gcm^{-3}. It is clear that the lower density allows the water molecules to move away from the surface and they prefer to cover the surface only partially in accord with the findings from our static calculations. In fact, these are partial coverages of 78% and 81% which agrees with the static calculations where the surface covered for 75% was particularly stable, rather than the 100% coverage. The water molecules adsorb in a flat fashion coordinating to the magnesium atom by their oxygen at 2.0 Å and to two lattice oxygen atoms (1.7-2.0 Å) by their hydrogen atoms. A pattern of adsorption is developing where the water molecules adsorb in diagonal rows across the surface, which alternate in a herringbone pattern in the direction in which the hydrogen atoms are pointing. It would seem though that the water molecules are too large to adsorb completely flat in this fashion and that each molecule is rotated somewhat with respect to its neighbour. Vacancies occur where hydrogens of neighbouring adsorbed molecules would become too close together. This pattern of adsorption disrupts the structure of the water in the vicinity of the surface, especially as a second layer prefers not to be adsorbed on top of the first explaining the sharp drop in density away from the surface in figure 4.16.

(a)

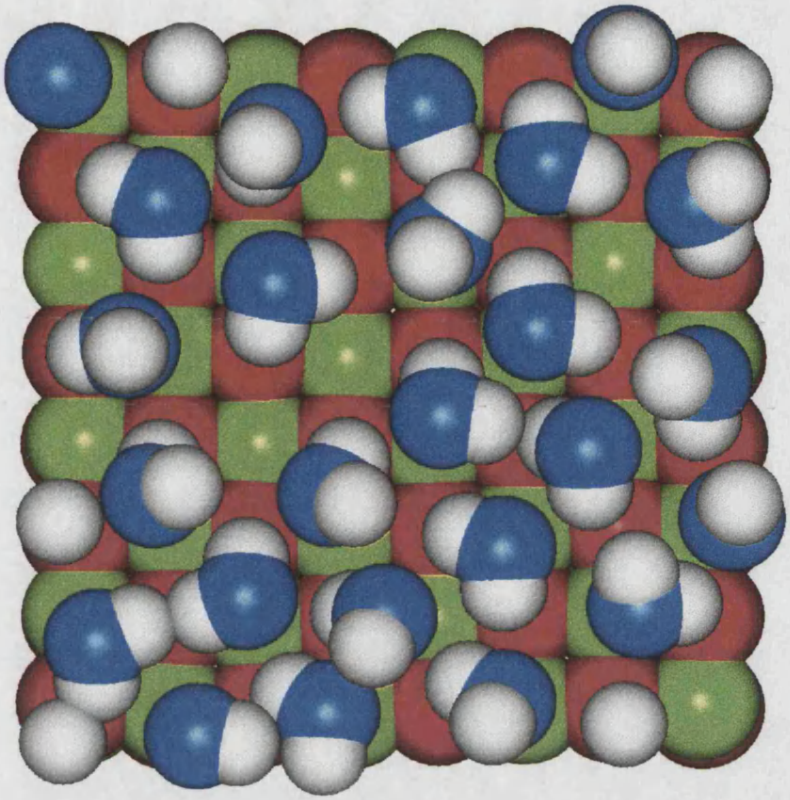

(b)

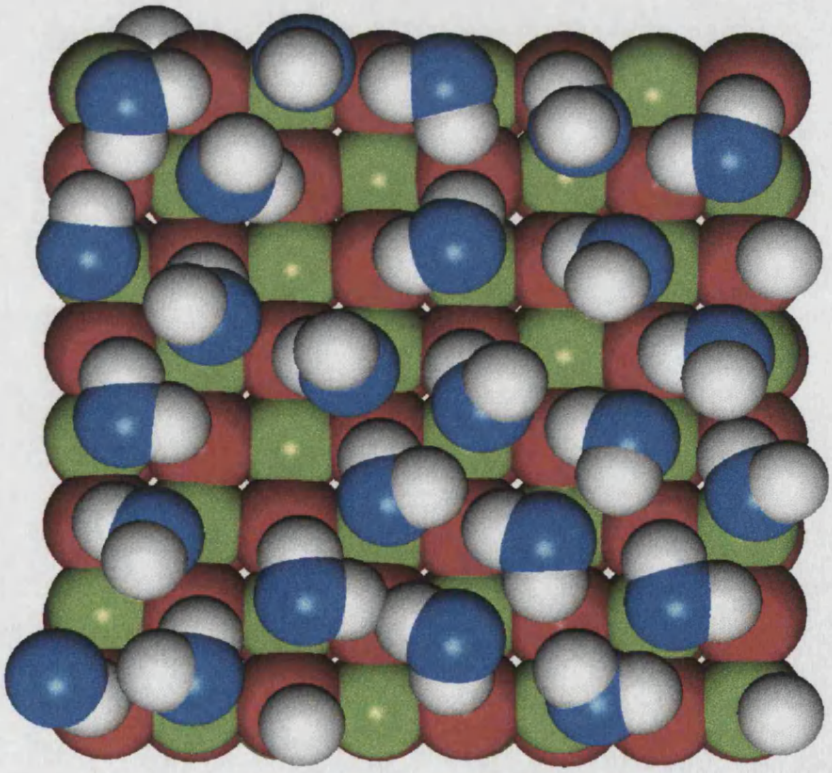

Figure 4.18 Snapshots of water adsorption on the MgO {100} surface at 300K and ρ = 0.23 gcm^{-3} after (a) 100 ps and (b) 150 ps (O=red, Mg=green, O_{water}=blue, H=white)

4.8.2 {310} Surface

The simulation of the {310} surface was run under the same conditions as for the {100} surface. The simulation cell contained 384 MgO units with 327 water molecules in a gap of 25 Å, the whole system consisting of 2460 species including shells.

The average surface energy of the unhydrated {310} surface at 300K is $\gamma = 1.54$ Jm^{-2}, somewhat lower than that found using static simulations (1.84 Jm^{-2}). Again, as with the {100} slab the surface energy of the NPT simulation of the hydrated {310} surface is rather high (2.74 Jm^{-2}), comparable to the NPT surface energy of the {100} surface (2.89 Jm^{-2}). This is not surprising as now we can expect all surface sites including the five-coordinated sites to be hydrated, not just the four-coordinated edge sites as in the static simulations, and we should expect the surface energies of the two surfaces to be similar, once again indicating that the {310} surface is a good model for an experimental {100} surface including steps. Figure 4.19 shows the {310} slab in the simulation box of liquid water.

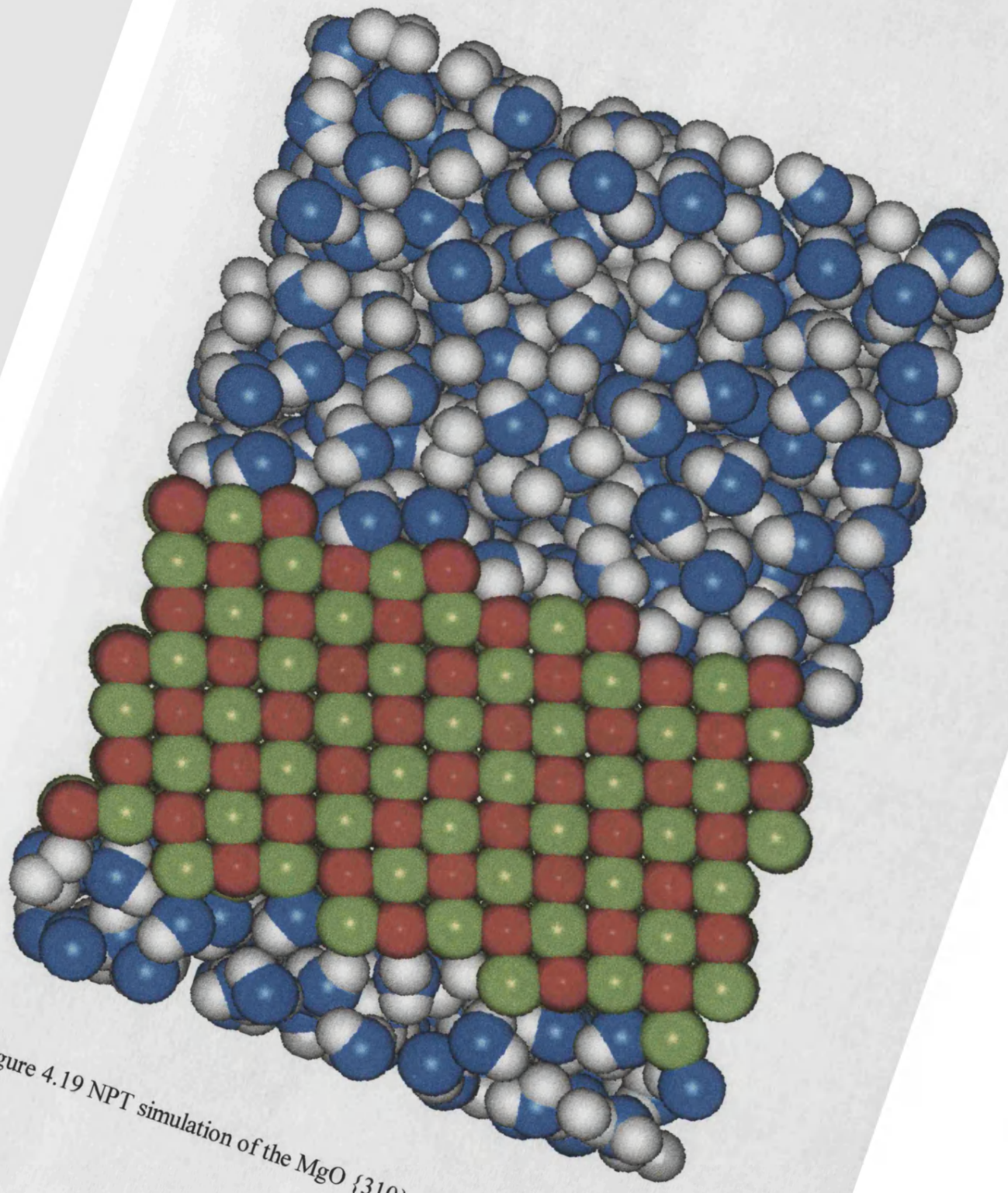

Figure 4.19 NPT simulation of the MgO {310} surface in water at 300 K.

Figure 4.20 shows the radial distribution functions of the Mg-O_{water} and $O_{lattice}$-H distances of the {310} slab in water and as with the {100} surface the first peaks agree with the static calculations and experiment (Forbes *et al.* 1992, Skipper *et al.* 1994). The Mg-O_{water} distance at 2.1 Å is larger than found on the {100} surface and this is due to the different mode of adsorption on the {310} surface where the oxygen of the water molecule adsorbs in a interstitial lattice site on the edge of the step coordinated to both the four-coordinated edge magnesium and a five-coordinated surface magnesium on the plane below (figure 4.21). The Mg-O_{water} distance of 2.1 Å corresponds to a bulk Mg-$O_{lattice}$ spacing. In addition, figure 4.21 shows that although all these edge positions are occupied by water molecules, not all the five-coordinated adsorption sites are occupied and water molecules tend to drift away from the surface.

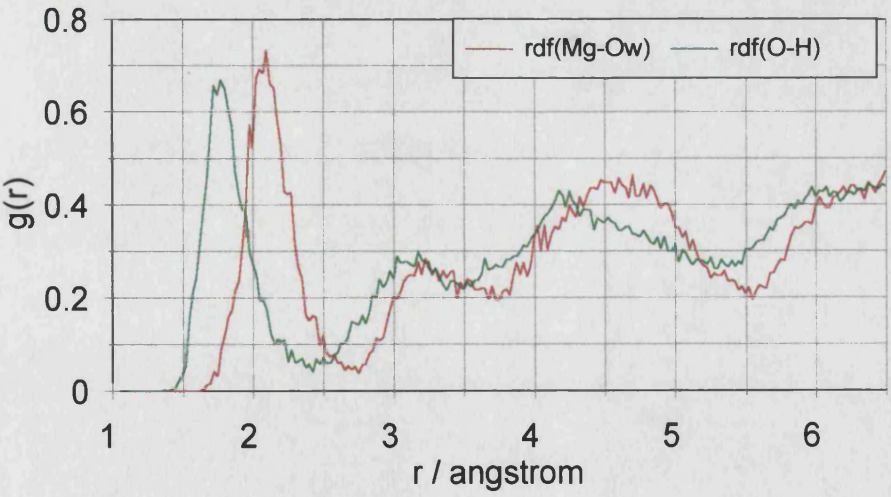

Figure 4.20 Mg-O_{water} and $O_{lattice}$-H radial distribution functions of NPT simulation

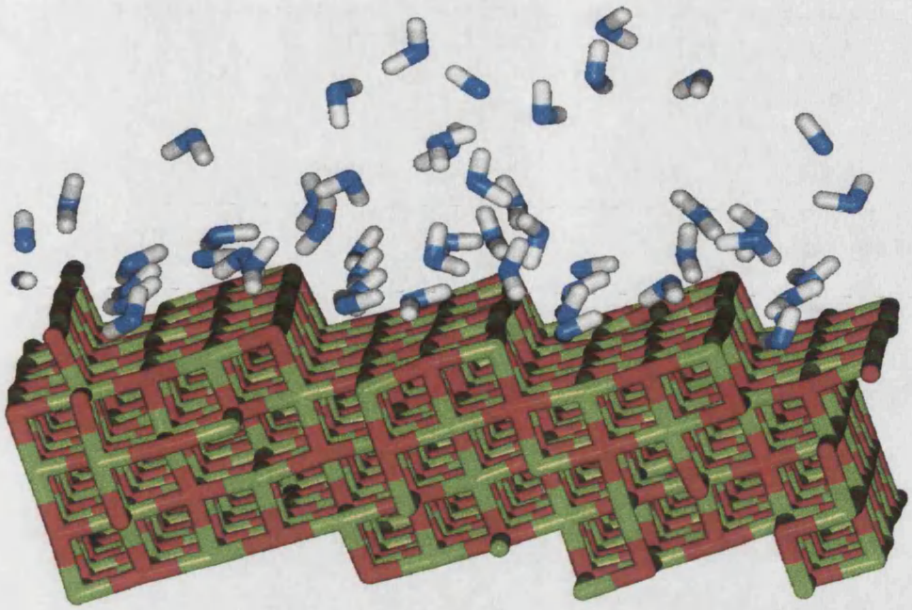

Figure 4.21 Snapshot of the NVT simulation at $\rho = 0.31$ gcm^{-3} and 300 K after 150 ps of the MgO {310} surface showing regular adsorption of the water molecules' oxygen atoms to the four-coordinated edge magnesium atoms and some five-coordinated magnesium atoms on the plane.

The MSD of the NPT simulation is plotted in figure 4.22 and the self-diffusion coefficient of the water molecules between the slabs is 6.1 x 10^{-9} m^2s^{-1} (*cf.* 1.15 x 10^{-9} m^2s^{-1} in pure water). To test whether the diffusion coefficient would decrease when increasing the gap between the MgO slabs, while increasing the number of water molecules to keep the initial density the same, we ran another simulation with a gap of 35 Å instead of 25 Å, but after 100 ps the diffusion coefficient at 5.7 x 10^{-9} m^2s^{-1} has not decreased significantly. In view of the above and figure 4.16 and the fact that in the slice of ρ3 of the {100} surface the diffusion coefficient had decreased with increasing simulation time it seems that the diffusion coefficient at a certain density is dependent on interactions between surface atoms and water molecules rather than the size of the gap between surfaces.

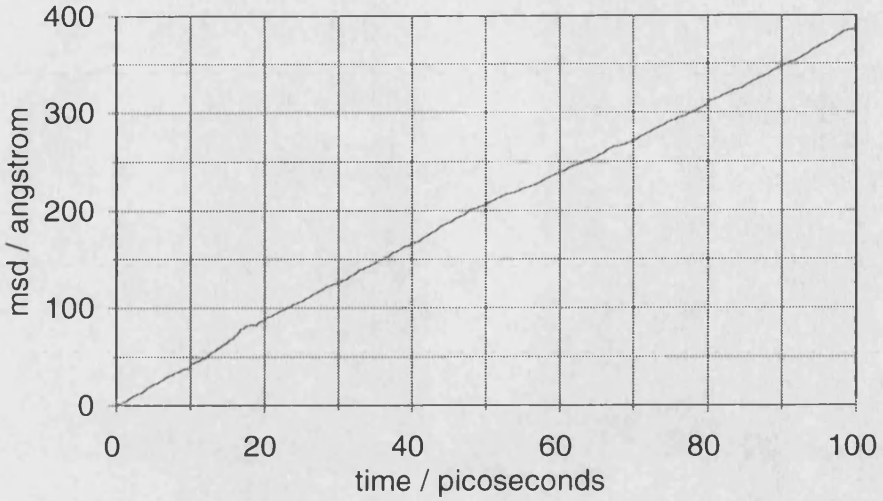

Figure 4.22 MSD of MD simulation at NPT of MgO {310} slab in water at 300K

Once again the density of the water between the {310} slabs is much lower than in the box of pure water at the same pressure (ρ = 1.3 gcm^{-3}) and as with the {100} slab we performed three more simulations at lower densities to investigate how the properties changed with density.

Type of Simulation	**<ρ> / gcm^{-3}**	**Water self-diffusion coefficient / 10^{-9} m^2s^{-1}**	**<E_{hydr}> /kJmol^{-1}**	**γ / Jm^{-2}**	**RDF / Å ($Mg\text{-}O_{water}$)**	**RDF / Å ($O_{lattice}$-H)**
NPT	0.93	6.1	+ 18.7	2.74	2.1	1.8
NVT	0.52	14.9	+ 4.6	1.68	2.1	1.8
NVT	0.39	20.8	- 2.9	1.47	2.1	1.8
NVT	0.31	15.4 16.7[1)] 15.4[2)]	- 15.1 - 13.2[1)] - 15.1[2)]	1.25 1.23[1)] 1.25[2)]	2.1	1.8

Table 4(XII) Data obtained from MD simulations of MgO {310} surface in water at 300K after 100 ps for NPT and 20 ps for NVT simulations (after [1)] 100 ps, [2)] 150 ps).

The self-diffusion coefficient of the three different simulation cells increases with decreasing density just like in the {100} simulations (table 4(XII)) and figure 4.23 shows the three plots. In addition, the diffusion coefficients do not increase smoothly from high to low density and again this may indicate that 20 picoseconds is not enough for the system to supply definitive data. From the {100} analogue we would expect the diffusion coefficient to decrease with increasing time. However, after running the box with density $\rho = 0.31$ gcm^{-3} up to 150 ps, the diffusion coefficient as well as the hydration and surface energies remain identical, indicating that in this case the system has come to a stable configuration.

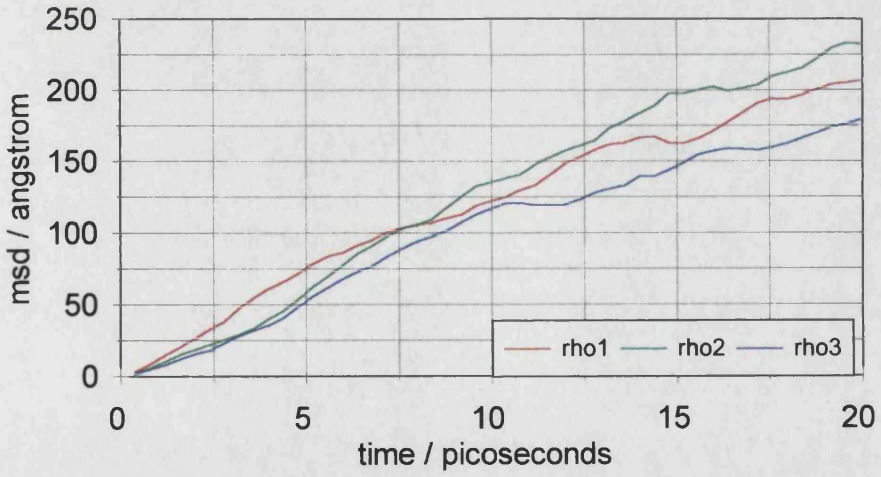

Figure 4.23 MSDs of NVT simulations of MgO {310} slab in water at 300K and the three different densities

The surface energies of the {310} slabs at lower water densities decrease with decreasing density coming more in line with the surface energies obtained from static

simulations (table 4(VII) 1.35 to 1.78 Jm^{-2}). The average hydration energies decrease progressively with decreasing density becoming negative and hence hydration of this surface becomes energetically favourable at low densities which again confirms that it is the interactions between adsorbed layer and water molecules in subsequent layers which is unfavourable.

4.9 Summary and Conclusion

We have used static simulations to model dissociative adsorption of water on the {100}, {111}, {310} and planar and micro-facetted {110} surfaces of CaO and MgO. The calculations are in accord with the available experimental data, *i.e.* they show that the low-coordinated sites represent the most energetically favourable sites for chemisorbed water.

In addition to dissociative adsorption we have extended our study to molecular adsorption of water onto five- and lower-coordinated surface sites modelled by the {100}, {310} and facetted {111} surfaces of MgO. Physisorption of water onto magnesium oxide surfaces is also energetically preferred at surfaces containing low-coordinated sites rather than the five-coordinated sites of the perfect {100} surface. However, coordination of the water molecules to hydroxylated surface ions at steps stabilises physisorption onto the five-coordinated surface ions and in fact some of the largest hydration energies occur for the physisorbed interactions on hydroxylated surfaces.

Specific predictions of the static simulations include:

The micro-facetted {110} and {111} surfaces are more stable than the planar surface, suggesting that these will be the surfaces observed experimentally.

The pure MgO {100} surface is generally not very amenable to dissociative adsorption unlike the pure CaO {100} surface. The MgO {100}, however, is amenable to physisorption of water onto the surface, although at full monolayer coverage it is only just energetically preferred.

There is a particularly stable surface reconstruction, especially for CaO, at a coverage of 75% on the chemisorbed {100} surface that is echoed in the case of molecular adsorption at low coverages (50-75%) due to the water molecules' intermolecular interactions.

Interactions between physisorbed water molecules may have a stabilising or destabilising effect depending on the degree of coverage and the geometry of the water molecules. However, the energy advantage of coordination between the water molecule's oxygen atom and a surface magnesium ion outweighs any disadvantages that the interactions between the water molecules may give.

Micro-facetted {110} surfaces energetically favour chemisorption at the low-coordinated edge positions at low partial coverages for both MgO and CaO, but at higher coverages the sites in the valley are preferred.

Chemisorption at the planar {111} surfaces of both MgO and CaO is very favourable, in agreement with Onishi *et al.* (1987) except that at high coverages the crystal becomes thermodynamically unstable and would rather form the {111} hydroxylated surface. Both chemisorption and physisorption is energetically favourable on the facetted {111} surface.

On the {310} surfaces two possible sites for chemisorption were compared, on the edge of the step and inside the step (valley site). The hydration energies of the four-coordinated edge sites are considerably more exothermic than their counterpart at the five-coordinated sites inside the step and dissociative adsorption of water will therefore preferentially take place at the low-coordinated atoms of the edge on top of the step. This adsorption behaviour is mirrored for physisorption on the four-coordinated edge sites. The physisorbed water molecules adsorb in the same position ready for hydroxylation. Hydroxylation of the edges encourages further physisorption of the five-coordinated surface sites.

From our study we can make some general predictions about the mode of dissociative adsorption, namely that there is a tendency at low coverages for the dissociatively adsorbed water to form dimers. Furthermore, in CaO the OH groups often tilt so as to form stronger hydrogen bonds on the surface. This does not occur for MgO, presumably due to a smaller lattice spacing in MgO.

Finally we used Molecular Dynamics simulations to model the adsorption of water onto the MgO {100} and {310} surfaces in a box of liquid water molecules which adds effects of both temperature and intermolecular interactions of the water molecules to the adsorption behaviour.

The average hydration energies for both the {100} and {310} surfaces show that in a liquid water environment adsorption is not energetically favourable. However, the positive hydration energy is lowered on decreasing the water density. At the lower density the {100} surface shows a tendency to become only partially covered by water molecules in agreement with the static simulations where the 50% and 75% partial coverages were most stable. The positive hydration energies appear to be caused by unfavourable interactions between the adsorbed water molecules and those in subsequent layers. In the case of the {310} surface the hydration energies do become negative indicating that at reduced water densities physisorption is energetically preferred as found in the static calculations of gaseous water adsorption. All four-coordinated adsorption sites are covered and some but not all five-coordinated surface sites as well, especially the ones neighbouring the edge sites. This agrees with the static simulations of physisorption on hydroxylated surfaces where the hydroxylated edge sites stabilised physisorption on the five-coordinated surface sites.

The self-diffusion coefficient of the water molecules between MgO slabs is considerably higher than the value in the simulation box of pure water and increases

with decreasing density, although it slows down with increasing simulation time indicating that once adsorption has taken place the water molecules remain immobile.

Further research on this subject should include MD simulations of the facetting of the {110} and {111} surfaces to investigate whether facetting occurs on heating and if the facetted surfaces are stable at high temperatures as found experimentally. As hydroxylation of the {310} surface was found to be energetically favourable MD simulations of physisorption onto hydroxylated surfaces is thus another extension of our static and MD simulations to date.

In addition, MD simulations of physisorption of water onto the CaO {100} would be interesting to compare with the MgO {100} surface and to investigate whether on this surface with a cation-oxygen distance of 2.4 Å, rather than 2.1 Å as in MgO, the water molecules would be able to adsorb in the same flat herringbone fashion but this time up to full monolayer coverage.

Another area worth investigating would be the solvation of magnesium and oxygen ions in liquid water and their possible aggregation into MgO crystals.

5 THE EFFECT OF CHEMI- AND PHYSISORPTION OF WATER ON THE SURFACE STRUCTURE AND MORPHOLOGY OF ALPHA-ALUMINA

5.1 Introduction

α–Al_2O_3 or corundum in its pure form, as sapphire when doped with Ti and Fe (Parker 1983a) and as ruby when doped with Cr, is widely used in high-pressure experiments and is also of technological importance in a range of industrial areas such as optics, electronics and ceramics applications (Boettger 1997). α–Alumina is widely used as a substrate for the growth of thin metal, semiconductor and insulator films in the microelectronics industry (Guo *et al.* 1992, Godin and LaFemina 1994). In view of its importance in these many areas it has been the subject of wide-ranging research, both experimental (Tsuchida *et al.* 1994, Kim *et al.* 1994, Tonejc *et al.* 1994, Shen and Lazor 1995, Guo *et al.* 1996, Kim *et al.* 1996, Boily and Fein 1996) and theoretical (Catlow *et al.* 1982, Mackrodt *et al.* 1987, Davies *et al.* 1989, Gale *et al.* 1992, Mackrodt 1992, Kenway 1993, 1994, Ching and Xu 1994, Jacobs and Kotomin 1994, Manassidis and Gillan 1994, Godin and LaFemina 1994, Streitz and Mintmire 1994, Gay and Rohl 1995, Kruse *et al.* 1996, Wilson *et al.* 1996a, Boettger 1997, Nygren *et al.* 1997).

Experimental studies have included the behaviour of α-alumina at high temperatures and pressures (Shen and Lazor 1995) in order to help understand processes in the Earth's interior, the properties of grain boundaries which control

ceramic behaviour (Kim *et al.* 1994) and catalytic activity as a function of specific surface area (Tsuchida *et al.* 1994). Recent experimental research has concentrated on adsorption of metals (Kim *et al.* 1996) and metal-organic molecules (Boily and Fein 1996) onto the corundum surfaces to study its possible use as an environmental remediation agent.

Early theoretical investigations of α-alumina were predominantly atomistic simulations of properties such as defect energies (Catlow *et al.* 1982), crystal morphology (Mackrodt *et al.* 1987) and impurity segregations (Davies *et al.* 1989), followed by computationally more expensive simulations such as stacking faults (Kenway 1993) and grain boundaries (Kenway 1994). Electronic structure calculations were initially mainly used to obtain interatomic potentials for atomistic simulations (Mackrodt and Stewart 1979, Gale *et al.* 1992) or to compare to and validate forcefield calculations (Mackrodt 1992). More recently *ab initio* techniques such as total energy calculations within the local density approximation have been used to calculate electronic and structural properties of corundum (Ching and Xu 1994) and elastic constants (Boettger 1997) while Hartree-Fock cluster calculations were used to model point defects (Jacobs and Kotomin (1994). Even so, first principles studies of surfaces (Manasidis and Gillan 1994, Godin and LaFemina 1994) and interfaces (Kruse *et al.* 1996) have mainly considered the (0001) basal plane.

One area which has received particular attention, both from experimental and theoretical groups, has been the adsorption of water onto α-alumina surfaces, for

instance the high-resolution electron-energy-loss spectroscopic (HREELS) studies of hydroxyl groups on the (0001) surface (Coustet and Jupille 1994, 1997), microcalorimetric measurements of the chemisorption of water as a function of temperature (Rossi *et al.* 1994) and embedded cluster calculations of the hydroxylation of the basal plane (Nygren *et al.* 1997).

The aim of the work described in this chapter is to investigate the effect of chemi- and physisorption of water on the surface structure and stability of four corundum surfaces and the resulting morphology. In addition to the {0001} basal plane, the surfaces studied are the $\{10\bar{1}1\}$, $\{11\bar{2}0\}$ and $\{22\bar{4}3\}$ surfaces, which are the principal faces observed in the experimental morphology (Dana 1958). In addition to the potential model of Lewis and Catlow (1985), whose potential parameters for MgO and CaO were used in chapter 4, we have modelled the same surfaces using an earlier potential model developed by Catlow *et al.* (1982) to investigate the sensitivity of the obtained hydration energies to different sets of potential parameters.

5.2 Potential Verification

We wished to simulate a hydrated aluminium oxide and an aluminium hydroxyl oxide to assess the suitability of our potential parameters to model hydrated structures. For this purpose we chose the structure of the hydrated alkali-free β-alumina $(Al_2O_3)_{11}.(H_2O)_2$ which was obtained and elucidated by Kato and Saalfeld (1977) to test the Al-H_2O interactions, and an aluminium oxide hydroxide AlO(OH) to test Al-OH and O-OH interactions (Busing and Levy 1958).

5.2.1 Hydrated β-Alumina $(Al_2O_3)_{11}.(H_2O)_2$

This hydrated alkali-free alumina, obtained by boiling β-alumina in concentrated H_2SO_4, has spacegroup P63/mmc with a = b = 5.600 Å, c = 22.702 Å, $\alpha = \beta = 90^0$ and $\gamma = 120^0$, which relaxed to a = b = 5.66 Å, c = 21.54 Å, $\alpha = 90^0$, $\beta = 92^0$ and $\gamma = 120^0$ using the Catlow *et al.* (1982) potential and to a = 5.72 Å, b = 5.66 Å, c = 21.20 Å, $\alpha = \beta = 90^0$ and $\gamma = 120^0$ using the Lewis and Catlow (1985) potential model. The crystal has a layered structure where each spinel type block is joined by a bridging oxygen and a water molecule to the next layer. Table 5(I) gives the experimental structure. The positions of bridging oxygen and water oxygens are only partially occupied where the ions are moving or oscillating between three sites but for the purpose of simulating the structure we placed those ions at the average of the three sites. The poor agreement for c is probably explained due to either there being more water molecules in the layer than detected experimentally (1.79 H_2O) or that we neglect thermal contributions which, because of weaker bonding between the layers, will be more affected by temperature.

$(Al_2O_3)_{11}.(H_2O)_2$			
spacegroup	P63/mmc		
a b c	5.60	5.60	22.70
$\alpha\ \beta\ \gamma$	90^0	90^0	120^0
Al	0.168	0.336	-0.106
	0.333	0.667	0.024
	0.333	0.667	0.173
	0.000	0.000	0.000
O lattice	0.157	0.314	0.049
	0.502	0.003	0.145
	0.333	0.667	-0.055
	0.000	0.000	0.140
O bridging	0.375	0.749	0.250
O water	0.647	0.295	0.250

Table 5(I) Experimental crystallographic structure of hydrated β-alumina (Kato and Saalfeld 1977)

The structure shown in figure 5.1a is the experimental structure although the hydrogen atoms belonging to the water molecule were not resolved by Kato and Saalfeld's (1977) x-ray diffraction experiment and have been added in such a way that they are pointing towards lattice oxygen atoms. Furthermore, the angle formed by the bridging oxygen and its two aluminium neighbours is not 180^0 as in pure β-alumina and as is shown in figure 5.1a. As mentioned above the bridging oxygen is at an average of three positions each with an Al-O-Al angle of 157.6^0.

$(Al_2O_3)_{11}.(H_2O)_2$			
	experimental	**Catlow *et al.* (1982)**	**Lewis & Catlow (1985)**
$r(AlO_{lattice})$ / Å	1.75 - 2.03	1.81 - 1.97	1.81 - 2.19
$r(AlO_{bridging})$ / Å	1.79	1.65	1.70 - 1.72
$r(AlO_{water})$ / Å	3.64	1.81 - 1.92	1.91 - 1.94
$r(O_{bridging}O_{water})$ / Å	2.65	4.00	2.87
$r(O_{lattice}$---H) / Å	-	1.72 - 1.92	1.71 - 1.80
$r(O_{water}H)$ / Å	-	0.97 - 0.99	0.98 - 0.99
angle $(AlO_{bridging}Al)$	157.6^0	$173.3 - 174.9^0$	131.8^0
angle $(O_{lattice}AlO_{lattice})$	$80.74 - 108.33^0$	$81.49 - 115.11^0$	$83.65 - 112.58^0$

Table 5(II) Calculated and experimental bond distances and angles in hydrated β-alumina

Both potential models simulated the hydrated β-alumina adequately although the Lewis and Catlow (1985) potential modelled the experimental distance between bridging oxygen and water oxygen atoms of 2.65 Å more accurately at 2.87 Å than the Catlow *et al.* (1982) potential where the water molecule moved away from the bridging oxygen to an oxygen-oxygen distance of 4.0 Å (table 5(II)). In neither minimum energy configuration is there evidence of hydrogen-bonding between the bridging oxygen and the water molecule's oxygen atom as suggested by Kato and Saalfeld (1977) although as stated they could not resolve the hydrogen positions. Hydrogen-bonding does occur in both simulated structures, but it is to lattice oxygens rather than the bridging oxygens. In the two simulated structures the water molecules' oxygen atoms move away from their initial site to form a bond to an aluminium ion in one block and then bridge the gap to form hydrogen bonds to lattice oxygens in the neighbouring block thus reinforcing the link made by the bridging oxygen. Figure 5.1b shows the minimum energy configuration of β-alumina obtained using the

potential parameters of Lewis and Catlow (1985). The simulated structure using the Catlow *et al.* (1982) potential model is visually very similar to that using the Lewis and Catlow (1985) potential and its salient points can be found in table 5(II).

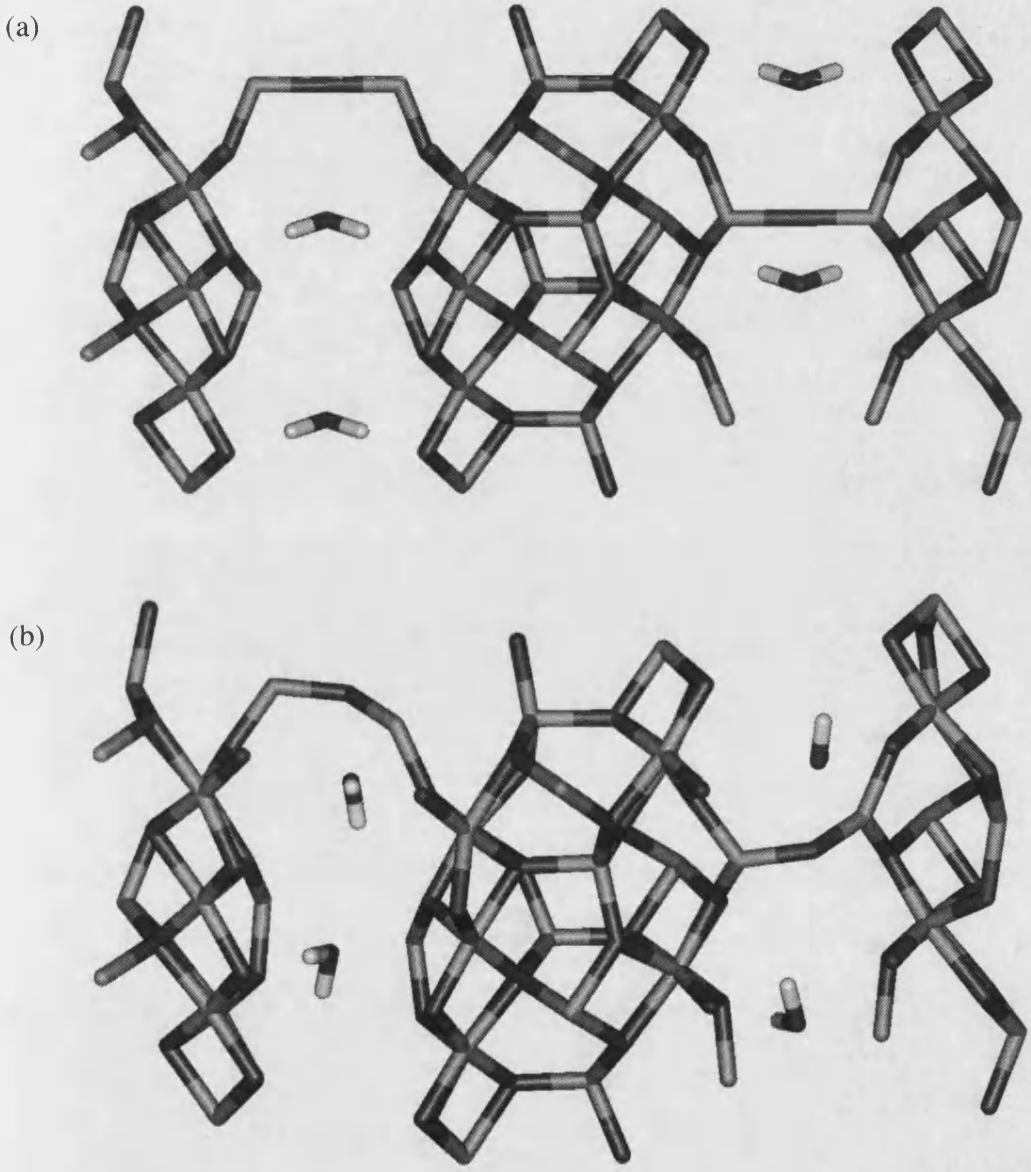

Figure 5.1 (a) Experimental and (b) calculated (Catlow and Lewis 1985) structure of hydrated β–alumina showing the average bridging angle of 180^0 in the experimental structure reduced to 132^0 in the calculated structure. The experimental hydrogens were not resolved. (O = dark grey, Al = pale grey, H = white)

5.2.2 Aluminium Oxide Hydroxide AlO(OH)

In the same way that simulating the structure of the hydrated β-alumina validated the use of our potential parameters we simulated the structure of diaspore AlO(OH) (Busing and Levy 1958) to test the interactions of the hydroxide potential parameters with the two alumina potential models. As stated in chapter 3, the potential parameters of the hydroxide ion used with the Catlow *et al.* (1982) potential model are those developed by Baram and Parker (1996) while those used with the Lewis and Catlow (1985) potential model were fitted by ourselves.

AlO(OH)									
	experimental			**Catlow *et al.* (1982)**			**Lewis & Catlow (1985)**		
space group	Pbnm			Pbnm			Pbnm		
a b c	4.4010	9.4210	2.8450	4.4362	9.1918	2.9752	4.4607	9.1110	2.9505
α β γ	90^0	90^0	90^0	90^0	90^0	90^0	90^0	90^0	90^0
Al	0.0451	0.8554	0.2500	0.0359	0.8436	0.2500	0.0517	0.8469	0.2500
$O_{lattice}$	0.7120	0.1989	0.2500	0.7677	0.2142	0.2500	0.7234	0.1994	0.2500
$O_{hydroxyl}$	0.1970	0.0532	0.2500	0.1797	0.0464	0.2500	0.1653	0.0531	0.2500
H	0.4095	0.0876	0.2500	0.4065	0.0620	0.2500	0.3916	0.0684	0.2500

Table 5(III) Experimental and simulated structural data of diaspore

Diaspore is an aluminium oxide hydroxide (AlOOH) with spacegroup Pbnm and a = 4.4010 Å, b = 9.4210 Å, c = 2.8450 Å and $\alpha = \beta = \gamma = 90^0$ (Busing and Levy 1958). Table 5(III) compares the experimental structure with the two simulated

structures. Both simulated structures have kept the experimental symmetry and give good agreement with the experimental structure although both are contracted in the b direction while being expanded in the c direction.

As expected from table 5(III) bond lengths and angles in the simulated structures closely resemble those of the experimental structure (table 5(IV)).

AlO(OH)			
	experimental	**Catlow *et al.* (1982)**	**Lewis & Catlow (1985)**
$r(AlO_{lattice})$ / Å	1.80	1.82, 1.83	1.85, 1.86
$r(AlO_{hydroxyl})$ / Å	1.97, 2.04	1.95, 1.99	1.98
$r(O_{hydroxyl}H)$ / Å	1.02	1.02	0.99
$r(O_{lattice}\text{---}H)$ / Å	2.13	1.90	1.70
angle ($Al\text{-}O_{lattice}\text{-}Al$)	111.10, 123.85	107.18, 122.61	100.40, 124.80
angle ($Al\text{-}O_{hydroxyl}\text{-}Al$)	108.52	108.42	103.19

Table 5(IV) Calculated and experimental bond distances and angles in diaspore

In view of the adequate agreement between the experimental and simulated hydrated β-alumina and aluminium oxide hydroxide structures we have confidence in both potentials to model the dissociative and molecular adsorption of water onto the α–alumina surfaces. The only feature which is cause for concern is the interaction between a fully coordinated aluminium and a water molecule which we have to be cautious of when we are applying this model to alumina surfaces.

5.3 Method

We modelled the hydration of a range of α–alumina surfaces which were hydroxylated and also hydrated by physisorption to full monolayer coverage as with MgO and CaO (chapter 4). In case of chemisorption of water a dissociated water molecule was adsorbed on every surface cation-oxygen pair and in effect every surface oxygen was replaced by two hydroxyl groups, as described in chapter 4.2.

The initial sites chosen for physisorption of water onto the surfaces were above surface oxygen ions and aluminium ions. Again, a range of adsorption modes of the water molecules were studied and the energetically most favourable configurations selected. When adsorbing onto the aluminium sites, the oxygen atom of the water molecule was initially positioned at the aluminium-oxygen distance of 2.0 Å, after which the surface was allowed to relax and find the minimum energy configuration. Adsorption on the surface oxygen sites was modelled by positioning one of the water molecule's hydrogen atoms at a hydrogen-bond distance of 1.8 Å [exp. 1.76-1.95 Å in ice (Kamb 1972)].

	Lattice energy / kJmol^{-1} Catlow *et al.* (1982)	**Lattice energy / kJmol^{-1} Lewis and Catlow (1985)**	**Enthalpy of formation / kJmol^{-1}**
$Al_2O_{3(s)}$	-15376.02	-15498.27	-1669.79
$Al(OH)_{3(s)}$	- 6648.85	- 6517.68	-1272.77
$H_2O_{(g)}$	-	-	-241.82

Table 5(V) Lattice energies and enthalpies of formation

The surface energies were again calculated with respect to liquid water while the hydration energies were calculated with respect to gaseous water as described in chapter 4.2. We used the heat of formation of gibbsite $Al(OH)_3$ (Tonejc *et al.* 1994) in a Born-Haber type cycle as before and the energies given in table 5(V) (Weast and Astle 1981) to evaluate the energy of reaction:

$$H_2O_{(g)} + O^{2-}_{(g)} \rightarrow 2OH^-_{(g)} \qquad (5.1)$$

The energy of dissociation for reaction (5.1) necessary to calculate the hydroxylation energies for α–alumina was found to be -743.7 $kJmol^{-1}$ for the Catlow *et al.* (1982) potential and -871.9 $kJmol^{-1}$ for the Lewis and Catlow (1985) potential.

The energy for a gaseous water molecule to be used in the calculation of molecular adsorption energies is the same for both potential models, as it is independent from the lattice energies, and was calculated to be -878.0 $kJmol^{-1}$.

5.4 Pure Surfaces

α–Alumina has a trigonal structure with spacegroup $R\bar{3}c$. The oxygen ions are approximately in the arrangement of hexagonal close packing with the cations between the oxygen layers octahedrally coordinated to six oxygens. We started with the hexagonal unit cell of a = 4.7590 Å, b = 4.7590 Å and c = 12.9910 Å, $\alpha = \beta = 90^0$ and $\gamma = 120^0$ (Deer *et al.* 1992). The bulk crystal was then allowed to relax to a minimum energy configuration giving a = 4.7805 Å, b = 4.7805 Å and c = 12.5607

Å, $\alpha = \beta = 90^0$ and $\gamma = 120^0$ for the Catlow *et al* (1982) and a = 4.8177 Å, b = 4.8177 Å and c = 12.6805 Å, $\alpha = \beta = 90^0$ and $\gamma = 120^0$ for the Lewis and Catlow (1985) potential models. Figure 5.2 is a top view of the basal plane showing the hexagonal unit cell and the arrangement of aluminium and oxygen atoms.

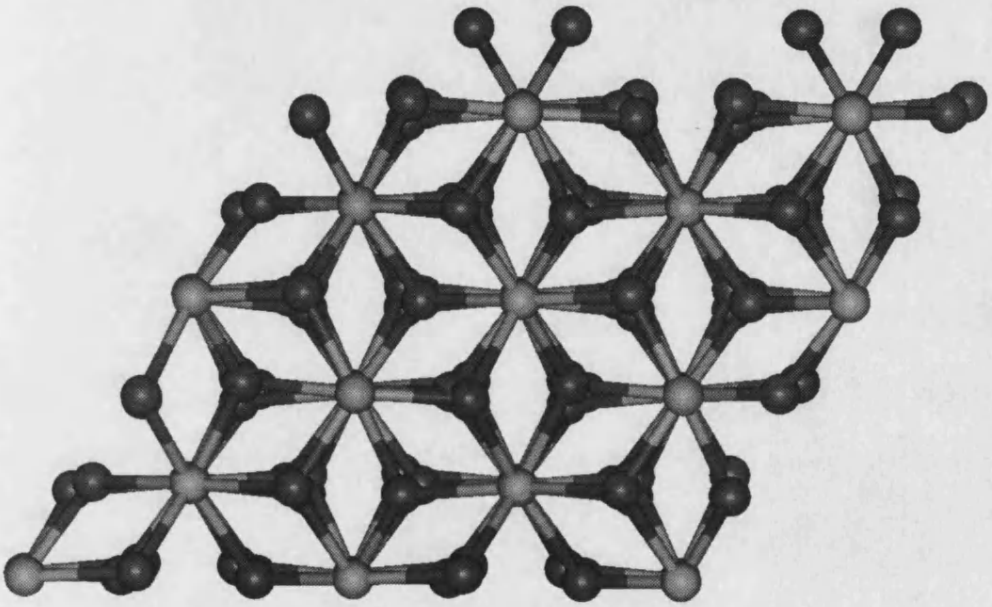

Figure 5.2 Top view of the {0001} surface of α-alumina (Catlow *et al.* 1982) (O = dark grey, Al = pale grey)

5.4.1 {0001} Surface

The basal plane has been the subject of numerous computational studies (Mackrodt *et al.* 1987, Mackrodt 1992, Godin and LaFemina 1994, Manassidis and Gillan 1994, Gay and Rohl 1995, Kruse *et al.* 1996). Two terminations are possible, one with aluminium atoms which is a non-dipolar surface while the oxygen terminated surface is dipolar and hence in order to simulate this surface we needed to

remove the dipole by moving half the oxygen ions to the bottom of the unit cell as described in chapter 2. The non-dipolar aluminium terminated surface is the most stable of the two planes and substantial relaxation of this surface takes place with respect to the bulk structure below. The stacking sequence of the planes is as shown in figure 5.3. Both potential models predict that the surface aluminium ions relax into the surface by approximately 0.5 Å, while the oxygen ions in the second layer move up slightly. The aluminium ions in the third layer move down again by about 0.1 Å but the next layer of aluminium ions and layers further down are at their bulk positions. The main changes in the surface structure are the first three cation planes, the first moving into the surface and the second and third moving closer together. This is in qualitative agreement with simulations by Mackrodt *et al.* (1987) using the potential of Mackrodt and Stewart (1979) who found a relaxation into the surface by the first cation plane of 59% while the two next aluminium planes decreased their interplanar distance by 49%. In addition, the same effect has been observed by Manassidis and Gillan (1994) using first-principles calculations based on DFT and Godin and LaFemina (1994) using a tight-binding model.

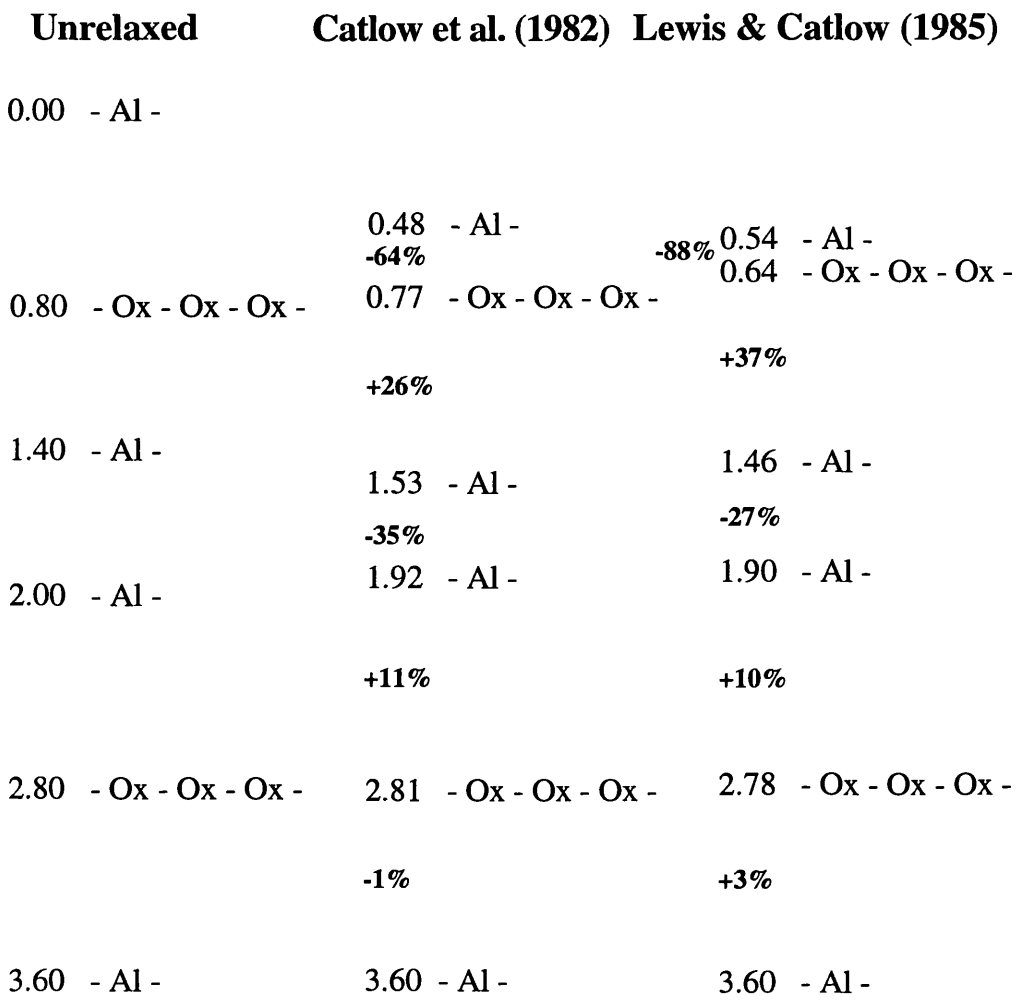

Figure 5.3 Stacking sequence of unrelaxed and relaxed aluminium terminated {0001} surface

The surface and attachment energies of the unhydrated surfaces are given in table 5(VI). Clearly the relaxation of the aluminium terminated surface gave rise to a large drop in the surface energy and hence an increase in stability of the surface. As expected the surface energy of the dipolar oxygen terminated surface, although lowered considerably through relaxation, is much larger than the aluminium termination and we would therefore not expect to see the oxygen terminated surface in unhydrated form. The attachment energies reflect the relative unrelaxed surface

energies in that the aluminium surface has a much lower attachment energy than the oxygen surface.

It is clear that on comparing the data for the two potential models the surface energies given by the Catlow *et al.* (1982) potential model are always higher than those by the Lewis and Catlow (1985) potential, both in unrelaxed and relaxed configuration. The attachment energies given by the Catlow *et al.* (1982) potential, however, are lower for the {0001} oxygen surface but higher or very similar ($\{22\bar{4}3\}$ surface) for the other surfaces.

Surface and Attachment energies of unhydrated α-Alumina						
	Catlow et al. (1982)			**Lewis and Catlow (1985)**		
Surface	$\gamma_{unrelaxed}$ / Jm^{-2}	$\gamma_{relaxed}$ / Jm^{-2}	E_{attach} / $kJmol^{-1}$	$\gamma_{unrelaxed}$ / Jm^{-2}	$\gamma_{relaxed}$ / Jm^{-2}	E_{attach} / $kJmol^{-1}$
{0001}Al	6.39	3.16	- 877.2	6.03	2.42	- 838.2
{0001}O	14.45	4.68	-2400.3	10.06	3.83	-2716.2
$\{10\bar{1}1\}$O	6.13	3.88	- 889.4	5.90	3.19	- 872.8
$\{11\bar{2}0\}$Al	13.83	5.20	-1562.9	13.54	4.20	-1556.8
$\{11\bar{2}0\}$O	4.97	3.15	- 493.4	4.83	2.68	- 487.8
$\{22\bar{4}3\}$Al	16.52	4.22	-5273.4	16.21	3.64	-5269.8
$\{22\bar{4}3\}$O	8.13	3.63	-1860.7	8.04	3.49	-1865.8

Table 5(VI) Comparison of surface and attachment energies of the unhydrated surfaces by both potential models.

Although higher, the surface energies obtained by the Lewis and Catlow potential model are closer to those obtained by Mackrodt *et al.* (1987) (γ = 2.03 Jm^{-2} and 2.52 Jm^{-2} for the relaxed {0001} and $\{10\bar{1}1\}$ surfaces respectively) and Streitz and Mintmire (1994) (γ = 2.67 Jm^{-2}, 2.13 Jm^{-2} and 1.81 Jm^{-2} for the relaxed {0001},

$\{10\bar{1}1\}$ and $\{11\bar{2}0\}$ surfaces respectively) than the surface energies obtained by the Catlow *et al.* (1982) potential model.

5.4.2 $\{10\bar{1}1\}$, $\{11\bar{2}0\}$ and $\{22\bar{4}3\}$ Surfaces

The $\{10\bar{1}1\}$ surface has only one termination which is non-dipolar and has oxygens in the topmost layer. The $\{11\bar{2}0\}$ and $\{22\bar{4}3\}$ surfaces each have two terminations which, apart from the aluminium terminated $\{11\bar{2}0\}$ plane are all non-dipolar. The oxygen-terminated $\{11\bar{2}0\}$ surface does not show as much relaxation as the other surfaces whose surface energies all decrease considerably on energy minimisation.

5.5 Hydroxylated Surfaces

The different surfaces were hydroxylated as discussed in section 5.3 and the resulting surface energies and energies of hydroxylation are collected in table 5(VII).

Surface and Hydration energies of hydroxylated α-Alumina				
Surface	Catlow *et al.* (1982)		Lewis and Catlow (1985)	
	γ_{hydrox} / Jm^{-2}	E_{hydrox} / $kJmol^{-1}$	γ_{hydrox} / Jm^{-2}	E_{hydrox} / $kJmol^{-1}$
{0001}Al	1.84	-203.2	1.75	-125.5
{0001}O	0.54	-374.2	0.63	-220.7
$\{10\bar{1}1\}$O	0.76	-243.4	0.47	-220.7
$\{11\bar{2}0\}$Al	2.42	-335.9	1.09	-375.6
$\{11\bar{2}0\}$O	1.63	-151.2	0.43	-204.1
$\{22\bar{4}3\}$Al	2.68	-381.4	2.90	-371.0
$\{22\bar{4}3\}$O	1.88	-299.7	1.81	-293.2

Table 5(VII) Comparison of surface and hydration energies of hydroxylated surfaces

It can be seen from table 5(VII) that the surface energies of the hydroxylated surfaces of α-alumina with the exception of the $\{11\bar{2}0\}$ surface are much more similar for the two potential models than the pure surface energies.

5.5.1 {0001} Surface

Both the aluminium and oxygen terminated {0001} surfaces have been stabilised by hydroxylation. However, the relative stabilities of the two planes have reversed, the oxygen terminated surface which in unhydrated form is less stable than the aluminium plane having lowered its surface energy considerably. The reason for this is similar to the hydroxylation of the dipolar {111} surfaces of MgO and CaO described in chapter 4. In order to remove the dipole, half the surface oxygens were moved to the bottom of the unit cell, leaving vacancies where the hydroxyl groups can adsorb. The resulting surface has a full layer of oxygens with a smooth layer of hydrogen atoms on top (fig. 5.4). The hydrogen atoms of the hydroxyl groups adsorbed in the oxygen vacancies slightly tilt towards the lattice oxygen atoms by 24.7^0 away from the normal to the surface while the hydrogen atoms adsorbed to the lattice oxygens equally tilt towards the hydroxyl oxygen atoms. However, at 2.3 Å the O--H distance is too large for hydrogen bonding. As expected the hydration energy (table 5(VII)) of the hydroxylated oxygen plane is large.

(a)

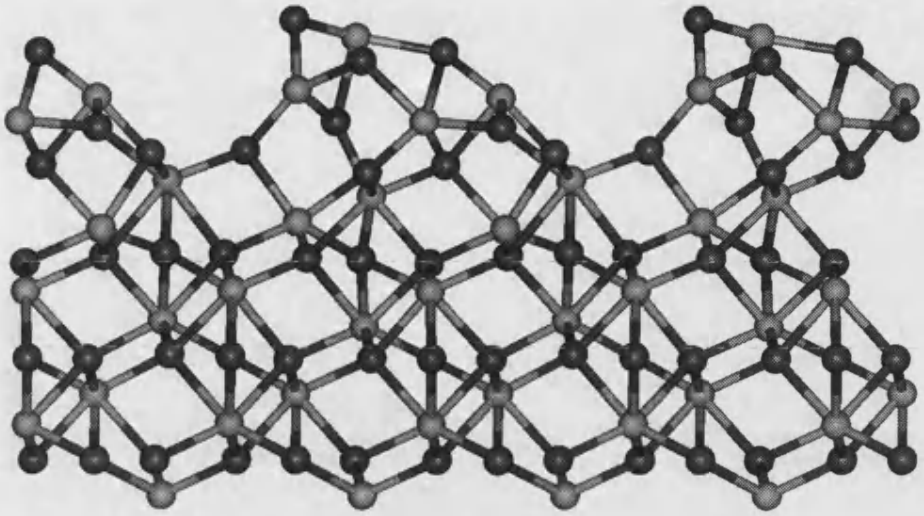

(b)

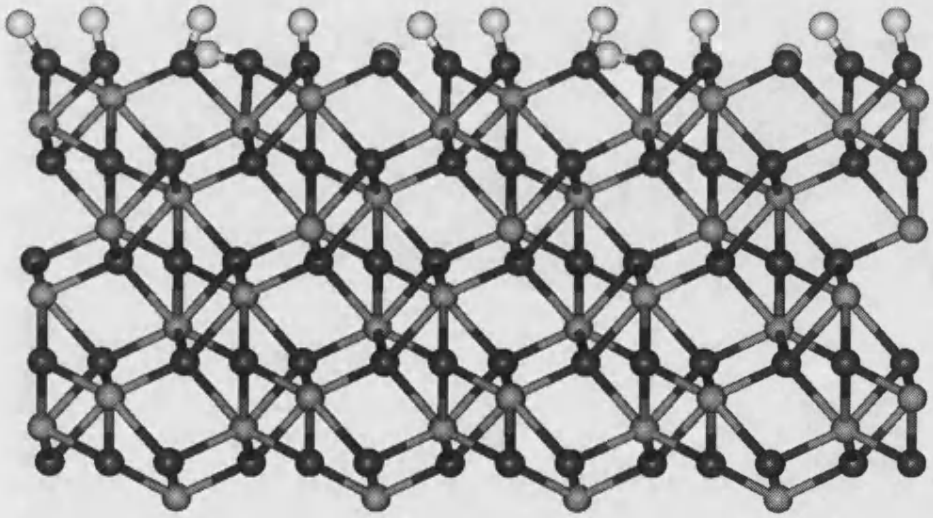

Figure 5.4 (a) Half vacant unhydrated oxygen terminated {0001} surface and (b) after hydroxylation (Catlow *et al.* 1982) (O = dark grey, Al = pale grey, H = white)

Similar tilting of the hydrogen atoms to the oxygen atoms takes place on the aluminium plane, but again the O--H distance at 2.18-2.27 Å is beyond the usual hydrogen bonding distance.

5.5.2 $\{10\bar{1}1\}$ Surface

The hydration energies for the hydroxylated $\{10\bar{1}1\}$ surfaces obtained by the two potentials are very similar and so is the pattern of adsorption on both surfaces. There are two different hydroxyl groups, one of which becomes bonded to two aluminium atoms while the hydrogen atoms form a pattern of hydrogen bonds between both hydroxyl and lattice oxygens at distances of 1.87 to 2.34 Å. It is probably this strong bonding of the hydroxyl group to the aluminiums and the network of hydrogen bonding which stabilises this surface so much relative to the other surfaces.

5.5.3 $\{11\bar{2}0\}$ Surface

The surface energies of the $\{11\bar{2}0\}$ planes obtained with the different potential models are very different. The Lewis and Catlow (1985) potential is much lower as was the case for the unhydrated surfaces. Both planes are stabilised considerably by hydroxylation of the surface. On the dipolar aluminium terminated plane by the Catlow *et al.* (1982) potential, one hydroxyl group tilts by 21.5^0 from the surface normal to bond to an aluminium at 1.72 Å while the other hydroxyl oxygen becomes bonded to two aluminiums at 1.76 and 2.10 Å. The hydrogen atoms lie flat to hydrogen-bond to two oxygen atoms at 1.89 and 2.25 Å. On the aluminium plane by the Lewis and Catlow (1985) potential the hydrogens behave identical with hydrogen bonds of 1.8 and 2.0 Å. However, on this plane both hydroxyl groups tilt towards aluminium atoms but at distances of 2.7-3.2 Å do not form any further bonds.

There is also a difference in adsorption pattern between the two oxygen terminated surfaces. On the plane obtained using the Catlow *et al.* (1982) potential, the hydroxyl groups are virtually normal to the surface with hydrogen bonds formed to the lattice oxygens between 1.81 and 2.1 Å, while on the Lewis and Catlow (1985) plane (fig. 5.5) all hydroxyl groups are bonded by their oxygen atoms to two aluminium atoms while their hydrogen atoms have tilted towards the surface giving a smooth plane. The relaxation to a flat surface may explain why the surface from the Lewis and Catlow (1985) potential is very stable with the lowest surface energy of the hydroxylated surfaces (0.43 Jm^{-2}).

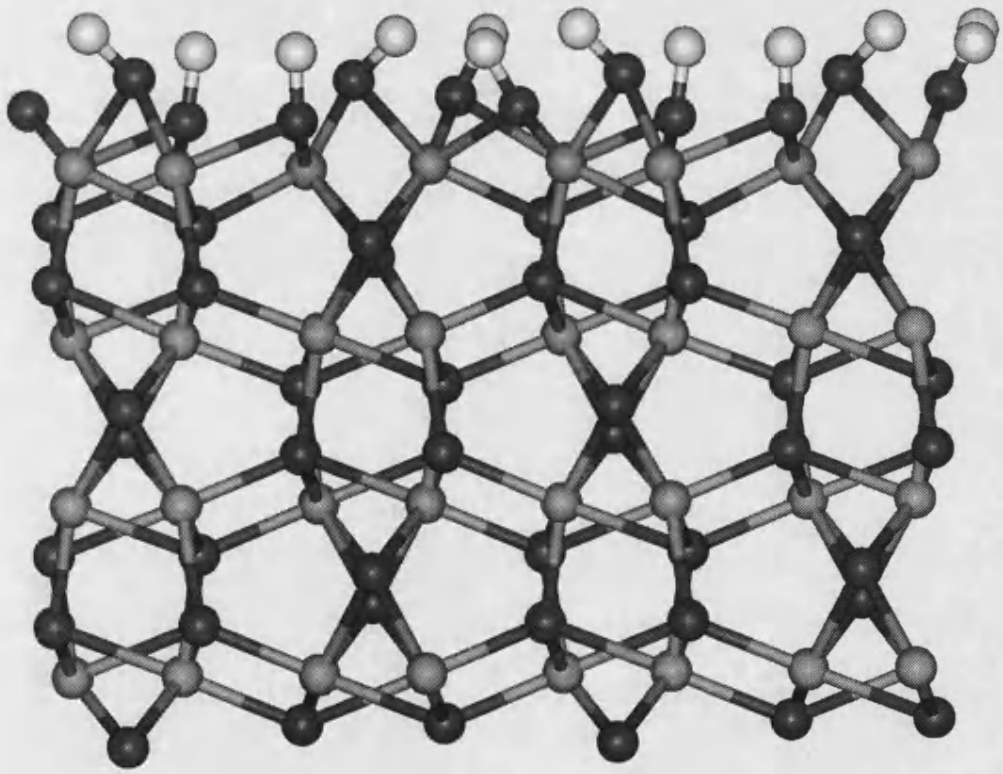

Figure 5.5 Hydroxylated oxygen terminated $\{11\bar{2}0\}$ surface (Lewis and Catlow 1985) (O = dark grey, Al = pale grey, H = white)

5.5.4 $\{22\bar{4}3\}$ Surface

The hydroxylated $\{22\bar{4}3\}$ surfaces have almost identical surface and hydration energies for the two potential models and as expected the surface configurations are very similar. On the aluminium terminated surface the oxygen atom of the hydroxyl group relaxed so that the oxygen bonds to two aluminium atoms, while the two hydrogen atoms form a network of hydrogen-bonds to lattice oxygen atoms. Similarly, some of the hydroxyl groups on the oxygen terminated surface form bonds to two aluminium atoms, while the hydrogen atoms form a network of hydrogen-bonds to lattice oxygens of between 2.1 and 2.4 Å.

5.6 Effect of physisorption of water

We now consider physisorption of water on α–alumina. The surface and hydration energies of the surfaces covered with physisorbed water are given in table 5(VIII). All the surfaces considered are stabilised with respect to the unhydrated surfaces and the hydration energies fall in a narrow range of approximately -120 to -180 kJmol^{-1}. The results for the two potential models are qualitatively similar for the different surfaces.

Surface and hydration energies of physisorbed α-Alumina surfaces				
Surface	Catlow *et al.* (1982)		Lewis & Catlow (1985)	
	γ_{phys} / Jm^{-2}	E_{phys} / $kJmol^{-1}$	γ_{phys} / Jm^{-2}	E_{phys} / $kJmol^{-1}$
{0001}Al	2.24	-153.4	1.67	-133.1
{0001}O	2.90	-184.7	2.69	-135.1
$\{10\bar{1}1\}$O	1.40	-200.4	1.30	-165.0
$\{11\bar{2}0\}$Al	4.30	-137.2	3.16	-153.4
$\{11\bar{2}0\}$O	1.75	-140.9	1.51	-126.4
$\{22\bar{4}3\}$Al	3.82	-130.3	2.89	-153.4
$\{22\bar{4}3\}$O	3.08	-123.2	2.56	-180.4

Table 5(VIII) Comparison of surface and hydration energies of surfaces with physisorbed water molecules.

5.6.1 {0001} Surface

In contrast to the hydroxylated {0001} surfaces where the hydroxyl groups adsorbed smoothly into the oxygen vacancies on the oxygen terminated plane, leading to an especially stable surface, when water molecules are physisorbed onto the oxygen plane they do not fit as easily into the vacant sites and hence the surface, although stabilised has a higher surface energy than both its aluminium terminated counterpart and the hydroxylated oxygen plane. The water molecules' oxygen atoms are coordinated to aluminium atoms at 1.78-1.93 Å for the Catlow *et al.* (1982) potential and 1.92 - 2.36 Å for the Lewis and Catlow (1985) potential model. There is an extensive network of hydrogen-bonding both to lattice oxygens (1.56 to 2.4 Å) and between the water molecules themselves (1.78 - 1.93 Å).

The water molecules on the aluminium terminated surface adsorb in a flat fashion (fig. 5.6), not unlike the water molecules physisorbed on the MgO {100} surface in the MD simulations described in chapter 4. The water molecules' oxygen atoms bond to aluminiums at about 1.85 Å while the hydrogens form hydrogen bonds to the lattice oxygen atoms of 1.91 to 2.28 Å. All bond distances are somewhat larger for the Lewis and Catlow (1985) potential than for the Catlow *et al.* (1982) potential model.

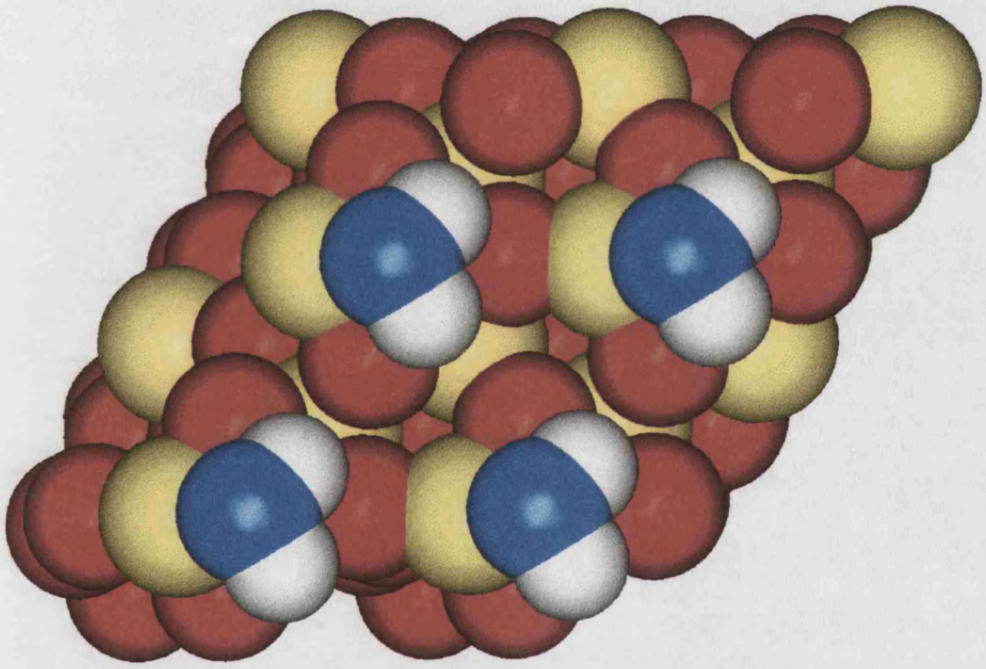

Figure 5.6 Aluminium terminated {0001} surface with physisorbed water molecules, obtained using the Lewis and Catlow (1985) potential. (O = red, Al = yellow, O_{water} = blue, H = white)

5.6.2 $\{10\bar{1}1\}$ Surface

The surface energies obtained by the two potentials for the $\{10\bar{1}1\}$ surface are virtually identical although the Catlow *et al.* (1982) potential gives the larger energy of hydration. As on the {0001} surface the water molecules adsorb by their oxygen atom to surface aluminiums (1.82-2.06 Å) and form hydrogen-bonds to lattice oxygen atoms (1.60-1.75 Å) although there is no real hydrogen-bonding between the water molecules themselves.

5.6.3 $\{11\bar{2}0\}$ Surface

Again, both potentials give similar stabilisations due to physisorption with comparable hydration energies. On the aluminium terminated surface, the water molecules adsorb to the surface aluminiums (Al-O = 1.83-2.06 Å) while the hydrogens form hydrogen-bonds to lattice oxygens (1.64-2.16 Å) but there are no noticeable intermolecular interactions between the water molecules.

The adsorption pattern on the oxygen terminated surfaces is similar to the aluminium planes. Rather than adsorb to the surface oxygen through a hydrogen-bond, the water molecules turn to coordinate their oxygen atoms to aluminium atoms (1.96-2.10 Å) while also hydrogen-bonding to both lattice oxygen atoms (1.62 Å) and at a longer distance (2.17 Å) to other water molecules.

5.6.4 $\{22\bar{4}3\}$ Surface

The molecular adsorption on the aluminium terminated surfaces shows as before coordination of the water molecules' oxygen atoms to aluminium atoms (1.85-1.92 Å) with some hydrogen bonding to lattice oxygen atoms (1.65 Å) in the structure due to the Catlow *et al.* (1982) potential but none on the Lewis and Catlow (1985) surface.

The adsorption on the oxygen planes is similar for the two potential models. The physisorbed water molecules lie flat on the surface in the same way as on the aluminium {0001} surface. The water molecules' oxygen atoms are coordinated to aluminium atoms (1.87-1.96 Å) and hydrogen-bonding occurs to lattice oxygen atoms (1.66-2.32 Å). In addition, on the Lewis and Catlow (1985) plane only, coordination to other water molecules occurs (2.4 Å). The stabilisation due to physisorption is somewhat larger for the Lewis and Catlow (1985) potential and so are the hydration energies. Interestingly, the hydration energy for the oxygen terminated plane is much higher than the aluminium plane in the Lewis and Catlow (1985) potential but is virtually identical for the Catlow *et al.* (1982) potential model. This may be due to the absence of intermolecular hydrogen-bonding on the Catlow *et al.* (1982) oxygen plane and/or the presence of hydrogen-bonding on the aluminium plane for the Catlow *et al.* (1982) but not for the Lewis and Catlow (1985) potential model.

5.7 Discussion

5.7.1 Surface Energies

The surface energies obtained using the two potentials are very different for the pure surfaces. The unrelaxed surface energies of the pure surfaces are much more similar than after relaxation which indicates that it is the surface relaxation which is the main factor determining the eventual surface energy. However, the surface energies obtained by the two potential models are in much better agreement when the surfaces are hydrated. Whether hydrated by physisorption or hydroxylated the surface relaxation is mainly due to rotation and relaxation of the water species, which leaves the underlying Al_2O_3 surface as bulk-terminated. Hence the two potentials give similar surface energies and hydration energies.

Although the relaxed surface energies of the unhydrated surfaces by the Lewis and Catlow (1985) potential model are much lower than those obtained by the Catlow *et al.* (1982) potential, they are still rather high compared to those obtained by other atomistic simulations, e.g. Mackrodt *et al.* (1987), who obtained a surface energy of γ = 2.03 Jm^{-2} for the aluminium basal plane (0001), and electronic structure calculations, for example Manassidis and Gillan (1994) who used DFT calculations which gave a surface energy of γ = 1.76 Jm^{-2} or Mackrodt (1992) who used a Hartree Fock method to obtain a surface energy of γ = 2.00 Jm^{-2} for the same surface. Streitz and Mintmire (1994), however, used an atomistic simulation method including variable charge transfer between cations and anions which gave a relaxed surface

energy of $\gamma = 2.67\ Jm^{-2}$ for the aluminium basal plane which is in between the values obtained by the two potentials used in this work and in line with the Lewis and Catlow (1985) potential.

5.7.2 Morphology

Figure 5.7 shows two frequently occurring experimental morphologies expressing the surfaces investigated in this chapter. The two morphologies are really two extremes which interchange when the $\{10\bar{1}1\}$ plane is (un)stabilised with respect to the $\{11\bar{2}0\}$ face.

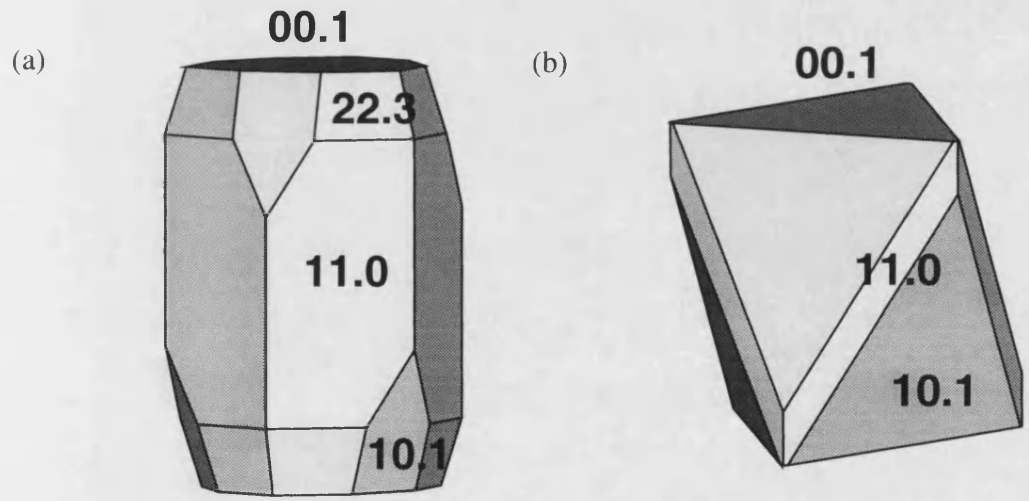

Figure 5.7 (a) and (b) Two experimental morphologies of α-alumina (Dana 1958)

The morphologies of the unhydrated corundum crystal are shown in figure 5.8 Comparing those with the experimental morphologies (fig. 5.7) it is clear that the equilibrium morphology obtained using the Lewis and Catlow (1985) potential model (fig. 5.8b) closely resembles the experimental morphology (fig. 5.7(a)). The Catlow

et al. (1982) potential gives an equilibrium morphology (fig. 5.8a) where the $\{22\bar{4}3\}$ face is not expressed, as in fig. 5.7(b). This equilibrium morphology seems to be somewhere midway between the two experimental morphologies. The growth morphology obtained from the attachment energies in table 6(VI) (fig. 5.8c), is identical for both potential models and does not resemble either experimental morphology very closely, the $\{11\bar{2}0\}$ surface being too stable.

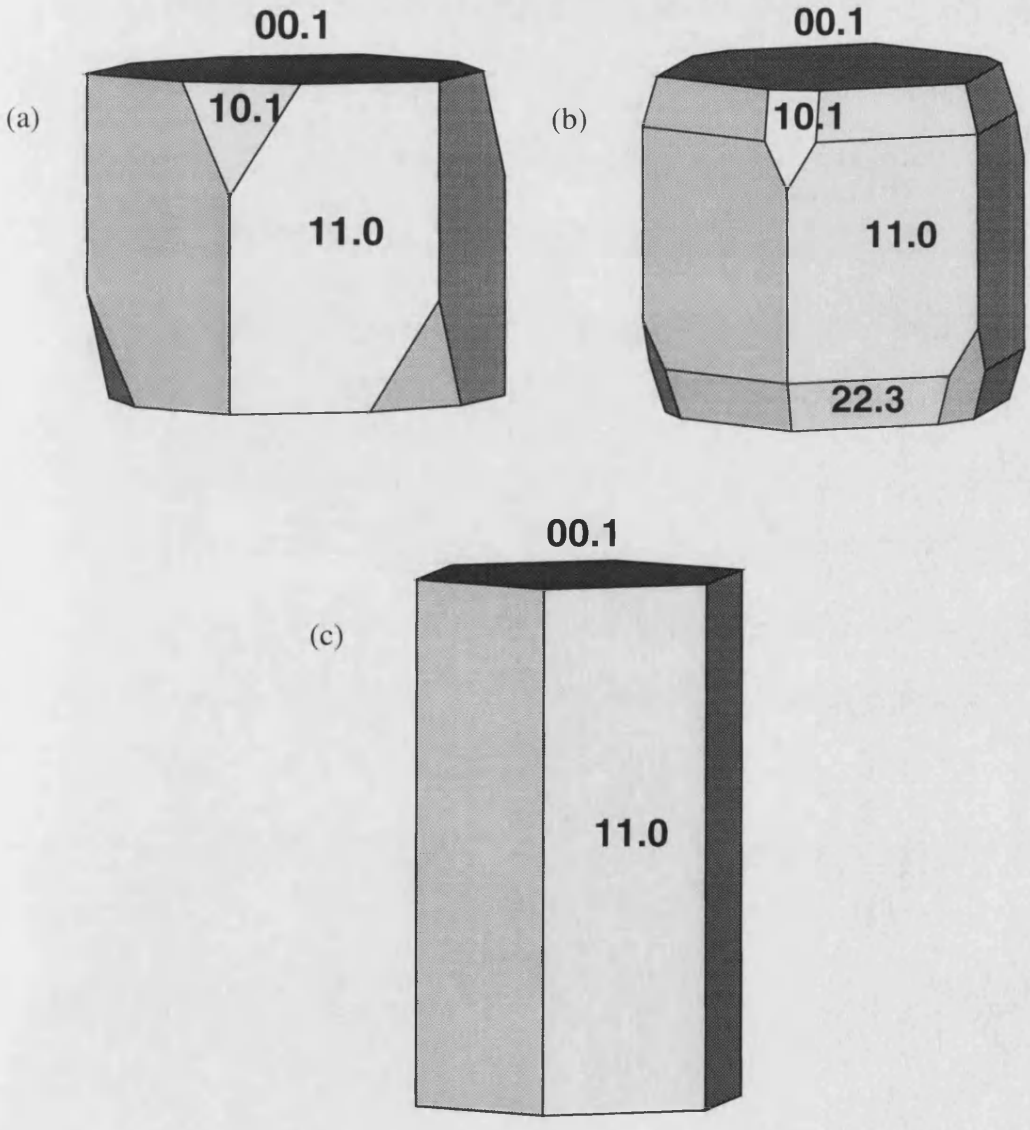

Figure 5.8 Calculated equilibrium morphologies of unhydrated crystal using (a) Catlow *et al.* (1982) and (b) Lewis and Catlow (1985) potential models, (c) growth morphology from attachment energies of both potentials

The morphologies of the hydroxylated surfaces (fig. 5.9) again show the Lewis and Catlow (1985) potential to give the morphology more closely resembling the experimental morphology, in this case somewhere between the two experimental morphologies. The morphology obtained by the Catlow *et al.* (1982) potential model is not unlike the experimental morphology in 5.7(b) but the $\{10\bar{1}1\}$ is too stable causing the $\{11\bar{2}0\}$ face to be removed from the morphology.

(a) (b)

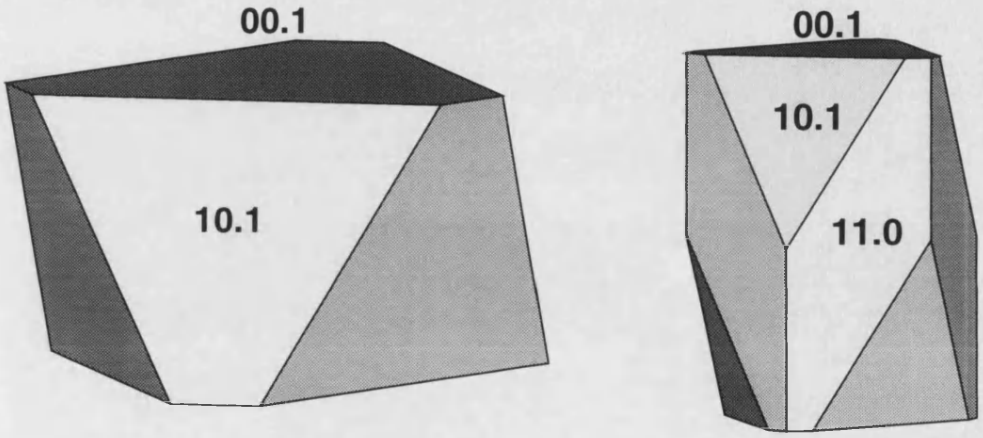

Figure 5.9 Morphologies of crystal with hydroxylated surfaces calculated from (a) Catlow *et al.* (1982) and (b) Lewis and Catlow (1985) potential models

Finally, figure 5.10 shows the morphologies obtained by both potentials from the crystal with molecularly adsorbed water on the surfaces. Clearly the morphology by the Lewis and Catlow (1985) potential is in better agreement with the experimental morphology of figure 5.7(b). Although the morphology obtained by the Catlow *et al.* (1982) potential model also resembles figure 5.7(b), as with the hydroxylated morphology it does not express the $\{11\bar{2}0\}$ face.

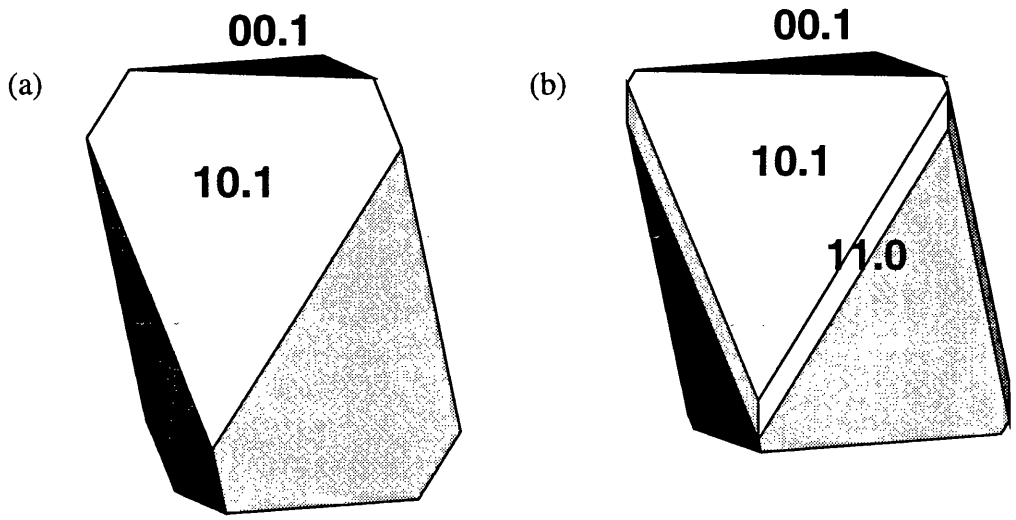

Figure 5.10 Morphologies of crystal with molecularly adsorbed water onto surfaces calculated from (a) Catlow *et al.* (1982) and (b) Lewis and Catlow (1985) potential models

From the above it seems that the morphologies obtained by the Lewis and Catlow (1985) potential are more in line with experimentally found morphologies. The high index $\{22\bar{4}3\}$ surface is only found in the unhydrated Lewis and Catlow (1985) equilibrium morphology but is too unstable to be expressed in any of the other calculated morphologies.

5.7.3 Hydration Energies

Both physisorption and hydroxylation of all surfaces is energetically favourable in agreement with previous calculations of hydroxylation of the {0001} surface (Nygren *et al.* 1997) and experimental investigations of the hydroxylated (0001) plane (Coustet and Jupille 1994). As the hydroxylation energies are always greater than the

hydration energies of molecular adsorption, it is expected that physisorption will be followed by chemisorption. For the {0001} surface this agrees with findings of Coustet and Jupille (1997) whose XPS and HREELS study of the {0001} surface after exposure to water showed the presence of hydroxyl groups but no molecular water. They mechanically cut the surface and cleaned it in ultra high vacuum conditions after dosing with water and as such we can expect both the oxygen plane (more stable in wet conditions when sample is cut) and aluminium plane (more stable in UHV conditions) to be present.

Table 5(IX) compares the range of hydration energies obtained in this work with experimental hydration energies of α-alumina. The calculated hydration energies for the most stable physisorbed surfaces range from -126.5 $kJmol^{-1}$ on the oxygen terminated $\{11\bar{2}0\}$ surface to -165.0 $kJmol^{-1}$ on the $\{10\bar{1}1\}$ surface for the Lewis and Catlow (1985) potential and from -140.0 to -200.4 $kJmol^{-1}$ for the same surfaces obtained by the Catlow *et al.* (1982) potential model. Della Gatta *et al.* (1977) and Rossi *et al.* (1994) carried out microcalorimetric measurements on a polymorphous sample of α-alumina and as such we can expect that the above stable surfaces will be present. They found heats of adsorption for molecularly adsorbed water of between -84 and -167 $kJmol^{-1}$ (Della Gatta *et al.* 1977) and -90 to -200 $kJmol^{-1}$ (Rossi *et al.* 1994) which agrees very well with our hydration energies for molecular water. Their energies are for molecular water coordinated by its oxygen to a surface aluminium atom corresponding to the adsorption we found to occur preferentially.

The calculated hydration energies for the most stable hydroxylated surfaces range from -204.1 kJmol^{-1} on the oxygen terminated $\{11\bar{2}0\}$ surface to -303.3 kJmol^{-1} on the oxygen terminated {0001} plane for the Lewis and Catlow (1985) potential and from -243.4 kJmol^{-1} on the $\{10\bar{1}1\}$ surface to -374.2 kJmol^{-1} on the oxygen {0001} plane by the Catlow *et al.* (1982) potential model. Again this range agrees very well with the value of -270 kJmol^{-1} found by Rossi *et al.* (1994) and -251 to -290 kJmol^{-1} by Della Gatta *et al.* (1977) for the chemisorbed water molecules.

Calculated and Experimental Hydration Energies		
α–Al_2O_3	$E_{physisorption}$ / kJmol^{-1}	$E_{chemisorption}$ / kJmol^{-1}
Catlow and Lewis (1985)	-126.5 to -165.0	-204.1 to -303.3
Catlow *et al.* (1982)	-140.1 to -200.4	-243.4 to -374.2
Experiment	-84 to -167 [1)] -90 to -200 [2)]	-251 to -290 [1)] -270 [2)]

[1)] Della Gatta *et al.* (1977), [2)] Rossi *et al.* (1994)

Table 5(IX) Comparison of calculated hydration energies with experiment

5.8 Summary and Conclusion

We have investigated the effect of molecular and dissociative hydration on the surface structure and morphology of the principal experimentally observed planes of α-alumina. As a result we can make the following observations:

On energy minimisation a large relaxation occurs of the aluminium basal plane from its bulk termination in agreement with previous atomistic simulations using different potential models and electronic structure calculations.

The surface energies obtained by the Lewis and Catlow (1985) and Catlow *et al.* (1982) potential models are higher than from electronic structure calculations possibly due to the lack of polarisation in the model.

The surface energies of the hydroxylated and molecularly hydrated surfaces are largely determined by the relaxation of the adsorbed species, rather than the alumina surface itself. As a result the hydration energies of chemi- and physisorption are largely independent of the potential model used.

The growth morphology obtained by the attachment energies does not agree with experimentally found morphologies. However, the equilibrium morphologies obtained by the Lewis and Catlow (1985) potential do agree, while the equilibrium morphologies from the Catlow *et al.* (1982) potential model give a reasonable fit.

The hydration energies of both physisorption and chemisorption of water onto the α-alumina faces agree very well with experimentally obtained hydration energies.

In future, it would be interesting to carry out electronic structure calculations to obtain a set of surface energies for the same surfaces. Even if, as expected from previous *ab initio* calculations (Mackrodt 1992, Manassidis and Gillan 1994), these

are lower than from the atomistic simulations they may still give similar morphologies as these are dependent on relative surface energies rather than the absolute values.

Another area for further research would be Molecular Dynamics simulations of the various surfaces in liquid water comparable to the MD simulations of MgO in chapter 4.

6 SURFACE STRUCTURE AND MORPHOLOGY OF CALCITE, ARAGONITE AND VATERITE

6.1 Introduction

Calcium carbonate is one of the most abundant minerals in the environment and of fundamental importance in many fields, both inorganic and biological. It is a building block of shells and skeletons (Beruto and Giordani 1993) and used as a carbon isotope counter in marine carbonates, with a view to assessing the relationship between the CO_2-induced greenhouse effect and climate (Romanek *et al.* 1992). Furthermore, calcium carbonate is important in ion exchange, due to its strong surface interactions with heavy metals in the environment (Park *et al.* 1996), in energy storage where the products of its endothermic decomposition into CaO and CO_2 can be stored and subsequently reacted exothermally to release the energy again (Chakraborty and Bhatia 1996) and in industrial water treatment (Dove and Hochella 1993). As such the different polymorphs, but especially calcite have been the subject of extensive and varied research.

The surface structure of calcite has been studied by a variety of methods, both in ultra-high vacuum such as the SEM studies of calcite by Goni *et al.* (1993) of the $\{10\bar{1}4\}$ surface and by Stipp and Hochella (1991) of the $\{10\bar{1}1\}$ plane, and in air (Stipp *et al.* 1996). AFM investigations under aqueous conditions (Ohnesorge and Binnig 1993) have been carried out to investigate a host of features such as distinct relaxation of surface oxygen ions on the $\{10\bar{1}4\}$ plane (Liang *et al.* 1996).

Various groups have studied factors influencing crystal growth such as the role of metastable hydrated phases in the precipitation of calcite (Clarkson *et al.* 1992) and dislocations in its dissolution (MacInnes and Brantley 1992). Gratz *et al.* (1993) and Hillner *et al.* (1993) used AFM to study calcite and found that crystal growth occurred through steps and spiral dislocations, while Stipp *et al.* (1996) investigating the $\{10\bar{1}4\}$ plane using scanning force microscopy (SFM) at intervals over some days showed that the steps spread one layer at a time. Recent experimental and theoretical research has included the formation and growth of rhombohedral pits on the $\{10\bar{1}4\}$ surface (Liang *et al.* 1996a, McCoy and LaFemina 1997).

Apart from surface features of pure calcite, a growing area of research is growth inhibition and morphology change. As the concentration of calcium carbonate in many natural waters exceeds the saturation level, the precipitation of calcite in industrial boilers, transportation pipes and desalination plants is of concern (Chakraborty *et al.* 1994) and it is therefore important to learn how morphology may be affected or induced. Often studies have concentrated on the incorporation in the crystal of foreign ions such as copper and manganese (Nassralla-Aboukais *et al.* 1996), iron (Katz *et al.* 1993) and other divalent cations (Brecevic *et al.* 1996), phosphate species (Suzuki *et al.* 1986, Dove and Hochella 1993) or organic matter (Cicerone *et al.* 1992). Earlier computational studies (Kenway *et al.* 1992, Parker *et al.* 1993) have confirmed experimental findings (Rajam and Mann 1990) that lithium and HPO_4^{2-} impurities radically change the morphology of calcite, and predicted that

magnesium ions would do likewise which was later confirmed by Compton and Brown (1994) who found that magnesium ions inhibit calcite growth.

Other methods of inducing morphology changes have included growing crystals using an organic template such as β-chitin (Falini *et al.* 1996) or an ammonium surfactant (Walsh and Mann 1995) to form aragonite, uncommon shapes of calcite (Wong *et al.* 1994, Archibald *et al.* 1996) or vaterite (Litvin *et al.* 1995) displaying different faces depending on the template material used (Mann *et al.* 1988, Didymus *et al.* 1995).

Finally, Beruto and Giordani (1993) have investigated the effect of induced electromagnetic fields to influence the morphology of calcium carbonate crystals.

The aim of the work described in this chapter is to investigate the effect of molecular adsorption of water on the surface structure, energies and hydration energies of the low index surfaces of calcite, aragonite and their metastable polymorph vaterite and to study the effect of hydration of the surfaces on the crystal morphology. We did some preliminary calculations on calcite using the potential by Pavese *et al.* (1996) but without the Morse potential which was replaced by the electrostatic interaction between carbon and oxygen. We considered both unhydrated and hydrated surfaces in a series of partial coverages to identify the strength of interaction with specific surface configurations and surface features. Amongst the important features are stepped surfaces, which as noted above are closely identified by experiment with growth mechanisms for calcite. We found that all surfaces

investigated would be hydrated to full monolayer coverage and thus when investigating aragonite and vaterite we concentrated on fully covered surfaces and then compared the different polymorphs with a view to obtain a better insight in the relative stabilities of the different structures.

6.2 Potential verification

For the pure calcium carbonate crystals we used the potential parameters derived empirically by Pavese *et al.* (1996) in their study of the thermal dependence of structural and elastic properties of calcite (chapter 3.5.2). The potential parameters used for the intra- and intermolecular interactions of the water molecules and between calcium carbonate surfaces and water molecules are described in chapter 3.7.3. We verified these potential parameters by simulating the structure of ikaite, a calcium carbonate hexahydrate. Ikaite is only formed at low temperatures of -1.6 to 3 ^{0}C in the presence of phosphate groups as both factors inhibit the formation of calcite or aragonite. It is metastable up to 25 ^{0}C at high pressures but at room temperature and atmospheric pressure it quickly decomposes to vaterite, the metastable precursor of calcite. The calculated and experimental crystallographic data are shown in table 6(I). Although the calculated structure has contracted with respect to the experimental structure, the symmetry and relative atomic coordinates are retained. Furthermore, these simulations were effectively at zero Kelvin and it is quite reasonable that at that temperature the crystal would be contracted.

IKAITE $CaCO_3.(H_2O)_6$						
	experimental			**calculated**		
spacegroup	C12/c1			C12/c1		
a b c	8.87	8.23	11.02	8.03	8.07	10.82
$\alpha\ \beta\ \gamma$	90.0	110.2	90.0	90.0	110.8	90.0
Ca	0.5000	0.6472	0.2500	0.5000	0.6169	0.2500
C	0.5000	0.3067	0.2500	0.5000	0.2733	0.2500
O carbonate	0.5000	0.1508	0.2500	0.5000	0.1255	0.2500
	0.5263	0.3849	0.1582	0.5314	0.3493	0.1657
O water	0.6163	0.7229	0.0916	0.6079	0.6868	0.0800
	0.7883	0.5576	0.3825	0.8054	0.5383	0.3807
	0.6703	0.8842	0.3593	0.6681	0.8671	0.3599
H	0.5680	0.6960	0.0020	0.5551	0.6711	- 0.0177
	0.6440	0.8350	0.0920	0.6836	0.7878	0.0884
	0.8720	0.5980	0.3540	0.8931	0.5873	0.3439
	0.8220	0.5880	0.4720	0.8495	0.5806	0.4741
	0.7740	0.8910	0.3500	0.7909	0.8683	0.3554
	0.6160	0.9810	0.3190	0.6198	0.9784	0.3227

Table 6(I) Calculated and Experimental crystallographic structure of Ikaite

The calculated bond distances and angles are in good agreement with their experimental counterparts as can be seen from table 6(II).

IKAITE $CaCO_3.(H_2O)_6$		
	experimental	**calculated**
r(CaC) / Å	4.61-5.52	4.44-5.71
$r(CaO_{water})$ / Å	2.39-2.56	2.35-2.61
r(CO) / Å	1.28	1.20-1.25
$r(CO_{water})$ / Å	3.24-3.79	3.09-3.66
r(CH) / Å	2.53-2.86	2.24-2.95
r(OH) / Å H-bond	1.73-1.92	1.74-1.86
$r(O_{water}H)$ / Å	0.96	1.00
angle (OCO) / deg.	119.9-120.2	119.6-120.4
angle ($HO_{water}H$) / deg.	103.8-105.0	102.0-103.0
torsion (OCO) / deg.	180.0	179.0

Table 6(II) Calculated and experimental bond distances and angles in Ikaite

The calculated lattice energy for ikaite is -9909 $kJmol^{-1}$, compared to a lattice energy of -5898 $kJmol^{-1}$ for calcite and -621 $kJmol^{-1}$ for a gaseous water molecule. Calculating the change in enthalpy at 298 K for ikaite, calcite and water, the change in interaction energy for the dissociation of ikaite per water molecule is 47 $kJmol^{-1}$. This compares to experimental values of 47 to 50 $kJmol^{-1}$ (Bischoff *et al.* 1993) which is an excellent agreement, particularly as no information concerning ikaite was used in the derivation of the potential parameters and temperature has been neglected in these simulations. This means that we can be confident that our potential model adequately describes the calcium carbonate polymorphs and their interactions with water and that the calculated heats of hydration will be a good indication of experimental energies.

6.3 Method

The hydration energy of molecular adsorption of water onto the calcium carbonate surfaces was calculated by comparing the energy of the pure surface and that of an isolated water molecule with the energy of the hydrated surface. For a selection of surfaces our study was extended to include hydration in a series of partial coverages (de Leeuw and Parker 1997) in which case, like MgO and CaO in chapter 4, many possible configurations of the partially hydrated surfaces were investigated to make sure that the most stable configuration was located. For example, energy variations for different configurations range from 3.9 kJmol^{-1} on the $\{10\bar{1}4\}$ surface to 221.0 kJmol on the $\{11\bar{2}0\}$ surface. The energies quoted in later sections refer to the energetically most favourable configuration obtained. Again, as in chapter 4, different ways of adsorption of the water molecules need to be taken into account as well.

Surface calcium and oxygen ions were elected as initial sites for adsorption of the water molecules after which the hydrated surface was allowed to relax. In case of binding to the calcium sites, the oxygen atom of the water molecule was positioned at the experimental Ca-O distance of 2.4 Å for a hydrated calcium salt (Forbes *et al.* 1992, Skipper *et al.* 1994) which is also the distance found in most hydrates containing calcium ions (Einspahr and Bugg 1980). Adsorption on the surface oxygen sites was modelled by positioning one water hydrogen atom at a hydrogen-bond distance of 1.8 Å [exp. 1.76-1.95 Å in ice (Kamb 1972)], in the same way as on MgO discussed in chapter 4. After relaxation, the resulting structure of the

hydrated surface was studied and its stability evaluated in terms of surface energy and hydration energy. The calculation of the surface energies and hydration energies of physisorption is identical to MgO (chapter 4.2).

6.4 Calcite

Calcite has a rhombohedral crystal structure with spacegroup $R\bar{3}c$ and a cleavage structure not unlike distorted rocksalt (Liang *et al.* 1996). Its hexagonal lattice vectors and angles are a = b = 4.990 Å, c = 17.061 Å, $\alpha = \beta = 90^0$ and $\gamma = 120^0$ (Deer *et al.* 1992) which were calculated to be a = b = 4.797 Å, c = 17.482 Å, $\alpha = \beta = 90^0$ and $\gamma = 120^0$ although we should emphasize that these data were used in the fitting of the potential model and not suprisingly are in accord. The bulk crystal was cut to obtain five planar surfaces, including the $\{10\bar{1}4\}$ surface which is found experimentally to be the dominant surface. The other surfaces considered are the {0001} basal plane, the $\{10\bar{1}0\}$, $\{10\bar{1}1\}$ and $\{11\bar{2}0\}$ surfaces. Furthermore, two stepped surfaces were considered, the $\{10\bar{1}3\}$ and the $\{10\bar{1}5\}$ surfaces, which are studied as models of an experimental $\{10\bar{1}4\}$ plane including growth steps. The {0001} and $\{10\bar{1}1\}$ surfaces can be terminated in two different ways, either by a layer of calcium ions or carbonate molecules. We need to be confident that the most stable plane is considered and therefore calculations have been performed on all possible planes for each surface.

6.4.1 Pure Surfaces

The surfaces were allowed to relax and their surface and attachment energies calculated (Table 6(III)).

Surface and Attachment Energies of Pure Calcite			
Surface (hexagonal indices)	$\gamma_{unrelaxed}$ / Jm^{-2}	$\gamma_{relaxed}$ / Jm^{-2}	E_{att} / $kJmol^{-1}$
$\{10\bar{1}4\}$	0.64	0.59	- 75.4
$\{10\bar{1}3\}$	1.04	0.75	-192.7
$\{10\bar{1}5\}$	0.90	0.74	-194.0
{0001}Ca	2.62	0.97	-334.3
{0001}CO_3	1.84	0.99	-204.7
$\{10\bar{1}0\}$	2.96	0.97	-759.6
$\{10\bar{1}1\}$Ca	2.07	1.23	-307.2
$\{10\bar{1}1\}CO_3$	2.04	1.14	-276.7
$\{11\bar{2}0\}$	1.71	1.39	-291.3

Table 6(III) Surface and attachment energies of unhydrated calcite

Planar and Stepped $\{10\bar{1}4\}$ Surfaces

The $\{10\bar{1}4\}$ surface consists of layers of calcium, carbon and one oxygen atom in a plane with the other two oxygen atoms above and below this plane (figure 6.1).

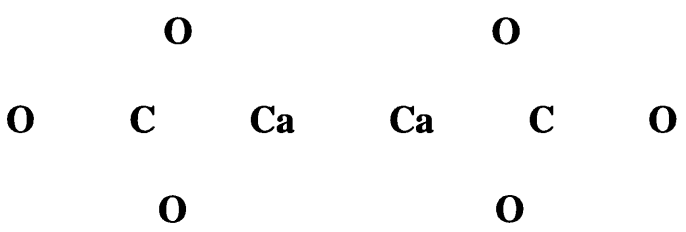

Figure 6.1 Schematic representation of the layering in the calcite $\{10\bar{1}4\}$ surface

As the carbonate groups cannot be split there is only one possible cut to obtain the surface. The planes contain two carbonate groups which differ in their orientation and as a result the oxygen atoms on the surface are in two different but equivalent orientations. From the surface and attachment energies in Table 6(III) it is clear that the $\{10\bar{1}4\}$ surface is both the most stable surface of the series and kinetically the most important. This agrees with both previous calculations (Kenway *et al.* 1992, Parker *et al.* 1993) and experimental findings (Blanchard and Baer 1992, Beruto and Giordani 1993, MacInnes and Brantley 1992, Hillner *et al.* 1993, Dove and Hochella 1993, Didymus *et al.* 1993, Heywood and Mann 1994).

The $\{10\bar{1}3\}$ surface consists of $\{10\bar{1}4\}$ planes, which are offset from each other by one atomic layer down the $\{10\bar{1}1\}$ cleavage plane (fig. 6.2a). Although, as expected from a stepped surface, the surface energy of the $\{10\bar{1}3\}$ surface at 0.75 Jm^{-2} is higher than that of the predominant $\{10\bar{1}4\}$ plane ($\gamma = 0.59$ Jm^{-2}), it is still very much more stable than the $\{10\bar{1}1\}$ surface itself, with a surface energy of 1.14 Jm^{-2} for its calcium terminated plane. The attachment energy of the stepped surface shows the same trend in that it is less than that of the $\{10\bar{1}1\}$ planes but not as small as that of the planar surface. This trend is repeated in the $\{10\bar{1}5\}$ surface which also consists of $\{10\bar{1}4\}$ planes. On this surface, however, they are offset by one atomic layer down the oxygen terminated plane of the {0001} surface (fig. 6.2b). Again this surface has both a higher surface energy of 0.99 Jm^{-2} instead of 0.74 Jm^{-2} like the $\{10\bar{1}3\}$ surface, and a higher attachment energy than that of the stepped surface. The step edges of the two stepped surfaces are parallel to the calcite rhomb edges in the

[48$\bar{1}$] direction in accordance with experimentally found steps on the {10$\bar{1}$4} surface (Gratz *et al.* 1993) and rhombohedral pits (Liang *et al.* 1996a).

(a)

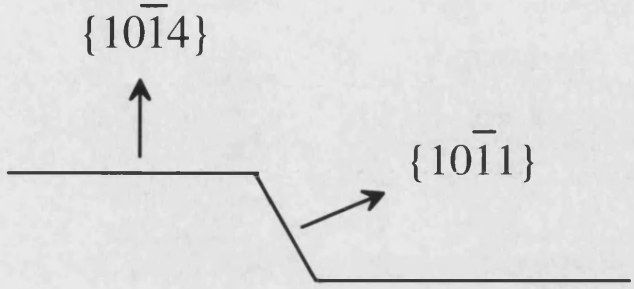

(b)

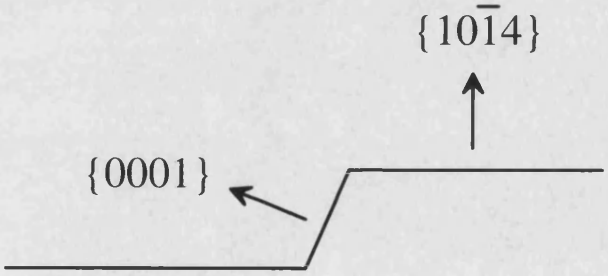

Figure 6.2 Schematic diagram of (a) the {10$\bar{1}$3} surface and (b) the {10$\bar{1}$5} surface.

Both the {10$\bar{1}$3} and {10$\bar{1}$5} surfaces are dipolar, which meant that we had to remove the dipole for the surface energy to converge as discussed in chapter 2. Hence half the calcium ions or carbonate groups on top of the edge were shifted to the bottom of the unit cell, in effect creating an edge with 50% vacancies. As a result the edges of both surfaces are crenellated (fig 6.3). There is no experimental evidence for this, however, work by Stipp *et al.* (1996) indicates that calcite growth occurs in 'tongues' perpendicular to a step edge and, as our crenellated edges resemble

'micro-tongues' of material, it does offer a tentative explanation as to how new material could be added to the step whilst leaving gaps between the new material.

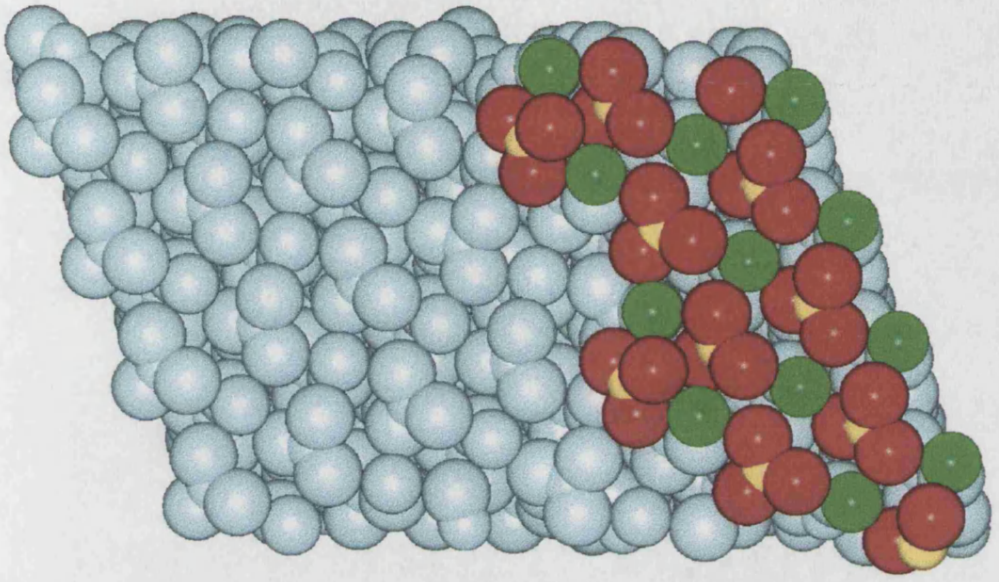

Figure 6.3 Plan view of the $\{10\bar{1}5\}$ surface showing the crenellated edge, with second and lower layers coloured blue (O = red, Ca = green, C = yellow)

{0001} Surface

The {0001} surface is a common twinning plane of calcite (Deer *et al.* 1992) consisting of alternating planes of calcium ions and carbonate groups. Both planes are dipolar and once again this dipole needs to be removed. The surface energies of the two planes are similar although the surface energies of the unrelaxed planes are very different, both from each other (2.62 Jm^{-2} for the Ca plane compared to 1.84 Jm^{-2} for the carbonate plane) and from their relaxed values. The latter indicates that substantial rearrangement and relaxation of the surface has taken place on energy minimisation, due to the vacant sites on the surface. In fact, on the calcium terminated surface, the carbonate groups in the layer below rotate into the surface vacancies to form an edged surface with the surface calciums at the apex of the edges (fig 6.4).

(a)

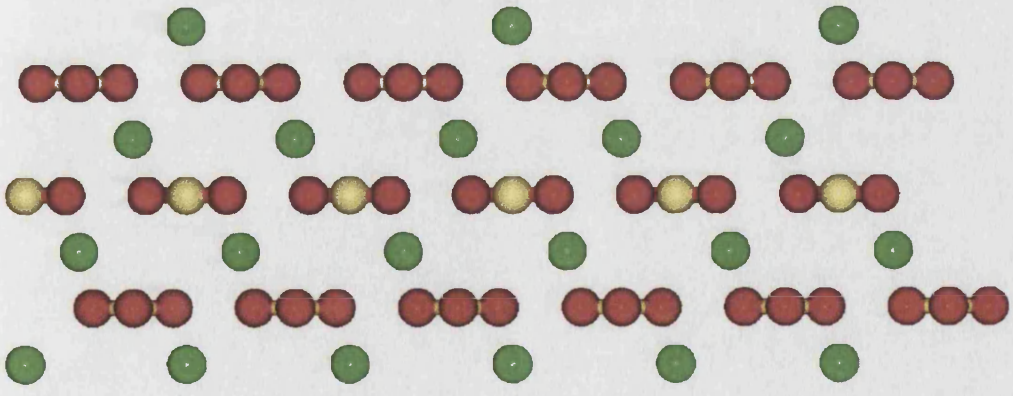

(b)

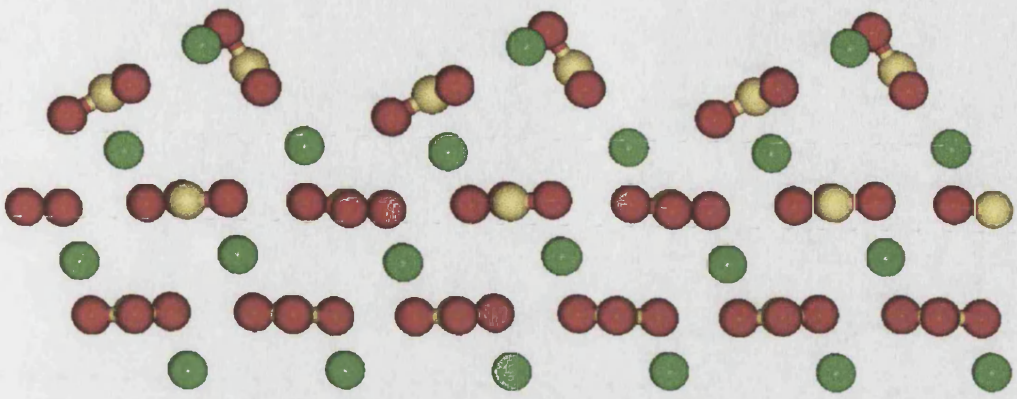

Figure 6.4 {0001} Surface (a) unrelaxed calcium terminated surface and (b) relaxed calcium terminated surface (O = red, Ca = green, C = yellow)

The attachment energies reflect the unrelaxed surface energies in that the carbonate plane has the lower attachment energy and hence would be formed preferentially.

$\{10\bar{1}0\}$ and $\{10\bar{1}1\}$ Surfaces

The $\{10\bar{1}0\}$ surface, like the $\{10\bar{1}4\}$ surface, can only be cut in one way and similar to the {0001} it is a dipolar surface with virtually the same surface energy of 0.97 Jm^{-2} although it has a very large attachment energy reflecting its large unrelaxed surface energy. This suggests that this surface will not be expressed in the growth form. Again, on energy minimisation a large relaxation of the surface takes place.

The $\{10\bar{1}1\}$ surface, which is the perfect cleavage plane of calcite (Stipp and Hochella 1991) again has two possible terminations, both dipolar. Both planes have similar surface and attachment energies, although the unhydrated carbonate surface has a lower surface and attachment energy than the calcium plane, while on hydration the calcium plane is found to be the more stable surface.

$\{11\bar{2}0\}$ Surface

The $\{11\bar{2}0\}$ plane exhibits bulk-like termination as does the $\{10\bar{1}1\}$ surface above, both in unhydrated as hydrated form. Like the $\{10\bar{1}4\}$ surface, the $\{11\bar{2}0\}$ plane has only one non-dipolar termination with planes consisting of both calcium ions and carbonate groups.

6.4.2 Hydrated Surfaces

To each of the faces we added water molecules and we did not consider chemisorption at this stage although there is some experimental evidence from XPS studies for the existence of HCO_3^- and $CaOH^+$ surface hydration species (Stipp and Hochella 1991). Table 6(IV) shows the surface energies of the surfaces after adsorption of a full monolayer of water, and the relevant energies of hydration.

Surface and Hydration Energies of Hydrated Calcite Surfaces		
Surface (hexagonal indices)	$\gamma_{hydrated}$ / Jm^{-2}	$E_{hydration}$ / $kJmol^{-1}$
$\{10\bar{1}4\}$	0.16	- 93.9
$\{10\bar{1}3\}$	0.67	- 93.4 *
$\{10\bar{1}5\}$	0.65	-117.7 *
{0001}Ca	0.68	- 79.2
$\{0001\}CO_3$	0.38	- 93.2
$\{10\bar{1}0\}$	0.75	-100.5
$\{10\bar{1}1\}$Ca	0.63	-113.4
$\{10\bar{1}1\}CO_3$	0.81	-100.9
$\{11\bar{2}0\}$	0.43	-138.5

Table 6(IV) Surface and hydration energies of calcite * Hydration on the edges only

Planar and Stepped $\{10\bar{1}4\}$ Surfaces

On hydration of the planar $\{10\bar{1}4\}$ surface, the water molecules adsorb uniformly onto the surface in two orientations. Although initially positioned upright, after energy minimisation their relaxed position is lying flat on the surface (fig. 6.5) which agrees with some configurations of water on clay surfaces (Chang *et al.* 1995). The water molecules' oxygen atoms are coordinated to the surface calcium ions at a distance of 2.4 Å, with the two hydrogen atoms pointing towards two surface oxygen ions. On the fully hydrated surface, all surface oxygen atoms are coordinated to two hydrogen atoms from two different water molecules. Although the hydrogen-bond lengths are different for the two molecules (1.89 and 1.97 Å) due to the differently oriented carbonate groups, the different surface oxygens are still effectively indistinguishable as they are all coordinated to a water molecule in each of the two different ways. The surface exhibits 1 x 1 symmetry in accordance with the AFM images of the plane of calcite in water by Ohnesorge and Binnig (1993).

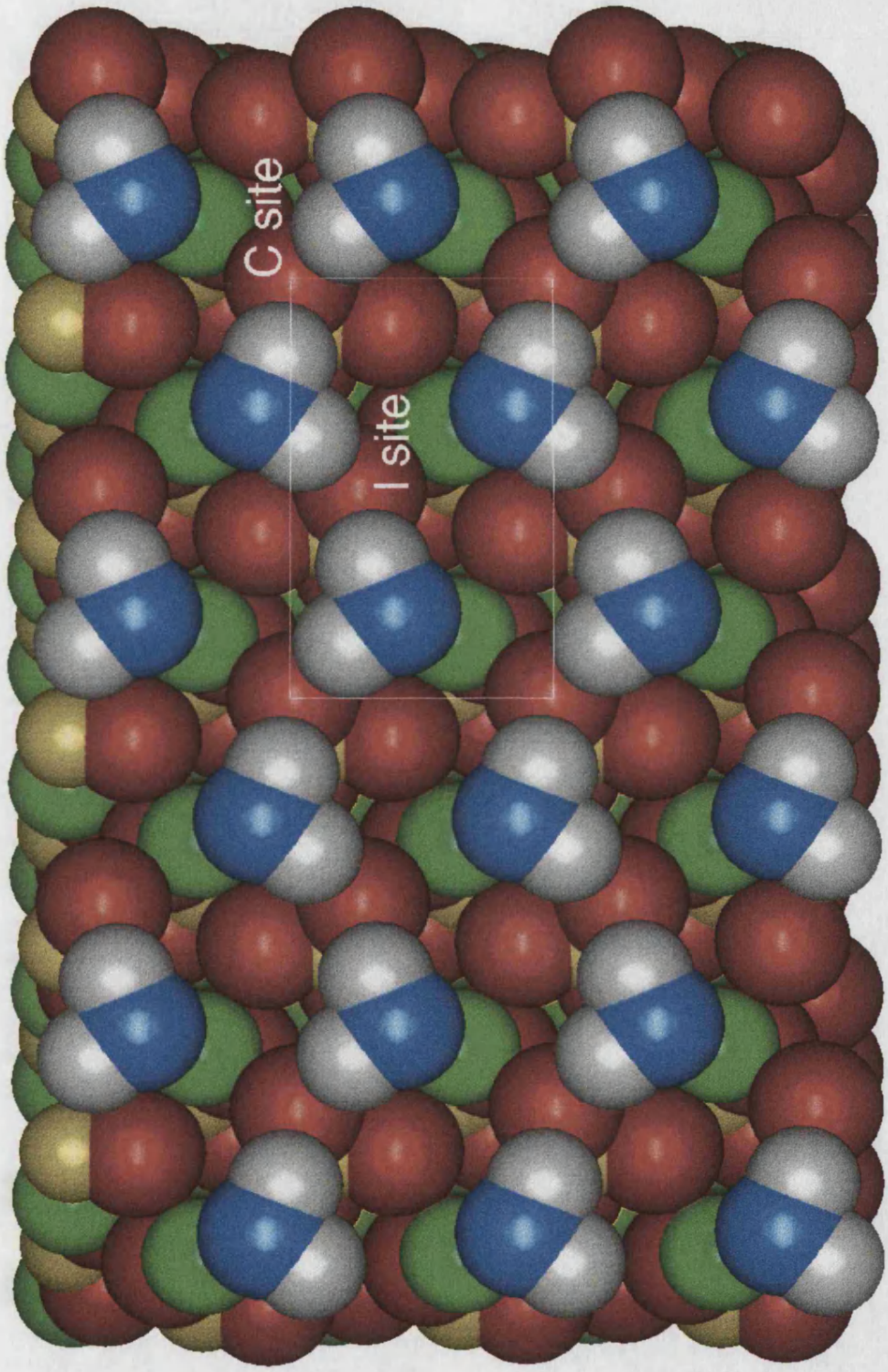

Figure 6.5 Plan view of the $\{10\bar{1}4\}$ surface showing different carbonate groups and flat adsorption of water molecules (O = red, Ca = green, C = yellow, O_{water} = blue, H = white)

However, when the surface is only partially covered by water molecules, the difference between the two O---H bondlengths becomes important and the surface oxygens relax distinctly showing a difference in height above the calcium/carbon plane of about 0.05 Å. This effect has been observed by Liang *et al.* (1996) in their AFM study of the surface in water who found that there was a structural difference between the oxygen ions of the differently orientated carbonate groups. Following their convention, on figure 6.5 the surface oxygens of the two differently oriented carbonate groups are labelled C site, at the corner of the unit cell, and I site, inside the unit cell. They found an average difference in height with respect to the surface of approximately 0.35 Å, although they suggest that this is exacerbated by surface deformation due to the AFM tip. This variance in height was proposed (Stipp and Hochella 1991, Liang *et al.* 1996) to be due to a different rotation of the carbonate groups in the carbonate planes. Our results agree with that proposition, although we cannot rule out a distinct distortion rather than rotation of the different carbonate groups. The fact that this result only occurs on partially hydrated surfaces is confirmed by Liang *et al.* (1996) who state that "water molecules are moved out of the way as the AFM tip scans the surface".

On the stepped surfaces, only the adsorption sites on the edges are considered as we were interested in distinguishing them from the adsorption sites on the flat $\{10\bar{1}4\}$ surface. On the MgO surfaces described in chapter 4 we found the edge sites to be energetically the most favourable sites and it would be interesting to see whether they are the most reactive sites on calcite as well.

On the steps of the $\{10\bar{1}3\}$ surface, the water molecules were originally placed with their oxygen atoms on top of the calcium ions and hydrogen ions pointing away from the surface. However, after energy minimisation, the water molecules have relaxed in two different ways: (i) on the plane on top of the edge with its oxygen atom coordinated to a calcium at 2.45 Å and one of its hydrogen atoms is coordinated to a lattice oxygen on the step edge at a hydrogen-bond distance of 1.48 Å (cf. H---O distance on MgO {310} step edge of 1.58 Å) while its other hydrogen atom is not coordinated to surface oxygen ions (fig. 6.6). (ii) The other water molecule adsorbs in the valley coordinated by its oxygen to the same calcium ion at 2.57 Å and one H hydrogen-bonded to lattice oxygens on the edge (1.54 Å) and on the plane below (1.61 Å). As can be seen from table 6(IV), the (partially) hydrated surface is more stable than the pure surface and the hydration energy is the same as that of the planar surface.

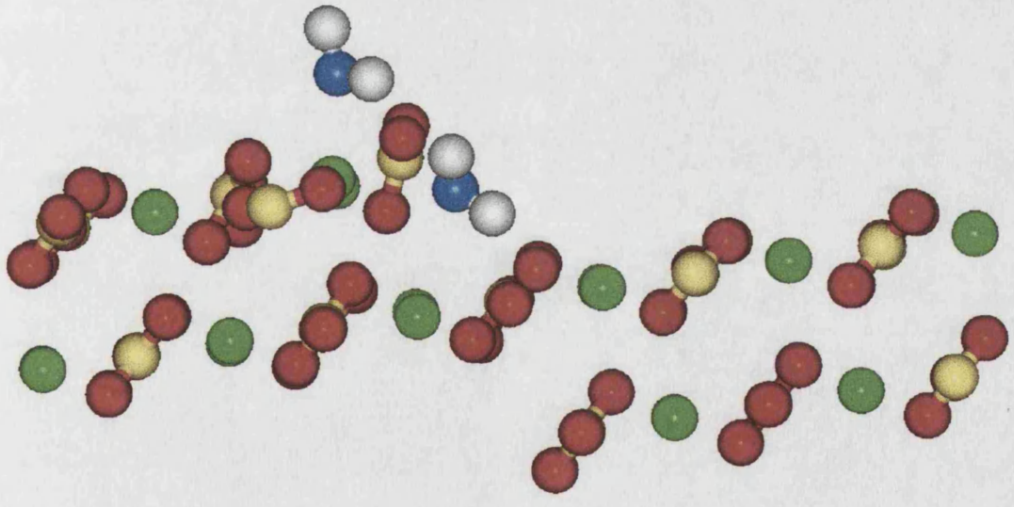

Figure 6.6 $\{10\bar{1}3\}$ surface showing two different patters of adsorption of water molecules both coordinating to through H-bonding to lattice oxygen atoms on the edge (O = red, Ca = green, C = yellow, O_{water} = blue, H = white)

The $\{10\bar{1}5\}$ surface has a much larger hydration energy than that of the planar $\{10\bar{1}4\}$surface. On this surface the water molecules are again adsorbed in two different ways similar to the $\{10\bar{1}3\}$ surface. They alternate along the edge, one with its oxygen atom closely coordinated to the edge calcium ion and within hydrogen bond distance of an edge oxygen ion. It is adsorbed flat onto the plane, much like the adsorption onto the planar surface. The second position is also coordinated to the edge calcium ion but with a hydrogen coordinated to a carbonate oxygen on the plane below the step.

{0001} Surface

Similar relaxation is seen on hydration of the calcium terminated plane to the pure calcium terminated {0001} surface. After energy minimisation the surface has relaxed in the same way as the unhydrated surface and the water molecules are adsorbed onto the calcium ions on the edge. It can be seen from table 6(IV) that although the Ca plane has been stabilised by hydration, it is to a much lesser extent than the $\{10\bar{1}4\}$ surface. The hydrated carbonate plane, however, has been stabilised by water adsorption to a much larger extent and is now the dominant of the two planes. In this case, the crystal surface has not relaxed appreciably, but the water molecules cluster around the surface carbonate groups filling in the vacant sites (fig 6.7). The water molecules in the clusters are coordinated to the surface both with their oxygen atom to surface calcium ions (2.35-2.59 Å) and by hydrogen-bonding to a surface oxygen (1.46-1.77 Å) sometimes bridging two carbonate groups. In addition, they also form extensive hydrogen-bonding between themselves, with

O---H distances ranging from 1.81 to 2.16 Å. The interactions between these adsorbed water molecules at full monolayer coverage account for an extra stabilising energy factor of -1.5 $kJmol^{-1}$ compared to non-interacting water molecules and this is the only surface where the water molecules interact in an energetically favourable way. On all other surfaces, the relative positions of the adsorbed water molecules have a destabilising effect indicating that adsorption to the surface outweighs any energy disadvantage due to intermolecular water interactions.

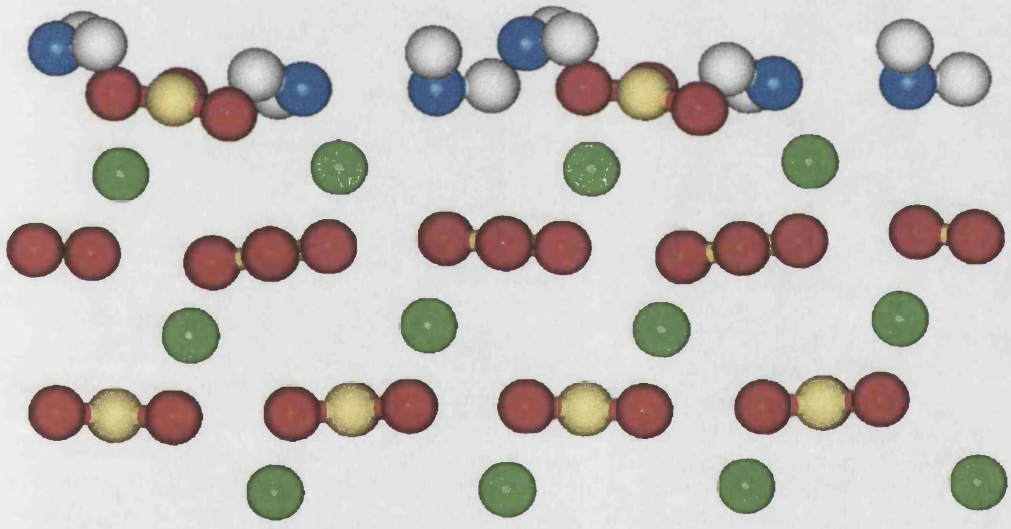

Figure 6.7 Hydrated carbonate {0001} surface showing no appreciable surface relaxation but clustering of the water molecules around the surface carbonate groups and in the vacancies. (O = red, Ca = green, C = yellow, O_{water} = blue, H = white)

$\{10\bar{1}0\}$ Surface

Adsorption of water onto the $\{10\bar{1}0\}$ surface has not such a marked effect on the surface energy as with the {0001} surface although the hydration energy is considerable. The water molecules adsorb in rows in two distinct and alternating ways, (i) coordinated by the oxygen atom to a surface calcium ion and both hydrogens coordinated to surface oxygen ions and (ii) with only one hydrogen coordinated to a surface oxygen. Although the water molecules do not interact with one another through proper hydrogen-bonding (O---H distance is 2.4 Å), any other configuration is less energetically favourable.

$\{10\bar{1}1\}$ Surface

In both the unhydrated but especially the hydrated crystal, only the surface carbonate groups rotate on relaxation, while the calcium ions and the carbonate groups from the third layer onwards (*ca.* 6 Å) remain at their bulk positions (fig 6.8). The water molecules adsorb into the vacancies resulting from the dipolar surface in three different positions. They closely coordinate to both surface and second layer calcium ions (2.31-2.51 Å) and oxygens (1.43-1.62 Å) although no hydrogen-bonding between the water molecules is evident.

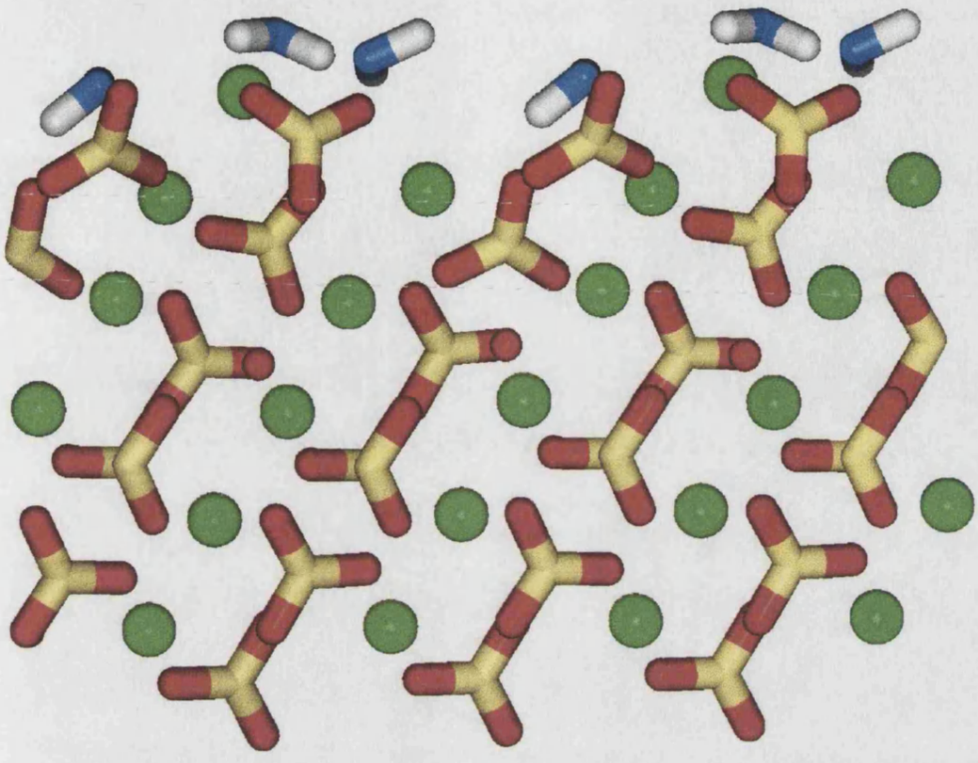

Figure 6.8 Hydrated calcium terminated $\{10\bar{1}1\}$ surface showing slight rotation of surface carbonate groups only and different adsorption modes for water molecules. (O = red, Ca = green, C = yellow, O_{water} = blue, H = white)

This relatively small rearrangement of the surface confirms the findings of Stipp and Hochella (1991), who studied the structure and bonding of the $\{10\bar{1}1\}$ cleavage plane by x-ray photoelectron sprectroscopy (XPS) and low-energy electron diffraction (LEED) to see whether hydration would lead to a thick, disordered or amorphous surface layer as suggested by Davids *et al.* (1987). They found, however, that apart from some possible rotation of surface carbonate groups, the surface for at least 10 Å into the crystal was ordered with bulk lattice dimension, a result which our calculations have borne out.

$\{11\bar{2}0\}$ Surface

The $\{11\bar{2}0\}$ surface is stabilised considerably by hydration with by far the largest hydration energy of the surfaces considered to date, as is clear from tables 6(III) and (IV). The water molecules adsorb in three distinct ways: (i) coordinated by the oxygen to three calcium ions at distances between 2.28 and 2.46 Å, (ii) coordinated by both hydrogens to surface oxygen ions at O---H distances of 1.53 and 1.56 Å, bridging two carbonate groups and (iii) with only one hydrogen closely coordinated to a carbonate group. There is no appreciable hydrogen-bonding between the adsorbed water molecules themselves and the very high hydration energy and surface stabilisation is thus entirely due to the close coordination of the water molecules to the surface. This is borne out by our preliminary calculations on partial hydration where initial adsorption of an isolated water molecule is energetically very favourable with increasing coverages leading to decreasing hydration energies.

6.5 Aragonite

Aragonite has an orthorhombic crystal structure with spacegroup Pmcn. We started from the experimental structure found by Dickens and Bowen (1971) with a = 4.9598 Å, b = 7.9641 Å and c = 5.7379 Å and $\alpha = \beta = \gamma = 90°$. The bulk crystal was allowed to relax giving a = 4.8314 Å, b = 7.8359 Å, c = 5.7911 Å and $\alpha = \beta = \gamma = 90°$. The crystal was then cut to obtain the following low index surfaces: {010}, {100}, {001}, {110}, {011}, {101} and {111}. All of these surfaces can be cut in

more than one way except the {100} surface, giving planes terminated by calcium ions and others terminated by oxygen ions of the carbonate groups, similar to calcite.

6.5.1 Pure Surfaces

Table 6(V) shows the surface and attachment energies of the unhydrated aragonite surfaces.

Surface and Attachment Energies of Pure Aragonite			
Surface	**$\gamma_{unrelaxed}$ / Jm^{-2}**	**$\gamma_{relaxed}$ / Jm^{-2}**	**E_{att} / $kJmol^{-1}$**
{010}Ca	1.24	0.96	-105.2
{010}CO_3	3.58	1.50	-314.8
{100}CO_3	2.23	1.50	-381.3
{001}Ca	2.71	1.05	-341.1
{001}CO_3	1.14	0.85	-120.1
{110}Ca	1.27	0.88	-101.2
{110}CO_3	3.93	1.04	-303.0
{011}CO_3	0.88	0.69	- 61.5
{011}CO_3	2.25	1.16	-167.6
{011}CO_3	1.40	0.99	-102.2
{011}CO_3	2.25	1.13	-167.6
{101}Ca	1.55	0.99	-145.6
{101}CO_3	1.78	1.08	-155.5
{111}Ca	2.87	1.40	-319.7
{111}Ca	2.44	1.03	-257.3
{111}CO_3	1.67	0.84	-177.1
{111}CO_3	2.44	1.02	-257.3

Table 6(V) Surface and attachment energies of unhydrated aragonite

{010} Surface

The {010} surface is a distinct cleavage plane expressed in the experimental morphology (Dana 1958). The surface energy of the pure unhydrated surface quoted in table 6(V) shows the calcium terminated plane to have a lower surface energy than the carbonate surface and hence to be the more stable surface plane. The attachment energies show the same trend in that the calcium terminated surface is the more important plane. The carbonate terminated plane shows considerable relaxation after energy minimisation. The reason is that on relaxation the surface carbonate groups rotate to lie flat on the surface rather than upright as in a bulk termination. The calcium terminated plane on the other hand shows hardly any relaxation.

{100} and {001} Surfaces

The {100} surface is the only aragonite plane with just one termination. It is generally not expressed in the experimental morphology of aragonite which agrees with the fairly high surface and attachment energies compared to those of the more stable surfaces.

The {001} surface has two possible terminations but neither has a very low surface energy in agreement with the fact that this surface is not expressed in the experimental morphology. Following the trend of the surface energies the attachment energy of the carbonate plane is much lower than that of the calcium plane indicating that this plane would be favoured.

{110} Surface

Twinning is common in aragonite and apart from a cleavage plane the {110} surface is also a twinning plane (Dana 1958). In both the unhydrated and hydrated form the calcium terminated surface is more stable than the carbonate plane and its attachment energy is considerably smaller than that of the carbonate plane. The calcium terminated surface does not relax appreciably on energy minimisation, but the carbonate plane does, from an initial surface energy of 3.93 Jm^{-2} to 1.04 Jm^{-2} after relaxation. This is due to the surface carbonate groups which rotate in the surface to lie flat. No such relaxation takes place on the calcium terminated plane, where the topmost carbonates are anchored by the surface calcium ions.

{011} Surface

The {011} surface has four different cuts which had to be investigated, all of which terminated by one or more surface oxygen ions. However, their surface energies vary greatly, as shown in table 6(V), from a very stable unhydrated surface with $\gamma = 0.69$ Jm^{-2} to one of the least stable planes of the aragonite series with a surface energy of 1.16 Jm^{-2}. The attachment energies of the different planes vary as well. The most stable plane also has the smallest attachment energy, although the two very unstable surfaces do not show a very high attachment energy.

{101} and {111} Surfaces

The {101} surface has again two distinct cuts, a calcium and a carbonate plane. Both have similar surface and attachment energies.

Like the {011} surface, the {111} is another surface with four possible terminations, two of which contain calcium ions in the surface layer. Both surface and attachment energies vary in a comparable pattern.

6.5.2 Hydrated Surfaces

Table 6(VI) shows the surface energies of the hydrated surfaces and their energies of hydration.

Surface and Hydration Energies of Hydrated Aragonite		
Surface	**$\gamma_{hydrated}$ / Jm^{-2}**	**$E_{hydration}$ / $kJmol^{-1}$**
{010}Ca	0.24	-105.2
{010}CO_3	1.77	- 21.2
{100}CO_3	0.93	-122.6
{001}Ca	0.62	- 93.6
{001}CO_3	0.90	- 39.4
{110}Ca	0.56	- 94.6
{110}CO_3	0.81	- 80.8
{011}CO_3	1.07	- 8.2
{011}CO_3	1.15	- 45.4
{011}CO_3	0.25	-113.8
{011}CO_3	0.50	-133.7
{101}Ca	0.53	- 98.7
{101}CO_3	0.62	-125.3
{111}Ca	1.03	-118.5
{111}Ca	0.79	- 90.6
{111}CO_3	0.64	- 84.4
{111}CO_3	0.72	- 84.0

Table 6(VI) Surface and hydration energies of aragonite

{010} Surface

On hydration the surfaces terminated with either calcium or carbonate planes behave in different ways. The calcium-terminated plane is stabilised by hydration as is shown in tables 6(V) and (VI) by the decreased surface energy. Indeed this surface, shown in fig. 6.9, is the most stable of the hydrated surfaces with a very low surface energy of 0.24 Jm^{-2}. There are two distinct ways that water molecules adsorb to the surface, although both are coordinated to a surface calcium as well as a surface oxygen through a hydrogen bond. There is some coordination between the two

different water molecules, although 2.5 Å is too long a distance for a formal hydrogen-bond.

In contrast, the carbonate terminated plane has been destabilised by hydration. Although the hydration energy shows that hydration is still energetically possible the surface energy has increased and it would thus be the very stable calcium terminated plane which is seen experimentally.

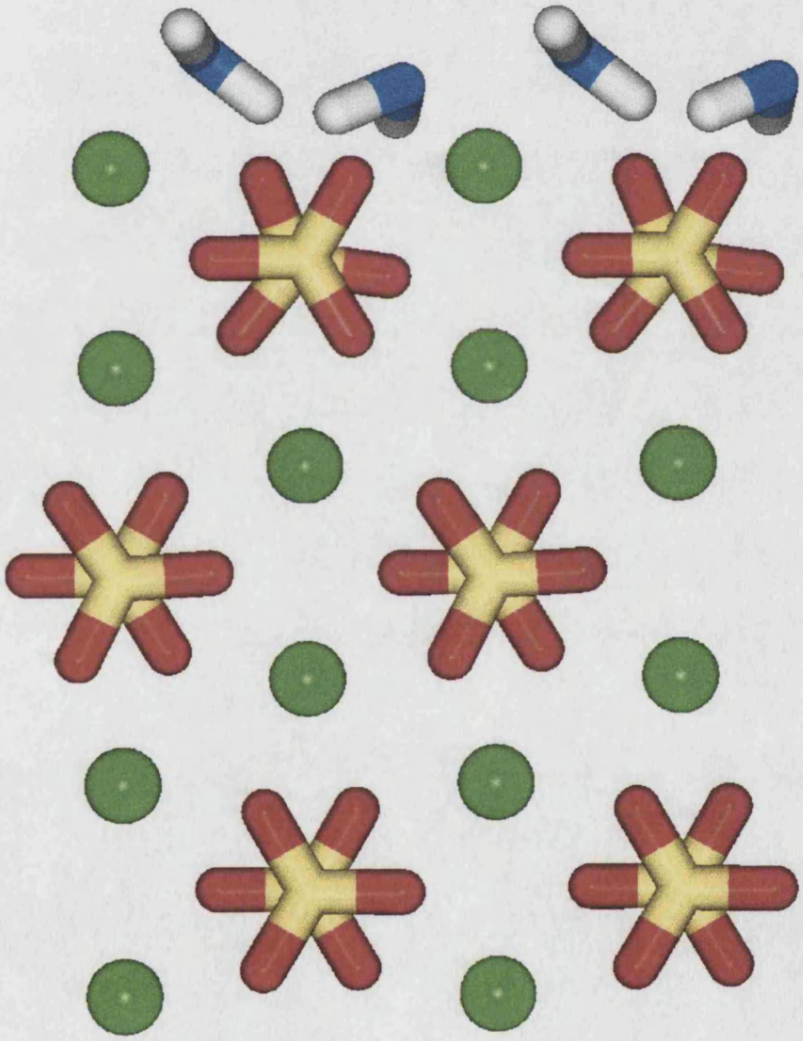

Figure 6.9 Hydrated calcium terminated {010} surface showing bulk termination of the surface and two distinct adsorption patterns for the water molecules. (O = red, Ca = green, C = yellow, O_{water} = blue, H = white)

{100} and {001} Surfaces

The {100} surface is stabilised by hydration with a large hydration energy of -122.6 $kJmol^{-1}$. The calcium terminated {001} plane is stabilised by hydration with a creditable hydration energy of -93.6 $kJmol^{-1}$. The hydrated carbonate plane, however, is even less stable than the pure surface, although the hydration energy shows that adsorption of water is energetically favourable.

{110} Surface

After hydration the {110} carbonate plane shows considerable relaxation from 4.13 Jm^{-2} to 0.81 Jm^{-2}. When viewing the hydrated calcium plane however (fig. 6.10), it is clear that apart from some slight movement in the surface ions, notably a slight tilting of the carbonate groups, no comprehensive rearrangement of the surface layers has taken place. Although both surfaces are non-dipolar, figure 6.10 shows that the calcium plane appears to have surface vacancies due to the arrangement of the calcium ions in the bulk crystal. The water molecules, rather than adsorb above the surface calcium ions, prefer to adsorb with their hydrogen atoms coordinating to two surface oxygens bridging the apparent calcium vacancy between two carbonate groups. The distance between surface calcium and water oxygen ion is 2.53 Å, somewhat larger than average (*ca.* 2.4 Å) but the distances between surface oxygen and the water molecules' hydrogen atoms at 1.51 and 1.56 Å are very short for O---H bonding and clearly the water molecules are closely coordinated to the surface. This

is borne out by the hydration energy, which at -94.6 $kJmol^{-1}$ while not the largest of the series of surfaces, is nevertheless appreciable.

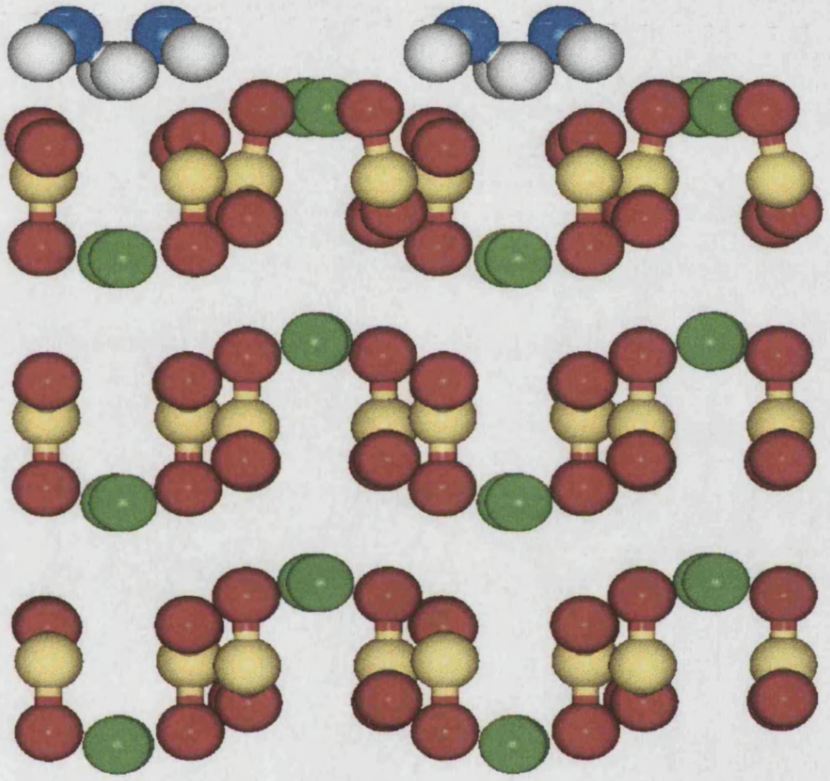

Figure 6.10 Hydrated calcium terminated {110} surface showing bridging of water molecules between surface carbonate groups and bulk-like termination of the surface. (O = red, Ca = green, C = yellow, O_{water} = blue, H = white)

{011} Surface

In contrast to most aragonite surfaces, the most stable of the four {011} planes is not further stabilised by hydration, but shows a considerable increase in surface energy to 1.07 Jm^{-2}. Its hydration energy at -8.2 $kJmol^{-1}$ is the least of the series and shows that adsorption of water onto this plane is only barely energetically favourable. Only two of the four planes show any stabilisation due to hydration, both with very large hydration energies of -113.8 and -133.7 $kJmol^{-1}$.

One of these surfaces (fig. 6.11) has become especially stable with a surface energy of 0.25 Jm^{-2}. The water molecules adsorb in three different positions, two of which are coordinated to a surface calcium ion (2.43-2.49 Å) in addition to coordinating their hydrogen ions to surface oxygen ions (1.48-1.63 Å). The third water molecule is not coordinated to the surface but instead forms connections to the other two water molecules which are coordinating with their hydrogen atoms to its oxygen atom. As such an extensive network between the water molecules themselves is formed which greatly stabilises the adsorption.

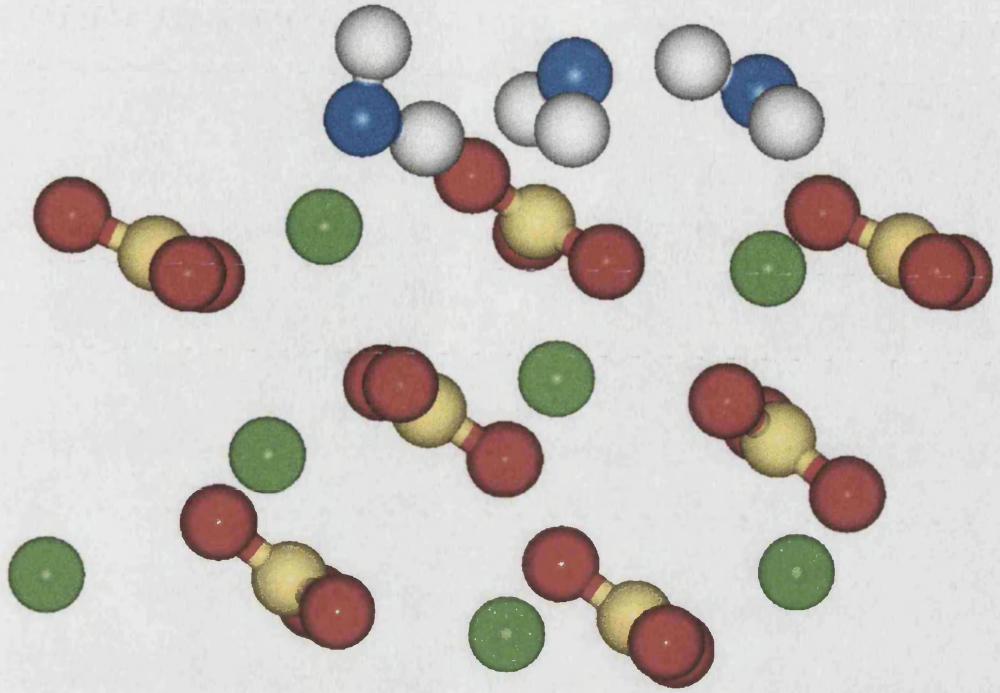

Figure 6.11 Hydrated calcium terminated {011} surface showing three adsorption patterns for water molecules including extensive intermolecular hydrogen-bonding. (O = red, Ca = green, C = yellow, O_{water} = blue, H = white)

{101} and {111} Surfaces

Both hydrated {101} planes have comparable surface energies and are stabilised by hydration to a similar extent. In the hydrated form the {101} surface is expressed in the calculated morphology, although in the unhydrated morphology this surface is overshadowed by the {111} surface which is not, however, expressed in the experimental morphology (Deer *et al.* 1992).

All four {111} surfaces are stabilised by hydration but none of the hydrated planes becomes especially stable despite extensive relaxation.

6.6 Vaterite

Vaterite, a metastable form of calcium carbonate and precursor of calcite and aragonite, is hexagonal with spacegroup P63 and a = b = 4.13 Å, c = 8.48 Å, $\alpha = \beta = 90^0$ and $\gamma = 120^0$ (Deer et al. 1992). However, there is considerable disorder of the carbonate molecules leading to partial occupancies of different carbonate sites. For this reason we have used the experimental structure elucidated by Meyer (1960) which uses spacegroup Pbnm to describe the crystal without allowing for carbonate disorder. The unit cell is twice the size of the original cell and the vectors and angles now become a = 4.13 Å, b = 7.15 Å, c = 8.48 Å, $\alpha = \beta = \gamma = 90^0$ which after energy minimisation relaxed to a = 4.43 Å, b = 6.62 Å, c = 8.04 Å and $\alpha = \beta = \gamma = 90^0$.

6.6.1 Pure Surfaces

In this structure all surfaces have both calcium and carbonate terminated planes. The surface and attachment energies are given in table 6(VII).

Surface and Attachment Energies of Vaterite			
Surface	$\gamma_{unrelaxed}$ / Jm^{-2}	$\gamma_{relaxed}$ / Jm^{-2}	E_{att} / $kJmol^{-1}$
{010}Ca	2.84	1.35	-342.8
{010}CO_3	0.78	0.62	- 79.9
{100}Ca	2.24	1.31	-168.6
{100}CO_3	1.76	1.39	-137.1
{001}Ca	3.15	1.40	-294.9
{001}CO_3	4.34	1.58	-373.1
{110}Ca	2.53	1.18	-249.9
{110}CO_3	1.69	1.04	-149.1
{011}Ca	2.98	1.22	-577.0
{011}CO_3	1.29	0.93	-186.6
{101}Ca	2.07	1.47	-186.2
{101}CO_3	1.91	1.07	-176.2
{111}Ca	1.64	0.82	-187.6
{111}CO_3	2.25	0.85	-245.4

Table 6(VII) Surface and attachment energies of unhydrated vaterite

{010} Surface

From table 6(VII) it is clear that the {010} carbonate plane is a very dominant surface with the lowest surface energy and the smallest attachment energy of the series. Although the calcium terminated plane is dipolar and hence is given vacancies in its surface, the carbonate plane is non-dipolar and the pure surface does not relax appreciably (*cf.* unrelaxed surface energy of 0.78 Jm^{-2} versus relaxed surface energy of 0.62 Jm^{-2}).

{100} and {001} Surfaces

Both the calcium and the carbonate terminated {100} surfaces have comparable and rather high surface energies when unhydrated. From the relaxed surface energies the calcium plane is thermodynamically more stable than the carbonate plane. In line with the unrelaxed surface energies the carbonate terminated plane has the smaller attachment energy and hence is more important in the growth form.

The {001} surfaces are dipolar planes and their surface and especially attachment energies are even higher than those of the {100} planes. Energy minimisation of both planes shows extensive relaxation and rearrangement of the surface, especially the carbonate plane whose unrelaxed surface energy of 4.34 Jm^{-2} drops to 1.58 Jm^{-2}. The surface calcium ions on the calcium terminated surface relax into the second, carbonate layer, some of which rotate all the oxygen atoms to coordinate to the relaxed calcium ions. In the carbonate plane, the surface carbonate groups rotate to lie flat in the surface.

{110}, {011}, {101} and {111} Surfaces

The {110} and {011} surfaces both have dipolar calcium terminated planes while the carbonate planes are non-dipolar. The {110} calcium terminated plane again shows extensive relaxation although the carbonate plane is still the more stable.

The {101} surfaces have dipolar planes and when unhydrated the carbonate plane has the lower surface energy although the attachment energies are very similar.

Both terminations of the {111} surfaces have similar surface energies although the attachment energy of the calcium plane is lower, making this plane kinetically the more important surface.

6.6.2 Hydrated Surfaces

We now consider the hydrated surfaces of vaterite. Table 6(VIII) shows the surface and hydration energies of the hydrated surfaces considered in this study.

Surface and Hydration Energies of Hydrated Vaterite		
Surface	$\gamma_{hydrated}$ / Jm^{-2}	$E_{hydration}$ / $kJmol^{-1}$
{010}Ca	0.91	- 91.7
{010}CO_3	0.22	- 86.8
{100}Ca	0.69	-111.0
{100}CO_3	0.55	-134.1
{001}Ca	0.70	- 85.9
{001}CO_3	0.82	-111.9
{110}Ca	0.52	-129.3
{110}CO_3	0.63	- 98.4
{011}Ca	0.82	-100.3
{011}CO_3	0.26	-106.7
{101}Ca	0.35	-181.4
{101}CO_3	0.68	-115.8
{111}Ca	0.51	- 88.8
{111}CO_3	0.69	- 78.1

Table 6(VIII) Surface and hydration energies of vaterite

{010} Surface

The surface energy of the hydrated carbonate surface changes considerably on energy minimisation, from 3.15 to 0.22 Jm^{-2}, but as figure 6.12 shows, this is due to rotation of the water molecules rather than rearrangement of the surface lattice ions. The water molecules adsorb in two distinct ways, both however are coordinated to a calcium ion and one lattice oxygen. The water molecules are too far apart for any hydrogen-bonding to take place. The oxygen atoms of the water molecules appear to move into sites which would be occupied by lattice oxygens if another layer of material was deposited on the surface. This is similar to adsorption of water onto the MgO {310} surface (chapter 4), where we found that water molecules would adsorb with their oxygen on a lattice oxygen site and hydrogens pointing towards magnesium sites.

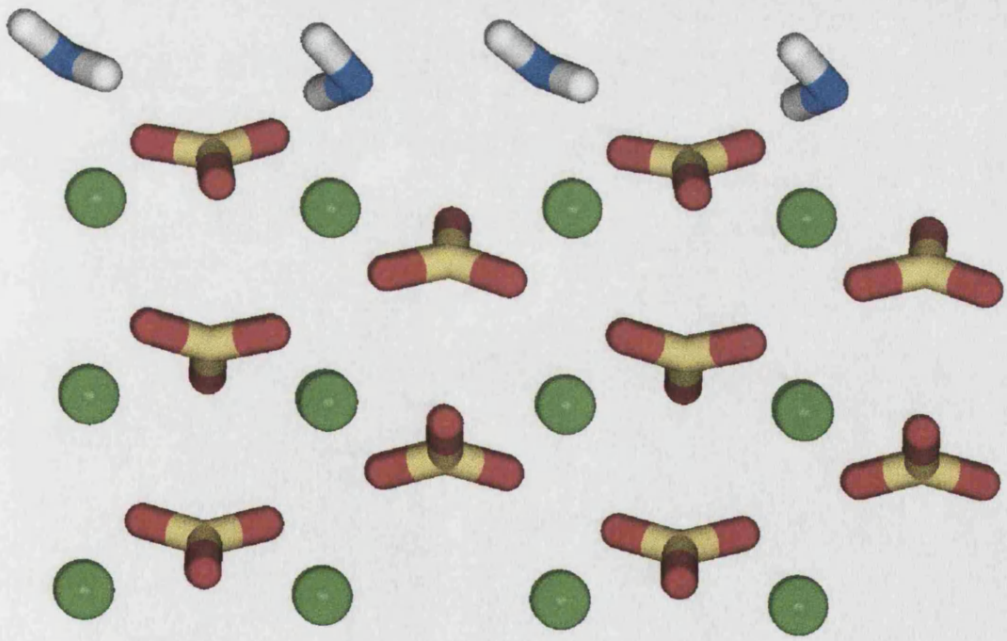

Figure 6.12 Hydrated carbonate {010} surface showing bulk termination and different modes of adsorption for the water molecules (O = red, Ca = green, C = yellow, O_{water} = blue, H = white)

{100} and {001} Surfaces

Adsorption of water stabilises both {100} terminations, the carbonate plane now becoming more stable than the calcium surface. The hydration energies are amongst the highest of the series.

Again, both {001} terminations are stabilised by hydration. The hydrated carbonate plane (fig. 6.13) shows that the surface carbonate groups have again rotated to lie flat in the plane. Some of the water molecules have moved into the carbonate vacancies created when removing the dipole. These are closely coordinated to a calcium ion (2.45 Å) and within H-bond distance of a lattice oxygen (1.6 Å). The other water molecules which are adsorbed on top rather than in the surface, are all coordinated to the surface oxygen ions by their hydrogen atoms (1.53-1.61 Å). In addition to this coordination to the surface, there is an extensive network of hydrogen-bonding between the adsorbed water molecules with O---H distances ranging from 1.79 Å to 1.96 Å.

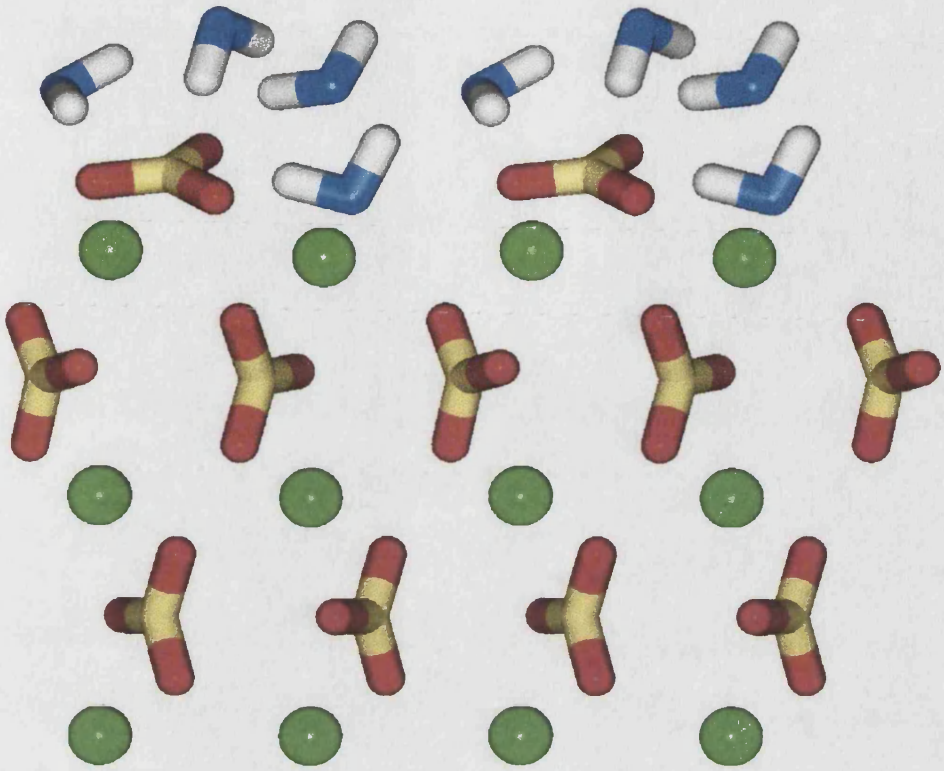

Figure 6.13 Hydrated carbonate {001} surface showing rotated surface carbonate groups and clustering of the water molecules in the surface vacancies. (O = red, Ca = green, C = yellow, O_{water} = blue, H = white)

{110} and {011} Surfaces

Both {110} planes are stabilised by water adsorption, the calcium terminated surface, which is dipolar, more so than the carbonate plane. The former also shows extensive relaxation and rearrangement on energy minimisation of its unhydrated plane (unrelaxed surface energy of 2.53 Jm^{-2} versus relaxed surface energy of 1.18 Jm^{-2}). Although unhydrated it is less stable than the carbonate plane, after adsorption it has a lower surface energy although neither plane is expressed in the morphology.

The {011} carbonate plane is non-dipolar and this surface, like the carbonate {010} plane, is remarkably stabilised by water adsorption from 0.93 Jm^{-2} to 0.26 Jm^{-2}, one of the most stable surfaces.

{101} and {111} Surfaces

After hydration the {101} calcium plane has become much more stable than the carbonate plane with a very low surface energy of 0.35 Jm^{-2} and at -181.4 $kJmol^{-1}$ it also has the largest hydration energy of the series of surfaces. Similar to the hydrated carbonate {001} surface, some of the water molecules on the calcium terminated {101} surface cluster in the calcium vacancies created when removing the dipole. One of the water molecules has moved into the surface coordinating to both a calcium (2.38 Å) and a carbonate oxygen (1.54 Å) in the second layer and another oxygen (1.49 Å) in the first carbonate layer. The second water molecule is also coordinated to a calcium ion (2.54 ÅA) and an oxygen ion (1.66 Å) in the second layer, while the topmost water molecule is closely coordinated to a surface calcium (2.37 Å) and oxygen ion (1.65 Å). There is no appreciable coordination between the water molecules themselves, although the two inner water molecules are at a rather long O---H distance of 2.1 Å.

We found for the {111} planes that both terminations are stabilised by hydration, the calcium terminated surface more so than the carbonate plane, as with most of the previous surfaces. The calcium plane is dipolar which gives the water molecules scope to adsorb in the surface vacancies. However, in addition to adsorbing in the

vacancies some water molecules cluster around the calcium ions in the second calcium layer (2.43-2.72 Å) and through O---H coordination form a bridge between the adjoining carbonate groups. The third water molecule does adsorb near the calcium vacancy closely coordinated to the other calcium ion (2.38 Å) and hydrogen bonded to two adjoining carbonate groups (1.68-1.87 Å). There is relatively little relaxation of the surface carbonate groups, although the calcium ions in the first few layers have relaxed towards the water molecules.

6.7 Discussion

The clearest result is that water molecules strongly prefer to coordinate to calcium ions, with H-bonding to the surface oxygen ions a significant but secondary effect. Even on surfaces which are greatly stabilised by water adsorption, the water molecules themselves usually do not interact significantly which each other, indicating that adsorption to the surface outweighs possible intermolecular interactions between the water molecules, such as hydrogen-bonding. These findings agree with the results obtained when hydrating MgO crystals (chapter 4), where we found that the Mg-H_2O interactions outweighed by far any intermolecular interactions between the water molecules.

All calcite and vaterite surfaces are stabilised by the adsorption of a monolayer of water. However, the $\{10\bar{1}4\}$ surface of calcite is still the dominant surface in both the unhydrated form and in aqueous environment. The dominance of the $\{10\bar{1}4\}$ plane agrees with experimental work by, for example, Ohnesorge and Binnig (1993) in

their AFM study of calcite in water and Heywood and Mann (1994) who showed optical micrographs of rhombohedral calcite crystals expressing the $\{10\bar{1}4\}$ face under aqueous conditions while Didymus *et al.* (1993), Goni *et al.* (1993) and Beruto and Giordani (1993) all show SEM micrographs containing rhombohedal calcite crystals under vacuum condition.

Apart from the planar $\{10\bar{1}4\}$ surface, the unhydrated $\{10\bar{1}3\}$ and the $\{10\bar{1}5\}$ planes are the most stable of the surfaces studied. As such they are good models for the experimental $\{10\bar{1}4\}$ surface including steps.

The very low surface energy of the hydrated $\{10\bar{1}4\}$ surface of 0.16 Jm^{-2} agrees well with the experimental surface energy of the natural cleavage plane found by Gilman (1960) of 0.23 Jm^{-2}, particularly when taking into account that the experimental surface was mechanically cut and will contain steps and other dislocations which would increase the surface energy as was seen from the higher surface energies of the stepped planes.

The hydration energies of calcite range from -138.5 $kJmol^{-1}$ for the very hydrophilic $\{11\bar{2}0\}$ surface to -79.2 $kJmol^{-1}$ for the calcium terminated $\{0001\}$ surface. This is in good agreement with the binding energy quoted by Liang *et al.* (1996) of -110.9 $kJmol^{-1}$ for water molecules adsorbed onto calcite, especially with our range of hydration energies of -93.9 to -117.7 $kJmol^{-1}$ for the dominant $\{10\bar{1}4\}$ surface and its stepped counterparts, the $\{10\bar{1}3\}$ and $\{10\bar{1}5\}$ surfaces.

Some of the aragonite surfaces, namely the carbonate {010} and, to a much lesser extent, the {001} plane have been destabilised by the adsorption of water. The {010} carbonate plane is more unstable than the calcium terminated surface, both in unhydrated and hydrated state and its attachment energy is much larger. The unhydrated {001} carbonate plane on the other hand has a lower surface energy and smaller attachment energy than its calcium counterpart, while on hydration the calcium plane becomes considerably more stable.

The large stabilisation of the calcium {010} surface confirms the suggestion of Aquilano and Rubbo (1996) who noted that the aragonite (010) surface was similar to that expressed by natural gypsum. They argued that the natural epitaxy of aragonite and gypsum implied that the (010) surface of aragonite must fit well on the water double layer of (010) gypsum, from which they implied that water on the aragonite (010) surface adsorbs in a quasi-ordered layer and stabilises this surface.

6.7.1 Morphology

Wulff (1901) and Gibbs (1928) showed that equilibrium morphologies can be obtained from the surface energies (tables 6(III) to (VIII)) (chapter 2.1.6). In contrast, a growth morphology is obtained from the attachment energies (Hartman and Bennema 1980) which relates the attachment energies to the rate of growth. The morphologies of calcite are shown in figure 6.14. The equilibrium morphology of the unhydrated crystal shows a residual $\{10\bar{1}1\}$ face, the effect of relaxation which disappears on hydration and does not show in the growth morphology, in agreement

with the experimental morphology where only the dominant $\{10\bar{1}4\}$ face is expressed (Didymus *et al.* 1993, Archibald *et al.* 1996).

(a) (b)

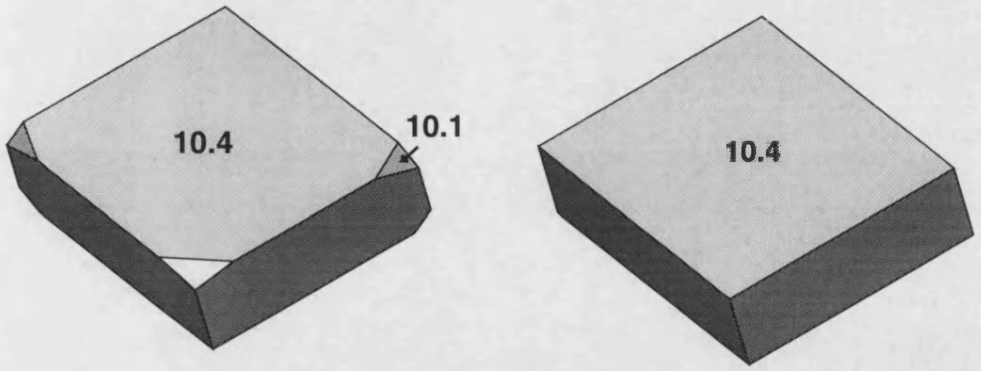

Figure 6.14 (a) Equilibrium morphology of unhydrated calcite and (b) kinetic morphology and equilibrium morphology of hydrated calcite

The equilibrium morphology of the hydrated aragonite crystal (fig. 6.15d) resembles the experimental morphology (fig. 6.15a) more closely than the unhydrated form (fig. 6.15b), which expresses the {111} surface, which is not found experimentally (Dana 1958). The unhydrated morphology also has some residual {001} face which is sometimes found experimentally (Deer *et al.* 1992). The calculated hydrated morphology agrees very well with the experimental morphology, being elongated and expressing the {010}, {011} and {110} faces (Dana 1958), although the {101} face is too stable compared to experimental morphologies. Heywood and Mann (1994) found that the predominant morphological form of aragonite expresses the {110} faces. The growth morphology (fig. 6.15c) shows the {011} and {110} faces in agreement with experiment (Deer *et al.* 1992) but not the {010} plane.

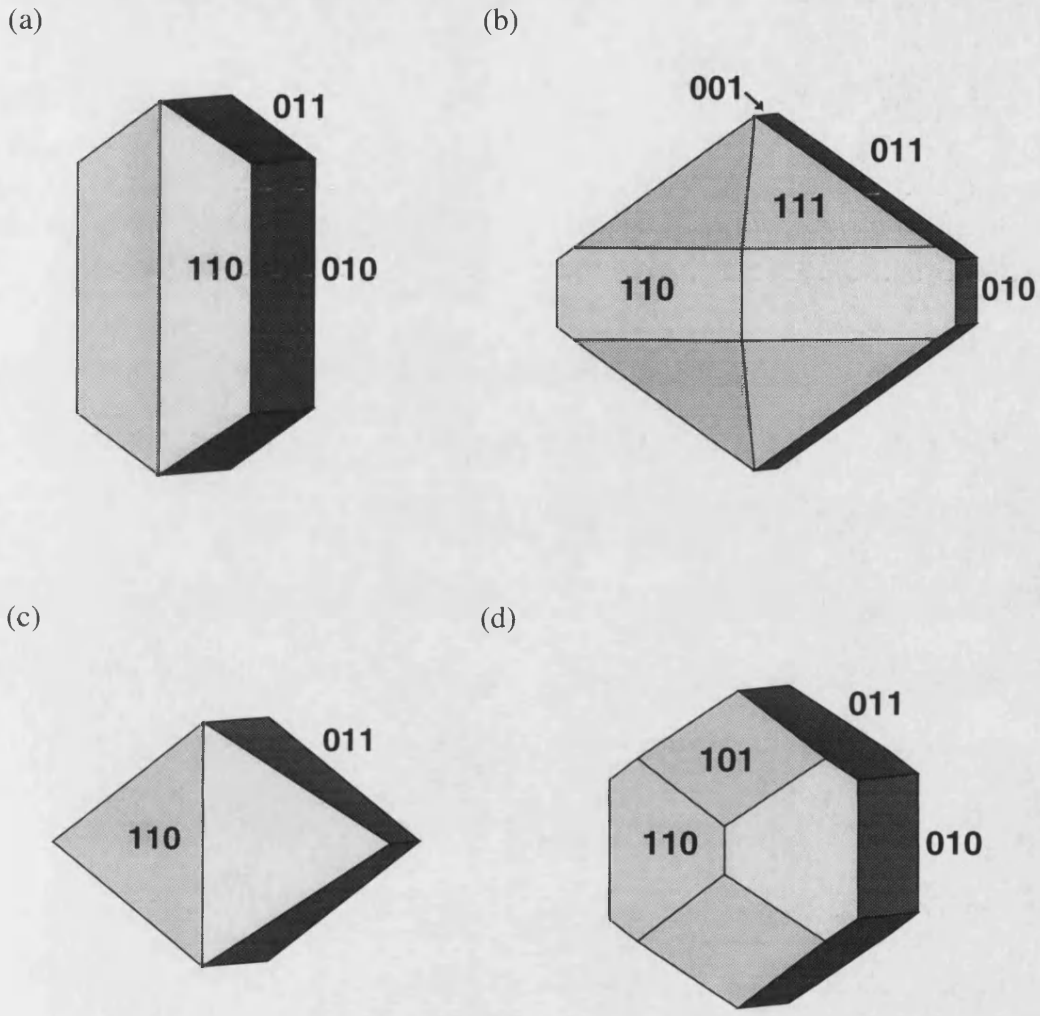

Figure 6.15 (a) Experimental morphology, (b) equilibrium morphology of unhydrated aragonite, (c) kinetic morphology and (d) equilibrium morphology of hydrated aragonite crystal

Less is known about the experimental morphology of vaterite under neutral conditions, other than that it can be found as spheres comprising needle-like units (Chakraborty *et al.* 1994) or ellipsoidal (Kabasci *et al.* 1996) and disc-like crystals (Didymus *et al.* 1993, Brecevic *et al.* 1996) The unhydrated equilibium morphology (fig. 6.16a) does not resemble either needles or discs although it is somewhat

ellipsoidal, as is the growth morphology (fig. 6.16b). The hydrated morphology (fig. 6.16c) is more disc-like in line with observed morphology.

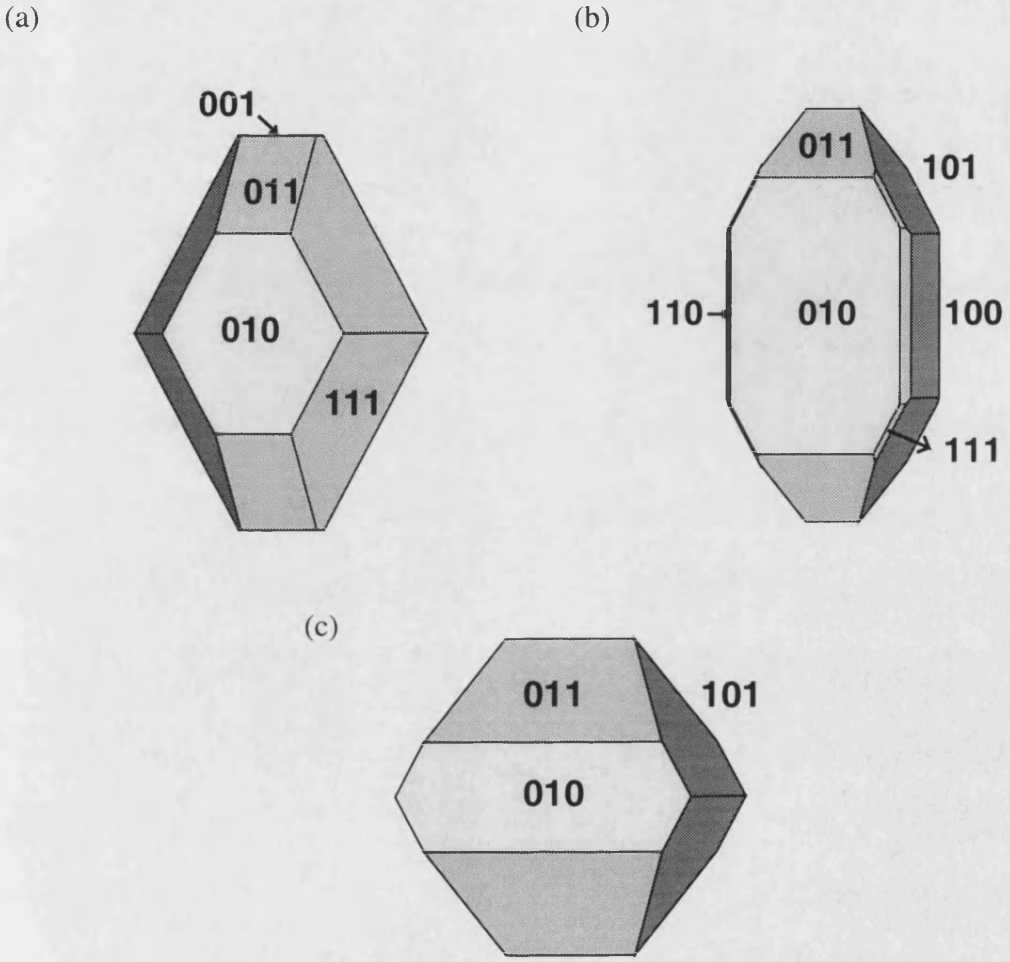

Figure 6.16 (a) Equilibrium morphology of unhydrated vaterite crystal, (b) kinetic morphology and (c) equilibrium morphology of hydrated vaterite crystal

According to Gibbs (1928) the energy of a crystal is made up of two components, a surface component which is important when the crystals are small, and a bulk component which becomes dominant at larger volumes:

$$E = \sum_i \gamma_i A_i + E_{lattice} \qquad (6.1)$$

where A is the surface area. The bulk lattice energies of calcite, aragonite and vaterite are given in table 6(IX). It is clear that at large volumes, when the surface component has become insignificant, aragonite will be the most stable form of calcium carbonate. These calculations have ignored temperature and zero point energy and the surface energies do not take into account entropy. Previous work has shown that these are not critical approximations and our findings agree with experiment, *i.e.* calcite is only more stable than aragonite because of its higher entropy (Beruto and Giordani 1993, Tauson *et al.* 1993).

The surface component at any given volume for the three polymorphs is always positive and for the hydrated surfaces can be expressed as a ratio which we found to be Calcite : Aragonite : Vaterite of 1.0 : 2.0 : 1.6. Thus when the crystals are small enough for the bulk lattice energy to be insignificant calcite is more stable than either aragonite or vaterite, although vaterite will be more stable than aragonite. This confirms that when vaterite is observed in calcium carbonate precipitation (Chakraborty and Bhatia 1996) this is due to kinetic rather than thermodynamic factors.

Polymorph	**Bulk Lattice Energy / 10^8 kJm^{-3}**
Calcite	-1.6867
Aragonite	- 1.7851
Vaterite	- 1.6577

Table 6(IX) Bulk lattice energies of calcium carbonate polymorphs

6.8 Summary and Conclusion

We have investigated the effect of hydration on the surface structure and morphology of the low-index planes of calcite, aragonite and vaterite. As a result we can make the following observations:

Our calculated crystallographic structure and dissolution energy of ikaite agree very well with experimental values (Dickens and Brown 1970, Bischoff *et al.* 1993). The surface and hydration energies for calcite are in excellent agreement with experimental findings (Gilman 1960) and previous calculations (Liang *et al.* 1996) giving confidence that they are also accurate for aragonite and vaterite.

When surfaces with two or more possible cuts are terminated by carbonate planes, the surfaces where the carbonate groups are lying flat will usually show bulk-terminations, but the surfaces where the carbonate groups are upright will display rotation of these groups to lie flat in the surface.

The $\{10\bar{1}4\}$ surface is the most stable surface of calcite. Hydration of the surfaces has a stabilising effect and when hydrated, the equilibrium morphology agrees with the experimentally found morphology as does the growth morphology. The $\{10\bar{1}3\}$ and $\{10\bar{1}5\}$ surfaces are good models for the experimental $\{10\bar{1}4\}$ surface including growth steps.

The $\{10\bar{1}4\}$ surface exhibits the same 1 x 1 symmetry and structural features of the surface oxygen ions as is found experimentally (Ohnesorge and Binnig 1993, Liang *et al.* 1996). Our calculations showed a distinct relaxation or rotation of differently oriented but otherwise equivalent surface carbonate groups when the surface is partially hydrated.

In agreement with LEED experiments (Stipp and Hochella 1991) the $\{10\bar{1}1\}$ surface and also the $\{11\bar{2}0\}$ plane both exhibit bulk-like termination of the surface with only some rotation of surface carbonate groups.

The calculated equilibrium morphology of the hydrated aragonite closely resembles its experimental morphology (Deer *et al.* 1992).

The stability and regularity of the hydrated {010} surface of aragonite confirms the theory of Aquilano and Rubbo (1996) based on natural epitaxy of aragonite (010) and gypsum (010) surfaces that the aragonite (010) surface should be stabilised by an ordered water layer to be able to fit well onto hydrated gypsum (010).

The calculated equilibrium morphology of the hydrated vaterite crystals resembles discs in agreement with vaterite crystals found by Didymus *et al.* (1993). The unhydrated and growth morphologies are elongated and perhaps more needle-like (Chakraborty *et al.* 1994).

The bulk lattice energies of the three polymorphs reflect their thermodynamic stability, in that the stability of calcite over aragonite is due to its higher entropy

content at elevated temperatures rather than its bulk lattice energy, which favours aragonite.

The relative surface contributions of the polymorphs show that in the crystal nucleation stage calcite is the most stable form while aragonite becomes more stable when the crystal is large enough for the bulk lattice energy to outweigh the surface energy terms.

In the future, we aim to extend our study to include dynamics to model the effect of temperature on the solid properties of the different polymorphs, investigating solid-solid phase changes, and the dynamics of interactions between water and calcium carbonate surfaces.

SUMMARY and CONCLUSION

In this thesis we have shown how atomistic simulation techniques can give an insight into the changes in structure and stability of a range of materials on adsorption of water. We have developed a polarisable water potential which is compatible with the potential models which are currently widely used in atomistic simulations, and most importantly, the water potential was shown to be transferable to different oxides and worked well for each example.

In chapter 4 we described the results obtained from simulations of water chemisorption and physisorption onto CaO and MgO surfaces in a series of partial coverages. Firstly the pure surfaces were studied and it was found that facetting of the more unstable {110} and {111} surfaces, exposing planes of the very stable {100} surface, decreased their surface energy considerably in agreement with the fact that these facetted surfaces have been observed experimentally and are inert against annealing.

The pattern of chemisorption on CaO and MgO is similar although the hydration energies show that CaO is more readily hydroxylated than MgO, especially the {100} surface which in MgO is not very amenable to hydroxylation in agreement with experiment and previous calculations. Physisorption on MgO is energetically favourable on all surfaces, although the three- and four-coordinated sites are preferred over the five-coordinated sites of the perfect {100} plane. However, hydroxylation of the edges on the {310} surface encourages physisorption on the

adjacent five-coordinated surface sites. The interactions between surface cations and the water molecules' oxygen atoms outweigh any intermolecular interactions between the water molecules themselves.

Molecular Dynamics simulations of physisorption of the {100} and {310} surfaces of MgO in a liquid water environment show that physisorption becomes energetically favourable only at lower densities. Adsorption on the {100} surface shows that 75% coverage is preferred in agreement with our static calculations.

In chapter 5 we have investigated chemisorption and physisorption of water onto a collection of α-alumina surfaces comparing two different potential models. Both models show the extensive relaxation in the basal plane reported in previous computational studies. The equilibrium morphologies agree well with experimental morphologies although the growth morphology does not. Although the two potentials give quite different surface energies for the unhydrated surfaces, the hydrated surface energies depend more on relaxation of the adsorbed species and hence the hydration energies are similar and independent of the potential model used. They are in good agreement with experimental hydration energies both for chemisorption and physisorption.

Chapter 6 compares three calcium carbonate polymorphs calcite, aragonite and vaterite and studies physisorption of water on their surfaces. We find that surface carbonate groups rotate to lie flat in the surface, but that otherwise surfaces do not relax significantly from the bulk termination. The hydrated equilibrium morphologies

agree with experimental morphologies where known. The bulk lattice energies of the three polymorphs correctly predict the aragonite form to be thermodynamically the most stable phase, while calcite is the most stable form in the crystal nucleation stage.

The calcite $\{10\bar{1}4\}$ surface is the most stable surface of calcite, it shows 1 x 1 symmetry and the same structural features of the partially hydrated plane as are found experimentally. The $\{10\bar{1}3\}$ and $\{10\bar{1}5\}$ planes are good models for the experimental stepped $\{10\bar{1}4\}$ surface.

In future it would be interesting to extend the molecular dynamics simulations on MgO to include the physisorption of the {310} surface with hydroxylated step edges to ascertain whether the stabilisation of the five-coordinated sites on the plane found in the static calculations also occurs in a liquid water environment. An MD simulation of the facetted {110} surface should also give more insight of behaviour of water molecules at four-coordinated step sites. The next step would then be to introduce Mg^{2+} and O^{2-} species in the simulation to model crystal growth on the various surfaces, and possibly H_3O^+ to adjust pH to allow for a more realistic environment. Further work on static calculations could include the modelling of etch pits which have been observed experimentally on the MgO {100} surface and dissolution of MgO units from low-coordinated sites.

Future work on the calcium carbonate polymorphs could include modelling the phase transitions between the polymorphs and using MD to model the interaction of water with the surfaces. Steps and dislocations are important in calcite growth and hence these could be the subject of further static calculations.

In addition to MD simulations of hydration of the various surfaces further static calculations on α-alumina could include a series of partial coverages of chemi- and physisorption of water on the surfaces. A different area would be to carry out *ab initio* calculations of initially the unhydrated surfaces to compare the surface energies obtained in this way and hence the equilibrium morphology with the surface energies from the two potential models to see whether the morphologies may be similar even though the absolute surface energies are different. Further electronic structure calculations could then include hydroxylated surfaces, for instance the oxygen terminated basal plane. A further area of research would be the study of water adsorption on silica and alumino silicates, such as zeolites.

References

Abriou D., Creuzet F., Jupille J., *Surf. Sci.*, **352**, 499, (1996)

Allen N.L., Mackrodt W.C., *Phil. Mag. B*, **69**, 871, (1994)

Allen M.P., Tildesley D.J., *Computer Simulation of Liquids*, Oxford University Press, Oxford, (1993)

Anderson P.J., Horlock R.F., Oliver J.F., *Trans. Faraday Soc.*, **61**, 2754, (1965)

Aquilano D, Rubbo M., *Mater. Sci. Forum*, **203**, 193, (1996)

Archibald D.D., Qadri S.B., Gaber B.P., *Langmuir*, **12**, 538, (1996)

Baram P.S., Parker S.C., *Phil. Mag. B*, **73**, 49, (1996)

Barrett N.T., Guillot C., Villette B., Treglia G., Legrand B., *Surf. Sci.*, **251**, 717, (1991)

Baudin M., Wojcik M., Hermansson K., *Surf. Sci.*, **375**, 374, (1997)

Bernardo D.N., Ding Y., Krogh-Jespersen K., Levy R.M., *J. Phys. Chem.*, **98**, 4180, (1994)

Bertaut F., *Compt. Rendu*, **246**, 3447, (1958)

Beruto D., Searcy A.W., Botter R., Giordani M., *J. Phys. Chem.*, **97**, 9201, (1993)

Beruto D., Giordani M., *J. Chem. Soc. Faraday Trans.*, **89**, 2457, (1993)

Binnig G., Rohrer H., Gerber Ch., Weibel E., *Phys. Rev. Lett.*, **49**, 57, (1982)

Binnig G., Quate C.F., Gerber Ch., *Phys. Rev. Lett.*, **56**, 930, (1986)

Bischoff J.L., Fitzpatrick J.A., Rosenbauer R.J., *J. Geology*, **101**, 21, (1993)

Blanchard D.L., Baer D.R., *Surf. Sci.*, **276**, 27, (1992)

Boettger J.C., *Phys. Rev. B*, **55**, 750, (1997)

Born M., Huang K., *Dynamical Theory of Crystal Lattices*, Oxford University Press, Oxford, (1954)

Boily J.-F., Fein J.B., *Geochim. Cosmochim. Acta*, **60**, 2929, (1996)

Brecevic L., Nothig-Laslo V., Kralj D., Popovic S., *J. Chem. Soc. Faraday Trans.*, **92**, 1017, (1996)

Bridgeman C.H., Skipper N.T., *J. Phys.: Condens. Matter*, **9**, 4081, (1997)

Brodtholt J., Sampoli M., Vallauri R., *Mol. Phys.*, **85**, 81, (1995)

Brodtholt J., Sampoli M., Vallauri R., *Mol. Phys.*, **86**, 149, (1995a)

Burghgraef H., Jansen A.P.J., Van Santen R.A., *Faraday Discuss.*, **96**, 337, (1993)

Busing W.R., Levy H.A., *Acta Cryst.*, **11**, 798, (1958)

Campbell I.M., *Catalysis at Surfaces*, Chapman and Hall Ltd, London, (1988)

Car R., Parrinello M., *Phys. Rev. Lett.*, **55**, 2471, (1985)

Catlow C.R.A., Norgett M.J., *UKAEA Report AERE-M2936*, (1976)

Catlow C.R.A., *Proc. R. Soc. A*, **333**, 533, (1977)

Catlow C.R.A., *J. de Physique*, **41C6**, 53, (1980)

Catlow C.R.A., Cormack A.N., *Chemistry in Britain*, 627, (1982)

Catlow C.R.A., James R., Mackrodt W.C., Stewart R.F., *Phys. Rev. B Condens. Matter*, **25**, 1006, (1982)

Catlow C.R.A., Mackrodt W.C., *Computer Simulation of Solids*, Springer Verlag, Berlin, (1982)

Catlow C.R.A., Cormack A.N., Theobald F., *Acta Cryst. B*, **40**, 195, (1984)

Catlow C.R.A., Freeman C.M., Islam M.S., Jackson R.A., Leslie M., Tomlinson S.M., *Phil. Mag. B*, **58**, 123, (1988)

Catlow C.R.A., Gale J.D., Grimes R.W., *J. Solid State Chem.*, **106**, 13, (1993)

Catlow C.R.A., Baram P.S., Parker S.C., Purton J., Wright K.V., *Phil. Trans. R. Soc. Lond. A*, **350**, 265, (1995)

Catlow C.R.A., *Computer Modelling in Inorganic Crystallography*, ed. C.R.A. Catlow, Academic Press, London, (1997)

Causa M., Dovesi R., Pisani C., Roetti C., *Surf. Sci.*, **175**, 551, (1986)

Chakraborty D., Agarwal V.K., Bhatia S.K., Bellare J., *Ind. Eng. Chem. Res.*, **33**, 2187, (1994)

Chakraborty D., Bhatia S.K., *Ind. Eng. Chem. Res.*, **35**, 1995, (1996)

Chang F-R.C., Skipper N.G., Sposito G., *Langmuir*, **11**, 2734, (1995)

Ching W.Y., Xu Y.-N., *J. Am. Ceram. Soc.*, **77**, 404, (1994)

Cicerone D.S., Regazzoni A.E., Blesa M.A., *J. Colloid Interface Sci.*, **154**, 423, (1992)

Clarkson J.R., Price T.J., Adams C.J., *J. Chem. Soc. Faraday Trans.*, **88**, 243, (1992)

Cleveland J.P., Schaffer T.E., Hansma P.K., *Phys. Rev. B.*, **52**, R8692, (1995)

Colbourn E.A., Mackrodt W.C., *Surf. Sci.*, **117**, 571, (1982)

Colbourn E.A., Mackrodt W.C., Tasker P.W., *J. Mater. Sci.*, **18**, 1917, (1983)

Colbourn E.A., Mackrodt W.C., *Physica B*, **131**, 41, (1985)

Colbourn E.A., *Surf. Sci. Reports*, **15**, 281, (1992)

Coluccia S., Tench A.J., Segall R.L., *J. Chem. Soc. Faraday Trans. 1*, **75**, 1769, (1979)

Coluccia S., Barton A., Tench A.J., *J. Chem. Soc. Faraday Trans 1*, **77**, 2203, (1981)

Compton R.G., Brown C.A., *J. Colloid Interface Sci.*, **165**, 445, (1994)

Coustet V., Jupille J., *Surf. Sci.*, **307**, 1161, (1994)

Coustet V., Jupille J., *Il Nuovo Cimento*, in press, (1997)

Curtiss L.A., Frurip D.J., Blander M., *J. Chem. Phys.*, **71**, 2703, (1979)

Cvetanovic R.J., Amenomiya Y., *Catal. Rev.*, **6**, 21, (1972)

Dana E.S., *A Textbook of Mineralogy*, John Wiley & Sons Inc., New York, (1958)

Dang L.X., Pettitt B.M., *J. Phys. Chem.*, **91**, 3349, (1987)

Davidon W.C., *AEC Report ANL-5990*, (1959)

Davids J.A., Fuller C.C., Cook A.D., *Geochim. Cosmochim. Acta*, **51**, 1477, (1987)

Davies M.J., Kenway P.R., Lawrence P.J., Parker S.C., Mackrodt W.C., Tasker P.W., *J. Chem. Soc. Faraday Trans.*, **85**, 555, (1989)

Delville A., Letellier M., *Langmuir*, **11**, 1361, (1995)

Deer W.A., Howie R.A., Zussman J., *Introduction to the Rock Forming Minerals*, Longman, Harlow, UK, (1992)

Deleuze M., Brantley S.L., *Geochim. Cosmochim. Acta*, **61**, 1475, (1997)

Della Gatta G., Fubini B., Stradella L., *J. Chem. Soc. Faraday Trans. 2*, **73**, 1040, (1977)

Dick B.G., Overhauser A.W., *Phys. Rev. B*, **112**, 90, (1958)

Dickens B. and Bowen J.S., *Journal of Research of National Bureau of Standards, Section A. Physics and Chemistry*, **75**, 27, (1971)

Didymus J.M., Oliver P.M., Mann S., De Vries A.L., Hauschka P.V., Westbroek P., *J. Chem. Soc. Faraday Trans.*, **89**, 2891, (1993)

Didymus J.M., Mann S., Benton W.J., Collins I.R., *Langmuir*, **11**, 3130, (1995)

Dorsey N.E., *Properties of ordinary Water-Substance*, Reinhold Publishing Corporation, New York, (1940)

Dove P.M., Hochella M.F., *Geochim. Cosmochim. Acta*, **57**, 705, (1993)

Duan Z., Moller N., Weare J.H., *Geochim. Cosmochim. Acta*, **59**, 3273, (1995)

Duffy D.M., Tasker P.W., *Phil. Mag A*, **50**, 143, (1984)

Duffy D.M., Tasker P.W., *Phil. Mag. A*, **54**, 759, (1986)

Dunski H., Jozwiak W.K., Sugier H., *J. Catal*, **146**, 166, (1994)

Duriez C., Chapon C., Henry C.R., Richard J.M., *Surf. Sci.*, **230**, 123, (1990)

Dyke T.R., Mack K.M., Muenter J.S., *J. Chem. Phys.*, **66**, 498, (1977)

Einspahr H., Bugg C.E., *Acta Cryst. B*, **36**, 264, (1980)

Ewald P.P., *Ann. Physik*, **64**, 253, (1921)

Fahmi A., Minot C., *Surf. Sci.*, **304**, 343, (1994)

Falini G., Albeck S., Weiner S., Addadi L., *Science*, **271**, 67, (1996)

Faux I.D., *J. Physics C*, **4**, L211, (1971)

Ferneyhough R., Fincham D., Price G.D., Gillan M.J., *Modell. Simul. Mater. Sci. Eng.*, **2**, 1101, (1994)

Firment L.E., *Surf. Sci.*, **116**, 205, (1982)

Fletcher R. and Powell M.J.D., *Computer J.*, **6**, 16, (1963)

Fletcher R. and Reeves C.M., *Computer J.*, **7**, 149, (1964)

Forbes R.T., York P., Fawcett V., Shields L., *Pharmaceut. Res.*, **9**, 1428, (1992)

Forester T.R., Smith W., *DL_POLY user manual*, CCLRC, Daresbury Laboratory, Daresbury, Warrington, UK, (1995)

Franks F., *The Physics and Physical Chemistry of Water*, Plenum Press, London, (1976)

Freeman C.M., Newsam J.M., Levine S.M., Catlow C.R.A., *J. Mater. Chem.*, **3(5)**, 531, (1993)

Fubini B., Bolis V., Bailes M., Stone F., *Solid State Ionics*, **32/33**, 258, (1989)

Gale J.D., Catlow C.R.A., Mackrodt W.C., *Model. Simul. Mater. Sci. Eng.*, **1**, 73, (1992)

Gale J.D., *Phil. Mag. B.*, **73**, 3, (1996)

Gale J.D., *J. Chem. Soc. Faraday Trans.*, **93**, 629, (1997)

Gay D.H., Rohl A.L., *J. Chem. Soc. Faraday Trans.*, **91**, 925, (1995)

Gear C.W., *Numerical Initial Value Problems in Ordinary Differential Equations*, Prentice-Hill, Englewood Cliffs, New Jersey, (1971)

Gerson A.R., Smart R.St.C., *Proceedings of International Workshop on Interfaces in Ceramic Materials*, in press, (1997)

Gibbs J.W., *Collected works,* Longman, New York, (1928)

Gillan M.J., Dixon M.J., *J. Phys. C*, **13**, 1901, (1980)

Gilman J.J., *J. Applied Phys.*, **31**, 2208, (1960)

Godin T.J., LaFemina J.P., *Phys. Rev. B*, **49**, 7691, (1994)

Goni S., Sobrado L., Hernandez M.S., *Solid State Ionics*, **63**, 786, (1993)

Goniakowski J., Bouette-Russo S., Noguera C., *Surf. Sci.*, 284, 315, (1993)

Goniakowski J., Noguera C., *Surf. Sci.*, **330**, 337, (1995)

Goniakowski J., Holender J.M., Kantorovich L.N., Gillan M.J., *Phys. Rev. B*, **53**, 957, (1996)

Goniakowski J., Gillan M.J., *Surf. Sci.*, **350**, 145, (1996a)

Gordon R.G. and Kim Y.S., *J. Chem. Phys.*, **56**, 3122, (1972)

Gorling A., Ackermann L., Lauber J., Knappe P., Rosch N., *Surf. Sci.*, **286**, 26, (1993)

Gratz A.J., Hillner P.E., Hansma P.K., *Geochim. Cosmochim. Acta*, **57**, 491, (1993)

Guo J., Ellis D.E., Lam D.J., *Phys. Rev. B*, **45**, 13647, (1992)

Guo X., Canney S., Kheifets A.S., Vos M., Fang Z., Utteridge S., McCarthy I.E., Weigold E., *Phys. Rev. B*, **54**, 17943, (1996)

Harding J.H., *Technical Report AERE R 13217*, Harwell, (1988)

Harding J.H., Parker S.C., Tasker P.W., *Non-Stoichiometric Compounds, Surfaces and Grain Boundaries and Structural Defects*, ed. J. Nowotny and W. Weppner, UKAEA, Harwell, (1989)

Harding J.H., *Rep. Prog. Phys.*, **53**, 1403, (1990)

Harding J.H., Pyper N.C., *Phil. Mag. Letters*, **71**, 113, (1995)

Harding J.H., *Computer Modelling in Inorganic Crystallography*, ed. C.R.A. Catlow, Academic Press, London, (1997)

Hargreaves J.S.J., Hutchings G.J., Joyner R.W., Kiely C.J., *J. Catalysis*, **135**, 576, (1992)

Harms A.C., Khanna S.N., Chen B., Castleman Jr. A.W., *J. Chem. Phys.*, **100**, 3540, (1994)

Hartman P., Bennema P., *J. Cryst. Growth*, **49**, 145, (1980)

Hayes D.M., Barber M. and Clarke J.H.R., *J. Chem. Soc. Faraday Trans.*, **10**, 1485, (1977)

Heggie M.I., Latham C.D., Maynard S.C.P., Jones R., *Chem. Phys. Lett.*, **249**, 485, (1996)

Henrich V.E., *Surf. Sci.*, **57**, 385, (1976)

Heywood B.R., Mann S., *Chem. Mater.*, **6**, 311, (1994)

Hillner P.E., Manne S., Hansma P.K., *Faraday Discuss.*, **95**, 191, (1993)

Hochella M.F., Eggleston C.M., Elings V.G., Thompson M.S., *Am. Miner.*, **75**, 723, (1990)

Hockney R.W., *Methods Comput. Phys.*, **9**, 136, (1970)

Hoover W.G., *Phys. Rev. A*, **31**, 1695, (1985)

Hugenschmidt M.B., Gamble L., Campbell C.T., *Surf. Sci.*, **302**, 329, (1994)

Ito T., Tashiro T., Kawasaki M., Watanabe T., Toi K., Kobayashi H., *J. Phys. Chem.*, **95**, 4476, (1991)

Jackson R.A., Price G.D., *Mol. Simul.*, **9**, 175, (1992)

Jacobs P.W.M., Kotomin E.A., *J. Am. Ceram. Soc.*, **77**, 2505, (1994)

Jacobs P.W.M., Rycerz Z.A., *Computer Modelling in Inorganic Crystallography*, ed. C.R.A. Catlow, Academic Press, London, (1997)

Jensen K., *Z. Phys*, **101**, 141, (1936)

Johnson D.A., *Some Thermodynamic Aspects of Inorganic Chemistry*, 2nd ed., University Press, Cambridge, (1982)

Jones C.F., Reeve R.A., Rigg R., Segall R.L., Smart R.St.C., Turner P.S., *J. Chem. Soc. Faraday Trans. I*, **80**, 2609, (1984)

Jorgensen W.L., Chandrasekhar J., Madura J.D., Impey R.W., Klein M.L., *J. Chem. Phys.*, **79**, 926, (1983)

Jorgensen W.L., *J. Am. Chem. Soc.*, **103**, 335, (1981)

Jorgensen W.L., *J. Chem. Phys.*, **77**, 4156, (1982)

Kabasci S., Althaus W., Weinspach P.-M., *Trans. Inst. Chem. Eng.* A, **74**, 765, (1996)

Kamb B., *Trans. Amer. Cryst. Assoc.*, **5**, 61, (1969)

Kamb B., Davis B.L., *Proc. of the Nat. Ac. of Sciences*, **52**, 1433, (1964)

Kamb B., *Water and Aqueous Solutions*, edited by R.A. Horne, John Wiley & Sons Inc., New York , (1972)

Kantorovich L.N., Holender J.M., Gillan M.J., *Surf. Sci.*, **343**, 221, (1995)

Kato K., Saalfeld H., *Acta Cryst. B*, **33**, 1596, (1977)

Katz J.L., Reick M.R., Herzog R.E., Parsiegla K.I., *Langmuir*, **9**, 1423, (1993)

Kenway P.R., Parker S.C., Mackrodt W.C., *Molecular Simulations*, **4**, 175, (1989)

Kenway P.R., Oliver P.M., Parker S.C., Sayle D.C., Sayle T.X.T., Titiloye J.O., *Mol. Simul.*, **9**, 83, (1992)

Kenway P.R., *Phil. Mag.*, *Phil. Mag. B*, **68**, 171, (1993)

Kenway P.R., *J. Am. Ceram. Soc.*, **77**, 349, (1994)

Kim D.-Y., Wiederhorn S.M., Hockey B.J., Handwerker C.A., Blendell J.E., *J. Am. Ceram. Soc.*, **77**, 444, (1994)

Kim Y., Cygan R.T., Kirkpatrick R.J., *Geochim. Cosmochim. Acta*, **60**, 1041, (1996)

Kittaka S., Sasaki T., Fukuhara N., Kato H., *Surf. Sci.*, **282**, 255, (1993)

Kittel C., *Introduction to Solid State Physics*, John Wiley & Sons Inc., New York, (1963)

Klepeis J.E., Terminello L.J., Lapiano-Smith D.A., *Phys. Rev. B*, **53**, 16035, (1996)

Kobayashi H., Yamaguchi M., Ito T., *J. Phys. Chem.*, **94**, 7206, (1990)

Kruse C., Finnis M.W., Lin J.S., Payne M.C., Milman V.Y., De Vita A., Gillan M.J., *Phil. Mag. Lett.*, **73**, 377, (1996)

Krynicki K., Green C.D., Sawyer D.W., *Faraday Discuss. Chem. Soc.*, **66**, 199, (1978)

Kuhs W.F., Finney J.L., Vettier C., Bliss D.V., *J. Chem. Phys.*, **81**, 3612, (1984)

La Placa S.J., Hamilton W.C., *J. Chem. Phys.*, **58**, 567, (1972)

LaFemina J.P., *Surf. Sci. Rep.*, **16**, 133, (1992)

Langel W., Parrinello M., *Phys. Rev. Lett.*, **73**, 504, (1994)

Langel W., Parrinello M., *J. of Chem. Phys.*, **103**, 337, (1995)

Lau K.F., Alper H.E., Thacher T.S., Stouch T.R., *J. Phys. Chem.*, **98**, 8785, (1994)

Lawrence P.J., *PhD Thesis*, University of Bath, (1988)

de Leeuw N.H., Watson G.W., Parker S.C., *J. Phys. Chem.*, **99**, 17219, (1995)

de Leeuw N.H., Watson G.W., Parker S.C., *J. Chem. Soc. Faraday Trans.*, **92**, 2081, (1996)

de Leeuw N.H., Parker S.C., *J. Chem. Soc. Faraday Trans.*, **93**(3), 467, (1997)

Leslie M., *SERC Daresbury Report* DL/SCI/TM31T, (1982)

Leslie M., *SERC Daresbury Laboratory Report DL/SCI-TM31T*, (1981)

van Leuken H., Lodder A., de Groot R.A., *Phys. Rev. B*, **45**, 4469, (1992)

Lewis G.V. and Catlow C.R.A., *J. Phys. C: Solid State Phys.*, **18**, 1149, (1985)

Li C., Li G., Xin Q., *J. Phys. Chem.*, **98**, 1933, (1994)

Liang Y., Lea A.S., Baer D.R., Engelhard M.H., *Surf. Sci.*, **351**, 172, (1996)

Liang Y., Baer D.R., McCoy J.M., Amonette J.E., LaFemina J.P., *Geochim. Cosmochim. Acta*, **60**, 4883, (1996a)

Lidiard A.B., Norgett M.J., *Computational Solid State Physics*, Ed. Herman, Dalton, Koehler, Plenum, (1972)

Lindman P.J.D., Gillan M.J., *J. Phys.: Condens. Matter*, **5**, 1019, (1993)

Litvin A.L, Samuelson L.A., Charych D.H., Spevak W., Kaplan D.L., *J. Phys. Chem.*, **99**, 12065, (1995)

Lo W.J., Somorjai Y.W.Ch.G.A., *Surf. Sci.*, **71**, 199, (1978)

MacInnes I.N., Brantley S.L., *Geochim. Cosmochim. Acta*, **56**, 1113, (1992)

Mackrodt W.C., Stewart R.F., *J. Phys. C*, **12**, 431, (1979)

Mackrodt W.C., Stewart R.F., Campbell J.C., Hillier I.H., *J. Phys. (Paris)*, **C6**, 64, (1980)

Mackrodt W.C., Davey R.J., Black S.N., Docherty R., *J. Cryst. Growth*, **80**, 441, (1987)

Mackrodt W.C., *J. Chem. Soc. Faraday Trans. 2*, **85**, 541, (1989)

Mackrodt W.C., *Phil. Trans. R. Soc. Lond. A*, **341**, 301, (1992)

Mackrodt W.C., Harrison N.M., Saunders V.R., Allan N.L., Towler M.D., Apra E., Dovesi R., *Phil. Mag. A*, **68**, 653, (1993)

Manassidis I., Gillan M.J., *J. Am. Ceram. Soc.*, **77**, 335, (1994)

Mann S., Heywood B.R., Rajam S., Birchall J.D., *Nature*, **334**, 692, (1988)

Marechal Y., *J. Phys. Chem.*, **97**, 2846, (1993)

Maurice V., Talah H., Marcus P., *Surf. Sci. Letters*, **284**, 431, (1993)

McCoy J.M., LaFemina J.P., *Surf. Sci.*, **373**, 288, (1997)

McFarlan R.L., *J. Chem. Phys.*, **4**, 60, (1936)

McHale J.M., Navrotsky A., Perrotta A.J., *J. Phys. Chem. B*, **101**, 603, (1997)

Meyer H.J., *Fortschritte der Mineralogie*, **38**, 186, (1960)

Mijoule C., Bouteiller Y., *Surf. Sci.*, **253**, 375, (1991)

Mills G.E., Hernandez E., *Fungus v1.1β Manual*, Royal Institution, London, (1993)

Mitchell P.J., Fincham D., *J. Phys.: Condens. Matter*, **5**, 1031, (1993)

Mott N.F., Littleton M.J., *Trans. Faraday Society*, **34**, 485, (1938)

Muhlhausen C., Gordon R.G., *Phys. Rev. B*, **23**, 900, (1981)

Mulheran P.A., *Phil. Mag. A*, **68**, 799, (1993)

Murray P.W., Leibsle F.M., Fisher H.J., Flipse C.F.J., Muryn C.A., Thornton G., *Phys. Rev. B*, **46 (19)**, 12877, (1992)

Muryn C.A., Tirvengadum G., Crouch J.J., Warburton D.R., Raiker G.N., Thornton G., Law D.S-L., *J. Phys.: Condens. Matter* , **1**, 127, (1989)

Narten A.H., Levy H.A., *J. Chem. Phys.*, **55**, 2263, (1971)

Nassralla-Aboukais N., Boughriet A., Fischer J.C., Wartel M., Langelin H.R., Aboukais A., *J. Chem. Soc. Faraday Trans.*, **92**, 3211, (1996)

Neddermeyer H., *Scanning Tunneling Microscopy*, Kluwer Academic Publishers, Dordrecht, Netherlands, (1993)

Noguera C., Goniakowski J., Bouette-Russo S., *Surf. Sci.*, **287/288**, 188, (1993)

Norgett M.J., *J. Physics C*, **4**, 298, (1971)

Norgett M.J., *Technical Report R7650*, Harwell Laboratory, (1974)

Nose S., *J. Chem. Phys.*, **81**, 511, (1984)

Nygren M.A., Petterson L.G.M., *J. Chem. Phys.*, **105**, 9339, (1996)

Nygren M.A., Gay D.H., Catlow C.R.A., *Surf. Sci.*, **380**, 113, (1997)

Odutola J.A., Dyke T.R., *J. Chem. Phys.*, **72**, 5062, (1980)

Ohnesorge F., Binnig G., *Science*, **260**, 1451, (1993)

Ohtani H., Wilson R.J., Chiang S., Mate C.M., *Phys. Rev. Lett.*, **60**, 2398, (1988)

Oliver P.M., Parker S.C., Mackrodt W.C., *Modelling Simul. Mater. Sci. Eng.*, **1**, 755, (1993)

Oliver P.M., *PhD Thesis*, University of Bath, (1994)

Oliver P.M., Parker S.C., Purton J., Bullett D.W., *Surf. Sci.*, **307**, 1200, (1994a)

Oliver P.M., Watson G.W., Parker S.C., *Phys. Rev. B*, **52**, 5323, (1995)

Onishi H., Egawa C., Aruga T., Iwasawa Y., *Surf. Sci.*, **191**, 479, (1987)

Pacchioni G., Clotet A., Ricart J.M., *Surf. Sci.*, **315**, 337, (1994)

Pacchioni G., Ferrari A.M., Bagus P.S., *Surf. Sci.*, **350**, 159, (1996)

Park N.-S., Kim M.-W., Langford S.C., Dickinson J.T., *J. Appl. Phys.*, **80**, 2680, (1996)

Parker S.C., *Solid State Ionics*, **8**, 179, (1983)

Parker S.C., *PhD thesis*, University College London, (1983a)

Parker S.C., Price G.D., *Advances in Solid State Chemistry*, **1**, 295, (1989)

Parker S.C., Kelsey E.T., Oliver P.M., Titiloye J.O., *Faraday Discuss.*, **94**, 75, (1993)

Parker S.C., Titiloye J.O., Watson G.W., *Phil. Trans. R. Soc. Lond. A*, **344**, 37, (1993a)

Parry, D.E., *Surf. Sci.*, **49**, 433, (1975)

Parry D.E., *Surf. Sci.*, **54**, 195, (1976)

Pavese A., Catti M., Parker S.C., Wall A., *Phys. Chem. Miner.*, **23**, 89, (1996)

Payne M.C., Stich I., De Vita A., Gillan M.J., Clarke L.J., *Faraday Discuss.*, **96**, 151, (1993)

Petch H.E., *Acta Crystallographica*, **1**, 1948, (1967)

Picaud S., Hoang P.N.M., Girardet C., *Surf. Sci.*, **278**, 339, (1992)

Prutton M., *Surface Physics*, Oxford University Press, Oxford, (1983)

Pugh S., Gillan M.J., Surf. Sci., **320**, 331, (1994)

Rajam S., Mann S., *J. Chem. Soc. Chem. Commun.*, 1789, (1990)

Ramamoorthy M., King-Smith R.D., Vanderbilt D., *Phys. Rev. B*, **49**, 7709, (1994)

Ramamoorthy M., Vanderbilt D., King-Smith R.D., *Phys. Rev. B*, **49**, 16721, (1994)

Ramos M.M.D., Stoneham A.M., Sutton A.P., Pethica J.B., *J. Phys.: Condens. Matter*, **2**, 5913, (1990)

Refson K., Wogelius R.A., Fraser D.G., Payne M.C., Lee M.H., Milman V., *Phys. Rev. B - Condens. Matter*, **52**, 10823, (1995)

Refson K., private communication, (1997)

Rick S.W., Stuart S.J., Berne B.J., *J. Chem. Phys.*, **101**, 6141, (1994)

Romanek C.S., Grossman E.L, Morse J.W., *Geochim. Cosmochim. Acta*, **56**, 419, (1992)

Rossi P.F., Oliveri G., Bassoli M., *J. Chem. Soc. Faraday Trans.*, **90**, 363, (1994)

Sander M., Engel T., *Surf. Sci. Letters*, **302**, 263, (1994)

Sanders M.J., Leslie M., Catlow C.R.A., *J. Chem. Soc. Chem. Commun.*, 1271, (1984)

Sangster M.J.L., Stoneham A.M., *Phil. Mag.*, **43**, 597, (1980)

Saul P., Catlow C.R.A., Kendrick J., *Phil. Mag. B*, **51**, 107, (1985)

Sayle D.C., *PhD thesis*, University of Bath, (1992)

Sayle T.X.T., Parker S.C., Catlow C.R.A., *Surface Science*, **316**, 329, (1994)

Scamehorn C.A., Hess A.C., McCarthy M.I., *J. Chem. Phys.*, **99**, 2786, (1993)

Scamehorn C.A., Harrison N.M., McCarthy M.I., *J. Chem. Phys.*, **101**, 1547, (1994)

Schroer P., Kruger P., Pollman J., *Phys. Rev. B*, **49**, 17092, (1994)

Shen G., Lazor P., *J. Geophys. Research*, **100**, 17699, (1995)

Schroder K.P., Sauer J., Leslie M., Catlow C.R.A., Thomas J.M., *Chem. Phys. Lett.*, **188**, 320, (1992)

Skinner A.J., La Femina J.P., Jansen H.J.F., *Am. Mineral.*, **79**, 205, (1994)

Skipper N.T., Soper A.K., Smalley M.V., *J. Phys. Chem.*, **98**, 942, (1994)

Soper A.K., Phillips M.G., *Chem. Phys.*, **107**, 47, (1986)

Stauffer L., Mharchi A., Saintenoy S., Pirri C., Wetzel P., Bolmont D., Gewinner G., *Phys. Rev. B*, **52**, 11932, (1995)

Stewart R.F., Mackrodt W.C., *J. Phys. C Solid State Phys.*, **10**, 1431, (1977)

Stich I., De Vita A., Payne M.C., Gillan M.J., Clarke L.J., *Phys. Rev. B*, **49**, 8076, (1994)

Stillinger F.H., Rahman A., *J. Chem. Phys.*, **60**, 1545, (1974)

Stipp S.L., Hochella M.F., *Geochim. Cosmochim. Acta*, **55**, 1723, (1991)

Stipp S.L., Gutmannsbauer W., Lehmann T., *Am. Mineral.*, **81**, 1, (1996)

Stoneham A.M., *Defects and their Structure in Non-metallic Solids*, edited by B. Henderson and A.E. Hughes, Plenum, New York, (1976)

Streitz F.H., Mintmire J.W., *Phys. Rev. B*, **50**, 11996, (1994)

Suzuki T., Inomata S., Sawada K., *J. Chem. Soc. Faraday Trans. I*, **82**, 1733, (1986)

Swanston D.M., McLean A.B., McIlroy D.N., Heskett D., Ludeke R., Munekata H., Prietsch M., DiNardo N.J., *Surf. Sci.*, **312**, 361, (1994)

Tasker P.W., *Technical Report AERE R9130*, AERE Harwell, (1978)

Tasker P.W., *Phil. Mag. A*, **39**, 119, (1979)

Tasker P.W., *J. Phys. C: Solid State Physics*, **12**, 4977, (1979a)

Tasker P.W., Duffy D.M., *Surf. Sci.*, **137**, 91, (1984)

Tasker P.W., Colbourn E.A., Mackrodt W.C., *J. Am. Ceram. Soc.*, **68**, 74, (1985)

Tauson V.L., Abramovich M.G., Akimov V.V., Scherbakov V.A., *Geochim. Cosmochim. Acta*, **57**, 815, (1993)

Titiloye J.O., Parker S.C., D.J. Osguthorpe, S. Mann, *J. Chem. Soc. Chem. Commun.*, **20**, 1494, (1991)

Titiloye J.O., Parker S.C., Mann S., *J. Cryst. Growth*, **131**, 533, (1993)

Tonejc A., Stubicar M., Tonejc A.M., Kosanovic K., Subotic B., Smit I., *J. Mater. Sci. Lett.*, **13**, 519, (1994)

Trokhymchuk A.D., Holovko M.F., Heinzinger K., *J. Chem. Phys*, **99**, 2964, (1993)

Tsuchida T., Ohta S., Horigome K., *J. Mater. Chem.*, **4**, 1503, (1994)

Varma S., Chen X., Zhang J., Davoli I., Saldin D.K., Tonner B.P., *Surf. Sci.*, **314**, 145, (1994)

Verlet L., *Phys. Rev.*, **159**, 98, (1967)

Vitek V., *MRS Bulletin*, **21**, 20, (1996)

Voter A.F., *MRS Bulletin*, **21**, 17, (1996)

Walsh D., Mann S., *Nature*, **377**, 320, (1995)

Watson G.W., Parker S.C.,Wall A., *J. Phys. Cond. Matter*, **4**, 2097, (1992)

Watson G.W., *PhD thesis*, University of Bath, (1994)

Watson G.W., Kelsey E.T., de Leeuw N.H., Harris D.J. and Parker S.C., *J. Chem. Soc., Faraday Trans.*, **92**, 433, (1996)

Watson G.W., Tschaufeser P., Wall A., Jackson R.A., Parker S.C., *Computer Modelling in Inorganic Crystallography*, ed. C.R.A. Catlow, Academic Press, London, (1997)

Weast R.C., Astle M.J., *CRC Handbook of Chemistry and Physics, CRC Press Inc.*, Boca Raton, USA, (1981)

Wilson M., Madden P.A., *J. Phys.: Condens. Matter*, **6**, 159, (1994)

Wilson M., Madden P.A., *J. Phys.: Condens. Matter*, **6**, A151, (1994)

Wilson M., Madden P.A., Costa-Cabral B.J., *J. Phys. Chem.*, **100**, 1227, (1996)

Wilson M., Exner M., Huang Y.-M., Finnis M.W., *Phys. Rev. B*, **54**, 15683, (1996a)

Woensdregt C.F., *Phys. Chem. Miner.*, **19**, 52, (1992)

Wong K.K.W., Brisdon B.J., Heywood B.R., Hodson A.G.W., Mann S., *J. Mater. Chem.*, **4**, 1387, (1994)

Wright K., Freer R., Catlow C.R.A., *Phys. Chem. Miner.*, **20**, 500, (1994)

Wu M-C, Estrada C.A., Corneille J. L., Goodman D. W., *J. Chem. Phys.*, **96**, 3892, (1992)

Wulff G., *Z. Kristallogr. Kristallgeom.*, **39**, 449, (1901)

Zhu S-B., Wong C.F., *J. Phys. Chem.*, **98**, 4695, (1994)